IMMANUEL KANT BALTIK FEDERAL UNIVERSITY
SEMENOV INSTITUTE OF CHEMICAL PHYSICS, RAS
PUSHKOV INSTITUTE OF TERRESTRIAL MAGNETISM, IONOSPHERE
AND RADIO WAVE PROPAGATION, RAS
RUSSIAN FOUNDATION FOR BASIC RESEARCH

ATMOSPHERE, IONOSPHERE, SAFETY

Proceedings
of IV International conference

Kaliningrad
2014

UDK 550.51
BBK 552.44
A92

A92 **Atmosphere, ionosphere, safety** / Supported by Russian Foundation of Basic Research ; ed. I. V. Karpov. — Kaliningrad, 2014. — 267 p.
ISBN 978-5-9971-0313-2

Proceedings of International Conference "Atmosphere, ionosphere, safety" (AIS-2014) include materials reports on: (I) — response analysis of the atmosphere — ionosphere to natural and manmade processes, various causes related geophysical phenomena and evaluate possible consequences of their effects on the human system and process; (II) — to study the possibility of monitoring and finding ways to reduce risk. Scientists from different countries and regions of Russia participated in the conference. Attention was given to questions interconnected with modern nanotechnology and environmental protection. Knowledge of the factors influencing the atmosphere and ionosphere can use them to monitor natural disasters and to establish the appropriate methods on this basis.

Content of the reports is of interest for research and students specializing in physics and chemistry of the atmosphere and ionosphere.

UDK 550.51
BBK 552.44

ISBN 978-5-9971-0313-2

The IV International conference "Atmosphere, ionosphere, safety" is the fourth event of the newly organized sequel. And again we are meeting at the same place, where previous three conferences AIS (2008, 2010, 2012) took place. The place that we have chosen for this conference, have admired the participants of AIS. Frankly speaking, this is not the only reason the convenience for the organizers is evident. But we are pretty sure that even those who visited us once would wish to update their good impressions on these absolutely wonderful places. But still we are here are not (only) for our amusement. Simply, as shown our not yet rich experience, these peaceful landscapes and the sand of the Baltic sea shore promote hot scientific discussions. We believe that the problems that will be considered here will be of central interests in the very near future.

The present meeting is devoted to:

(i) analysis of the atmosphere-ionosphere response on natural and man-made processes, the reasons of occurrence of the various accompanying geophysical phenomena, and an estimation of possible consequences of their influence on the person and technological systems;

(ii) study of the monitoring possibility and search of the ways for the risk level decrease. Discussion of the physical and chemical processes accompanying the observable geophysical phenomena is supposed.

The physical and chemical phenomena proceeding in the upper atmosphere and the ionosphere occur in the conditions and the scales which are not available in usual laboratories. Problems existing here are of interest for a wide range of the investigators working in various areas of a science and techniques. For example, they include such problems as a precision of satellite navigation in various regimes of solar activity. They also include problems of radiochemical physics as well as its various implications. They include the measurements of ocean water salinity, humidity of soils, the state of plant cover, weather forecast, and water balance of the Earth. It's necessary to carry out the additional researches which are connected with the high human activity in the atmosphere - ionosphere system, leading to occurrence of new risks. They concern with an active development of the manned and uninhabited orbital systems, aircraft, new kinds of communication, etc. Non-stationary atmosphere - ionosphere system is the subject of powerful natural affects. Its lower level is disturbed by earthquakes, volcanic eruptions, typhoons, thunder-storms. From above it is influenced by the geomagnetic storm. As a result of these processes such disturbing factors, as powerful atmospheric perturbations, electric currents, electromagnetic radiations in the various spectrum ranges, the plasma and optical disturbances, an accelerated particles, the increased level of a radioactivity, and changing of ionic and molecular components. Besides, the microwave radiation of highly excited particles of the ionosphere accompanying the processes of increase of solar activity and appearance of the magnetic storms exerts negative influence on the mankind. The knowledge of the influencing factor origin allows to use them for disaster monitoring and to create the corresponding techniques on this base. Great attention should also be given to the issues interrelated with modern nanotechnology, and environmental protection.

ORGANIZING COMMITTEE

Chairs

A. A. Berlin	ICP RAS, Moscow (RU)
M. G. Golubkov (vice)	ICP RAS, Moscow (RU)

E. N. Golubeva	MSU, Moscow (Russia)
A. A. Gribankova	I. Kant Baltic Fed. Univ., Kaliningrad (RU)
I. V. Karpov	I. Kant Baltic Fed. Univ., Kaliningrad (RU)
M. Y. Melnikov	MSU, Moscow (Russia)
A. I. Nikitin	IEPCP, Moscow (RU)
A. D. Petrov	Cent. Chem. Phys. Atm., Moscow (RU)
I. I. Shagimuratov	WD IZMIRAN, Kaliningrad (RU)
A. V. Yurov	I. Kant Baltic Fed. Univ., Kaliningrad (RU)
I. N. Chudnovskaya	MSU, Moscow (Russia)

INTERNATIONAL ADVISORY COMMITTEE

Chairs

G. V. Golubkov	ICP RAS, Moscow (RU)

N. Alonso-Vante	Univ. de Poitiers, Poitiers (FR)
R. J. Buenker	UW, Wuppertal (DE)
V. L. Bychkov	MSU, Moscow (Russia)
D. K. Callebaut	UAntwerp, Antwerp (Belgium)
L. S. Chudnovsky	ICP RAS, Moscow (Russia)
A. Z. Devdariani	SPbU, Saint-Petersburg (Russia)
G. C. Dijkhuis	TU, Eindhoven (Netherlands)
S. M. Frolov	ICP RAS, Moscow (RU)
V. L. Frolov	Radio Phys. Res. Inst., N.-Novgorod (RU)
G. Grampp	TU, Graz (AT)
M. Hayakawa	UEC, Tokyo (JP)
K. Hattori	Chiba University, Chiba (JP)
A. I. Kokorin	ICP RAS, Moscow(RU)
A. A. Lushnikov	ICP RAS, Moscow (RU)
I. I. Morozov	ICP RAS, Moscow (RU
A. A. Namgaladze	MSTU, Murmansk (RU)
M. Parrot	LPCE/CNRS (FR)
G. Peach	UCL, London (UK)
F. Rebentrost	Max-Planck Inst. Quantenopt., Munich (DE)
B. M. Shevtsov	ICRR WP (RU)
W. Trommer	TU, Kaiserslautern (DE)

CONTENTS

Plenary sessions (PL)

Section D: Ionosphere dynamics and atmosphere — ionosphere coupling(D)

Section P: Electromagnetic and optical phenomena in the atmosphere including long-lived and plasma objects (P)

Section S: Information systems of the environment monitoring and the accident prevention (S)

Poster sessions (Post)

PL-1

On the Conductivity and External Electric Currents in the Global Electric Circuit

Alexander A. Namgaladze, Mikhail I. Karpov

Physics Department, Murmansk State Technical University,
Sportivnaya st. 13, 183010, Murmansk, Russia

The physics of the electrical charges transport in the global electric circuit (GEC) is considered. The GEC consists of the positively charged ionosphere and negatively charged Earth with the electric potential gradient of ~130 V/m at sea level. Thunderstorms and rain/shower clouds act as a generator in the GEC and produce upward electric current. The conduction electric current of ~2—3 pA/m^2 flows downward through the so called fair-weather regions. Total electric current in the GEC is ~1,8 kA [1].

The GEC is influenced by ionization of the neutral particles by the galactic cosmic rays and radioactive gases, such as radon. The negatively charged heavy particles produced due to the air ionization may act as a potential nucleus of water vapors and coagulate into big heavy drops which precipitate down under the action of the gravity force. The positively charged particles being lighter move upward with the rising fluxes of the warm air. Thus, the charge separation occurs under the action of the convectional transport and gravitational sedimentation of the charged particles, and the external electric current is generated. It is directed upward against the electric field between positively charged ionosphere and negatively charged Earth surface and produces additional electric potential difference between them. Under the conditions of polluted air with increased aerosol density this mechanism is more effective, because charges produced by the ionization interact with aerosols, and newly formed charges recombine with each other much slower than the primary charges. The greater ionization rate, air humidity and aerosol density, the more intense external electric current is generated.

It is known that during earthquake preparation radon density increases several times and thermal anomalies as well as clouds are often registered in the vicinity of the fault several days before the earthquakes [2—3]. We suppose that conditions over the active tectonic fault favour the increase of the external electric current. It leads to the generation of the additional electric fields registered by Intercosmos-Bulgaria-1300 and DEMETER satellites over regions with seismic activity [4—5], and the electromagnetic [$\boldsymbol{E} \times \boldsymbol{B}$] plasma drift causes the total electron content (TEC) disturbances over the epicenter and magnetically conjugated areas [6].

The numerical calculations using the Upper Atmosphere Model (UAM) shows that the external electric current density that four orders greater than conduction fair-weather current is required to produce the seismogenic electric fields in the ionosphere, which generate the TEC disturbances observed several days before significant earthquakes [7—8]. The external electric current density used in the UAM calculations agrees with the estimated values of seismogenic external electric current [9], electric current generated during rock stress [10] and currents associated with the thunderstorm activity [11—13].

In order to find out the accurate characteristics of the seismogenic electric current one have to solve jointly the set of coupled equations: the continuity, heat balance and momentum equations for all sorts of charged particles taking into consideration particles ionization, recombination, attachment of charges to aerosols as well as the action of the electric field, gravity and friction forces and pressure gradients. It means that it is impossible to model electric current over the faults responsible for the TEC variations before earthquakes taking into account solely conductivity current flowing under the action of the electric field and friction forces only [14—15].

1. M. J. Rycroft, K. A. Nicoll, K. L. Aplin and R. Giles Harrison, *Recent advances in global electric circuit coupling between the space environment and the troposphere*, Journal of Atmospheric and Solar-Terrestrial Physics, V. 90—91, 2012, pp. 198—211.

2. S. Pulinets and D. Ouzounov, *Lithosphere—Atmosphere—Ionosphere Coupling (LAIC) model — An unified concept for earthquake precursors validation*, Journal of Asian Earth Sciences, 2011, V. 41, I. 4—5, pp. 371—382.

3. G. Guangmeng and Y. Jie, *Three attempts of earthquake prediction with satellite cloud images*, Natural Hazards and Earth System Sciences, 2013, V. 13, pp. 91—95.

4. M. Gousheva, D. Danov, P. Hristov and M. Matova, *Ionospheric quasi-static electric field anomalies during seismic activity in August—September 1981*, Natural Hazards and Earth System Sciences, 2009, V. 9, pp. 3—15.

5. X. Zhang, X. Shen, S. Zhao, Lu Yao, X. Ouyang and J. Qian, *The characteristics of quasistatic electric field perturbations observed by DEMETER satellite before large earthquakes*, Journal of Asian Earth Sciences, 2014, V. 79, Part A, pp. 42—52.

6. A. A. Namgaladze, M. V. Klimenko, V. V. Klimenko, and I. E. Zakharenkova, *Physical Mechanism and Mathematical Modeling of Earthquake Ionospheric Precursors Registered in Total Electron Content*, Geomagnetism and Aeronomy, 2009, V. 49, No. 2, pp. 252—262.

7. A. A. Namgaladze, *Earthquakes and global electrical circuit,* Russian Journal of Physical Chemistry B, 2013, V. 7, I. 5, pp 589—593.

8. M. I. Karpov, A. A. Namgaladze, and O. V. Zolotov, *Modeling of Total Electron Content Disturbances Caused by Electric Currents between the Earth and the Ionosphere*, Russian Journal of Physical Chemistry B, 2013, V. 7, No. 5, pp. 594—598.

9. V. M. Sorokin, A. K. Yaschenko, A. K., V. M. Chmyrev, and M. Hayakawa, *DC electric field amplification in the mid-latitude ionosphere over seismically active faults*, Natural Hazards and Earth System Sciences, 2005, V. 5, pp. 661—666.

10. F. Freund, I. G. Kulahci, G. Cyr, J. Ling, M. Winnick, J. Tregloan-Reed and M. Freund, *Air ionization at rock surfaces and pre-earthquake signals*, Journal of Atmospheric and Solar-Terrestrial Physics, 2009, V. 71, pp. 1824—1834.

11. R. J. Blakeslee, H. J. Christian and B. Vonnegut, *Electrical Measurements Over Thunderstorms*, Journal of Geophysical Research, 1989, V. 94, No. 13, pp. 13135—13140.

12. E. P. Krider and J. A. Musser, *Maxwell currents under thunderstorms*, Journal of Geophysical Research, 1982, V. 87, No. C13, pp. 11171—11176, 1982.

13. J. Le Mouel, D. Gibert and J. Poirier, *On transient electric potential variations in a standing tree and atmospheric electricity*, Comptes Rendus Geoscience, 2010, V. 342, No. 2, pp. 95—99.

14. R. G. Harrison, K. L. Aplin, M. J. Rycroft, *Atmospheric electricity coupling between earthquake regions and the ionosphere*, Journal of Atmospheric and Solar-Terrestrial Physics, 2010, V. 72, I. 5—6, pp. 376—381.

15. V. V. Denisenko, M. Ampferer, E. V. Pomozov, A. V. Kitaev, W. Hausleitner, G. Stangl and H. K. Biernat, *On electric field penetration from ground into the ionosphere*, Journal of Atmospheric and Solar-Terrestrial Physics, 2013, V. 102, pp. 341—353.

PL-2

Mesosphere: Where the Earth Faces the Space

Oleg S. Ugolnikov

Space Research Institute, Russian Academy of Sciences,
Profsoyuznaya st., 84/32, Moscow 117997 Russia

The lecture describes the properties of high neutral layer of the atmosphere, the mesosphere. Together with stratosphere, this layer plays the defending role for the life on the Earth: solar UV-radiation, the meteoroid streams are moderated there. Oxygen and ozone interaction with UV-rays creates two layers of heating in the atmosphere, forming its temperature distribution.

Vertical transport leads to the strong cooling in the summer mesosphere, which is the coldest place on the Earth. Temperature can fall below 150 K, giving the possibility for polar mesospheric (or noctilucent) icy clouds to be created. These clouds are regularly observed at the latitudes above 50°, but were never seen before 1885. The possible reason is cooling of summer mesosphere. It can be caused by human activity increasing the CO_2 amount in high atmosphere. Being the basic greenhouse gas in the troposphere, carbon dioxide plays the opposite role in the mesosphere, decreasing the temperature by the radiative cooling mechanism.

Direct investigations of the mesosphere are difficult since there is no possibility to place the measuring device into this layer for a long time. The basic method is the remote sensing from the satellites or from the ground. The least expensive measuring scheme is the twilight background analysis using wide-field polarization camera [1]. The accuracy of temperature measurements between 70 and 85 km is comparable with present satellite data.

Polarization measurements also allow to detect the dust scattering in the mesosphere, which is present permanently and increases during the meteor streams activity. Dust is found to appear at the altitudes about 81—83 km, this is close to the average altitude of noctilucent clouds. Meteor dust seems to be the basic source of condensation nuclei for the cloud icy particles.

The work is supported by Russian Foundation for Basic Research, grant No. 12-05-00501-a.

1. O.S. Ugolnikov and I.A. Maslov. Summer mesosphere temperature distribution from wide-angle polarization measurements of the twilight sky. Journal of Atmospheric and Solar-Terrestrial Physics, 2013, v. 105—106, pp. 8—14.

PL-3

Principle of Locality and Modernization of Radio Occultation Method for Remote Sensing of the Earth and Planets

Alexander G. Pavelyev[1], Stanislav S. Matyugov[1], Alexey A. Pavelyev[1]

[1] Kotelnikov' Institute of Radio Engineering and Electronics Russian Academy of Sciences Fryazino Branch Vvedenskogo sq. 1 Fryazino Moscow Region 141190 Russia

Summary. Principle of locality is introduced for modernization of the radio occultation (RO) remote sensing technology as applied for investigation of the atmospheres and ionospheres of the Earth and planets. According to this principle a neighborhood of a tangential point where the refractivity gradient is perpendicular to the radio ray trajectory introduces the main contribution to variations of the amplitude and phase of the radio waves passed through a layered medium. The derivatives on time of the RO signal phase and Doppler frequency variations can be recalculated into the refractive attenuation if the positions of a tangent point or centre of spherical symmetry are known relative to locations of the RO transmitter and receiver. If absorption effect in the layered medium is absent the principle of locality establishes an equality between the refractive attenuations found from the RO signal intensity and phase variations. Several important findings are consequences of the locality principle: (i) if position of the center of symmetry is known then the total absorption along the ray path can be determined; (ii) in the case of low absorption the height, displacement from the radio ray perigee, and tilt of the inclined ionospheric (atmospheric) layers can be determined; (iii) the contributions of the layered and irregular structures in the RO signal can be separated and parameters of layers and turbulence can be measured at a single frequency using joint analysis of the amplitude and phase variations. A new index of ionospheric activity is intro-

duced as measured from the phase of radio waves passed through the ionosphere and its high correlation with S4 scintillation index is established. This correlation indicates the significant influence of ionospheric layers on variations of characteristics of radio waves. Specially for the troposphere the altitude distributions of the weak total absorption (about of 1—2 db) of the radio waves at GPS frequencies in the Earth atmosphere corresponding to influence of the oxygen and water vapor is measured with accuracy better than 0.1 db. Obtained results expanded the applicable domain of the RO method.

Introduction. The Radio Occultation (RO) method is a powerful remote sensing tool applied during last 50 years for investigation of the atmospheres and surfaces of the Earth and planets [1]. Effectiveness of the RO method applied for investigation of the Earth's ionosphere can be compared with radio tomographic approach [2].Unlike the radio tomographic approach the RO method is based on the assumption of the spherical symmetry of the ionosphere and atmosphere [1]. This assumption implicitly utilizes the locality principle which previously has not been formulated explicitly. This basic principle is important for expanding the applicable domain and improving accuracy of the RO method.

Highly stable signals synchronized by atomic frequency standards and radiated by GPS satellites at frequencies of 1575.42 MHz and 1227.60 MHz, create at altitudes from 0 to 20,000 km global radio fields that can be used for modernization of the RO method and designing new tools for global monitoring of natural processes in the magnetosphere, ionosphere and neutral atmosphere.

An important connection between the intensity and derivatives on time of the phase, eikonal, Doppler frequency of radio waves propagating through the ionosphere and atmosphere has been found by theoretical analysis and confirmed by the processing of the RO radio-holograms [3—5]. This connection is a basis of the locality principle and allows, in particular, measuring the real height, slope, and displacement of Es-layers from the RO ray perigee. This connection allows, in principle, determining the position and orientation of the fronts of internal waves, which opens a new area of geophysical applications for remote sensing of the internal waves in the atmospheres and ionospheres of Earth and other planets [4].

Principle of locality. Formulation of the principle of locality can be derived using a connection [3,4], which relates the eikonal acceleration a and refractive attenuation $X_p(t)$ of RO signal emitted by a transmitter G and received by satellite L after passing through a spherically symmetric medium:

$$1 - X_p'(t) = m'a,\ a = \frac{d^2\Phi(t)}{dt^2} = \lambda\frac{dF_d(t)}{dt},\ m' = d_2'(1 - d_2'/R_0)/(dp_s'/dt)^2;\ p_s' = |O'D'|;\ \Phi(t) = \int_G^L n(l)dl - R_0 \quad (1)$$

where λ is the length of radio waves; and d_2', R_0 are the distances along the straight lines $D'L$ and GL, respectively; D' is the projection of the center of symmetry O' onto the line GL; $\Phi(t)$ is the difference of the eikonal of radio waves propagating along the trajectory GTL and length GL as a function of time t;

$n(l)$ is the refractive index; and dl is the differential length of the radio ray. The eikonal acceleration a (1) is proportional to the time derivative of the Doppler frequency of radio waves $F_d(t)$. Equality (1) is fulfilled under the following condition [4]:

$$\left|\left(p' - p_s'\right)\frac{dR_{1,2}'}{dt}\right| \ll \left|p_s'\frac{dp_s'}{dt}\right| \tag{2}$$

When absorption is absent, $X_p'(t)$ coincides with the refractive attenuation $X_a(t)$, which is determined using the RO amplitude data [3—7]:

$$X_p'(t) \equiv X_a(t)\,;\, X_a(t) = I / I_0 \tag{3}$$

where I_0 and I are the intensities of radio waves before and after the moment when the radio ray enters the medium. Identity (3) is fulfilled for the tangential point T', which is the perigee of the radio ray relative to the center of symmetry O'. Naturally, the refractive attenuation $X_a(t)$ measured from the RO intensity data does not depend on position of the point T' on the ray GTL. However the calculated value of the refractive attenuation $X_p'(t)$ does depend on the coefficient m' (1) and location of the tangent point T' on the ray GTL. This permits to formulate the principle of locality under the conditions of single ray radio wave propagation and absence of absorption [6,7]: **the refractive attenuations $X_p'(t)$ and $X_a(t)$ are equal if and only if the evaluation of $X_p'(t)$ are provided using coefficient m' corresponding to the centre of spherical symmetry O'.** According to the locality principle the amplitude and phase variations of radio waves registered at the point L may be considered as connected with influence of a small neighborhood of the ray perigee T' corresponding to the spherical symmetry centre O'.

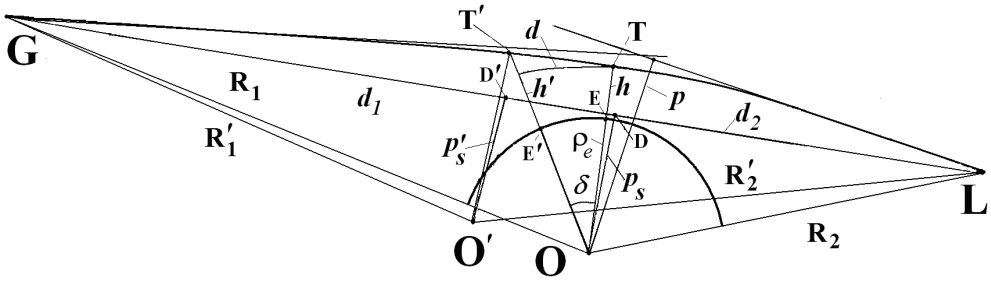

FIGURE 1. Scheme of radio occultation measurements.

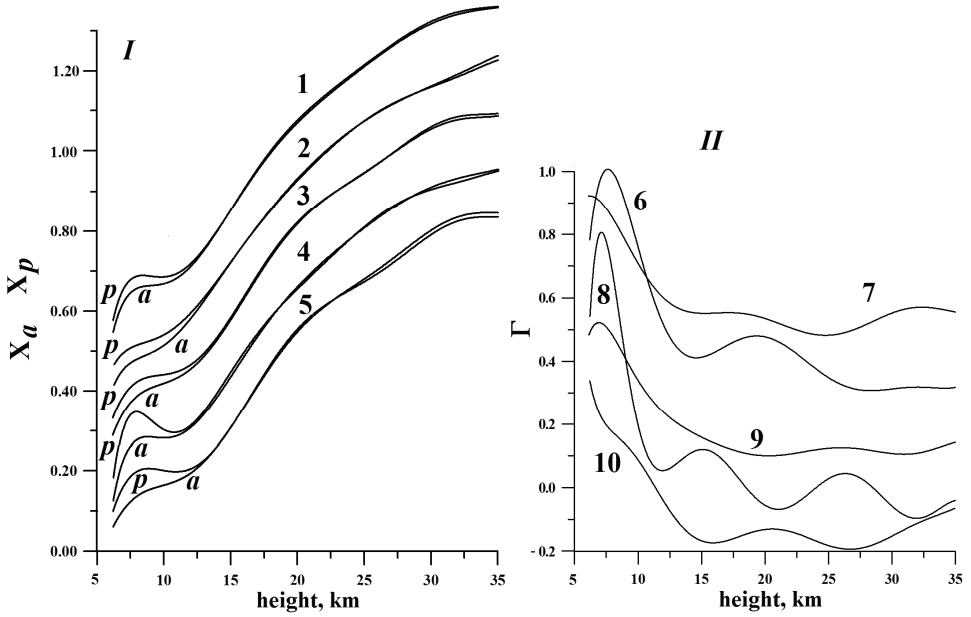

FIGURE 2. I. Comparison of the refractive attenuations $X_p(h)$, $X_a(h)$ (curves 1—5, indexes "p" and "a", respectively). Curves 1—4 are displaced for convenience by 0.6; 0.4; 0.2; 0.1. II. The total absorption Γ corresponding to the refractive attenuations $X_p(h)$, $X_a(h)$ calculated from curves 1—5 (right panel). Curves 6, 7, 9, and 10 are shifted for comparison. Minimum and maximum values of absorption Γ for curves 6—10 are equal to —0.1, 0.62; —0.01, 0.43; —0.1, 0.81; —0.064, 0.336; and —0.02, 0.46 db, respectively.

Consequences of the locality principle. Next important findings follow from the locality principle.

1. Determination of the total absorption. If position of the center of symmetry is known (for example, when the point O' coincides with the Earth's center O) then the total absorption Γ in the atmosphere (ionosphere) can be defined by eliminating from the measured value $X_a(t)$ the refractive attenuation found from the eikonal variations.

$$\Gamma = -10 \lg \frac{X_a(t)}{X_p(t)} \tag{4}$$

Fig. 2 (I) shows the vertical profiles of the attenuations $X_a(h)$ and $X_p(h)$ (curves *1—5*); Figure 2 (II) demonstrates the corresponding altitudinal depen dences of total absorption Γ, which were obtained from the data of five experiments that were carried out using the *CHAMP* satellite on June 16, 2003 (curves *6—10*). The measurement sessions correspond to the north polar regions: No. 122: 77.6° N, 141.0° W at 02:27 LT (local time); No. 173: 80.9° N, 337.1° W at 17:35 LT;

No. 0030: 77.9° N, 83.5° W at 20:59 LT; No. 0159: 83.0° N, 258.6° W at 21:40 LT; and No. 0203: 76.3° N, 37.9° W at 16:56 LT. The $X_a(h)$ and $X_p(h)$ profiles are almost coincident at heights between 12 and 30 km, and are noticeably different below 12 km (Figure 2(I)). This indicates that a weak but perceptible absorption with a mean value of Γ equal to 0.0096 ± 0.0024 db/km is present in the atmosphere, which corresponds to the RO data at the 32 cm wavelength [6] obtained on the *MIR*-geostationary satellites trans-ionospheric links, and coincides with the theoretical results [7].

2. Determination of the tilt, height, and displacement of the inclined layers. If the center of symmetry does not coincide with the point O, the principle of locality states: $X_a(t) \equiv X_p'(t)$. This allows finding, if absorption is absent, the displacement d of the tangential point T' with respect to the point T as well as the layer height h' and its inclination δ (Figure 1):

$$d = d_2' - d_2 = d_2 \frac{A_a - A_p}{A_p};\ d_2 = \sqrt{R_L^2 - p_s^2},\ h' = h + \Delta h,\ \Delta h = \frac{d\delta}{2},\ \delta = \frac{d}{r_e},\ r_e = |TO| \quad (5)$$

where A_a and A_a are the amplitudes of variations of the refractive attenuations $X_a(t)$ and $X_p(t)$, which are determined, for example, using the Hilbert numerical transform. The amplitude of refractive attenuation $X_p(t)$ is evaluated using coefficient m corresponding to the centre of Earth (or planet). The value of d is positive (or negative) depending on the sign of the difference $A_a - A_p$, with the point T' being located on the *GT* or *TL* lines, respectively. Relationship (5) is fulfilled if one of the satellites is much farther away from the center of symmetry than the other. This condition is usually satisfied during the Earth or planetary RO missions [4]. Examples of application of equation (5) for estimation of the location, inclination and real height of ionospheric layers are given in [6,7]. The standard definition of the perigee of the radio ray in the RO method as the minimal value of the distance to the surface of the ray path leads to an underestimation (bias) of layers altitude in the atmosphere (ionosphere) Earth and planets. This error is zero for horizontal layers and increases with their inclination.

3. Relationships between the eikonal variations and intensity scintillations index S4. Index S4 (I), as measured from intensity variations, should be correlated with index S4 (F), defined by the second derivative on time of the eikonal of the RO signal at GPS frequencies F1 and F2. According to the principle of locality in the case of spherical symmetric medium there exist the next connections:

$$S4(X_a) = \sqrt{\frac{\langle X_a^2 \rangle - \langle X_a \rangle^2}{\langle X_a \rangle^2}};\ S4(X_p) = \sqrt{\frac{\langle X_p^2 \rangle - \langle X_p \rangle^2}{\langle X_p \rangle^2}};\ S4(X_a) \equiv S4(X_p) \quad (6)$$

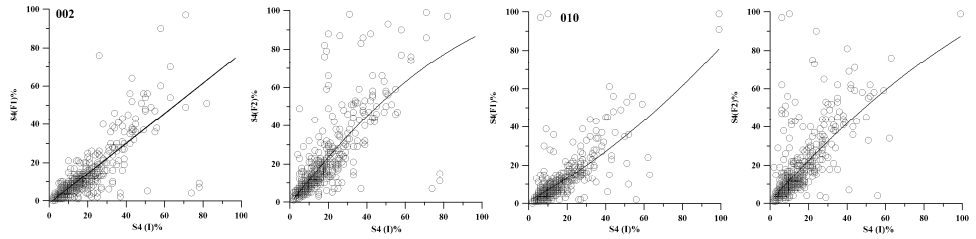

FIGURE 3. Correlation of index S4(I) measured from the intensity variations of the GPS RO signal at frequency F1 and parameters S4(F1) and S4(F2) found from the eikonal variations at GPS frequencies F1 and F2.

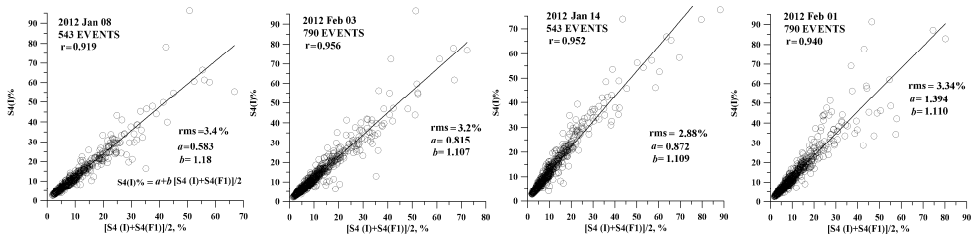

FIGURE 4. Correlation of indexes S4(I) and [S4(F1)+S4(I)]/2.

Figures 3 and 4 show the results of correlation of index S4(I), defined by the variations of the intensity I at the frequency F1 with indexes S4(F1), S4(F2) mea sured from the second derivative of the phase paths excess at frequencies F1, F2 during FORMOSAT-3 RO events held in January and February 2012. Circles in Figures 3 and 4 correspond to the experimental values of index S4 (I) (vertical axis) and S4 (F1), S4(F2) (horizontal axis). The solid curves in Figures 3 and 4 are regression lines and have been found by least squares method. The correlation coefficient of index S4(I) to S4(F1) and S4(F2) varies in the intervals 0.69 to 0.78 and 0.70—0.75, respectively. The correlation coefficient of index S4(I) with combined index [S4(F1)+S4(I)]/2 is very high and changes in the interval 0.91—0.97. Measured correlation values indicate a significant contribution of regular layered irregularities in the ionospheric variations of the amplitude and phase of the RO signals at frequencies F1, F2. High correlation between variations of the indexes S4(I) and S4 (F1), S4(F2) indicates substantially lower influence of the small-scale irregularities on the RO signal as compared with the contribution of the layered structures in the ionosphere.

Conclusion. The principle of locality extends the applicable domain of the RO method, widens possibilities and opens new directions of the RO geophysical applications to remote radio sensing, including the study of multilayered structures and wave processes in the atmospheres and ionospheres of the Earth and planets.

Acknowledgments. This work was supported in part by Program no. 22 of the Presidium of the Russian Academy of Sciences, by the Fundamental Research Program of the Physical Sciences Division of the Russian Academy of Sciences, IV.13 and Russian Foundation of Basic Research grant No. 13—02—00526-a.

References

1. Yakovlev O.I., Pavelyev A.G., Matyugov S.S. *Radio occultation monitoring of the atmosphere and ionosphere* URSS Edition. Moscow, 2010, 206 pp. ISBN 978-5-397-01227-0.

2. Kunitsyn V, Tereshchenko E. *Ionospheric Tomography.* Springer-Verlag: Berlin: 2003.

3. Liou Y.A. and Pavelyev A.G. *Simultaneous observations of radio wave phase and intensity variations for locating the plasma layers in the ionosphere* Geophys. Res. Letters 2006. V. 33. №23. L231021—5.

4. Pavelyev A.G., Liou Y.A., Wickert J., Gavrik A.L., Lee C.C. Eikonal acceleration technique for studying of the Earth and planetary atmospheres by radio occultation method *Geophys. Res. Lett.* 2009. V. 36. doi:10.1029/2009GL040979, L21807, 1—5.

5.Liou Y.A., Pavelyev A.G., Liu Shuo-Fang, Pavelyev A.A., Yen Nick, Huang C.-Y., and Fong Chen-Joe *FORMOSAT-3/COSMIC GPS RadioOccultation Mission: Preliminary Results.* IEEE Transactions on Geoscience and Remote Sensing. 2007. V. 45. №11. P. 3813—3826.

6. Pavelyev A.G, Zhang K. Liou Y.A., Pavelyev A.A., Wang C.S., Wickert J., Schmidt T., Kuleshov Y. *Principle of Locality and Analysis of Radio Occultation Data.* IEEE Transactions on Geoscience and Remote Sensing. 2013. V. 51. №6. Pt.1. doi: 10.1109/TGRS.2012.2225629. P. 3240—3249.

7.Pavelyev, A. G.; Liou, Y. A.; Zhang, K.; Wang, C. S.; Wickert, J.; Schmidt, T; Gubenko V.N.; Pavelyev, A.A.; and Kuleshov, Y. Identification and localization of layers in the ionosphere using the eikonal and amplitude of radio occultation signals Atmos. Meas. Tech., 5, 1—16, 2012. doi:10.5194/amt-5-1-2012.

PL-4

Estimations of Electric Field Penetration from Ground into the Ionosphere

Valery V. Denisenko

Institute of Computational Modelling of the Russian Academy of Sciences
Siberian Branch, Krasnoyarsk, 660036, Russia

There exists an idea that some features of quasi-static electric fields in the ionosphere measured by spacecrafts like DEMETER can be earthquake precursors. A few physical processes which can provide such a relation are widely discussed last decade. The most popular of them is the electric field penetration from the Earth's surface into the ionosphere through the atmospheric conductor.

We have created a few models of the penetration [1, 2]. The Earth's atmosphere is studied as a conductor that unites ionosphere and ground. Steady state charge conservation law with Ohm's law produce the 3-D equation for the electric potential. We calculate the spatial distribution of the electric conductivity tensor in the ionosphere using the models IRI, MSISE, IGRF as it is described in [3] and use the empirical model of atmospheric conductivity [4]. The problem is simplified much if the magnetic field is vertical and conductivity depends only of the height, since in such a case Hall conductivity does not matter and the only Pedersen and field-aligned conductivities are involved in the equation for the electric potential.

We use the boundary conditions with correspond to given vertical component of the electric field at ground and zero currents to the ionosphere from the magnetosphere. It is shown that if the adjoined ionosphere is taken into account then the ionospheric electric field becomes about twice less.

From mathematical point of view it is an elliptical boundary value problem of Neumann type. If we additionally fix the average value of the potential the solution exists and it is a unique one. We construct it numerically by Fourier transformation over the horizontal coordinates. Many test calculations are done to choose the necessary parameters of the numerical method which are enough to give a good approximation for the solution.

We set the input parameters which look typical for moderate earthquakes like electric field of about 100 V/m near ground with typical horizontal scale of a few hundred km.

The result electric field in the ionosphere in such a case does not exceed 1 μV/m under night-time conditions and it is about ten times less under day-time ones. This is our main result.

So our detailed analysis of the possibility of the electric field penetration from the Earth's surface into the ionosphere through the atmospheric conductor gives the negative result. It is in contrast with the models like [5, 6], which explain values which can be measured since they are of the same order of magnitude as electric fields always existing in the ionosphere of a few mV/m strength due to ionospheric and magnetospheric generators.

The boundary condition that means zero vertical current in the atmosphere at the height of 90 km is set in the model [5]. This model would be valid if the medium above this boundary has zero conductivity in horizontal directions. It completely excludes the ionospheric conductor above 90 km that in fact is thousands times larger than conductivity below this height.

In the model [6] the upper boundary with the same condition is shifted to the height of 170 km that is principally better than 90 km in [5] since conductivity of E-layer is taken into account in this case. We think that they do not include F-layer because of the common point of view that by reason of the acceleration by Ampere's force the conductor is drifting, because of that the electric field in medium’s frame of reference becomes zero and so the current density becomes zero. This is valid for the day-time ionosphere but there is only decrease of the effective conductivity of the night-time ionosphere. This effect is described more or less quantitatively in [3] with effective Pedersen and Hall conductivities. Typically the in-

come of the F-layer to the integral Pedersen conductance in the night-time ionosphere is about 2.5 times larger than conductance below 170 km is. So, the integral Pedersen conductance is made about 3.5 times less in that model that makes electric field 3.5 times stronger. Of course, the typical time of the process is important for the value of the effective Pedersen conductance. We use the values after one hour that is roughly the same as averaging over 3 hours.

Our analysis of the results of [6] shows that the current about 11 A goes into the cylinder r<300 km in the ionosphere through the atmosphere from ground and current about 80 A goes by the ionosphere from this cylinder to infinity. It contradicts to the charge conservation law and so the model does not look as a correct one.

It can be mentioned that the penetration in frame of our model is thousands times larger than it is shown in [7] where existence of huge conductivity across magnetic field above 150 km is indirectly supposed while it is not so in real ionosphere.

We also analyze the models [8, 9] which use a popular idea to explain the electric field penetration to the ionosphere by the vertical extrinsic current that exists due to the turbulent diffusion of air with embedded charged particles of aerosol and convection. It is shown that their values of the output parameters do not fit to the input ones thousands times and the effect is negligible if the errors are removed. In fact an extrinsic current due to nonzero charge density cannot exist during valuable time. If a charge is placed into a conducting medium, it is compensated by charges of the opposite sign by a conductivity current after some period of time that is much less than an hour in the Earth's atmosphere near ground. The relaxation time quickly decreases with height. Exclusion of this process is the main inadequate feature of those models.

The model [10] is based on atmospheric current generation by extrinsic underground currents. The authors mix two opposite approaches. They neglect conductivity currents in ground, but use the idea that the charges on the surface create electric field outside the body, while the last property is usual for a conductor. In fact the surface charge density defines only the difference between normal electric fields at two sides near the surface. The fields themselves are also defined with other charges. The model would be valid if somebody additionally moves the negative charges up to the ionosphere while the underground extrinsic current in the model moves positive charges to the surface of ground and leaves negative charges below the domain of its existence. Since no additional extrinsic current from underground to the ionosphere is present in the model, we must take into account the couple of positive at the surface and negative at some deepness charged layers. It approximately means a flat capacitor with almost zero electric field outside, namely above ground. Theirfore no current goes to the atmosphere due to such a vertical underground extrinsic currents. So this part of the paper [10] is inadequate.

In fact our models as well as the models like [5—7] which use given vertical component of the electric field above ground and present no generator in the atmosphere and above it need some underground generator "behind screen". Such a generator moves electric charges horizontally and push them into or from air where the vertical component of the electric field is positive or negative, since in view of Ohm's law it corresponds to vertical current density.

The model [11] does not use concept of underground generator. It explains the electric field variations near ground as consequences of the atmospheric conductivity variations. Since usually the voltage between ionosphere and ground is of about 300 kV because of the global thunderstorm activity, a proper current from the ionosphere to ground exists. It corresponds to the fair weather electric field near ground. The observed conductivity variations which appear because of the presence of radon and aerosols permit to explain an about four times smaller or larger electric field near ground in comparison with the fair weather value [11].

This research is supported by grant 12—05—00152 from the Russian Foundation for Basic Research.

1. M. Ampferer, V.V. Denisenko, W. Hausleitner, S. Krauss, G., Stangl, M.Y. Boudjada and H.K. Biernat. Decrease of the electric field penetration into the ionosphere due to low conductivity at the near ground atmospheric layer. *Annales Geophysicae.* V. 28, 2010. pp. 779—787.

2. V.V. Denisenko, M. Ampferer, E.V. Pomozov, A.V. Kitaev, W. Hausleitner, G. Stangl and H.K. Biernat. On electric field penetration from ground into the ionosphere. *Journal of Atmospheric and Solar-Terrestrial Physics.* V. 102, 2013, pp. 341—353. DOI: 10.1016/j. jastp.2013.05.019

3. V.V. Denisenko, H.K. Biernat, A.V. Mezentsev, V.A. Shaidurov and S.S. Zamay. Modification of conductivity due to acceleration of the ionospheric medium. *Annales Geophysicae.* 2008, V. 26, pp. 2111—2130.

4. M.J. Rycroft and A. Odzimek. Effects of lightning and sprites on the ionospheric potential, and threshold effects on sprite initiation, obtained using an analog model of the global atmospheric electric circuit. *Journal of Geophysical Research.* 2010. V. 115, A00E37, doi:10.1029/2009JA014758.

5. V.P. Kim, V.V. Hegaj, and P.V. Illich-Switych. On the possibility of a metallic ion layer forming in the E-region of the night mid-latitude ionosphere before great earthquakes. *Geomagnetism and Aeronomy.* V. 33, 1994, pp. 658—662.

6. V.P. Kim, J.Y. Liu and V.V. Hegai. Modeling the pre-earthquake, electrostatic effect on the F region ionosphere. *Advances in Space Research.* V. 50, 2012, pp. 1524—1533.

7. V.V. Grimalsky, M. Hayakawa, V.N. Ivchenko, Yu.G. Rapoport and V.I. Zadorozhnii. Penetration of an electrostatic field from the lithosphere into the ionosphere and its effects on the D-region before earthquakes. *Journal of Atmospheric and Solar-Terrestrial Physics.* V. 65, 2003, pp. 391—407.

8. V.M. Sorokin, V.M. Chmyrev and A.K. Yaschenko. Electrodynamic model of the lower atmosphere and the ionosphere coupling. *Journal of Atmospheric and Solar-Terrestial Physics.* V. 63, 2001, pp. 1681—1691.

9. V.M. Sorokin, A.K. Yaschenko and M. Hayakawa. A perturbation of DC electric field caused by light ion adhesion to aerosols during the growth in seismic-related atmospheric radioactivity. *Natural Hazards and Earth System Sciences.* V. 7, 2007, pp. 155—163.

10. C.L. Kuo, J.D. Huba, G. Joyce and L.C. Lee. Ionosphere plasma bubbles and density variations induced by pre-earthquake rock currents and associated surface charges. *Journal of Geophysical Research.* V. 116, A10317, 2011. doi:10.1029/2011JA016628. 2011.

11. R.G. Harrison, K.L. Aplin and M.J. Rycroft. Atmospheric electricity coupling between earthquake regions and the ionosphere. *Journal of Atmospheric and Solar-Terrestrial Physics.* V. 72, 2010, pp. 376—381. doi:10.1029/2011JA016628. 2011.

PL-5

Disturbances in the Upper Atmosphere and Ionosphere from the Sources on the Earth Surface

Ivan Karpov[1,2], Sergey Kshevetskii[1], Olga Borchevkina[1], Alexander Radievsky[1,2] and Alexey Karpov[1]

[1] Immanuil Kant Baltic state university, Kaliningrad, Russia
[2.] West Department of IZMIRAN, Kaliningrad, Russia

One of the major problems of the dynamics of the upper atmosphere and ionosphere is to explain the impact of the processes in the lower atmosphere on the dynamics of the upper atmosphere and ionosphere. This influence is manifested in such observed phenomena as meteorological control of variations in the parameters of the upper atmosphere, the ionospheric effects of stratospheric warming / coolings, the occurrence of ionospheric precursors of earthquakes, the response of the ionosphere to strong meteorological disturbance (storms, typhoons), etc. Until now, no satisfactory physical interpretation of the observed phenomena, however, the basic hypothesis is based on the need for mechanisms of excitation in the lower atmosphere and the vertical propagation of acoustic-gravity waves (AGW).

In experimental studies found that the time delay in the appearance of ionospheric disturbances may be a few hours compared to the beginning of the perturbation in the lower atmosphere, and ionospheric effects are localized in close pro ximity to areas of disturbances in the lower atmosphere. Such small time delays and spatial localization of ionospheric disturbances suggest that an important part in the implementation of such actions take AGW with small spatial and temporal scales. Such waves having vertical scale comparable to the height scale of atmosphere and a period close to the Brunt-Vaisala period, can propagate almost vertically. In addition, poorly understood the role of infrasonic waves, which may vertically propagate from the disturbance areas in the lower atmosphere and reach heights of the upper atmosphere. Such waves can participate in the implementation of the different atmospheric layers links.

The purpose of the experimental part of the work is that to identify the frequency characteristics of acoustic-gravity waves (AGW) in the lower atmosphere and in the observations of ionospheric TEC (Total Electron Content) parameter. The purpose of the theoretical part is to study the response of the upper atmosphere on the propagation of short-scale AGV from the lower atmosphere.

Experimental observations in the atmosphere and ionosphere conducted during the period of the solar terminator (ST). As you know, ST is a regular source of perturbation parameters of the atmosphere. Many publications drew attention to the fact that in passage of the solar terminator in the ionosphere amplified variations

with periods of short-scale HBV. In this paper, we continue the selection TEC variations with periods AGW from observations of GPS satellite signals during the passage of the solar terminator.

Observations of variations in the lower atmosphere are made using the two-wavelength (532 nm, 1064 nm) atmospheric lidar. Observations began in before sunrise (~ 1 hour before sunrise), and lasted about 1—2 hours after sunrise. The variations of lidar signal intensity are obtained the corresponding variations of atmosphere parameters. The observations were executed in Kaliningrad in 02.2012—03.2012. The example of the spectrum of lidar signal intensity is shown on the fig. 1.

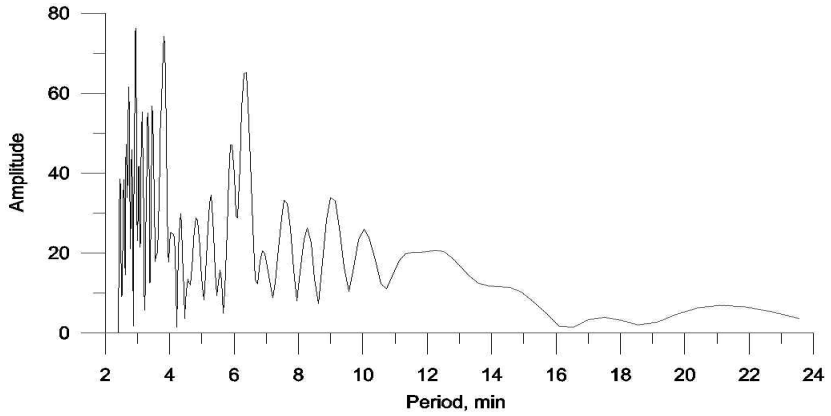

FIGURE 1. The spectrum of lidar signal variations on the height ~5km.

As seen in Figure 1 in the spectrum variations of atmosphere parameters are present harmonics with periods of ~ 4 min. (infrasound) and harmonics with periods 6—10min. (IGW).

The spectral characteristics of the TEC variations in the ionosphere were determined from observations of GPS satellite signals to mid-latitude stations during the period of ST. The dynamics of the spectrum TEC variations in passage ST shown in fig. 2. As can be seen in Fig. 2 during the passage of ST in the ionosphere are observed the amplification of variations with periods of about 6—10 min. both morning and evening. Thus, during the period of the solar terminator in the lower atmosphere and ionosphere has been increasing variations with periods of infrasonic waves and short scale IGW.

The report presents the results of studying the propagation of infrasonic waves and IGW with periods close to the Brunt-Vaisala period from sources on Earth's surface to the upper atmosphere. The two-dimensional non-hydrostatic numerical model of the propagation of AGW based on the solution of the hydrodynamic equations for wave disturbances and taking into account the nonlinear and dissipative processes in the propagation of waves, and the interaction between them were used in the calculations. As a source of wave disturbances defined by pressure disturbances on the Earth's surface area extending ~ 20 km (point source).

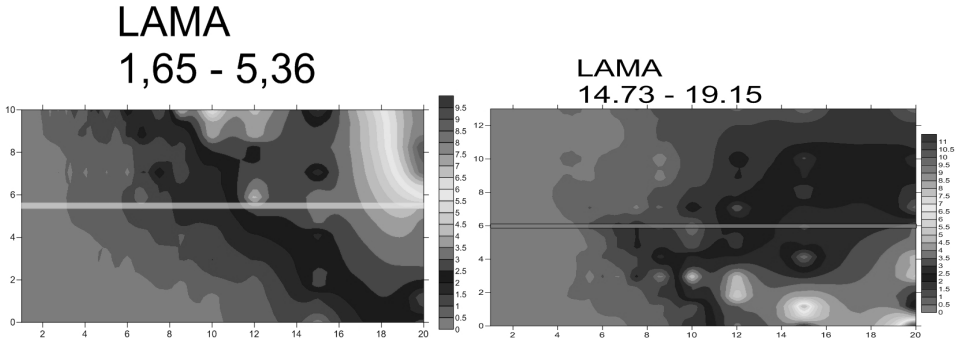

FIGURE 2. The dynamics of the spectrum f TEC variations during morning (left) and evening (right) ST passing/ The solid line correspond the sunrise/sunset time.

The variability of the source of perturbations described by a superposition of ten harmonic functions with periods of 3 to 10 minutes. The solutions of the model equations were obtained for the two variants of the perturbation source — continuous and pulsed.

Fig. 3 shows the spatial distribution of wave perturbations in temperature (Fig. 3) and the mean temperature (Fig. 4), due to dissipation of waves for several time points after the beginning continuous operation of the terrestrial source. As can be seen from Fig.3, the wave disturbances after 0.5 h observed heights in all atmosphere directly above the source and reach heights of ~ 300 km distances at ~ 500 km in the horizontal direction from it. It can be noted a pronounced character waveguide propagation of atmospheric disturbances in the region below ~ 200 km in 1—2 hours after the start of a continuous source. The spatial localization of atmospheric wave perturbations and their scale, evidently related to the perturbation of the background state of the atmosphere. As can be seen from Figure 4, a significant increase in mean temperature at 0.5 hour after the power is observed at altitudes of 300 km and horizontal distances from the source of ~ 100 km. Over time, after ~ 2hours, area perturbation decreased to a height of 200 km and extends horizontally up to ~ 1000 km. The length of the field perturbation background state of the atmosphere in the horizontal direction, as shown in Fig. 3, influences on the formation of the waveguide propagation of wave disturbances in the upper atmosphere. The expansion in the horizontal direction of the perturbation of the upper atmosphere is accompanied by an increase in the length field of the waveguide propagation.

The most interesting feature of the results of the calculations is that the emergence of large-scale disturbance on the heights of the upper atmosphere (initially at altitudes of 300 km) significantly affect the propagation of AGW from a ground source. This influence is evident in the fact that in the upper atmosphere waveguide is formed in which waves with periods shorter than the Brunt-Vaisala period.

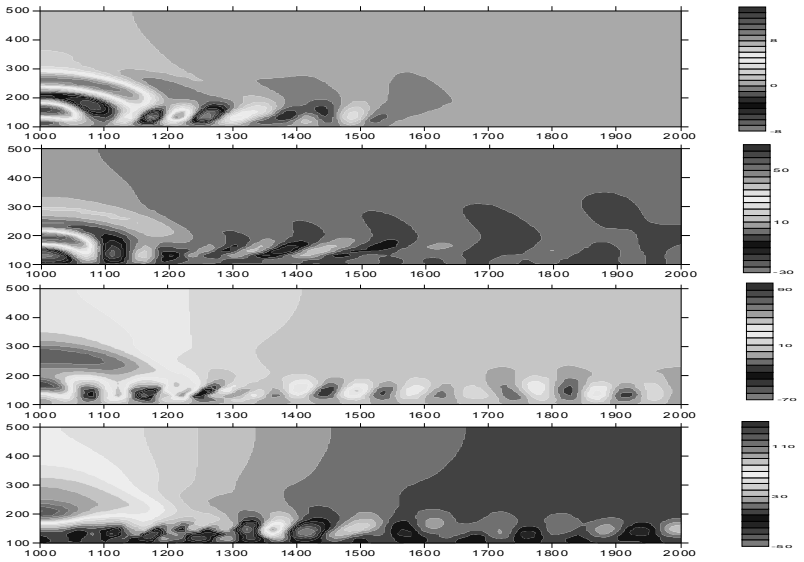

FIGURE 3. Wave temperature perturbations in 0.5 h, 1.0 h, 2.0 h, 3.0 h (top to bottom) after the start of a continuous source. The X axis is the horizontal distance from the source (source coordinate X = 1000 km). Y-axis height.

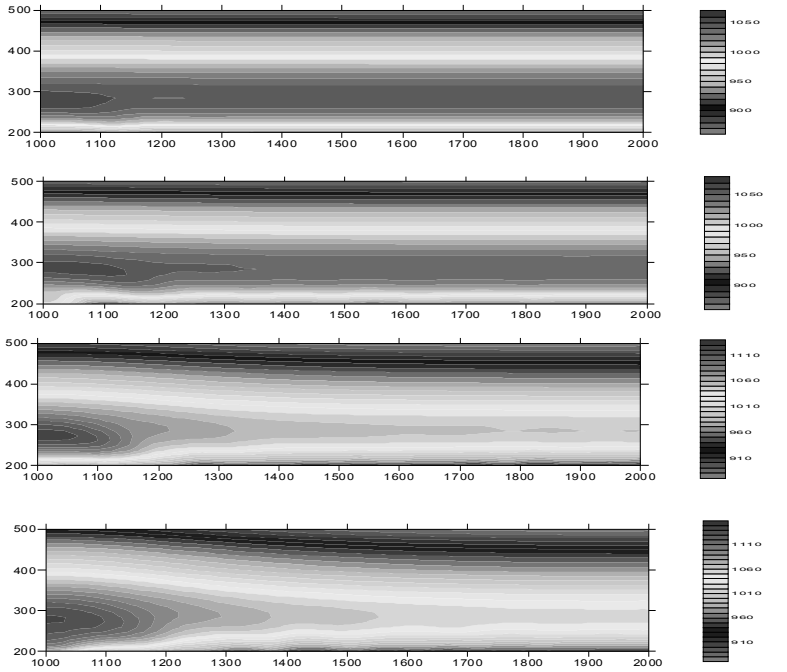

FIGURE 4. Mean Temperature of the atmosphere over 0.5 h, 1.0 h, 2.0 h, 3.0 h (downward) after the start of continuous source. The X axis is the horizontal distance from the source (source coordinate X = 1000 km). Y-axis height.

The wave disturbances in the upper atmosphere appear rather quickly after the ground source AGW (less than 0.5 hours) and over time extend to a distance of ~ 1000 km from the source of excitation. The area of mean temperature perturbations initially formed at altitudes of 300 km due to dissipation of infrasonic waves propagating. Over time, the area of the background state perturbations expanded in both the vertical and horizontal directions, dropping to a height of ~ 250 km and extending to about 1000 km across. The expansion in horizontal direction is determined so that a significant horizontal distance in a waveguide includes of IGW propagating from the ground source.

Thus, the reaction of the upper atmosphere on the propagation of AGW from Earth surface area is manifested in the formation of large-scale perturbations of the atmospheric parameters at altitudes of 200 km. An important condition for the formation of such an area is the generation of infrasonic waves by ground source.

The appearance large-scale disturbance influences on propagation of AGW in the upper atmosphere and leads to the waveguide propagation of waves with periods shorter than the period Brunt — Brent along the Earth surface at altitudes of 200.

PL-6

Ball Lightning Investigations in 2012—2013

Vladimir L. Bychkov[1] and Anatoly I. Nikitin[2]

[1] M. V. Lomonosov Moscow State University, Moscow, 119991, Russia
[2] Talrose Institute for Energy Problems of Chemical Physics, Russian Academy of Sciences, Moscow, 117829, Russia

Symposia on Ball Lightning (BL) have been undertaken in 2010, 2012. Publications [1—4] have considered a situation with BL from 2008. During 2012—2013 years the activity in these area has been continued. Several meetings were carried out, such as in Sochi, Russia, where every year is undertaken a session devoted to BL and another section with, strictly speaking, non-conventional plasmas in which nuclear processes and processes with release of energy takes place. In Yaroslavl state university under the leadership of Prof. A. I. Grigoriev were undertaken regular biannual meetings where questions connected with BL were considered [5, 6]. Among topics, devoted to BL, were dusty plasmas, discharges and electrohydrodynamics of charged liquids. A special section devoted to BL and plasmoid physics has been carried out in Institute for High Temperature RAS by Prof. A. I. Klimov At the conference devoted to Magneto-plasma aerodynamics. A special attention at these meeting was attracted to observation properties of BL. During this period the team of G. D. Shabanov [7], the team of passed away S. E. Emelin [8] and A. I. Kli-

mov [9] continued their investigations with creation of fire balls and plasma vorticle structures in different discharges over liquids and gases, also with application of the external influence.

During these years the area of Gatchina discharge and its plasmoids investigations has transformed to a self-consisting area of discharge investigations [10—14]. Realized plasmoids have observational features resembling natural BLs. There are still questions about their plasma modeling though their gasdynamic structure has been established both theoretically [13] and experimentally [14].

During this period experiments on silicon-type BL created in discharges were continued. This direction has appeared after work [15], connected with linear lightning interaction with sand and with work [16], connected with lightning discharges interaction with metals, dielectrics and organic materials. First successful experiments were realized with an application of doped silicon plates [17, 18]. In works [8] have been achieved substantial results showing an opportunity of creation of exploding artificial BL in specially designed discharge tubes for production of BL with complex composition on a base of Basalt. These results connection with real BL was analyzed in [19].

In work [20] have been continued attempts to produce BL with a help of high voltage pulse generator at explosion of coils with complex forms. The key idea of magnetic energy input to plasma is under the investigation. Long lived plasma objects with 1.6 s lifetime have been obtained.

Kopeikin [21] has been started repetition of Corum's experiments on production of artificial BL with a help of Tesla coils. He states that he could realize combustive objects of a chemical nature like those of Corum's.

Experiments on excitation of fireballs in liquid nitrogen have been made. Optical properties of these objects have been investigated [22].

Fresh works devoted to an existing state of art in the BL area have been appeared [23, 24]. In [23] the state of existing BL databanks and the information gathered in them has been analyzed. Typical differences arising in connection with character of places and countries in which observations are made are revealed. New glance on a state of BL investigations and the BL problem one can find in [24]. In [25] has appeared a review of BL problem from a chemical energy point of view. It shows a possible role of BL material combustion.

In the work [26] new statistical data on BL observation in France are presented. Presented statistical data add little new to the existing picture of BL properties except for specificity caused by geographical, and physical and chemical properties of an environment and psychological features of observers.

In [27] a glass after interaction of possible BL object with a mirror was analyzed. In [28] thorough investigation of a BL movie in Dolgoprudny city was carried out. Paper [29] continued collection of BL observations cases collected by personal reviewing, literature and internet. Fresh observations of a fireball in China [30] are under active discussion; however, published results do not confirm the fact that it was a real BL but not the arc discharge. We have to mark an appearance of usual skeptic work on reality of BL [31], basing on the possibility of phosphenes

being generated by the energetic radiation from lightning flashes and thunderstorms. One can be amazed by an ignorance of authors with respect to cases of BL impact on a skin and a body of people. Development of models devoted to high energy BL was made in works [22, 32—34]. New versions of former ideas on a nature of low energy BL have appeared in [35] and [36].

Even short indication of works and investigations made during these years can show that the activity of teams and researches practically did not cease, though the front of investigations was very wide that leaded to scatter of forces and decrease of efforts possibilities.

In works on BL theory it is possible to consider as the general tendency the following. In the dispute on what is BL a discharge in air, or a material object, most likely is carrying before one the second point of view. Activity of the researchers, keeping an idea about BL as about an autonomous object, as in the field of the theory, and practice noticeably surpasses the activity of their opponents. In this connection it is necessary to note, that the question on BL nature of the large size — type of UFO and the BLs appearing in clouds in an absence of flying devices remains open. Since high pressures and presence of an atmospheric aerosol, leading to fast recombination of the charged particles and loss of their energy at these heights do not allow to apply methods developed for a hot plasma [36] to the description of BL. On the other hand these questions stimulate researches of the basics of an existing electrodynamic paradigm, in many conclusions of which N. Tesla doubted at carrying out of his successful experiments on realization of BLs in Colorado-Springs [20].

In the field of BL theory the increasing recognition obtains an idea about BL as about an object having a cover and possessing a unipolar electric charge, for the first time stated in [38—409]. Presence of the BL uncompensated charge allows to give a reasonable explanation to many electric effects caused by it, and also to explain features of its movement. Moreover, the model of BL with the unipolarly charged core, placed inside a dielectric cover, allows to explain widely known cases of BL energy measurement when the density of this energy has appeared to be more than 10^{10} J/m^3. According to this model, the basic part of BL energy is stored in a form of kinetic energy of particles — carriers of the electric charge. In this connection it is expedient to pay a special attention to researches of location methods of the charged particles (or the ordered dynamic systems) possessing large kinetic energy in the limited area of space. These researches are important, just as a studying of "potential" forms of energy storage (chemical energy, dissociation and ionization energy of molecules, etc.), which account allows to find an explanation of BL energy sources, making only some percents of its basic energy. Unfortunately, among the researchers, considering BL as an electrical neutral low-energy object, the persistent unwillingness to take into consideration the specified above approach to model of unipolar BL is observed. One of the reasons of such unwillingness is "strangeness" of some researchers, at which the belief in correctness of their models is similar to dogmatism of adherents of various religions (this was noticed by Stenhoff [41]). Another reason is not so harmless, as this. Last years the

term "ball lightning" became a “place plum” of everything, which is not clear yet. Authors of various fantastic ideas about a world arrangement (which in any way are not confirmed with practice) assert that display of their ideas occurs just through the BL phenomenon. Thus they do not take the trouble to explain the observable properties of BL in their theories or on the basis of known physical principles. As a result the solving of BL problem is subsided by them into a very long-term future, when problems like an explanation of the nature of a dark matter, microscopic black holes, etc. will be found. It allows to a human society to consider BL researches as frivolous and even to carry them to the pseudo science category. For overcoming of these undesirable phenomena the actively working researchers of BL should learn to listen each other, to co-ordinate the efforts and to inform a society through the mass media and the popular scientific literature authentic data on a true state of affairs in the field of BL researches.

Among experimental achievements it is necessary to note:

1. Starting and all-round studying of a new type of the electric discharge named by authors “the Gatchinsky discharge“ [42]. Experiments of the St.- Petersburg scientists have been reproduced in many countries [11—13, 43—46].

2. Experiences of the Belarus, Brazilian, Israeli, American and Russian researchers on studying processes of silicon and other materials burning [16—18, 47].

1. V. L. Bychkov and A. I. Nikitin (eds), *Proceedings of 11th International symposium on ball lightning (ISBL-10) and 4th International symposium on unconventional plasmas (ISUP-10),* 2010, Kaliningrad, Russia.

2. I.V. Karpov (ed), *Book of abstracts AIS 2010: Atmosphere, Ionosphere, Safety,* 2010, Kaliningrad, Russia.

3. I.V. Karpov (ed), *Book of abstracts AIS 2012: Atmosphere, Ionosphere, Safety*, 2012, Kaliningrad, Russia.

4. I.V. Karpov (ed), *Book of abstracts AIS 2012: Atmosphere, Ionosphere, Safety. Section P: Electromagnetic and optical phenomena in the atmosphere including long-lived and plasma objects*, 2012, Kaliningrad, Russia.

5. A. I. Grigoriev (ed), *Proceedings of 9th International conference: Wave electrodynamics of conducting liquid. Long-lived plasma objects and poorly investigated forms of natural electric discharges in atmosphere*, 2011, Yaroslavl, Russia.

6. A. I. Grigoriev (ed), *Proceedings of 10th International conference: Wave electrodynamics of conducting liquid. Long-lived plasma objects and poorly investigated forms of natural electric discharges in atmosphere*, 2013, Yaroslavl, Russia.

7. G. D. Shabanov, A. G. Krivshich, O. M. Zherebtsov and G. E. Gavrilov, *Ball lightning — its creation and some features, modeling in our experiments*, Proceedings of 10th International conference: Wave electrodynamics of conducting liquid. Long-lived plasma objects and poorly investigated forms of natural electric discharges in atmosphere, 2013, Yaroslavl, Russia, pp. 216—225.

8. S. Emelin, V. Bychkov, A. Astafiev, A. Kovshik, A Pirozersky. Plasma combustion nature of artificial ball lightning. IEEE Transactions on Plasma Science. 2012. V. 40, Issue 12. P. 3162—3165.

9. A. I. Klimov, *Vortex plasmoids created by high-frequency discharges,* In: Bychkov V.L., Golubkov G. V. and Nikitin A. I. (eds) The Atmosphere and Ionosphere. Elementary processes, Discharges and Plasmoids, 2013, Springer, Dordrecht, pp. 251.

10. U. Fantz, S. Kalafat, R. Friedl and S. Briefi, *Generation of an atmospheric plasmoid from a water discharge: An analysis of the dissipated energy*, 2013, J. Appl. Phys. V. 114, pp. O43302.

11. S. V. Anpilov, V. L. Bychkov, N. P. Savenkova and R. N. Kuz'min, *Gatchinskyi discharge modeling,* Proceedings of 10th International conference: Wave electrodynamics of conducting liquid. Long-lived plasma objects and poorly investigated forms of natural electric discharges in atmosphere, 2013, Yaroslavl, Russia, pp. 250—255.

12. V. L. Bychkov, N. P. Savenkova, S. V. Anpilov and Y. V. Troshiev, *Modeling of vorticle objects created in Gatchina discharge,* 2012, IEEE Transactions on Plasma Science V. 40, pp. 3158—3161.

13. V. L. Bychkov, S. V. Anpilov and N. P. Savenkova, *Gasdynamic modeling of "a plasmoid" created by the Gatchina discharge,* Khimicheskaya Fizika, 2014, V. 33, №2, pp. 58—63.

14. S. I. Stepanov, *Ultrasonic probing of a plasmoid.* Proceedings of 10th International conference: Wave electrodynamics of conducting liquid. Long-lived plasma objects and poorly investigated forms of natural electric discharges in atmosphere, 2013, Yaroslavl, Russia, pp. 200.

15. J. Abrahamson and J. Dinniss, *Ball lightning caused by oxidation of nanoparticle networks from normal lightning strikes on soil*, 2000, Nature, V. 403, pp. 519—521.

16. S. E. Emelin, V. S. Semenov, V. L. Bychkov, N. K. Belisheva and A. P. Kovshyk, *Some objects formed in the interaction of electrical discharges with metals and polymers*, 1997, Tech. Phys. V. 42, pp. 269—277.

17. S. K. Lazarouk, A. V. Dolbik, V. A. Labunov and V. E. Borisenko, *Spherical plasmoids formed upon the combustion and explosion of nanostructured hydrated silicon*, 2006, JETP Letters, V. 84, pp. 581—584.

18. G. S. Paiva, A. C. Pavão, E. A. de Vasconcelos, O. Jr. Mendes and E. F. da Silva, *Production of ball-lightning-like luminous balls by electrical discharge in silicon,* 2007, Phys. Rev. Letts. V. 98, pp. 048501-1-048501-4.

19. V. L. Bychkov, *Model of ball lightning with an oxide cover*, Proceedings of 10th International conference: Wave electrodynamics of conducting liquid. Long-lived plasma objects and poorly investigated forms of natural electric discharges in atmosphere, 2013, Yaroslavl, Russia, pp. 27—34.

20. A. N. Vlasov, *Experimental installation "Ingir —Mega — -15" for generation of long lived plasmoids,* Proceedings of 10th International conference: Wave electrodynamics of conducting liquid. Long-lived plasma objects and poorly investigated forms of natural electric discharges in atmosphere, 2013, Yaroslavl, Russia, pp. 246—250.

21. V. V. Kopeikin, *Three-contour Tesla transformer for creation of ball lightning,* Proceedings of 10th International conference: Wave electrodynamics of conducting liquid. Long-lived plasma objects and poorly investigated forms of natural electric discharges, 2013, pp. 118—120; K. L. Corum, James F. TCBA NEWS, volume 8, #3, 1989. Tesla's production of electric fireballs by Corum Corum & Associates, Inc. 8551 State Troute 534 Windsor, Ohio 44099.

22. D. L. Kirko and A. S. Savelov, *Spheroidal luminescence in liquid nitrogen and water,* Proceedings of 10th International conference: Wave electrodynamics of conducting liquid. Long-lived plasma objects and poorly investigated forms of natural electric discharges. 2013, pp. 96—99.

23. A. Keul, *The ball lightning controversy: Empirical case studies, forces of nature and cultural responses,* In: Pfeifer K and Pfeifer N (eds) Forces of nature and cultural responses. Springer, Dordrecht, 2013, pp. 27—48.

24. R. Doe *Ball lightning: an elusive force of nature*. In: Pfeifer K and Pfeifer N (eds) Forces of nature and cultural responses. Springer, Dordrecht, p. 7—26.

25. V.L. Bychkov, *Unsolved Mystery of Ball Lightning.* in Atomic processes in basic and applied physics, Eds. V. Shevelko and H. Tawara; Springer, Berlin-Heidelberg, 2012. pp. 3—24.

26. R. Picolli, *A statistical study of ball lightning events observed between 1994 and 2011*, Lightning Strike Research Laboratory. 2012, www.labofoudre.com

27. V. Bychkov, G. Zharik, E. Eisaks, V. Nizovtsev and K. Khodataev, *Possible ball lightning impact to a mirror.* Book of abstracts AIS 2012: Atmosphere, Ionosphere, Safety. Section P: Electromagnetic and optical phenomena in the atmosphere including long-lived and plasma objects. 2012, Kaliningrad, Russia, pp. 8—10.

28. A. I. Nikitin, T. F. Nikitina and A. M. Velichko, *Analysis of video filmed June 3, 2009 in town Dolgoprudny, Russia,* Proceedings of 10th International conference: Wave electrodynamics of conducting liquid. Long-lived plasma objects and poorly investigated forms of natural electric discharges in atmosphere, 2013, Yaroslavl, Russia, pp. 149—165.

29. V. L. Bychkov and D. N. Vaulin, *New data of ball lightning observation*, Materials of 20th Russian conference of cold transmutation of nucleus of chemical elements and ball lightning. 2013. Loo, Sochi, Krasnodar region, pp. 27.

30. C. Jianyong, Y. Ping and X. Simin, *Observation of the Optical and Spectral Characteristics of Ball Lightning,* 2014, Phys. Rev. Lett. V.112, pp. 035001.

31. V. Cooray, G. Cooray and J. Dwyer, *On the possibility of phosphenes being generated by the energetic radiation from lightning flashes and thunderstorms*, 2011, Physics Letters A 375, pp. 3704—3709.

32. V. L. Bychkov, A. I. Nikitin and G. C. Dijkhuis, *Ball Lightning Investigations.* In: Bychkov V. L., Golubkov G. V. and Nikitin A. I. (eds) The atmosphere and ionosphere. Dynamics, Processes, and Monitoring. Springer, Dordrecht, pp. 201—373, 2010.

33 A. I. Nikitin, *Small-sized and composite ball lightning*, Intern. Journ. 'Unconventional Electromagnetics and Plasmas' (UEP), 2012, V. 4, pp. 105—116.

34. A. I. Nikitin, *New approach to solving of ball lightning problem — change of paradigm*, 2012, Vestnik RAEN, №2, pp. 19—30.

35. J. J. Lowke, D. Smith, K. E. Nelson, R.W. Crompton and A.B. Murphy, *Birth of ball lightning*, 2012, J. Geophys. Res. V. 117, pp. D19107.

36. O. Meshcheryakov, *Ball lightning — aerosol electrochemical power source or a cloud of batteries,* 2007, Nanoscale Res. Lett. V. 2, №3, pp. 319.

37. J. M. Donoso, J. L. Trueba and A. Raňada, *The Riddle of Ball Lightning,* The Scientific World J. 2006, V. 6, pp. 254—278.

38. R. F. Avramenko, V. L. Bychkov, A. I. Klimov and O. A. Sinkevich (eds). *Ball lightning in laboratory,* Khimia publishers, Moscow, 1994.

39. A. I. Nikitin, *An electrical capacitor as the element of the power core of ball lightning*, Electrical Technology Russia, 1998, №4, pp. 70—85.

40. A. I. Nikitin, *The dynamic capacitor model of ball lightning*, Proc. 6th Int. Symp. on Ball Lightning (ISBL99), 1999, Antwerp, Belgium, pp. 91—95.

41. M. Stenhoff, *Ball lightning. An unsolved problem in atmospheric physics,* Kluwer/Plenum, New York, 1999.

42. G. D. Shabanov, *Optical properties of long-lived luminescent formations*, Pis'ma v Zhur. Tekhnich. Fiziki. 2002, V. 28, pp. 81—86.

43. B. Juettner, S. Noak, A. Versteegh and G. Fussmann, *Long-living plasmoids from a water discharge at atmospheric pressure*, Proc. 28th Int. Conf. on Phenom. in Ioniz. Gases. Prague, Czech Republic, 2007, pp. 2229—2234.

44. S. E. Emelin and A. L. Pirozerski, *Some questions of power-consuming plasma-chemical ball lightning,* 2006, Khim. Fiz., V. 25, pp. 83—89.

45. N. M. Kogut, A. A. Novikov and V. V. Sevastyanov, *Long-lived plasma formations*, Proc. 10th Int. Symp. on Ball Lightning (ISBL10) and 3rd Int. Symp. on Unconventional Plasmas (ISUP10), 2008, Kaliningrad, Russia, pp. 84.

46. Y. Sakawa, K. Sugiama, T. Tanabe and R. More, *Fireball generation in a water discharge*, The Japan Society of Plasma and Nuclear Fusion Research, 2006, V. 1, pp. 039—1.

47. K. D. Stephan and N. Massey, *Burning molten metallic spheres: one class of ball lightning?* J. Atmos. Solar-terr. Physics. 2008, V. 70, pp. 1589—1596.

PL-7

Systems of the Keywords Identification and Informational Safety

I. Chudnovskaya

LomonosovMoscowStateUniversity, inchud@bk.ru

Devices for keywords (KW) detecting, that became known because of the papers they described, were generally used for the solution of the military problems and needs of federal agencies. It was reported, that these systems were used on military aircraftboard with a dictionary of KW representing names of alternate aerodromes. Data are available forusing the devices of KWdetectingby the U. S. federal agencies in telephone communication lines. In the United States it was planned to create a voice terminal for navigation route making using the priori speech meteorological information for different geographical points.

Currently, the problem of creation of the intelligent terminal with touch input incoming voice data is being solved. Ways of building such terminal may be different. The first oneis the work in a narrow domain. Such devices have already decent performance, but annoy the consumer, forcing him to work in narrowly specified domain. The second way is the revealing of the KW domain distribution of given dictionary at time window. Let's take a look at the different information security problems that can be solved by using the detection system of key words.

The problem of the informational messages selection. Data sources: the broadcastingof television andradio stations, phone messages on domesticand internationallong-distance and cellular communication lines(the implementation of such an analysisrequires an appropriateinternational agreement), for textual informationanalysis of individual articles in periodicals and electronic-mediachannels.

Letthe analyzed sample have registeredM of the KW from severalspecialized dictionaries. Then we finda dictionary with the highest number of registered KW and after that rank the dictionariesin descending order of the detectedKW. The fields of applicationof this approach are following: the selection of the materialfor further analytical consideration, the creation of an archive of the phone callsin district police stations and fire services,etc.

The decoding of the KW in unlimited information samples is more challenging problem. The problem is posed similarly, but in this case the informational message has no defined internal borders. Finitization of such information messages can be done by force, for example, at a specified time interval, and in case of the change of thematic dictionaries. The scope: the replenishment of the data archive; the building of the predictive analytic models with the calculation of latent (preparatory) and the relaxation time constants. Examples: identifying policy rate changes, the state reconstruction analysis under the statements of politicians and the press; the identification of preparing natural disasters, man-triggered events, accidents;the estimation of the economic damage and repair work on the calculated value of the relaxation time constant.

Highly reliable KW identificationis characterized by the following features. The volume of the dictionary is not huge. The main aim is to detect KW with lowprobability of false alarmandmissing. The scope: KW allocationassociated with terrorist actsor representing a highinformational value, removing the unwanted KW transmissionof voice messages via communication channels or adjusting dialed text message by removingthe relevant KW. Sources of information: textperiodicals, voice messagesin different communicationchannels.

Management Information Systems. KW allocation systems are used to solve the social problems of management. If there are several specialized dictionaries of KW, the following problems can be solved:

— identification of the most important subjects of speech utterances for this period of time;

— construction of the corresponding information models rankings for a given subject;

— study of the development of the information model in time, etc.

Inspeech KW allocation systems with the analysis of non-verbalspeech characteristicsthe following tasks can also be solved:

— sharing the groupof speakers to the appropriate social strata;

— sharing voice message announcers on the relevant an thropological features;

— determining the emotional state of the voice messagespeaker.

Proceeding to a more detailed exposition of the problems of the information management systems,as one of the examples, we can consider the problem of policy adjustment of the head of state based on the analysis of discourse in the media. Posing such a task can be accomplished using the algebra of the conflict, where the opponents are the director and the state's population. The director must develop the

current doctrine that advances his goal for the effective control. From the viewpoint of algebra conflict the director can develop an effective doctrine only when it has data on the bridgehead of the "enemy", has reliable information about the mood of the state's population. The director can obtain the data on the bridgehead of the "enemy" from media and public opinion on the predicted KW highlighted for example in the Internet. Having formulated the necessary doctrine, the director can specify it with the latest survey data and analysis in the media and Internet.

A less complicated examples considering "non-revolutional" process control. This model is based on the analysis of the economic factors in the development process, and the setting of optimism/pessimismpublic evaluation of this process. Usingthe setwofactors, it is possible to build a sustainable model of development process. The aboves cheme also helps to solve the more specific tasks, for example, evaluation of the effectiveness of television programs, advertising, etc.

Information systems for emergencies. Let's consider the possibility of applying the KW allocation systems for the detection and resection of the technological and geophysical disasters coordinate detection. For this purpose, one can use (with appropriate international agreement) the KW detection in telephone conversations. If the phone number of the subscriber and his coordinates are registered, we can roughly estimate the coordinates and scale of the emergency situation. The changes of the geographical coordinates of subscribers in time can carry information about the speed of the evacuation and estimate the destruction zone in an emergency situation. Creating such a system will enable the rapid detection of the technological and geophysical emergencies leading to major destruction.

Let's observe the realization of the key word high lining system. The incomingdata can be represented as texts, speech signals,test files to a computer, etc. The speech information regulation seems to be the most complicated technical problem, because it's solvation is divided into two steps:

— automatic detection of the key words from the speech flow;

— automatic regularization of the processed speech information.

Some questions must be observed for the successful solvation of the incoming speech flow regularization problem:

— which algorithms will be used for the automatic regularization;

— what technical requirements are put forward for the characteristics of the key words detection, based on the possibility of the incoming information selection;

— the analysis of the developed key word detection and automatic joint speech distinction systems should be made based on the technical restrictions of the conditionsof the speech signal reception; besides the question of the possibility of use of that systems must be solved.

Mentioned features of the selection of speech messages via key words is considered as the selection of the most valuable messages (MVM — OCS). The most valuable message selection effectiveness depends on the chosen thesaurus (key words dictionary on the given thematic) and the algorithm of the processing of the selected key words sequence in time.

Considering the algorithm of theprocessing of the selected time sequence of the key words, we note thata separate word or a sentence can't be the element of text intentioninterpretation. However some problems can be solved using separately selected key words.

The problem, mentioned above can be stated the following way. There is a key word dictionary with volume $C_g[C_1^g,\ldots,C_G^g]$. The keyword sequence $\Pi(C) = C_i,\ldots..,C_j$is being registered at time interval $T[t_1,t_2]$. Belonging to this thesaurusis defined as follows:

$$C_g[\ldots] = \sup\{C_g[C_1^g,\ldots,C_G^g] \cap \Pi(C)\} \quad (1)$$

Sup{…} ise valuated taking multiplicity of thesequence $\Pi(C) = C_i,\ldots..,C_j$. into account. Thet hesaurus number isbeing given to the selected key word sequence $\Pi_g(C) = C_i(g),\ldots..,C_j(g)$. The selection of the most valuable messages is done using the following criteria. The varieties of the most valuable messages (ОЦС) are a priory set in g-thesaurus: $ОЦС_m(g) = C_{m1}(g)\rightarrow\cdots\rightarrow C_{mf}(g)$. The belonging to the $ОЦС_m$ is being defined the following way:

$$ОЦС_m(g) = \sup\{C_i(g),\ldots,C_j(g)] \cap [C_{m1}(g)\rightarrow\cdots\rightarrow C_{mf}(g)]\} \quad (2)$$

Considering the types of messages that can be detected by recognizing the key words, we start with the observation of the frequency allocation algorithm for pulsating formation when some sequence $ОЦС_m(g)$ is "pulsing" in given thesaurus. Analyzing the time evolution of aggregate synchronous formations, various invariants, such as themes of resonantsocial events can be built. Destruction of synchronicity may indicate the duration of the resonance social event, or serve as a harbinger of major social upheaval (extreme events). Set of synchronous resonance topics can be seen as a harbinger of major social upheavals and can develop forward-looking solutions of socioeconomic government structures.

There are currently three main established areas of speech recognition.

Detection of isolated words,when there is a pause between neighboring words. The beginning of each word is known when such method is being used. Recognition system is configured to recognize a certain amount of words from a few dozen to several thousand. Recognition system can be configured for a particular speaker or a cooperative of speakers. The recognition of words, that are not included in the dictionary, is not allowed.

Undivided speech recognition system. Working conditions are the same as for the recognition of isolated words, however, the presence of a pause between adjacent words is optional.

Key words (KW) recognition system. Working conditions are the same as for continuous speech recognition, however, restrictions on the amount expressed by the words do not overlap, while the dictionary of KW themselves is limited from a few to several dozen.

Comparing the above areas of words recognition, we see that the most difficult task is to allocate the KW. It should be noted, that in case of a larger amount of vocabulary the tasks of continuous speech recognition and KW recognition convergeasymptotically. In the early stages of continuous speech recognition system, apparently, it is preferable to solve it as the task of KW allocation.

An important requirement to the developed speech recognition systems isthe conditions of registration: frequency range of the speech signal, the signal- to-noise ratio; electrodynamic transducer type (carbon or dynamic microphone), the presence of reverberations in the transmission channels, with or without adjusting the settings on the speaker.

The following specifications for speech recognition systems must meet:

1) the operating frequency range must not be worse than 0.3—3.4 kHz;
2) S/N ratio more than 10 dB;
3) microphone — electret or dynamic;
4) reverb distortion of the transmission channel should be eliminated;
5) any speaker of the message;
6) the size of the dictionary 100—5000 words;
7) detection characteristics for words: the probability of detecting more than 0.95, probability of false alarm not less than $10—^{3}$.

The above requirements for speech recognition system are very strict and require additional research to develop pattern recognition algorithms.

Requirements 3) and 5) are the most stringent. Solving the problem in this case is possible via redundant system, i. e. increasing the total number of standards for one word recognition to 10—20. Also 7) is very strict requirement, as the best result obtained by IBM, is the probability of detection 0.99 with adjustment for the speaker.

ARPA SUR Project overview and existing technologies, show that the system of automatic speech understanding must consistently perform the following tasks:

1) acoustic analysis (selection parameters of the speech wave);
2) phonetic analysis (detection the presence of consonants and vowels);
3) choice of words (comparison of the sequence of sounds with options pronouncing the word);
4) syntax analysis (check as recognized word syntactically consistent with the already -chosen words);
5) semantic analysis (check of the meaning of the transmitted message);
6) pragmatic analysis (prediction of the most likely following word based on a preliminary analysis of speech and the nature of the task)

Having compared the results of tests of various speech recognition systems, we give a brief summary of the results achieved.

1) When setting the speaker of the voice message in the ideal transmission channel in the band phone tract, with high-quality microphone and without additive noise the probability ofdetection is 0.95 and probability of false alarm of 0.001.

2) The presence of additive noise while working with cooperative speakers increases the probability of false alarm to 0.01;

3) The transition from one KW to the word form (two or more consecutive KW) dramatically reduce the probability of false alarm.

4) Speech recognition system having a large branching factor, or performing the phonemic speech recognition have a low probability of detection and high probability of false alarm.

5) There are no real time key word allocation systems, with a 0.95 probability of detection and false alarm probability less than 10^{-3}.

6) As the primary description of the speech signal the spectral slices or linear prediction coefficients are being used, which are experiencing significant variations with linear distortions in the transmission channel and with the change of the announcer of the voice message.

Thus, to effectively solve the problem of ordering of the voice messages it's important to choose effective primary parameters of the speech signal. Such selection may be done as a result of a theoretical analysis of the equations that describe the speech formation.

1. Chudnovskaya I. N., Chudnovskii L. S. Individ v informacionno-kommunikativnomprostranstve: Mnogourovnevaya model' funkcionirovaniya. LAPLAMBERTAcademicPublishing, Saarbryuken, Germaniya, 2011

2. Chudnovskii L. S., Minaev V. A., Chudnovskaya I. N. Rechevyetehnologii v kriminalisticheskoifonoskopii. Krasnoyarsk: Krasnoyarskayavysshayashkola MVD Rossii, 1997.

PL-8

Characteristic Features of IR Spectra of Explosives and ICAO Taggants in the Vapor State

Shavkat Sh. Nabiev[1], Dmitry B. Stavrovskii[2], Lyudmila A. Palkina[1], Elena N. Golubeva[3], Vitold L. Zbarskii[4], Nicolai V. Yudin[4] and Vladimir M. Semenov[5]

[1] National Research Center "Kurchatov Institute", 1, Kurchatov sq., Moscow, 123182 Russia
[2] Prokhorov General Physics Institute of the Russian Academy of Sciences, 38, Vavilov Str., Moscow, 119991 Russia
[3] Lomonosov Moscow State University, 1, Leninskie Gory, Moscow, 119991 Russia
[4] D. Mendeleyev University of Chemical Technology, 9, Miusskaya sq., Moscow, 125047 Russia
[5] National Research University "Moscow Power Engineering Institute", 14, Krasnokazarmennaya str., Moscow, 111250 Russia

Nowadays, efficient countermeasures to prevent terrorist attacks with the use of explosive devices based on different explosives make one of the crucial tasks of operation units of every state.

Earlier it was noted [1], that detection of explosive vapors in the open atmosphere is a direct detection method which sets it apart from the approaches making use of explosive and explosive device signatures. With the view of solution of the task of detection and identification of explosive vapors and microparticles, a range

of portable and stationary detectors based on mass-spectrometry (MS), gas chromatography (GC), ion mobility spectrometry (IMS), etc.) methods has been devised and is already in use [2].

Of late, a number of laser-optical methods featuring high sensitivity of the analysis of trace amounts of substances in the atmosphere has come into practice of local and remote detection of explosive vapors and microparticles [3,4]. Among these are the methods based on Reflection-Absorption IR Spectroscopy, Cavity Ringdown Spectroscopy (CRDS), Raman Spectroscopy and its modifications — Surface Enhanced Raman Spectroscopy (SERS), Tunable Diode Laser Spectroscopy (TDLS), Laser Photoacoustic Spectroscopy (LPAS), etc.

However, the evolution of laser-optical methods of detection of explosive vapors is still at the initial stage [1, 3]. A successful solution of the tasks of detection and identification of explosive vapors in actual practice is restricted by a number of problems the major of which is relatively low concentration of explosives in the air at room temperature. For instance, the vapor concentration of some explosives at the temperature of 298 K is equal to: $5.5 \cdot 10^{-6}$ Torr (7.7 ppb) for trinitrotoluene (TNT), $3.3 \cdot 10^{-9}$ Torr (6.0 ppt) for hexogen (RDX), and $1.16 \cdot 10^{-8}$ Torr (18.0 ppt) for pentaerythritoltetranitrate (PETN) [5]. The situation is dramatized by the fact that most of the explosives are mixture products containing additives, process-related impurities, and products of chemical conversions. [1].

In order to increase the efficiency of detection of concealed plantings of explosives with low saturated vapor pressure, on March'1 of 1991 in Montreal under the convention of the International Civil Aviation Organization (ICAO) [6] it was suggested to make highly volatile additions (ICAO taggants), at the level of 0.1—0.5% mass, components of explosives, plastic explosives included. At the same time, ICAO taggants cannot affect the operational performances of plastic explosives, and the saturated vapor pressure of the taggants at room temperature must be 3—5 times higher than that of RDX and PETN.

The four compounds suggested for use for chemical marking of explosives were: ethylene glycol dinitrate (EGDN), $C_2H_4(NO_3)_2$, para-nitrotoluene (4-NT), ortho-nitrotoluene (2-NT), $C_7H_7NO_2$ and 2,3-dimethyl-2,3-dinitrobutane (DMDNB), $C_6H_{12}(NO_2)_2$. These compounds have the following saturated vapor pressure values (at $T = 298$ K): $7.6 \cdot 10^{-2}$ Torr (EGDN), $4.89 \cdot 10^{-2}$ Torr (4-NT), $14.4 \cdot 10^{-2}$ Torr (2-NT), and $2.07 \cdot 10^{-3}$ Torr (DMDNB) [5].

The practical use of laser-optical methods of diagnostics of explosives and ICAO taggants requires detailed information on their vibrational spectra. This information is also necessary for a study of mechanisms of reactions involving explosives and ICAO taggants in the atmosphere, determination of the nature of their conversions and for the analysis of the applicability limits of the laser detection methods of explosive and ICAO taggant vapors in atmospheric air.

Meanwhile, the data on the spectra of explosive vapors are scarce and sometimes even contradictory, and the data on the parameters of the molecules of explosives, such as their absorption cross-section, are missing whatsoever. An exact assignment of the bands in the spectra is hindered by a complicated vibration-rotational structure of the molecules of explosives and interference of impurity bands with the bands of the molecules under study.

As far as ICAO taggants are concerned, they were devised with the view of specific analytical detection methods, in particular, GC and IMS. [7]. Therefore, the basic attention on selection of ICAO taggants was paid to the following parameters: high saturated vapor pressure, chemical (thermal) stability, storage time, compatibility with explosives (plastic explosives), availability of commercial manufacturing, etc. No examination was given to spectroscopic properties of the taggants, more specifically, absorption spectra parameters in the IR range which are required for the application of laser gas-analytical equipment based on IR absorption as one of the most sensitive methods of local and stand-off analysis [1].

This paper considers IR Fourier spectra of explosives (TNT, RDX, PETN) and ICAO taggants (EGDN, 2-NT, 4-NT, DMDNB) in the vapor state over a wide range of frequencies (4000—500 cm^{-1}) and temperatures (293—383 K).

With the aim in view of gaining spectroscopic data, special experimental techniques have been developed for registration of IR spectra of vapors of explosives and ICAO taggants. A procedure has been devised for preparation of TNT, RDX, PETN, EGDN, 2-NT, 4-NT and DMDNB samples of high purity (with the main material content min. 99.8 %) using modern methods of their synthesis and decontamination.

Modern quantum chemistry methods are used for determination of equilibrium geometrical configurations of TNT, RDX, PETN, EGDN, 2-NT, 4-NT, and DMDNB molecules and calculation of fundamental vibrational frequencies. The as-gained experimental and theoretical data make the basis for assignment of the observable vibrational bands. Estimates have been made of the magnitudes of absorption cross-sections for the most intensive bands in the IR spectra of TNT, RDX, PETN, 2-NT и 4-NT in the vapor state. With the aim of specifying the physical and chemical processes occurring on heating and evaporation of TNT, RDX, and PETN, as well as definition and identification of their characteristic volatile components, mass-spectra and sub-THz spectra of these explosives have been investigated.

IR spectra of the gas phase of RDX and PETN are proven to contain intensive bands of their decomposition products, first of all formaldehyde and nitrogen oxides (N_2O and NO). Recrystallized products, even with high-degree purification ($\geq$ 99.7 %), have bands of a dissolvent (acetone) (Fig. 1). The data of sub-THz spectrometry and mass-spectrometry confirm the results gained with the IR Fourier analysis.

The presence of decomposition products in noticeable amounts even at comparatively low temperatures combined with low pressure of saturated vapors of RDX, PETN and plastic explosives made on their basis at temperatures close to the room temperature may complicate appreciably the tasks of detection and identification of trace amounts of these explosives in atmosphere with the methods not only of laser spectroscopy but also with MS, GC and IMS methods [8].

Investigations of the IR Fourier spectra of ICAO taggants have revealed that, in contrast to RDX and PETN, their gas phase has no bands of gaseous decomposition products of the taggants. A number of absorption bands in the spectra of ICAO taggants are well isolated and have fairly high intensity in the frequency range of 800—1600 cm^{-1} (Fig. 2).

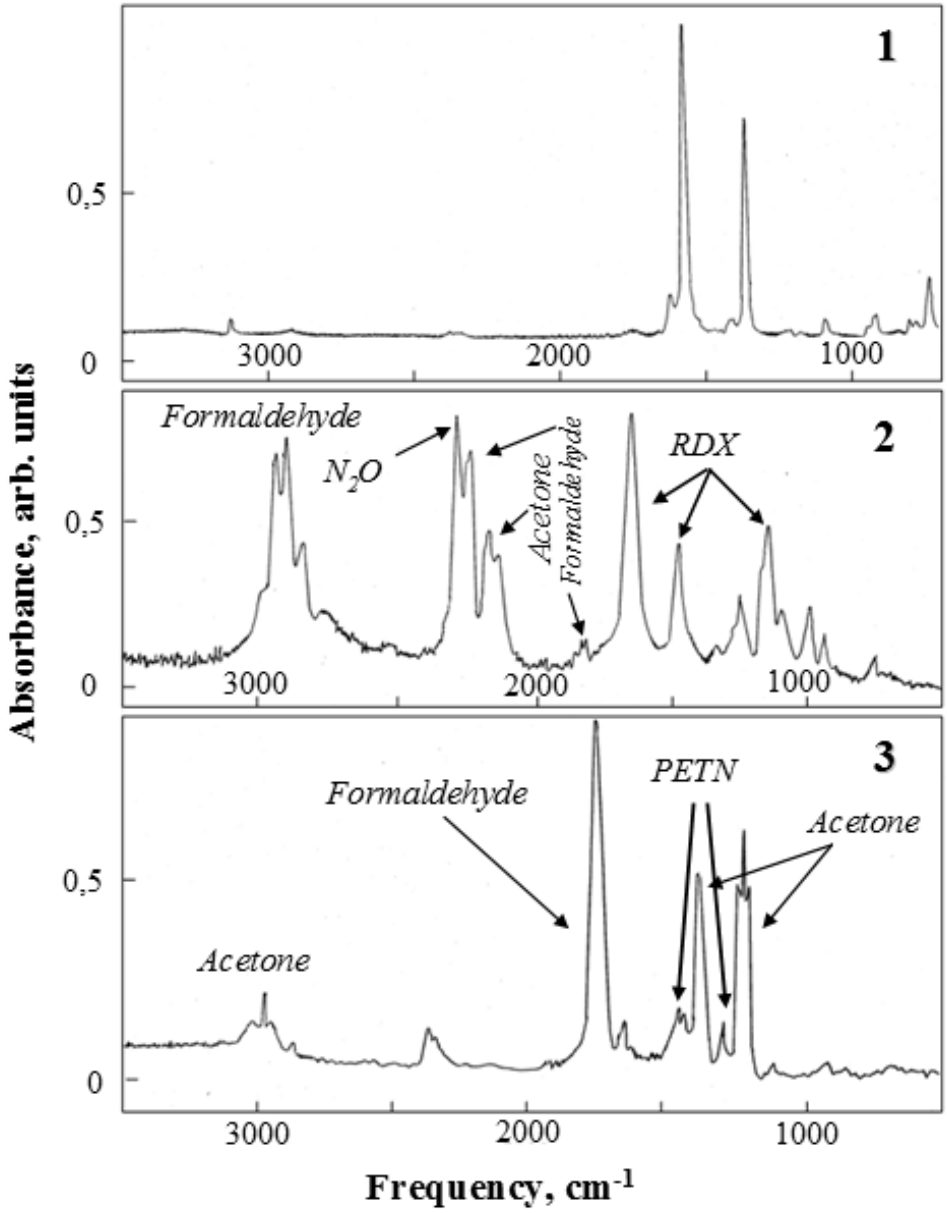

FIGURE 1. FTIR spectra of TNT (1), RDX (2) and PETN (3) vapors (T = 358, 370 and 340 K, respectively) over the range of 3500 to 500 cm^{-1}

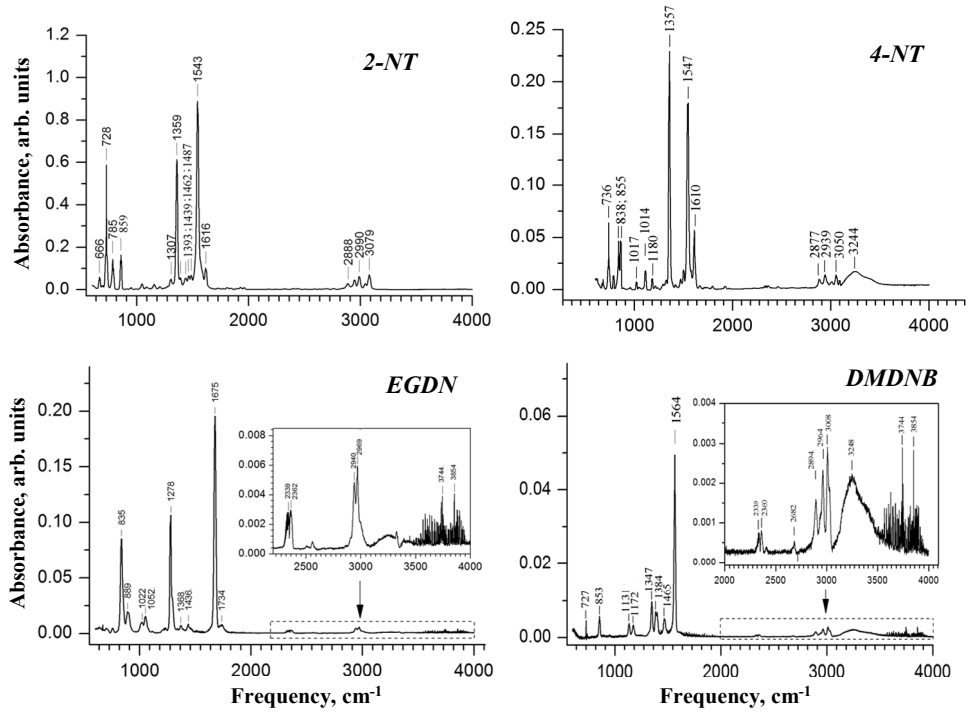

FIGURE 2. FTIR spectra of 2-NT, 4-NT, EGDN and DMDNB vapors (T = 295 K) over the range of 4000 to 500 cm^{-1}.

A conclusion was driven at that application of the potentialities of modern laser technologies combined with the obtained spectroscopic data for THT, RDX, PETN, EGDN, 2-NT, 4-NT and DMDNB will provide the means of reliable detection of explosives and ICAO taggants in the atmosphere at the ppb level. An appreciable functional enhancement of laser-optical methods of detecting explosives and ICAO taggants, and delimitation of applicability of these methods can be held within the concept of building an integrated multiwave detection system comprising a series of laser detectors and mounted on a teleoperated mobile platform [1]. In certain situations, such multiwave detection systems mounted on mobile teleoperated platform may offer appreciable advantage over other monitoring systems for local or stand-off visual inspection of items and objects in search of traces of explosives and for on-line air testing of ICAO taggants presence in portals, ventilation systems, etc.

1. Sh. Sh. Nabiev and L. A. Palkina, *Abstr. of III Intern. Conf. "Atmosphere, ionosphere, safety" (AIS-2012)*, Kaliningrad, Russia, 2012. pp. 122—124.
2. J. S. Caygill, F. Davis and S. P. J. Higson, *Talanta*, 2012, vol. 88, pp. 14—29.
3. Z. Bielecki, J. Janucki, A. Kawalec, et al., *Metrol. Meas. Syst.*, 2012, vol. 19, pp. 3—28.
4. L. A. Skvortsov, *Quantum Electron.*, 2012, vol. 42, pp. 1—11.
5. H. Östmark, S. Wallin, H. G. Ang, *Propell. Explos. Pyrotech.*, 2012. vol. 37. pp. 12—23.

6. *Convention on the Marking of Plastic Explosives for the Purpose of Detection* (Montreal, 1 March 1991), ICAO, Doc. 9571 (http://www.icao.org/).
7. S. V. Nekhoroshev, Yu. P. Turov, V. P. Nekhoroshev, A. V. Nekhorosheva, *Rus. J. Analyt. Chem*., 2010, vol. 65, pp. 1012—1019.
8. Sh. Sh. Nabiev, D. B. Stavrovskii, L. A. Palkina, et al., *Rus. J. Phys. Chem. B*, 2013, vol. 7, pp. 203—219.

PL-9

Quantum-Chemical Calculations of Spectral Parameters as a Way of Molecular Structure Definition

Elena N. Golubeva[1], Oleg. I. Gromov[1], Ekaterina M. Zubanova[1,2], and Georgii M. Zhidomirov

[1] Chemistry Department, Moscow State University, 119991, Lenin Hills, 1—3, Moscow, Russian Federation
[2] Semenov Institute of Chemical Physics RAS, 119991, Kosygin st. 4, Moscow, Russian Federation
[3] Boreskov Institute of Catalysis SB RAS, 630090, pr. Lavrentieva 5, Novosibirsk, Russian Federation

One of the most important tasks of chemistry is definition of composition and structure of active, short-lived species. Knowing those, one can establish mechanisms of complicated organic, bioorganic, photochemical processes, etc., with the aim to rule over them. However, in most cases it is nearly impossible to get structural parameters of intermediates using standard experimental methods such as X-ray diffraction, EXAFS, etc. A little bit easier to obtain spectral characteristics (e. g., absorption bands in UV-Vis and IR region, Spin-Hamiltonian parameters) of intermediates with the help of special technique like time resolved methods. Interpretation of spectral data is widespread and well developed field of science allowing obtaining important, but, as usual, incomplete information. In recent times calculations of spectral parameters performed on post-Hartree-Fock or density functional levels of theory show very good agreement with experiment. That is why quantum-chemical calculations become a powerful approach to molecular structure definition. The approach includes selection of series of appropriate model structures, their geometry optimization, and calculation of spectral characteristics. Comparing experimental and theoretical values of different structures one can find out the model with most correspondent parameters.

In this paper we present the example of identification of structure of novel organometallic species using quantum chemical calculations based on density functional theory (DFT). Complexes of Cu(I) compounds with organic radicals are proposed to be intermediates of catalytic reactions [1,2] such as controlled radical polymerization [3], carbonylation [4], and C-Cl bond metathesis [5], etc. Cu(I) com-

plexes with a wide variety of alkyl-type radicals [6—8] form under γ-radiolysis or photolysis of Cu(II) compounds. Combination of EPR and UV-Vis studies coupled with quantum-chemical calculations reveal that photolysis of tetrachlorocuprates of quaternary ammonium (e. g., $(N(C_6H_{13})_4)_2[CuCl_4]$) in chloro-organic solvents (chlorobenzene, chloroform, and 2-chlorobutane) at 77 K results in formation of two paramagnetic copper-containing products, possibly, organocuprates, denoted as **1-Cu** and **2-Cu** [9] (Fig. 1).

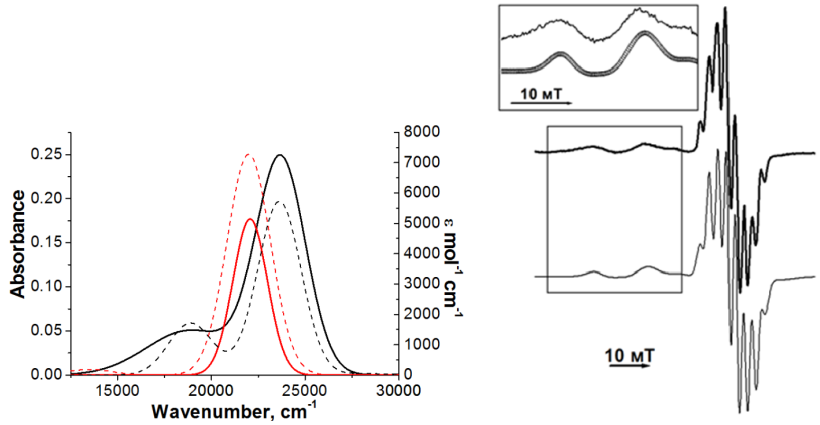

a *b*

FIGURE 1. a)Gaussian-shaped bands of **1-Cu** (black solid) and TD-DFT calculated UV-Vis spectra of model structure **I** (black dash) and Gaussian-shaped band of **2-Cu** (red solid) and TD-DFT calculated UV-Vis spectra of model structure **II** (red dash); b) EPR spectra of products of photolysis of tetrahexylammonium tetrachlorocuprate (black solid) and model spectrum as linear combination of **1-Cu, 2-Cu** and alkyl radicals (rounds, gray). 77K.

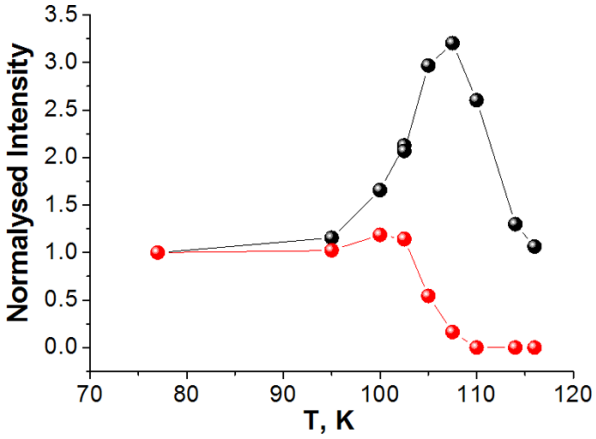

FIGURE 2. Normalized intensities of the bands with maxima at 18862 and 23696 cm^{-1} (black) and 22066 cm^{-1} (red) during annealing of products of photolysis of $(N(C_6H_{13})_4)_2[CuCl_4]$) in 2-chlorobutane.

Due to dependences of spectral bands intensities on temperature (Fig. 2) the following scheme of photolysis was proposed:

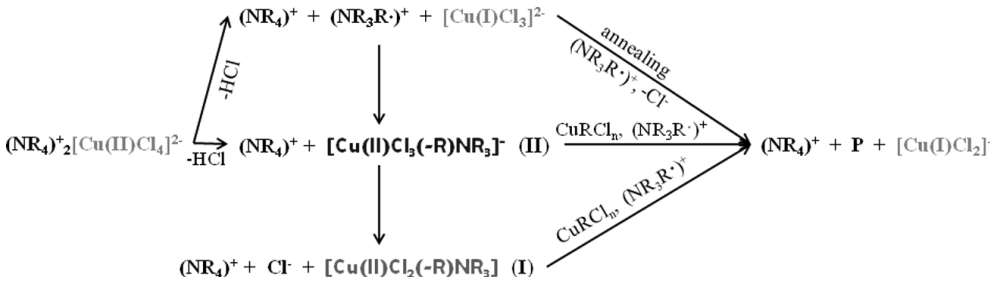

As results from this scheme, **1-Cu** (λ_{max} = 22066 cm^{-1}) corresponds to $[NR_4^+](R`\cdot)[CuCl_3^{2-}]$, where R`· is alkyl-type radical formed by alkyl tale of tetrahexylammonium cation. **2-Cu** (λ_{max} = 18862 and 23696 cm^{-1}) corresponds to $[NR_4^+](R`\cdot)[CuCl_2^-]$. For verification of this hypothesis quantum-chemical calculations (PBE/6—311G++(3df,3pd)) of a number of model structures (Fig. 3) was performed. It was shown that all these structures correspond to minima on potential energy surfaces. The calculated UV-Vis spectrum (TD-DFT/B(38HF)P86/aug-def2-TZVPP/COSMO) of the model structure **IV** ($[NR_4^+](R`\cdot)[CuCl_2^-]$ (Fig. 1,a, black dash) being scaled by 0.91 factor matches the experimental spectrum of **1-Cu** (Fig. 1,a, black solid). The same, calculated spectrum of **V** $[NR_4^+](R`\cdot)[CuCl_2^-]$ (red dash) is similar to experimental spectrum of (Fig. 1,a, red solid).

EPR spectrum of **2-Cu** as well as main values of g- and hfc tensors were obtained experimentally in annealing of the photolyzed sample to 100 K [8]. The g-tensor values of $[NR_4^+](R`\cdot)[CuCl_2^-]$ calculated on B(38HF)P86/CP(PPP)/IGLO-III/IGLO-II level are very close to those of **2-Cu**, which confirms the conclusions made from modeling of electronic spectra. Spin-Hamiltonian parameters of $[NR_4^+](R`\cdot)[CuCl_3^{2-}]$ calculated at the same level were used for construction of **1-Cu** spectra. The experimental EPR spectrum at 77 K (Fig.1,b, black solid) was found to be very similar to one evaluated using ODF-3 program [10] with experimental magnetic resonance parameters of $[NR_4^+](R`\cdot)[CuCl_2^-]$, calculated parameters of $[NR_4^+](R`\cdot)[CuCl_3^{2-}]$, and parameters (combined experimental and calculated) of alkyl radicals ($CH_3CH(\cdot)(CH_2)_3CH_2$- and -$CH_2CH(\cdot)CH_2$-) (Fig.1,b, rounds, gray).

Consequently, DFT calculations of spectral parameters of possible intermediates of photochemical reduction of chlorocuprates in organic solutions allow us to establish the intermediates structures and to confirm the reaction mechanism.

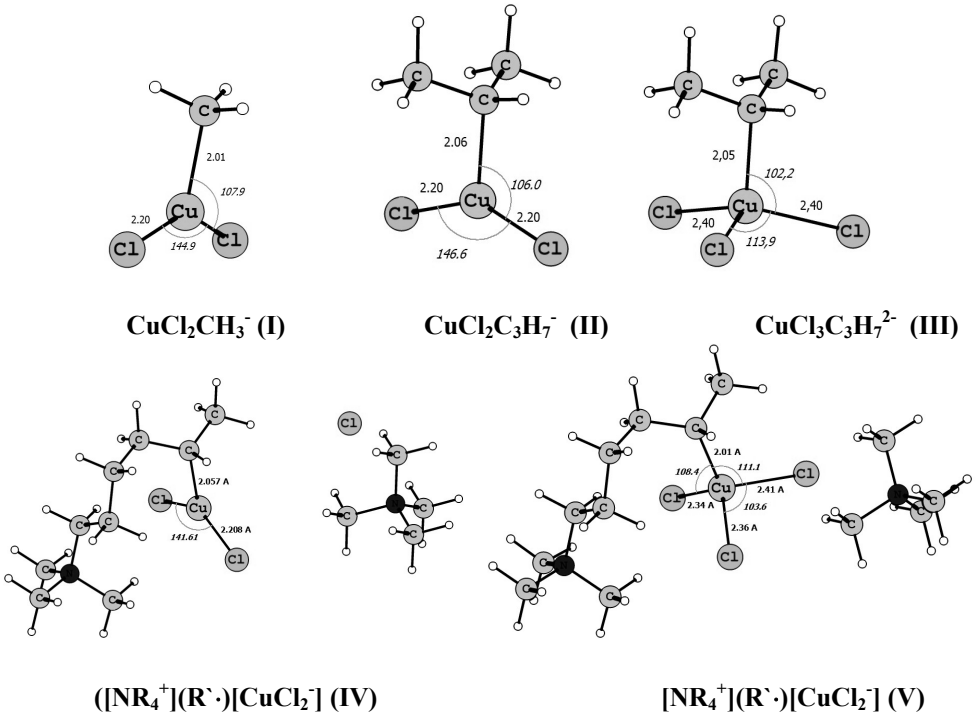

$CuCl_2CH_3^-$ (I) **$CuCl_2C_3H_7^-$ (II)** **$CuCl_3C_3H_7^{2-}$ (III)**

($[NR_4^+](R`\cdot)[CuCl_2^-]$ (IV)** **$[NR_4^+](R`\cdot)[CuCl_2^-]$ (V)

FIGURE 3. The geometries of some model organocuprates.

This work was partially supported by RFBR (grant 13-03-420). Quantum-chemical calculations were performed using resources of Supercomputing Center of Lomonosov Moscow State University.

1. M. P. Brown and K. Austin, *The New Physique*, Publisher, London, 2002, pp. 25—30.

1. A. Burg, D. Meyerstein, *Inorganic/Bioinorganic Reaction Mechanisms,* 2012, 64, pp. 219—261.

2. N. Navon, G. Golub, H. Cohen, D. Meyerstein, *Organometallics*, 1995. 14, 12, pp. 5670—5676.

3. W. A. Braunecker, K. Matyjaszewski, *Prog. Polym. Sci.*, 2007, 32, 1, pp. 93—146.

4. A. Szulz, D. Meyerstein, H. Cohen, *Inorg. Chim. Acta*, 1998, 270, 1—2, pp. 440—445.

5. E. N. Golubeva, D. N. Kharitonov, D. I. Kochubey, et al, *J. Phys. Chem. A*, 2009, 113, 38, pp. 10219—10223.

6 G. Ferraudi, *Inorg. Chem.* 1978, 17, pp. 2506—2508.

7. H. Cohen, D. Meyerstein, *Inorg. Chem*, 1986, 25, pp. 1505—1506.

8. E.N. Golubeva, A.V. Lobanov, V.I. Pergushov, et al, *Dokl. Chem.* (Engl. Transl.) 2008, 421, pp. 171—173/

9. E.N. Golubeva, O.I. Gromov and G.M. Zhidomirov *J. Phys. Chem. A,* 2011, 115, pp. 8147—8154.

10. A. Kh. Vorobiev, and N.A. Chumakova, *Nitroxides — Theory, Experiment and Applications*, Rijeka: InTech, 2012.

Applications of Pulsed and Continuous Detonations: In Search for Energy Efficient Solutions

Sergey M. Frolov, Victor S. Aksenov, Vladislav S. Ivanov, Victor A. Smetanyuk, Igor O. Shamshin, Sergey N. Medvedev, Konstantin A. Avdeev, and Fedor S. Frolov

Center for Pulsed Detonation Combustion, Semenov Institute of Chemical Physics, 4, Kosigin Street, Moscow 119991, Russia

Introduction

A Pulsed Detonation Combustor (PDC), a tube of 150 mm diameter and 5.5 m length equipped with the mechanical valve and manifolds for separate delivery of natural gas and air (Fig. 1), as well as a continuous-detonation annular combustor (CDC) of 400 mm diameter and 300 mm height with the annular gap of 30 mm width equipped with the manifolds for separate delivery of hydrogen and air (Fig. 2) were designed, manufactured and tested within a research program aimed at experimental studies of energy efficiency of the thermodynamic cycle with detonation combustion (Zel'dovich cycle).

FIGURE 1. Pulsed detonation combustor operating on natural gas and air. The open end (far end) is immersed into a furnace.

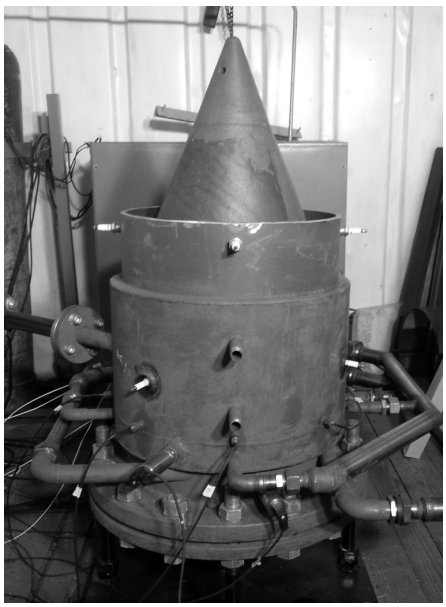

FIGURE 2. Continuous detonation combustor operating on hydrogen and air.

Pulsed Detonation Combustor

The PDC consists of two coupled sections: the mixing/ignition section with a spark-ignition source (ignition energy less than 1 J; 2 to 4 standard automobile spark plugs) and the burner duct — a straight tube with obstacles. The shape, pitch, and blockage ratio of obstacles vary with distance from the ignition source to facilitate deflagration-to-detonation transition (DDT). This variation first ensures the fastest possible flame acceleration for generating a sufficiently strong shock wave, and then it ensures the fastest possible transition of this shock wave to a detonation due to its focusing at shaped obstacles of low hydrodynamic drag. The end of the burner duct is immersed into the furnace.

The operation cycle of the PDC consists of several stages. Their duration is controlled by a digital controller. Both components of the mixture are delivered in MIS through separate lines equipped with check valves. Natural gas containing 98.9 % methane (according to certificate) is fed into the burner through the receiver 200 liters in volume at overpressure of 0.3 bar connected to the natural gas manifold via a control valve. Ambient air is fed into the PDC with a vortex blower, which provides airflow up to 0.5 m^3/s.

In the first stage the PDC is filled with a mixture of natural gas and air. When filling the PDC with a combustible mixture the mass flow rates of components are adjusted to ensure that mixture composition is close to stoichiometric (mixture composition is checked by chromatographic analysis of probes taken in several tube sections), i. e. the volume concentration of methane is (9.5 ± 0.3)%. To avoid leakage of fresh mixture through the open end of the burner duct the PDC is filled only partly with the mixture. The digital controller sets the time of filling the burner duct to avoid leakage through its open end even for the most undesired condition of DDT failure: a mixture is completely burned in both the detonation and deflagration modes.

In the second stage, after shutoff of natural gas supply (with a fast-acting valve) multi-point fuel-air mixture ignition is triggered in MIS followed by automatic stopping of air supply, fast flame acceleration in the burner duct and DDT at a distance of ~ 3.5 m from the ignition source for ~20 ms after ignition.

In the third stage, the shock wave exits from the duct open end followed by the outflow of the detonation products.

In the fourth stage, the PDC is first purged with air for a short time and then the supply of natural gas and air is resumed, thus the next cycle starts.

The (currently) maximum operation frequency of the PDC in the detonation mode is 5 Hz.

The PDC has several specific features as compared to conventional burners.

First, contrary to conventional burners with combustion taking place in the flame outside the burner producing a low-density jet with the maximum velocity of ~ 200 m/s and maximum temperature of ~1800^{o}C, in the PDC combustion is completed inside the burner duct producing a long-penetrating and highly energetic

pulsed jet of detonation products possessing a very large flow velocity (above 1000 m/s), high temperature (about 2500°C), and high density (about 2 kg/м^3) at the outlet of the burner duct. Such jet allows heating different objects in a very short time. For example, Fig. 3 shows the photos of a bulk of metal shavings before and after the 100-second impact of pulsed jets generated by the PDC at operation frequency 4 Hz. Clearly, metal shavings got melted.

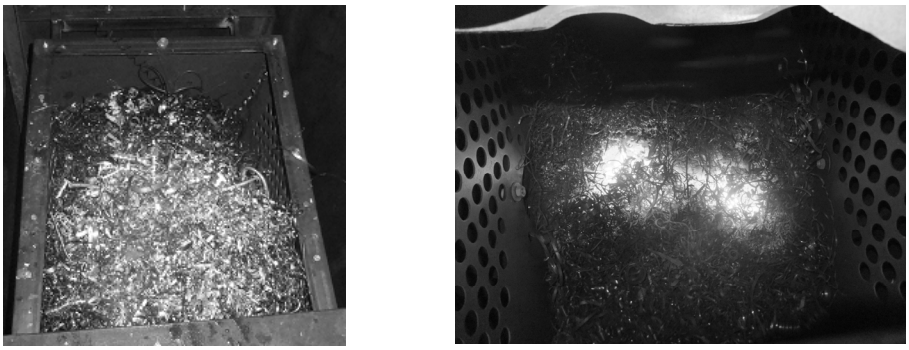

a *b*

FIGURE 3. Metal shavings before (a) and after (b) the 100-second impact of PDC jets.

Second, due to periodic filling of PDC with a portion of cold fuel — air mixture, followed by burning of this portion in the traveling detonation wave and outflow of hot detonation products into the furnace interior, the temperature of PDC structural elements achieves a certain maximum steady state value. The steady-state temperatures of PDC structural elements were measured in the course of long-duration testing in a pulse-detonation mode with a frequency of 2 Hz without forced cooling. Experiments showed that the maximum steady-state temperature (~ 500°C) is reached after approximately 200 s of PDC operation in DDT-enhancing obstacles located in a part of the burner duct periodically traversed by the detonation wave. The walls of the PDC in this part of the burner duct were estimated to heat up to ~ 400—430 °C during the time on the order of 1000 s. In the part of the burner duct periodically traversed by the deflagration wave the walls and interior elements were heated to a steady-state temperature of no more than ~ 300—330 °C. Thus, the results show that the forced cooling is generally required only in the parts of the burner duct traversed by the detonation wave.

Third, the PDC produces low NOx emission as compared to conventional burners. As a matter of fact, the characteristic time of high-temperature processes in the PDC is considerably shorter than in conventional burners and therefore the NOx emission index is considerably (by a factor of 3) lower despite the detonation temperature is about 700°C higher than the typical combustion temperature of methane — air mixture.

Fourth, despite the PDC is considered as a noisy device, our measurements showed that the use of proper noise reduction techniques allows reducing noise level to acceptable values. As an example, Fig. 4 shows the time dependence of the noise level measured by a precise sound level meter outside the furnace chimney equipped with noise suppression elements. The numbers in Fig. 4 mark the characteristic portions of the curve: 1 is the background noise, 2 is the noise of air blower, 3 is the noise at PDC operation with frequency of 1 Hz, 4 is the noise at PDC operation at 2 Hz, and 5 is the noise at PDC operation at 4 Hz. It is seen that the maximum noise level at the outlet of furnace chimney is about 105 dB which is below the allowable standard value.

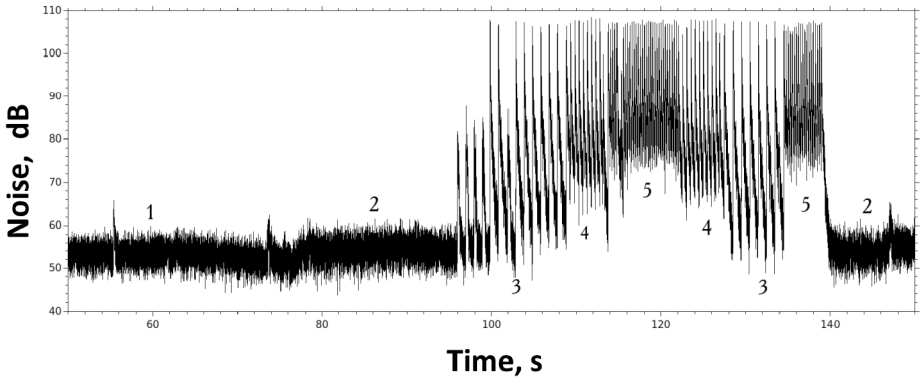

FIGURE 4. PDC noise level at the outlet of furnace chimney.

Continuous Detonation Combustor

To understand how the CDC operates, consider an annular channel formed by the walls of two coaxial cylinders. Mounting an injector head at the bottom of the cylinders to provide supply of fuel components into the annular channel and a nozzle at the other end of the channel makes an annular flow reactor. Combustion in such a reactor can be realized in different ways: either as in an ordinary burner or according to a Voitsekhovskii scheme, when the mixture is burned in detonation waves traveling in tangential direction over the bottom of the annular channel. The detonation wave burns fuel mixture injected into the CDC during one wave revolution in the annular channel (in the case of a single wave). The angular frequency of rotation of the detonation wave in a medium-size chamber is of the order of 10^5 rpm and higher. The oxidation of fuel in the wave occurs in the mode of self-ignition at high pressures and temperatures. Therefore, the efficiency of the combustion process in the CDC, ceteris paribus, will be higher than in the conventional burner (the process occurs at higher pressures behind the shock wave). Use of the CDC promises great benefits, at least theoretically, for the aerospace and energy industries. In particular, because the fuel burns in the CDC continuously, a turbine

can be installed at the nozzle exit, on a common shaft with the compressor driving air into the annular combustion chamber. Given that the speed of the turbine is on the order of 10^4 rpm, during one revolution of the turbine, the detonation wave makes ten or more turns, i. e., the exhaust gas flow through the turbine can be considered nearly steady with some pulsations. In this configuration, a gas turbine with a CDC is very similar to a conventional gas turbine, but instead of continuous combustion, a detonation wave continuously circulates in the CDC.

Figure 5 shows high-speed video frames of the CDC exhaust plume and the luminosity of the detonation continuously rotating in the annular CDC gap.

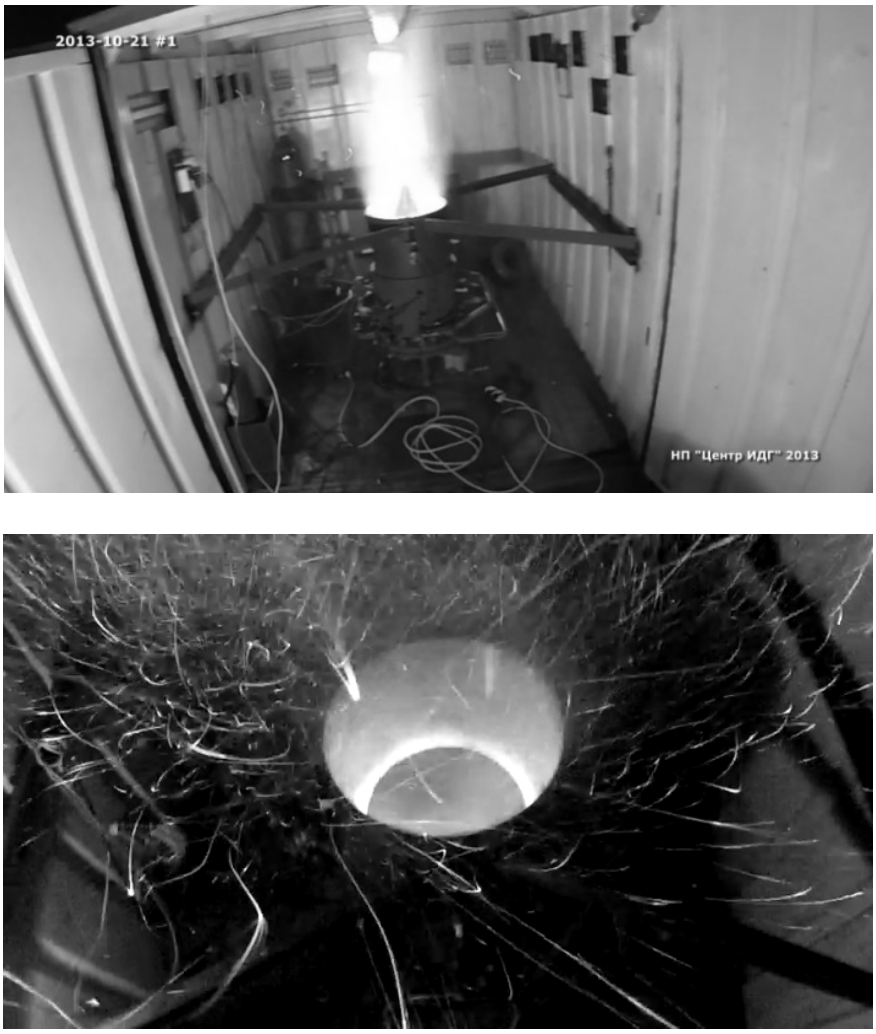

FIGURE 5. High-speed video frames of the CDC exhaust plume (top) and detonation luminosity in the annular gap (bottom).

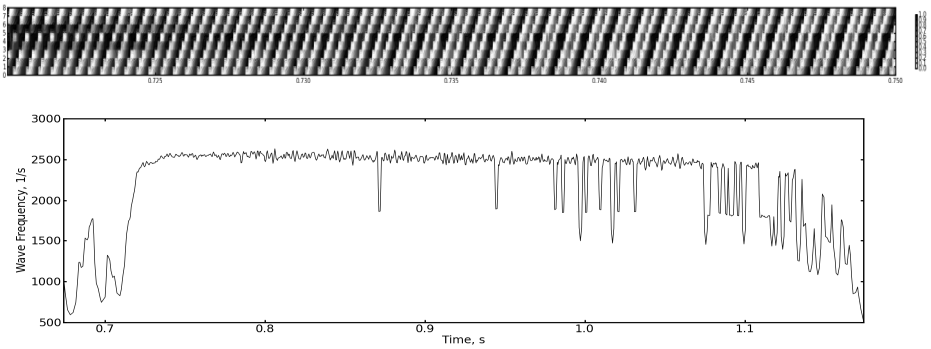

FIGURE 6. Distance — time diagram for the wave process in the CDC (top) and detonation rotation frequency vs. time (bottom).

Fig. 6 shows the records of 8 ionization probes arranged equidistantly in a single circumferential section of the CDC (top) and the measured dependence of the detonation rotation frequency on time (bottom). The X-axis in the records corresponds to time and the Y-axis corresponds to the probe number (from 1 to 8).

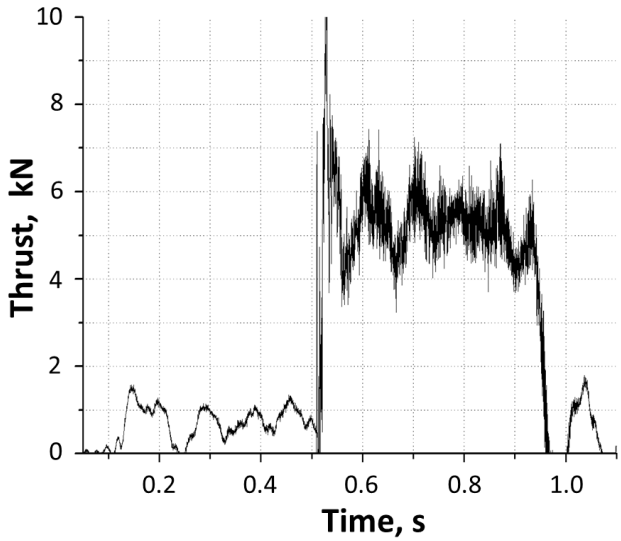

FIGURE 7. Measured thrust of the CDC.

The maximum brightness in the records corresponds to the maximum ionization current attained in the detonation front. As a matter of fact, these records represent the distance — time diagram for the wave process in the CDC and the slopes of bright lines represent the detonation propagation velocity. According to these records the average detonation propagation velocity is 1950 m/s, which is very

close to the thermodynamic detonation velocity in the stoichiometric hydrogen — air mixture. According to the lower diagram in Fig. 6 during most of the operation time the rotation frequency is about 2.5 kHz, which corresponds to the mode with two detonation waves simultaneously propagating in one direction (rotation of a single detonation wave at a given velocity would result in the frequency of ~1.3 Hz).

Figure 7 shows the measured thrust of the CDC in the mode with two detonation waves. In this figure, ignition starts at 0.51 s and fuel supply is terminated at 0.94 s. The fuel-based specific impulse in this experiment is equal to 3200 s indicating high energy efficiency of the thermodynamic cycle with detonation combustion.

Conclusions

Two large-scale devices utilizing the thermodynamic cycle with pulsed and continuous detonation combustion (Zel'dovich cycle) have been designed, manufactured and tested, namely the PDC and CDC. These devices can be considered as prototypes of industrial burners of new generation which are capable of producing lengthy and energetic pulsed or continuous supersonic plumes of high-temperature combustion products at essentially decreased fuel consumption and NOx emission as compared to conventional burners in metallurgy, chemical engineering, waste incineration, etc.

This work was partly supported by the Research Program No. 26 "Combustion and Explosion" of the Presidium of the Russian Academy of Sciences.

PL-11

Radiochemical Physics of the Upper Earth Atmosphere

G. V. Golubkov[1], M. I. Manzhelii[1], A. A. Lushnikov[2]

[1] *Semenov institute of chemical physics of Russian academy of sciences, Moscow, Russia*
[2] *Karpov institute of physical chemistry, Moscow, Russia*

The splash of large scale studies of physicochemical processes in the atmosphere observed during last three decades is explained by growing interest to the propagation processes of electromagnetic signals from satellites and RLS. It became clear that collision and radiation processes involving the Rydberg complexes play a fundamental role in the shaping of the radio signals. The influence of highly excited molecular states, where a weakly bounded electron occupies a remote orbit (with the radius much exceeding the size of the residual ion) is appreciable and should be thoroughly investigated for the correct interpretation of the information carrying by the electromagnetic waves [1—3].

Accumulated vast material serves as a basis for forming a new direction of chemical physics — radiochemical physics of the upper atmosphere. It includes the study of the group of physicochemical processes responsible for the origin of the super-background decimeter ultra-high frequency (UHF) and far infrared (IR) radiation and its propagation in the atmosphere perturbed by the Sun activity. The present article discusses the goals and the tasks of radiochemical physics and its possible implications. We mean satellite measurements of the salinity of oceans, of soil humidity, of the state of plant cover, weather forecast and the water balance of the Earth. These items are actively conducted within the Program SMOS of the European Agency for Cosmic Research.

Strong geomagnetic perturbations in the ionosphere caused by raising Sun activity change appreciably the quantum and optical properties of D- and E- layers. Under these conditions the non-coherent super-background radiation of decimeter range forms. The intensity profile of this radiation strongly depends on the frequency of the electromagnetic waves and the level of the perturbation. The transitions between the orbital degenerated Rydberg states of quasimolecules $A^{**}N_2$ и $A^{**}O_2$ are assumed to cause the radiation. These states themselves efficiently form in nonequilibrium two-temperature plasma either by capturing the ionospheric electrons or by the direct radiation from the Sun flares.

The key point for describing this phenomenon is the account for the interactions of the Rydberg atoms and molecules with the molecules of the carrier gas. The orbital degenerate states of each Rydberg particle A** form by an important atmospheric process — *l*-mixing that leads to the degeneracy of the weakly bounded electron over the angular momentum by collisions with the neutral molecules. Long-range interaction between them leads to the formation of a quasimolecule, whose states for a given principal quantum number *n* are split into multiplets characterized by the angular momentum L with respect to the alien neutral molecule [4]. The distances between the multiplet levels ($\Delta n = 0$) well correspond to the wavelengths of decimeter range.

Rydberg's states in neutral carrier gas

The energy levels of Rydberg's states are located right beneath the ionization threshold. The respective wave functions describe the weakly bounded electron whose orbit lies at the distances exceeding by orders of magnitude the characteristic atomic sizes. Therefore the radiation efficiencies from these states are strongly affected by the surrounding carrier gas [1—3]. The energy of the Rydberg level is given by the principle quantum number *n* and the angular momentum *l* with respect to the ion core. The levels belonging to the states with large *l* are independent of *l* (orbital degeneration). These very states are the most statistically stable, because the valent electrons moves mainly far away from the ionic core.

The *l*-mixing is the process of formation of the degenerate states that are just a superpositions of the states with large angular momenta. In the upper atmosphere this process is rapid and is practically irreversible. The *l*-mixing erases the quantum

differences between atoms and molecules. The radiation spectrum thus ceases to depend on the chemical structure of the residual core [1]. The *l*-mixing goes efficiently at sufficiently high density (10^{12} cm^{-3}) of the carrier gas which corresponds to the altitudes not exceeding 110 km. The criterion for the efficiency of the l-mixing is the condition that at least one neutral molecule M is located inside the sphere of radius $2n^2a_0$ (the size of the Rydberg cloud around the atom A**), where a_0 is the Bohr radius. The interaction between the alien molecule M and the residual core A** leads to the formation of a quasimolecule A**M whose potential energies are characterized by the angular momentum L of the weakly bounded electron with respect the molecule M. The shapes of the respective potential curves can be expressed in terms of the characteristics of the elastic scattering of a slow electron by the molecule. The optical transitions between split and degenerate states belonging to the same principal quantum number *n* correspond to the radio waves within the decimeter range. The transitions between the states with slightly different principle numbers ($\Delta n << n$) are responsible for the IR radiation from the Rydberg complexes.

At the altitudes h < 50km the Rydberg states of the complexes A** cannot be occupied because of the extinction processes that go predominantly by the interaction of the Rydberg complexes with non-excited molecules of oxygen via the intermediate ion complex $A^+(nL)O_2^-(s)$ (the harpoon mechanism). The point is that the negative molecular ion O_2^- has a set of autoionization vibration s-excitations located within the background of the ionization continuum. Besides, the concentration of the free electrons drops down as the altitude diminishes [3]. As the result of interplay between these two factors the atmospheric layer radiating radio waves within the decimeter range forms between 80 and 110 km.

Nonequilibrium two-temperature plasma

The increase of the Sun activity leads to the formation of two types of nonequilibrium plasmas in the atmospheric E- and D- layers: recombination plasma and photoionization plasma [2]. The first type is the nonequilibrium two-temperature plasma wherein the Rydberg states are populated by the collisional transitions of the free electrons to bound states as a result of inelastic interactions of the free electrons with neutral molecules of the carrier gas. The electron temperature T_e can change from 1000 to 3500 K, whereas the temperature T_a of the carrier gas in the layer is much lower: 200—300 K. This mechanism of the formation of the Rydberg states dominates in the lower D-layer. The reaction of the vibrational excitation of the molecular nitrogen through the formation of the negative nitrogen ion $e^- + N_2(\mathrm{v}=0) \rightarrow N_2^- \rightarrow e^- + N_2(\mathrm{v}\geq 1)$ is mainly responsible for the thermalization of the free electrons.

For determining the altitude dependence of the partial populations $m_{A^{**}X_2}(n,L)$ of the Rydberg complexes A**N_2 and A**O_2 on the temperature T_e and concentration of medium ρ_a the code «Rydberg» was developed in [3] that allows one to retrieve the function $n_e(\rho_a)$ which has can be parametrized as $n_e(\rho_a) = n_e(\rho_a^\circ)\left[\rho_a^\circ/\rho_a\right]^{0.89}$ within the interval of altitudes 60—110 km. Here $n_e(\rho_a^\circ)$ and ρ_a° are the concentration of electrons and the carrier gas density at the upper altitude H° = 110 km.

The two temperature photoionization plasma emerges during 20—30 min under the action of wide band radiation from Sun flares. This process is due to the multiquantum excitations of the electronic states where the spin forbiddances for the respective radiation transitions are removed by the interactions with the molecules M of the carrier gas. The occupancy of the Rydberg states in this case should be essentially different from that for the recombination plasma. Indeed, because the occupancy is driven by the flux from lower energy states, the bottle neck of the sink does not form. This circumstance leads to the active population of the low lying Rydberg states. At n = 20—40 their occupancies should exceed those in the recombination plasma by the factor 2—3. The difference in the populations of highly excited Rydberg states (large n) in the photoionization plasma from those in the nonequilibrium recombination plasma consists in the fact that they are additionally exhausted due to photoionization. At not large n the Rydberg and low lying states are exhausted by the predissociation processes including the non-adiabatic transitions via intermediate valence ion configurations and a resonance (not resonance) transfer of the internal energy by the interactions with the carrier gas with the subsequent thermalization of the carrier gas. The temperature growth in increasing the altitude from 40 to 60 km evidences in favor of this mechanism. Under these conditions the l-mixing is suppressed and the influence of the surrounding medium becomes minimal [3].

The emergence of two temperature plasma should lead to the irradiation within RF range, whose specifics within the frequency interval 0.8—8.5 GHz is of primary interest. In normal ionospheric conditions the intensity flux I_{tot} at frequency ν = 1.6 GHz is small and it jumps sharply up near 1.8 GHz. The ionospheric perturbations triggered by the Sun activity produce appreciable changes in the behavior of I_{tot} within the considered frequency range. Such is the case for this interval, where the increase in the density of the carrier gas ρ_a° and the electron concentration $n_e(\rho_a^\circ)$ lead to the formation of a specific dependence of the spectrum on the frequency of radiation: an intersection of the curves $I_{tot}(n_e(\rho_a^\circ), T_e)$ at an isolated point $\nu_f^{(1)} = 1.4$ GHz emerges within wide interval of the plasma parame-

ters [3]. This behavior of the plot is referred to as the «waist point». The position of this point is independent of $n_e(\rho_a^\circ)$, and T_e, whereas the flux intensity $I_{tot}^{(1)} = I_{tot}(\nu_f^{(1)})$ displays the quadratic growth in $n_e(\rho_a^\circ)$. This fact is clearly demonstrated in Fig. 1, where the solid and dash lines correspond to the families of curves $I_{tot}(\nu)$ respectively for the electron concentrations $n_e(\rho_a^\circ) = 10^4$ cm^{-3} и $n_e(\rho_a^\circ) = 1.2 \cdot 10^4$ cm^{-3}.

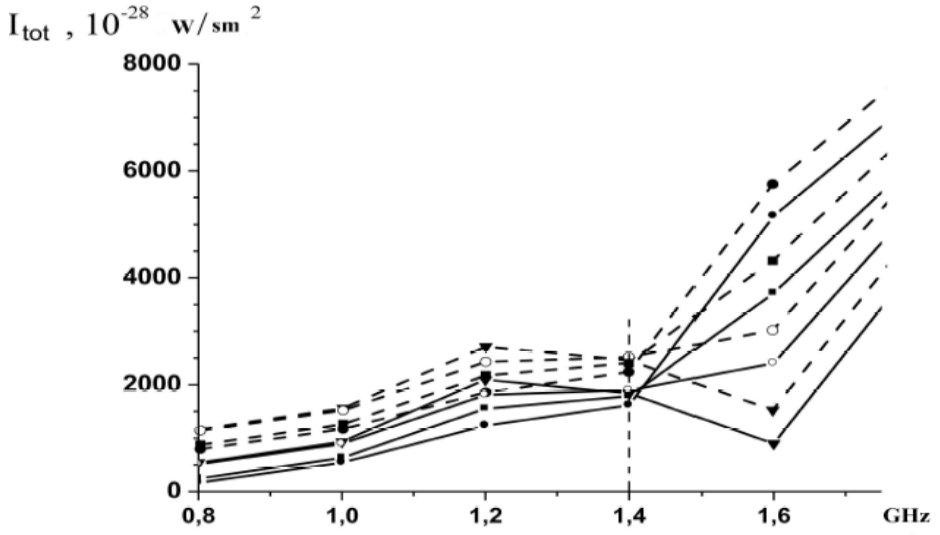

FIGURE 1. Dependence of the radiation power flux I_{tot} on ν for different electron temperatures: at T_e = 1000 K marked by ▼, T_e = 2000 K marked by o, T_e = 1500 K marked by ■, and T_e = 2000 K marked by ●

It is important to note that the measurements of the intensity flux $I_{tot}(\nu, I_{tot}^{(1)}, T_e)$ within the frequency band 0.8—1.8 GHz allow for uniquely determining its dependence on T_e. Indeed, the passive measurements at two frequencies ($L_1 > \nu_f^{(1)}$ and $L_2 < \nu_f^{(1)}$) define the absolute values of two ratios

$$I_{tot}^{(1)} / I_{tot}(L_1, I_{tot}^{(1)}, T_e),$$

and

$$I_{tot}^{(1)} / I_{tot}(L_2, I_{tot}^{(1)}, T_e),$$

and thus the average electron temperature $\overline{T}_e$ in the irradiating layer 80—100 km together with the respective dependence $I_{tot}(\nu, I_{tot}^{(1)}, \overline{T}_e)$. The latter is of special importance for determining the errors in the localization of the GPS system by doing simple ground based measurements. In addition, within the code «Rydberg» one can determine the change in the position of the bottle neck on the parabolic dependence on n_e (ρ_a°), i. e., to retrieve the parameters of the two temperature plasma of D-layer. In addition, the independent satellite measurements of the frequency profile of long wave IR spectrum open the opportunity for calculating the distribution of the Rydberg complexes in D-layer at different geomagnetic conditions, which is an independent task [2].

It should also be noted that the presence of the wasp point within the interval 0.8—1.8GHz provides the grounds for the purposeful realization of a number of practical implications of above mentioned phenomena.

The atmospheric Rydberg complexes in SMOS experiments

The experiments conducting within the frames of the Program SMOS of the European Cosmic Agency aim at the studies of the soil humidity over the continental regions of Europe, South America, and Near East as well as the World Ocean water salinity. To this end the reflection and absorption of UHF-radiation at the fixed frequency $\nu_f^{(1)} = 1.4$ GHz is used. The compilers of the SMOS program assume that this frequency of UHF radiation is most sensitive to the changes of soil humidity and water salinity of oceans. On the other hand, the direct measurements in ambient conditions showed that the maximal effect is reached only at day time when the UHF radiation is definitely due to the Sun activity [4]. Therefore, the main source of radiation around the frequency $\nu_f^{(1)}$ is the Rydberg states of D-layer forming at day time. Therefore use of this frequency should give the most reliable results because of the single parameter dependence of the spectrum on the electron concentration. A deviation from $\nu_f^{(1)}$ makes the measurements essentially ambiguous, for the radiation intensity $I_{tot}(\nu, I_{tot}^{(1)}, T_e)$ depends on the electronic temperature (see Fig. 1).

Since the D-layer is responsible for non-coherent UHF radiation, a possible measurement scheme can be designed for the case where the radiating layer (80—110 km) is located between the satellite and the aircraft. Then the fluxes of captured and reflected radiations are given by the following simple expressions:

$$I_{\text{sat}}^{(z)} = I_{\text{D}}^{(z)} + I_{\text{D}}^{(z)}(1 - f_w)^2 k_r, \quad (1)$$

$$I_{\text{aer}}^{(z)} = I_{\text{D}}^{(z)}(1 - f_w)^2 k_r, \quad (2)$$

$$I_{\mathrm{E}}^{(z\downarrow)} = I_{\mathrm{D}}^{(z)}(1 - f_w)\,, \tag{3}$$

$$I_{\mathrm{E}}^{(z\uparrow)} = I_{\mathrm{D}}^{(z)}(1 - f_w)\,k_r\,, \tag{4}$$

where $I_{\mathrm{D}}^{(z)}$ is the incident flux of UHF radiation from D-layer averaged over time. The values $I_{\mathrm{sat}}^{(z)}$, $I_{\mathrm{aer}}^{(z)}$, $I_{\mathrm{E}}^{(z\downarrow)}$ и $I_{\mathrm{E}}^{(z\uparrow)}$ are the radiation fluxes received by the satellite (including the direct radiation from D-layer and the radiation reflected from the Earth surface), the radiation reflected from the Earth surface and received by the aircraft antenna, incident flux toward the surface, and reflected flux respectively. The value f_w is the extinction factor accounting for the weather conditions, and k_r is defined as the reflection efficiency, i.e. $k_r = I_{\mathrm{E}}^{(z\uparrow)} \big/ I_{\mathrm{E}}^{(z\downarrow)}$. On combining expressions (1)-(4) yields the following two expressions,

$$I_{\mathrm{D}}^{(z)} = \frac{\Delta\left[k_r(\eta - 1)\right]^{1/2}}{1 - k_r}\,, \tag{5}$$

$$f_w = 1 - \left[k_r(\eta - 1)\right]^{-1/2}\,. \tag{6}$$

Here $\eta = I_{\mathrm{sat}}^{(z)} \big/ I_{\mathrm{aer}}^{(z)}$, and $\Delta = I_{\mathrm{E}}^{(z\downarrow)} - I_{\mathrm{E}}^{(z\uparrow)}$. The advantage of exp. (5) and (6) is the fact that their right-hand sides contain only relative values. It is worthwhile to note that in absence of the weather perturbations ($f_w \to 0$), for the «mirror» reflection the coefficient $k_r \to 1$ and the value $I_{\mathrm{sat}}^{(z)}$ should convert to $2I_{\mathrm{D}}^{(z)}$, as it follows from exp. (1). Direct vertical measurements of the incident and reflected radiation fluxes exp. (1)-(4) as functions of time t open up the opportunity to trace the evolution of the atmospheric D-layer in different geographic conditions. This is an independent task, the solution of which should promote new studies of the dynamics of water balance on the Earth. The change of the value $f_w(t)$ defined by exp. (6) is of importance for solving the meteorological problems. Equations (1), (2) and (5), in their turn, allow one to determine the value $I_{\mathrm{D}}^{(z)} = I_{\mathrm{sat}}^{(z)} - I_{\mathrm{aer}}^{(z)}$ and, respectively, can serve as the criteria of the precision in retrieving the parameters of nonequilibrium two-temperature plasma. The time measurements of $I_{\mathrm{D}}^{(z)}(t)$ according to the above described scheme will afford one to attack the fundamental task on the dynamics of nonuniformities in the atmospheric D-layer. Moreover, the simultaneous use of its quadratic dependence on the electron concentration $n_e\,(\rho_a^{\circ})$ at the frequency $\nu_f^{(1)} = 1.4$ GHz and the quadratic dependence of the «bottle neck» position on frequency ν in the band 4.0—8.5 GHz [3] within the

interval $n_e\ (\rho_a^\circ) = 1.0 \cdot 10^4 - 5.0 \cdot 10^4$ cm^{-3} will allow one to measure the depth distribution of the soil humidity (see Fig. 2). The next important problem is related to the dynamics of the factor $f_w(t)$ behavior whose value is limited by the absorption and the scattering of radio-waves in the frequency range 0.8—8.5 GHz by atmospheric aerosols that form in the lower layers of the atmosphere [5, 6].

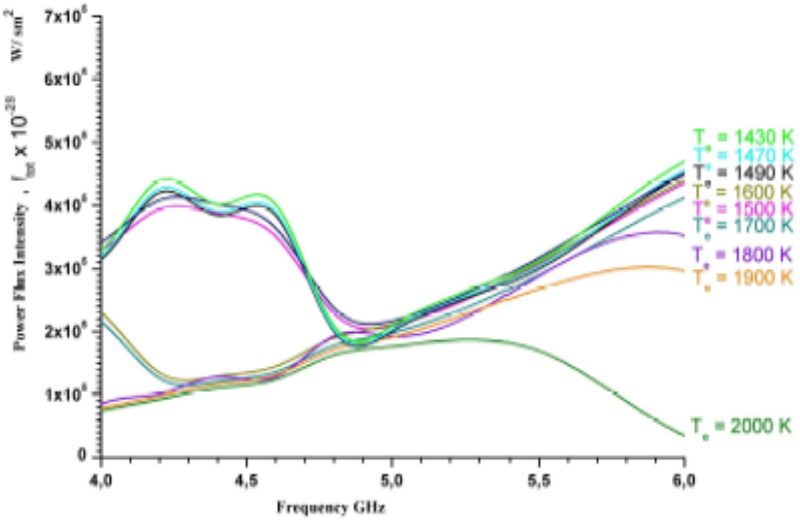

FIGURE 2. I_{tot} as a function of ν for $n_e = 10^4$ cm^{-3} and various T_e values [3].

1. G. V. Golubkov, M. G. Golubkov, M. I. Manzhelii, Russ. J. Phys. Chem. B **6**(1), 112 (2012).
2. G. V. Golubkov, M. G. Golubkov, M. I. Manzhelii, Dokl. Phys. **57**(12), 461 (2012).
3. G. V. Golubkov, M. G. Golubkov, M. I. Manzhelii, Russ. J. Phys. Chem. B **8**(1), 103 (2014).
4. Y. H. Kerr, P. Waldteufel, J. P. Wigneron, et al., IEEE Trans. Geosci. Remote Sens. 39(8), 1729 (2001).
5. A. A. Lushnikov, V. A. Zagaynov, and Yu. S. Lyubovtseva, in: The Atmosphere and Ionosphere. Dynamics, Processes and Monitoring, Ed. by V. L. Bychkov, G. V. Golubkov, and A. I. Nikitin (Springer, Heidelberg, London, New York, 2010), p. 69.
6. A. A. Lushnikov, in: The Atmosphere and Ionosphere. Elementary Processes, Discharges and Plasmoids, Ed. by V. L. Bychkov, G. V. Golubkov, and A. I. Nikitin (Springer, Heidelberg, London, New York, 2013), p. 79.

Formation Mechanisms of Longitudinal Variations in *F*2 region Ionospheric Electron Density at Different Latitudes during Solstice Period

Maxim V. Klimenko[1], Vladimir V. Klimenko[1], Alexander T. Karpachev[2], and Konstantin G. Ratovsky[3]

[1] West Department of Puskov IZMIRAN, RAS, Kaliningrad, Russia
[2] Puskov IZMIRAN, RAS, Troitsk, Moscow Region, Russia
[3] Institute of Solar-Terrestrial Physics SB RAS, Irkutsk, Russia

One of the most important properties of the ionosphere is its longitudinal variability, the study of which has been paid close attention, especially during the last 20 years. This is due to the fact that the longitudinal variations of ionospheric parameters are comparable in magnitude with the daily variations and, therefore, are important for the prediction of radio wave propagation conditions both in quiet geomagnetic conditions, and at change of the solar wind parameters and interplanetary magnetic field.

The first studies of longitudinal variations of ionospheric parameters were performed using Ariel satellite data [1]. Then, these studies were continued in IZMIRAN using IK-19 satellite data (see, e. g., [2—6]). In recent years the studies of longitudinal variations in ionospheric parameters were also carried out based on the data obtained by radio occultation method [7, 8] and the global network of GPS receivers [9]. However, all these studies focused on individual cases and don't set a goal to get a global morphological picture of the longitudinal variations in the ionospheric parameters. Satellite data, in principle, allow to study the longitudinal variations in the ionosphere. However, the only satellite, which carried out sounding of the ionosphere at almost all longitudes and latitudes is the Intercosmos-19 (IK-19). The data of this satellite used by us in this study, along with ground-based ionosondes.

Currently, there are a number of the ionosphere models, both in our country and abroad. In all these models the near-Earth environment characteristics such as conductivity, electric field, composition, temperature and dynamics of the neutral atmosphere are the input parameters, that is defined on the basis of empirical models. In such models as GSM TIP (Kaliningrad), UAM (Murmansk), CTIPe, TIME GCM (USA), GAIA (Japan) the composition, temperature and dynamics of the neutral atmosphere and ionosphere, ionospheric conductivity and electric field are calculated self-consistently. A distinctive feature of the GSM TIP, UAM and CTIPe models is the self-consistent description of the plasmasphere parameters and

electric field of ionospheric (dynamo-field) and magnetospheric origin. Note that in the GSM TIP model there are considered the mismatch of geographic and geomagnetic axes as well as zonal and meridional electromagnetic drift of the ionospheric plasma, which are the important elements at modeling the longitudinal variations in the Earth's ionosphere and the plasmasphere. GSM TIP model can correctly account for all the mechanisms that are involved to explain the longitudinal variations in the ionospheric parameters at different latitudes.

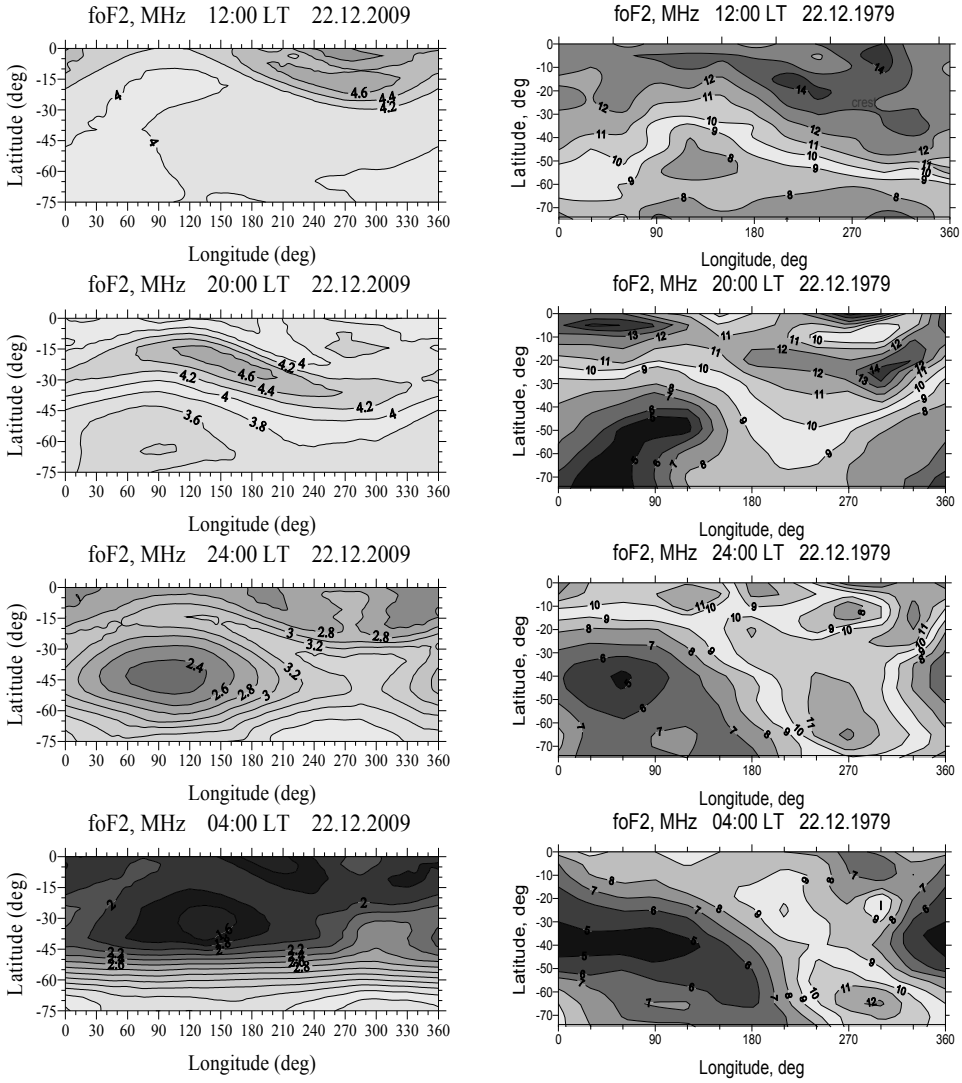

FIGURE 1. Global distributions of *foF*2 in the summer Southern Hemisphere according to the IK-19 data (right panel), and GSM TIP model results (left panel) for nighttime (20:00, 24:00, 04:00 LT — sequence of bottom maps) and daytime (12:00 LT — top).

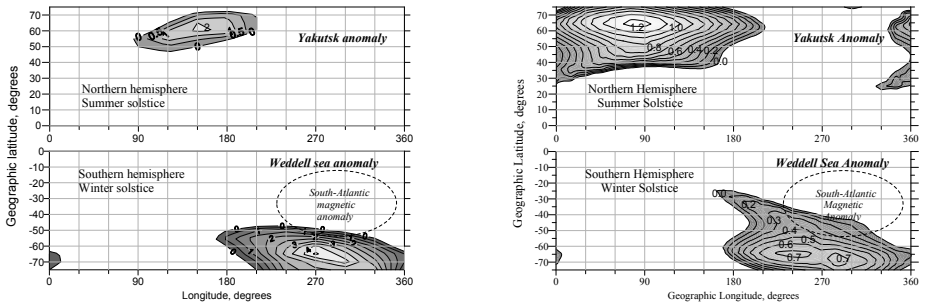

FIGURE 2. Distribution of positive difference between midnight and near-noon *foF*2 values showing WSA and YA regions. Left — IK-19 data, right — GSM TIP model results.

We have used by this in our study at considering the formation of longitudinal variations in the Weddell Sea Anomaly (WSA) like anomaly (sub-auroral latitudes) and equatorial anomaly.

Figure 1 presents the nighttime and daytime *foF*2 global distributions (LT-maps) in the summer Southern Hemisphere obtained from the IK-19 satellite data and GSM TIP model results. It is evident the occurrence of local sub-auroral maximum in *foF*2 at 24:00 and 04:00 LT at 65°S, 270°E both for IK-19 observation and GSM TIP model results and mid-latitude nighttime maximum at 45°S, 250°E at 20:00 LT for IRI model results. Similar to these maxima there are sub-auroral maxima in Fig. 5 at 60°N, 90°E for GSM TIP model results, 60°N, 150°E for IK-19 observation data and mid-latitude nighttime maximum at 25°N, 120°E both for GSM TIP model results and IK-19 observation data. At the locations of sub-auroral nighttime maximum there are local minimum in daytime *foF*2 distribution. From all datasets it is evident that at the certain sub-auroral region the nighttime *foF*2 values exceed the daytime ones, and this feature determines the WSA occurrence that firstly was found using ionosonde measurements [10]. According to [11, 12] there are similar anomaly in Northern Hemisphere that recently was named Yakutsk Anomaly (YA). To more clearly distinguish the WSA and YA region, we calculated the difference between midnight and near-noon *foF*2 values. The regions of the positive difference are shown in Fig. 6 that clearly demonstrated the WSA and YA locations according to IK-19 satellite data and GSM TIP model results.

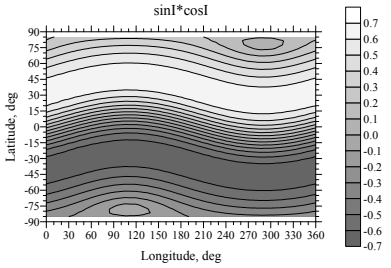

FIGURE 3. The function of effectiveness of meridional component of thermospheric wind velocity in vertical ionospheric plasma transport determines as multiply *sinI·cosI*.

It is evident that WSA and YA cover a wide range in latitude and longitude. The WSA and YA maxima are indeed seen near the Yakutsk and Weddell Sea locations at sub-auroral latitudes. The IK-19 data show that the YA ($\Delta foF2$ = 1.5 MHz) is noticeably weaker than the WSA (4.5 MHz). From other hand we do not reveal essential distinctions between the WSA and YA from the GSM TIP simulations (both anomalies maxima are about 0.5 MHz). This is explained by the fact that the Earth's magnetic field in the GSM TIP model is approximated by a tilted dipole which does not enable to take into account the real difference in distance between the geographic and geomagnetic poles for the Northern and Southern Hemispheres.

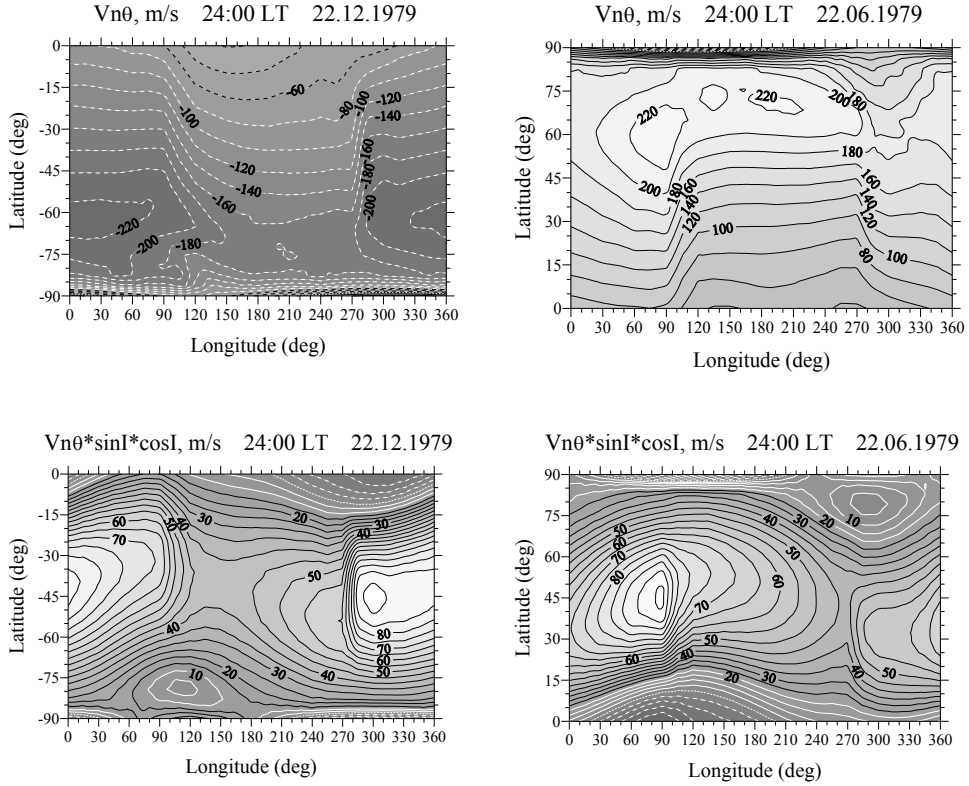

FIGURE 4. Longitudinal variation in nighttime (24:00 LT) meridional component of thermospheric wind velocity at height of 300 km (positive in southward direction — top panel) and its contribution to the vertical plasma transport velocity (bottom panel) obtained using GSM TIP model for December (left) and June (right) solstice conditions in solar activity maximum.

So, we can suggested that the essential distinctions be tween the longitudinal location and night-to-day *foF*2 values of WSA and YA observed by IK-19, modeled by GSM TIP models exist due to the differences in a distance between the geographic and real geomagnetic poles for the Northern and Southern Hemispheres that agrees to the [12, 13] suggestions. Note that both IK-19 topside satellite data, and GSM TIP model results don't reproduce the existence of two MSNA maxima at different longitudinal locations in Northern Hemisphere that were observed and modeled previously [12—14]. The possible reason for this is the different solar activity and large time differences in observations of IK-19 (1979—1980, 00:00—04:00 LT), CHAMP and COSMIC (2000—2010, 20:00—24:00 LT) that could result in global distribution of the geomagnetic field and ionization level that play an important role in the formation of the WSA and YA [13—15].

There are some main hypothesis and suggestions concerning to the main drivers and sources for WSA and YA formation and changes: (1) prolonged Solar UV and EUV photoionization in high latitude of summer hemisphere due to later sunset and the effectiveness of geomagnetic meridional component of the thermospheric neutral wind [13, 16]; (2) the field-aligned plasma flow from the protonosphere/plasmasphere [13]; (3) the dayside-to-nightside plasma transport due to high-latitude magnetospheric convection [17]; (4) an increase of the pre-reversal enhancement of equatorial vertical plasma drift [12]. In our opinion, these are the main mechanisms of WSA and YA formation. We will try to resolve completely this problem in a this paper in detail using GSM TIP model results. Note that the GSM TIP model take into account the offset between geographic and geomagnetic axes and produced self-consistent calculation of the thermosphere-ionosphere system and dynamo electric field and magnetospheric convection, that allows to identify the role of all mentioned processes in the WSA and YA formation.

The offset between geographic and geomagnetic axis leads to that the effectiveness of the vertical plasma transport along the geomagnetic field lines due to merdional neutral wind is proportional to the $sinI \cdot cosI$ (I is the magnetic inclination), which is maximal at longitude of ~105°E in the Northern Hemisphere and longitude of ~ 75° W in the Southern Hemisphere. (see Fig. 3). The longitudinal variation in thermospheric wind efficiency was examined in [13] as a basic factor for the formation of WSA-like anomaly. The main source of thermospheric wind is the heating by the UV and EUV radiation on the dayside, the Joule heating and the heating by the precipitating auroral electrons on the night side. The superposition of these sources generates the maximum in meridional equatorward wind on the nightside when the geomagnetic pole is located on the dayside. As a result the meridional wind velocity on the nightside of Northern Hemisphere have maximum on geographical meridian of ~ 105° E, and on the nightside of Sothern Hemisphere have maximum on geographical meridian of ~ 75° W (see Fig. 4). Finally we determined the contribution of meridional component of thermospheric wind velocity to the vertical plasma transport velocity (see Fig. 4).

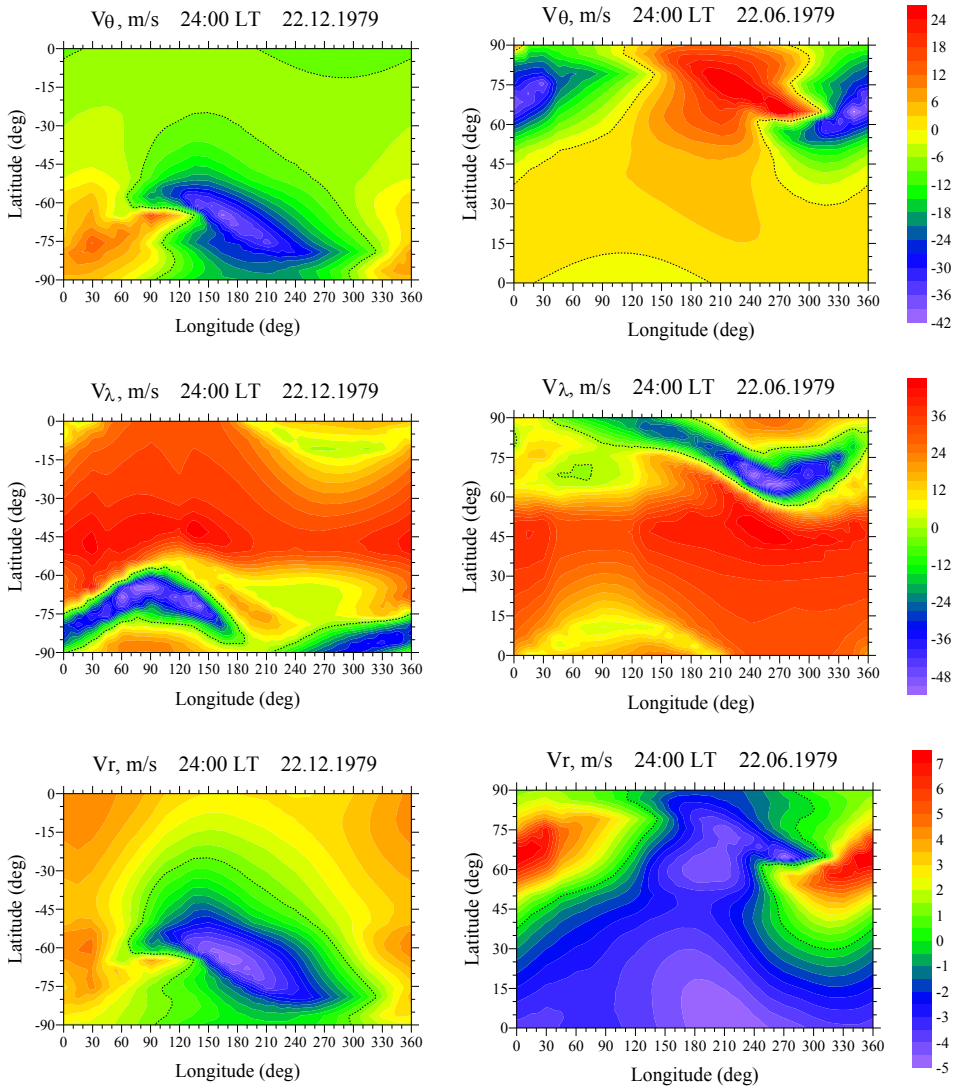

FIGURE 5. Longitudinal variations in meridional (positive from north to south), zonal (positive from west to east) and vertical (positive upward) electromagnetic drift velocity at a height of 300 km in the Southern Hemisphere (left panel) and in the Northern Hemisphere (right panel) calculated in the model GSM TIP at 24:00 LT.

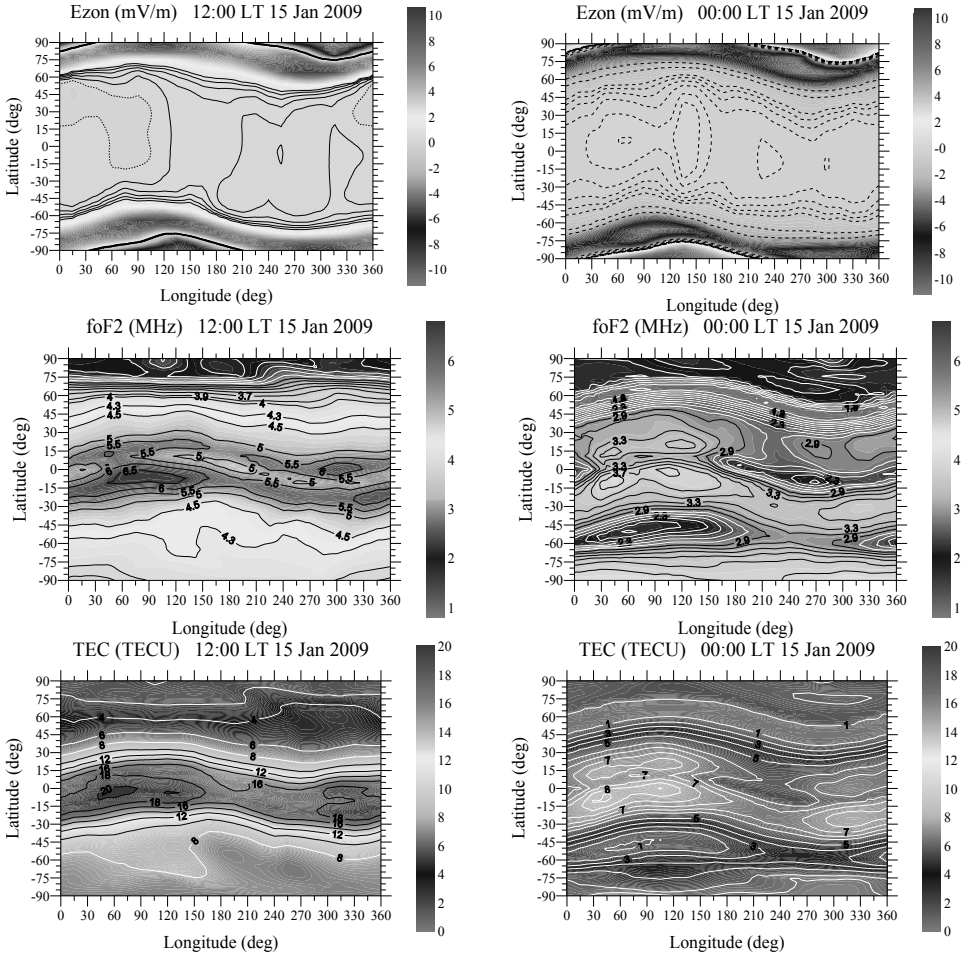

FIGURE 6. Daytime (at the left) and nighttime (on the right) longitudinal variation in zonal electric field (positive in eastward direction — top panel), *foF*2 (middle panel) and *TEC* (bottom panel) for January 15, 2009 obtained using combination of TIME GCM and GSM TIP models.

Another mechanism for the formation of longitudinal variations in the ionosphere is the electric field, causing the electromagnetic plasma drift across the geomagnetic field at heights of the ionosphere *F* region and above. Figure 5 shows the maps of longitudinal variations in the electromagnetic drift velocity at a height of 300 km, calculated in the GSM TIP model in the Northern and Southern Hemispheres at night. At high latitudes, the meridional component of $\boldsymbol{E} \times \boldsymbol{B}$ drift leads to the plasma removal from the day side to the night through the pole and to the formation of ionization tongue with high plasma density on the night side. It is seen that the equatorward plasma drift, forming a tongue of ionization occurs at longitudes of 180—270° in the Southern Hemisphere and at longitudes of 180—270° in the Northern Hemisphere. Zonal drift in the Northern Hemisphere leads to a shift in

tongue of ionization mainly in a westward direction, shifting westward the maximum of plasma density. In the Southern Hemisphere there is a more complicated picture. At longitudes of 180° and more it is the eastward plasma drift, shifting the maximum plasma density in this direction. However, at the same longitudes, closer to the pole, plasma drift is directed eastward, resulting in the greatest plasma accumulation occurs at line where zonal plasma drift velocity equals zero. The vertical plasma drift velocities in the region of formation of the tongue of ionization are small and pointing downward, resulting in a slight decrease in the plasma density. Note that with increasing distance from high latitudes the value of longitudinal variations is significantly reduced, and at the equator ше becomes completely invisible. This is due to the fact that in these calculations at the lower boundary of the GSM TIP model (80 km) the mesospheric tides are not considered.

Accounting of the tides leads to a more complex picture of longitudinal variations in the electron density. This is clearly seen in Fig. 6, which shows the calculation results obtained using the GSM TIP model with TIME GCM output data at height of 80 km. In particular, this figure clearly shows the longitudinal variations in *foF*2 and *TEC*, which confirms the concept of "four waves" in January 2009. The main mechanism of these variations, as stated earlier, is the zonal electric field.

References

1. Eccles D., King J.W., Rothwell P.J. Longitudinal variations of the mid-latitude ionosphere produced by neutral-air wind // J. Atm. Terr. Phys.- 1971. V. 33. N 3. P. 371—377.

2. M.G. Deminov, A.T. Karpachev, Longitudinal effect in the night middle latitude ionosphere on Intercosmos-19 satellite data. Geomagnetism and Aeronomy, 1988, V. 28, №1, P. 76—80 (in Russian).

3. A.T. Karpachev, Mechanisms of longitudinal effect in electron density of the night equatorial anomaly of the outer ionosphere. Geomagnetism and Aeronomy, 1988, V. 28, №4, P. 620—624 (in Russian).

4. *A. T. Karpachev and N. A. Gasilov Variations of the Vertical Plasma Drift with Longitude in the Midlatitude Nighttime Summer Ionosphere Deduced from Measurements of hmF2 //* Geomagnetism and Aeronomy, *V. 38. №5. P. 617—623. 1998.*

5. *Karpachev A.T., Gasilov N.A. Zonal and meridional wind components derived from Intercosmos-19 hmF 2 measurements // Adv. Space Res. V. 27. №6/7. P. 1245—1252. 2001.*

6. *A. T. Karpachev, N. A. Gasilov, and O. A. Karpachev* Causes of *NmF*2 Longitudinal Variations at Mid- and Subauroral Latitudes under Summer Nighttime Conditions // Geomagn. Aeronomy V. 50. №4. P. 482—488. 2010.

7. C. H. Lin, C. C. Hsiao, J. Y. Liu, and C. H. Liu, “Longitudinal structure of the equatorial ionosphere: time evolution of the four-peaked EIA structure,” Journal of Geophysical Research A, vol. 112, no. 12, p. A12305, 2007.

8. N.M. Pedatella, J.M. Forbes, A. Maute et al. Longitudinal variations in the F region ionosphere and the topside ionosphere-plasmasphere: Observations and model simulations // J. Geophys. Res. V. 116, A12309, doi: 10.1029/2011JA016600, 2011.

9. E. Yizengaw Global Longitudinal Dependence Observation of the Neutral Wind and Ionospheric Density Distribution // International J. of Geophysics. v.2012. Article ID 342581. 2012 doi: 10.1155/2012/342581.

10. Bellchambers, W.H., and Piggott, W.R. Ionospheric measurements made at Halley Bay. Nature 182, 1596—1597, 1958.

11. Mamrukov, A.P. Evening anomalous enhancement of ionization in *F* region. Geomagn. Aeron. 21(6), 984—988, 1971.
12. Lin, C.H., Liu, C.H., Liu, J.Y. et al. Midlatitude summer nighttime anomaly of the ionospheric electron density observed by FORMOSAT-3/COSMIC, *J. Geophys. Res.*, 115, A03308, doi:10.1029/2009JA014084, 2010.
13. Liu, H., Thampi, S.V., and Yamamoto, M. Phase reversal of the diurnal cycle in the midlatitude ionosphere. J. Geophys. Res. 115, A01305, doi:10.1029/2009JA014689, 2010.
14. Ren, Z., Wan, W., Liu, L. et al. Simulated midlatitude summer nighttime anomaly in realistic geomagnetic fields. J. Geophys. Res., 117, A03323, doi: 10.1029/2011JA017010, 2012.
15. Knyazeva, M.A., Zubova, Yu.V., and Namgaladze, A.A. Weddell Sea Anomaly: Investigation using the global numerical model. Proc. XXXth URSI General Assembly in Istanbul (August 2011) http://www.ursi.org/proceedings/procGA11/ursi/GP1—59.pdf, 2011.
16. Dudeney J.R., and Piggott, W.R. Antarctic ionospheric research, in Upper Atmosphere Research in Antarctica. Antarct. Res. Ser. AGU 29, 200—235, 1978.
17. Penndorft, R. The average ionospheric conditions over the Antarctic in Geomagnetism and Aeronomy, Antarctic Research Series 4, 1—45, 1965.

D-2

Comparison of the Upper Atmosphere Model Magnetic Maps with the Empirical IRI Model Results and the TEC GPS Data

Maria G. Botova[1], Alexander A. Namgaladze[1], and Yulia V. Romanovskaya[1]

[1] Murmansk State Technical University, Sportivnaya St., 13, 183010 Murmansk, Russia

We continue testing the numerical Upper Atmosphere Model (UAM) [1] using the empirical International Reference Ionosphere model [2] and GPS TEC data. The UAM is the global, three-dimensional, time-dependent, numerical model simulating the thermosphere, ionosphere and plasmasphere of the Earth as a single system. The UAM allows performing the fully self-consistent numerical calculations as well as alternatively modeling using the empirical models, for example, the model of neutral composition and temperatures NRLMSISE-00 [3].

We have calculated electron density and total electron content global distributions for two solar activity levels ($F_{10,7}$~ 90 and $F_{10,7}$~ 180) and for different seasons using two UAM versions. They are: 1) the version with neutral densities and temperature calculated by the empirical NRLMSISE-00 model (marked as UAM-TM) and 2) the fully self-consistent version with theoretically calculated thermospheric parameters (marked as UAM-TT). The calculation results are presented as magnetic maps and are compared with the global parameters distributions provided by the IRI-2007 model and GPS TEC data.

Input parameters are set for both versions identically: 1) solar UV and EUV spectra are taken from the model [4]; 2) the electric potential drops across the polar caps are calculated by the empirical AE-index relation [5]; 3) precipitating fluxes are calculated by the empirical model [6].

Magnetic maps have been calculated for two solar activity levels and different seasons. The low solar activity ($F_{10,7} \sim 90$) is presented by the December solstice of 2004 and April equinox of 2005. The high solar activity ($F_{10,7} \sim 180$) is presented by the December solstice of 2000 and April equinox of 2002.

Initial conditions were prepared for the each date using the following procedure: 1) firstly, model data was calculated according to the empirical NRLMSISE-00 and IRI-2007 models for the ionosphere and thermosphere respectively; 2) to obtain the stationary state of the ionosphere and thermosphere two consequent runs were performed; 3) then five model days were calculated. The paper presents the results for the 24:00 UT of the fifth model day (00:00 UT, next day).

The results obtained by the UAM and the IRI-2007 are presented as magnetic maps of the NmF2 and TEC common logarithms in the Figure 1 and Figure 2 correspondingly. The Figure 2 presents also GSP TEC data. In the figures the solid black line corresponds to the geographic equator, the black dot — to the Sun location.

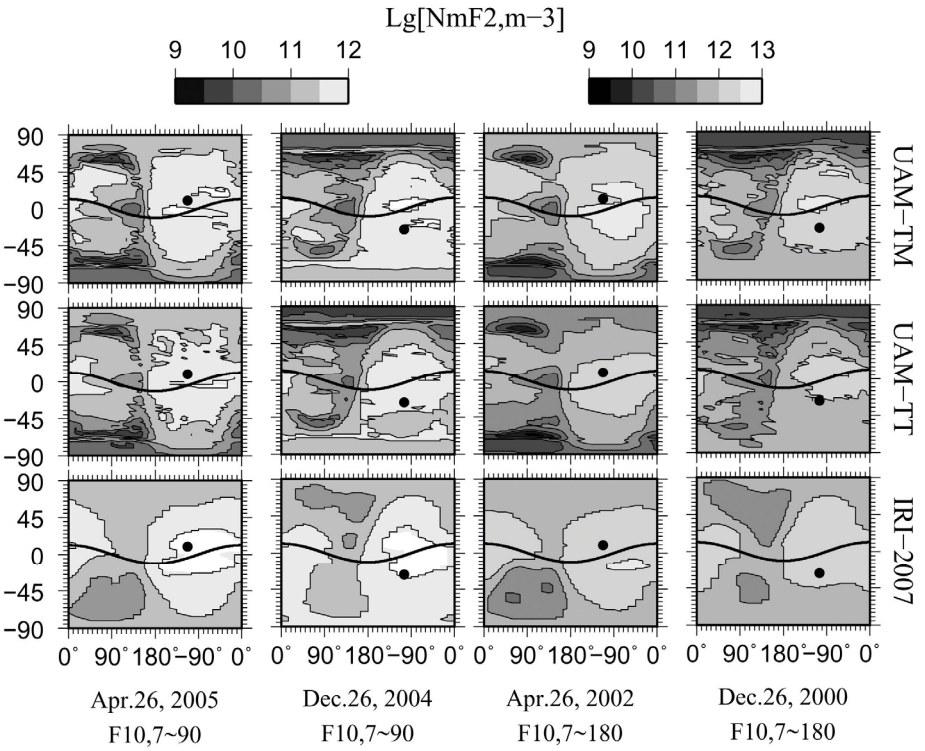

FIGURE 1. Magnetic maps of the NmF2 common logarithm calculated by the UAM-TM and UAM-TT versions for two solar activity levels and two seasons in comparison with the IRI-2007 values.

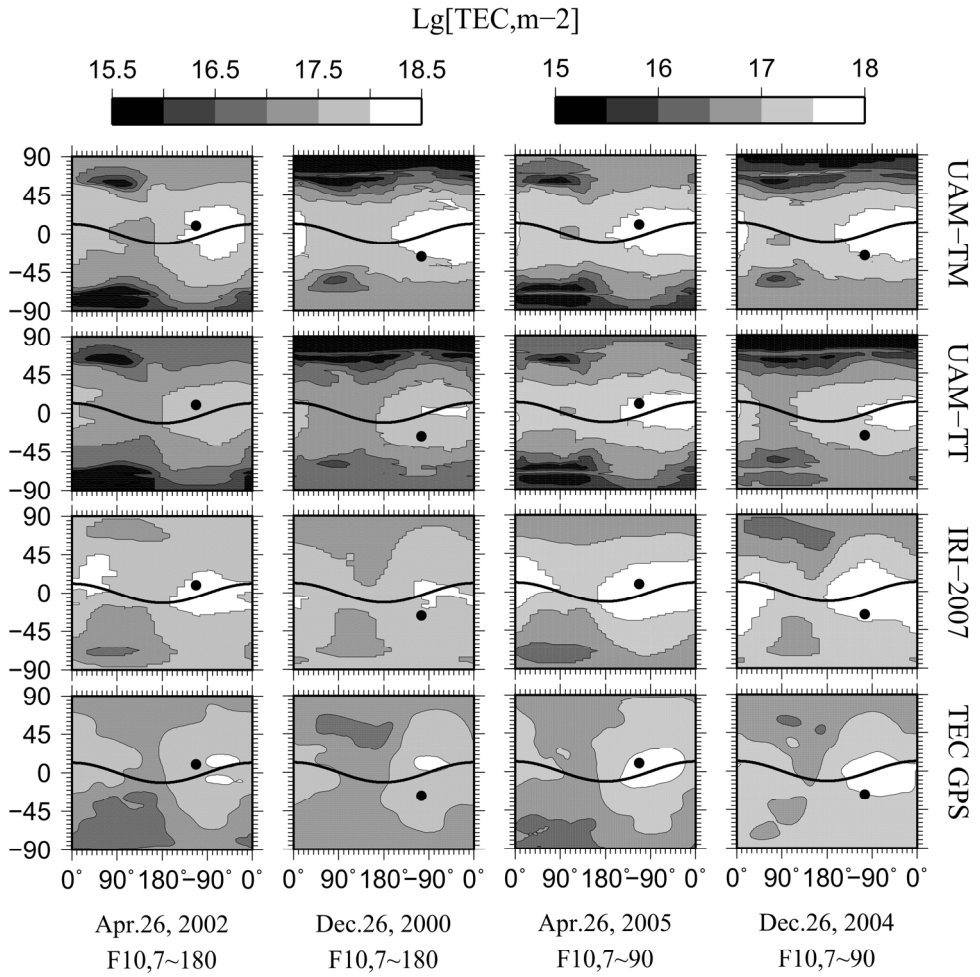

FIGURE 2. Magnetic maps of the TEC common logarithm calculated by the UAM-TM and UAM-TT versions for two solar activity levels and two seasons in comparison with the IRI-2007 values and the GPS TEC data.

In the figures we can see that the IRI-2007 distributions have less contour lines and are smoothed in comparison with the UAM maps. This fact is explained by the observation data smoothing which is used in the empirical models construction. The UAM magnetic maps demonstrate the locations and magnitudes of the NmF2 and TEC maxima which agree as a whole with the IRI results and TEC data as well as the main ionospheric trough location. The main differences between the UAM results and IRI and GPS TEC values take place in the polar caps where any observations practically absent and the polar wind forms so-called “light ion trough”.

References

1. A.A. Namgaladze, O.V. Martynenko and A.N. Namgaladze, Global model of the upper atmosphere with variable latitudinal integration step, *International Journal of Geomagnetism and Aeronomy*, 1, 1998, pp. 53—58.

2. D. Bilitza, B.W. Reinisch, International reference ionosphere 2007: improvements and new parameters, *Advances in Space Research*, 42, 2008, pp. 599—609.

3. J.M. Picone, A.E. Hedin, D.P. Drob, A.C. Aikin, NRLMSISE-00 empirical model of the atmosphere: Statistical comparisons and scientific issues, *Journal of Geophysical Research*, 107 (A12), 2002, p. 1468.

4. A.A. Nusinov, Dependence of the short-wave solar radiation intensity on the activity level, *Journal of Geomagnetism and Aeronomy*, v. 24, No. 4, 1984, pp. 529—536, (in Russian).

5. D.R. Weimer, N.C. Maynard, W.J. Burke, C. Liebrecht, Polar cap potentials and the auroral electrojet indicies, *Planetary and Space Science*, v. 38, No. 9, 1990, pp. 1207—1222.

6. D.A. Hardy, M.S. Gussenhoven, E.A. Holeman, A statistical model of auroral electron precipitation, *Journal of Geophysical Research*, v.90, 1985, pp. 4229—4248.

D-3

Estimation of Contribution of Various Sources to Ionospheric Variability

Konstantin G. Ratovsky, Andrey V. Medvedev, and Maxim V. Tolstikov

Institute of Solar-Terrestrial Physics of Siberian Branch of Russian Academy of Sciences, 664033, Irkutsk, Russia

The main topic of the paper is an estimation of the contribution of various sources to the ionospheric variability. The estimation is based on the analysis of the F2 peak density (NmF2) variability obtained from 2003—2012 dataset of the DPS-4 Digisonde [1] installed at Irkutsk, Russia (52.3N, 104.3E) in November, 2002. In order to obtain the variability, we calculated the relative NmF2 disturbances (ΔNmF2) that are the percentage differences between the observed ($NmF2_{OBS}$) and the 27-day median ($NmF2_{MED}$) values:

$$\Delta NmF2(\%) = (NmF2_{OBS} - NmF2_{MED})/NmF2_{MED} \cdot 100\,\%.$$

The variability (σNmF2) is considered as the root mean square of ΔNmF2. For different tasks we used different types of averaging. Annual averaging was used for studying year-to-year changes in the variability (solar cycle variations). To study the difference between the day- and nighttime variability we made separate averaging for the day- and nighttime using ground terminator as a day-night boundary. To obtain the diurnal-seasonal pattern of the variability we performed averaging over years for each local time and day of year.

Figure 1 shows the year-to-year variations of daytime and nighttime σNmF2 with superimposed variations of annual running mean Ap-index.

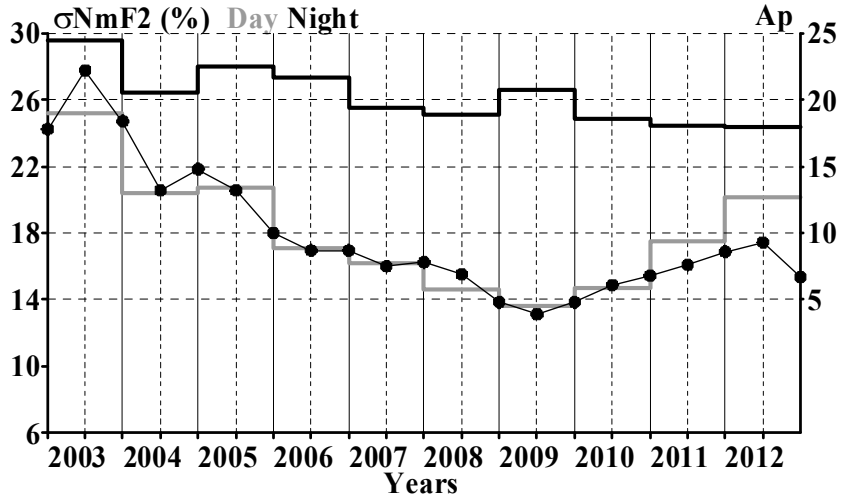

FIGURE 1. Year-to-year variations of daytime (grey bars) and nighttime (black bars) σNmF2 with variations of annual running mean Ap-index (black line with circles).

The nighttime variability is larger than the daytime one with the largest difference in 2009. The daytime variability shows a clear increase with the geomagnetic activity, whereas, the nighttime σNmF2 does not show a clear dependence on the geomagnetic activity.

Figure 2 shows the diurnal-seasonal pattern of σNmF2 resulting from averaging ΔNmF2 over 2003—2012 years for each local time and day of year. Despite a noticeable scatter of values due to averaging over a small number of years, some features are clearly seen. The high and low values of σNmF2 are separated approximately by sunrise-sunset lines (white dashed) superimposed on the pattern. This feature is well pronounced in winter and less pronounced in summer.

For detailed consideration of the seasonal behavior we performed 27-day smoothing of the data shown in Fig. 2 and averaging over day- and nighttime hours using ground terminator as a day-night boundary. The results are shown in Fig. 3.

The nighttime variability show clear seasonal behavior with maximum in winter (~ 31 %), minimum in summer (~ 19 %), and intermediate values at equinoxes (~ 24 %). The winter-summer difference (σ(Dec22) – σ(Jun22)) is ~ 10 % and the equinox-solstice difference (σ(Mar22) + σ(Sep22) – σ(Dec22) – σ(Jun22)) is ~ – 1 %. The daytime variability shows a multi-peak behavior with maxima in December, April-May and September-October (~ 19 %) and minima in July, February and November (~ 16 %). The winter-summer difference is ~3 % and the equinox-solstice difference is ~ 2 %. The daytime winter-summer difference is noticeably less than the nighttime one.

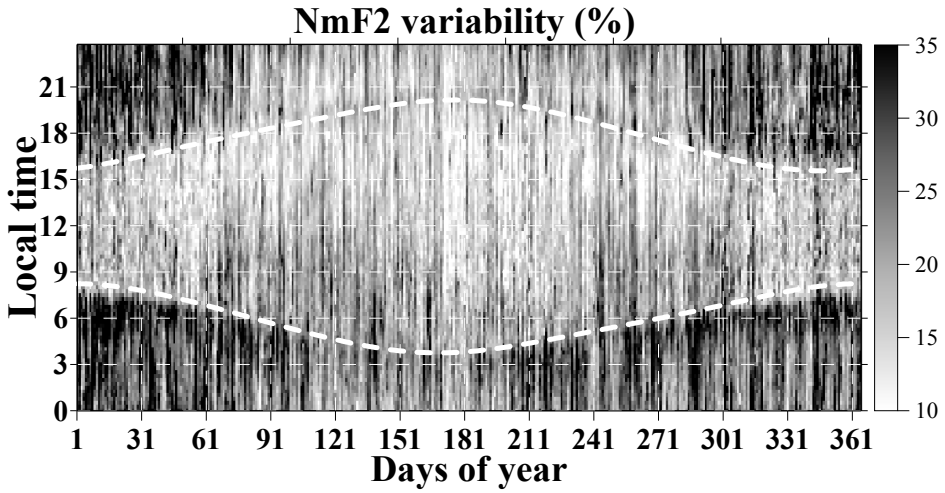

FIGURE 2. Diurnal-seasonal pattern of σNmF2 (2003—2012 averaging).

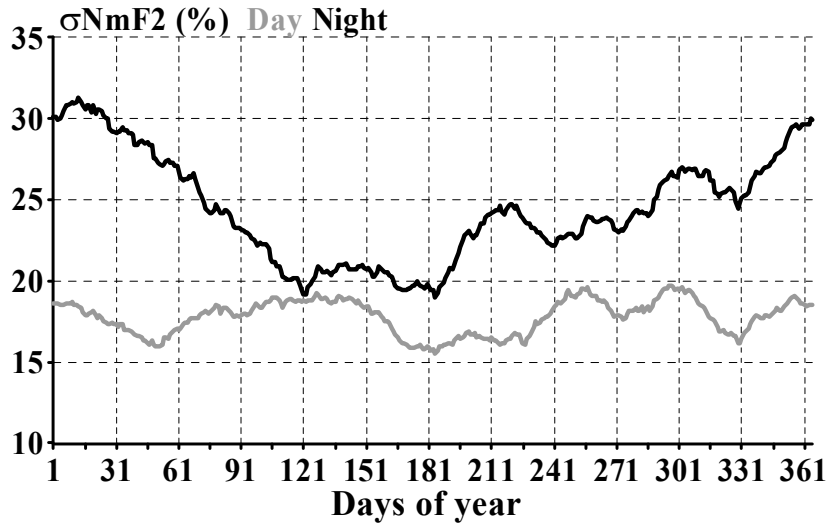

FIGURE 3. Seasonal behavior of daytime (grey) and nighttime (black) σNmF2.

Using the year-to-year variations of the daytime variability (Fig. 1) we may estimate geomagnetic and meteorological activity contributions to the NmF2 variability. Under the geomagnetic contribution we imply the variability associated with effects of geomagnetic storm and geomagnetically disturbed conditions (e. g., [2], [3], [4], and references therein); whereas the meteorological contribution is the variability caused by processes in the lower atmosphere (planetary waves, tides, and internal gravity waves) [5].

Epoch of 2009 is characterized by extremely low level of the geomagnetic and solar activity (annual mean Ap = 4 nT, annual mean F10.7 = 71 s. f. u.). Neglecting the geomagnetic contribution in this year and believing that the variability is caused only by the meteorological impact, we estimate that meteorological contribution to the NmF2 daytime variability is about 14 %. This estimation agrees closely with those obtained by different methods (~ 15 % from Rishbeth and Mendillo [6], and ~ 13 % from Deminov et al. [7] and Araujo-Pradere et al. [8]). A detailed comparison with these methods is presented in Table 1. Our estimation is noticeably less than ~ 20 % obtained by Forbes et al. [9]. The reason is that they did not separate the day and night variability and obtained a higher estimation due to the higher nighttime variability. If we average the day- and nighttime variabilities of 2009, we get a close estimation of ~ 20 %.

TABLE 1. Estimations of meteorological contribution to NmF2 daytime variability

Reference	Estimation	Data set	Method
This paper	13.6 %	Irkutsk ionosonde, 2009	Using only 2009 data
[6]	15.0 %	Slough ionosonde, 1973, 1979	Using semiannual amplitudes of σNmF2 and Ap
[7]	12.7 %	Irkutsk ionosonde, 2007—2010	Using only geomagnetically quiet data
[8]	13.3 %	Ionosondes at 40—60º geomagnetic latitudes, 1981—1988	Using only geomagnetically quiet data

The geomagnetic contribution may be estimated using the linear regression of the NmF2 daytime variability on the annual mean of Ap-index. As a result, we obtain that the geomagnetic contribution (percentage response of NmF2 to geomagnetic activity) is ~ 0.8 % per Ap unit, which is close but slightly less than the Rishbeth and Mendillo [6] estimation (~ 1 % per Ap unit). It should be noted the estimation were made by significantly different methods: we used the year-to-year variations of σNmF2 and Ap-index, whereas, Rishbeth and Mendillo [6] obtained their estimation by comparison of the semiannual amplitudes of σNmF2 and Ap. Taking into account the different geomagnetic latitudes of the stations (Irkutsk, 42N GLAT and Slough, 48N GLAT), the agreement may be considered as satisfactory.

The nighttime variability (Fig. 1) does not show a clear dependence on the geomagnetic activity, while the nighttime effects of geomagnetic storms are well known. To explain this disagreement, it is necessary to consider the reasons why the nighttime variability noticeably exceeds the daytime one (see Figs. 1—3). This feature agrees completely with the results of the papers [6], [7], and [8]. This night-day difference may be explained by the photochemical control effect on the variability [6], [8]. At the nighttime the photochemical control is weaker, and the ionospheric electron density is more sensitive to the geomagnetic and meteorological activity [6]. The chemical control influence can also be used to explain an unclear dependence of the nighttime variability on the geomagnetic activity. An enhance-

ment of the variability caused by geomagnetic storm effects competes with a reduction associated with chemical control increase. Such an explanation was proposed by Araujo-Pradere et al. [8] for interpreting a reduction in the nighttime variability at high latitudes with increasing geomagnetic activity. Mikhailov et al. [10] found decreasing the post-midnight winter NmF2 enhancement amplitude with increasing solar activity and explained this decrease by increasing recombination rate (i.e. chemical control). Another manifestation of the chemical control effect is that the occurrence of the very strong foF2 nighttime enhancements decreases as solar activity grows [11].

The seasonal behavior of the NmF2 variability (Fig. 3) is affected by the following factors: (1) the photochemical control seasonal variations [8]; (2) the geomagnetic activity seasonal variations [6]; and (3) the meteorological activity seasonal variations [5]. The factor (1) enhances the winter-summer difference, whereas the factor (2) increases the amplitude of semi-annual variations (equinox-solstice difference). Most likely, the factor (1) dominates in the nighttime ionosphere, whereas the dominance of a factor at the daytime depends on the regional specifics. The cases of the negative winter-summer difference [6] may be explained only by the factor (3).

The main results of this paper are the following. We obtained the diurnal, seasonal and solar activity pattern of the NmF2 variability at Irkutsk. Using the year-to-year (solar cycle) variations of the variability, we estimated the geomagnetic and meteorological activity contribution and found our estimates to be close to the known results. We proposed an explanation of the obtained diurnal, seasonal and solar activity pattern of the NmF2 variability in terms of the geomagnetic and meteorological effects, and the sensitivity of the ionospheric electron density to the geomagnetic and meteorological impacts. It should be noted that we proposed only a qualitative explanation that should be tested by model calculations.

The reported study was supported by RFBR, research project No. 14-05-00578.

1. B.W. Reinisch, D.M. Haines, K. Bibl, I. Galkin, X. Huang, D.F. Kitrosser, G.S. Sales, and J.L. Scali, *Ionospheric sounding support of OTH radar*, Radio Sci., 1997, 32 (4), pp. 1681—1694.

2. M.J. Buonsanto, *Ionospheric Storms: A Review*, Space Sci. Rev., 1999, 88, pp. 563—601.

3. G.W. Prolss, *On explaining the local time variation of ionospheric storm effects*, Ann. Geophys., 1993, 11 (1), pp. 1—9.

4. A.V. Mikhailov, *Ionospheric F2-Layer Storms*, Fis. Tierra, 2000, 12, pp. 223—262.

5. J. Lastovicka, *Forcing of the ionosphere by waves from below*, J. Atmos. Solar-Terr. Phys., 2006, 68, pp. 479—497.

6. H. Rishbeth and M. Mendillo, *Patterns of F2-layer variability*, J. Atmos. Solar-Terr. Phys., 2001, 63, pp. 1661—1680.

7. M.G. Deminov, G.F. Deminova, G.A. Zherebtsov, and N.M. Polekh, *Statistical properties of variability of the quiet ionosphere F2-layer maximum parameters over Irkutsk under low solar activity*. Adv. Space Res., 2013, 51, pp. 702—711.

8. E.A. Araujo-Pradere, T.J. Fuller-Rowell, M.V. Codrescu, and D. Bilitza, *Characteristics of the ionospheric variability as a function of season latitude local time and geomagnetic activity*, Radio Sci., 2005, 40, RS5009, http://dx. doi. org/10.1029/2004RS003179.

9. J.M. Forbes, S.E. Palo, X. Zhang, *Variability of the ionosphere*. J. Atmos. Solar-Terr. Phys, 2000, 62, pp. 685—693.

10. A.V. Mikhailov, M. Förster, T.Y. Leschinskaya, *On the mechanism of the post-midnight winter NmF2 enhancements: dependence on solar activity*, Ann. Geophys., 2000, 18, pp. 1422—1434.

11. O. Pirog, M. Deminov, G. Deminova, G. Zherebtsov, and N. Polekh, *Peculiarities of the nighttime winter foF2 increase over Irkutsk*. Adv. Space Res., 2011, 47, pp. 921—929.

D-4

Seismic Climatology Trends on the Background of Solar Activity

T.L. Gulyaeva

Institute of Terrestrial Magnetism, Ionosphere and Radio Wave Propagation, IZMIRAN, Kaluzskoe Sh.4, Troitsk, Moscow 142190, Russia

Recent investigations indicate relations of space weather parameters with seismic activity in the lithosphere before, during and after earthquakes. Though the earthquake affects the surrounding space within the restricted area the prolonged effects and frequency of occurrence of the earthquakes may have cumulative effects on the atmosphere, magnetosphere and ionosphere structure and variability. The long-term relationship is investigated in the present study between the earthquake M5.0+ occurrence and the solar activity characterized by the sunspot number, SSN, and solar radio flux, F10.7, for a period from 1964 to 2013. It is found that the global number of earthquakes tends to grow towards the solar minimum. The anti-correlation between global earthquake occurrence and the phase of solar cycle is expressed through the trends of earthquakes decrease towards growing SSN and F10.7. The growing earthquake occurrence is expected during the current low intensity 24th solar cycle. The latitudinal and longitudinal distribution of the earthquakes reveals the zone of enhanced seismic activity located at longitudes between 120° to 210°E and latitudes from 40°S to 60°N with greater earthquake occurrence in the South hemisphere equatorial region.

It is recognized that there are pre-earthquake phenomena comprised of the local magnetic field variations, electromagnetic emissions at the different frequency ranges, excess radon emanation from the ground, changes in water chemistry, water condensation in the atmosphere leading to haze, fog or clouds, atmospheric gravity waves rising up to the ionosphere, changes in the ionospheric Total Electron Content (TEC) and the F2 layer peak electron density [1—4]. The seismic-

ionospheic theories and lithosphere — atmosphere — ionosphere models explain the earthquake-ionosphere coupling processes by electromagnetic wave propagation, acoustic gravity wave, atmospheric electricity and geochemical channel [4—7]. The ionosphere precursors of earthquakes and the magnetosphere storm effects on seismic events are widely investigated [7—14]. Though the earthquake affects the surrounding space within the restricted area (of 100 to 4,000 km radius) the prolonged effects and frequency of occurrence of the earthquakes may have cumulative effects on the ionosphere structure and variability [15].

The main source of ionosphere ionization is attributed to intensity of solar electromagnetic radiation, particularly, at wavelengths of solar X-rays which are absorbed by the Earth's upper atmosphere producing the ionospheric plasma. The ionospheric plasma is a complex function of variations and coupling in solar, geomagnetic, and seismic activities such as solar flares, sunspot number, solar wind, interplanetary magnetic field (IMF), geomagnetic storms, and earthquakes.

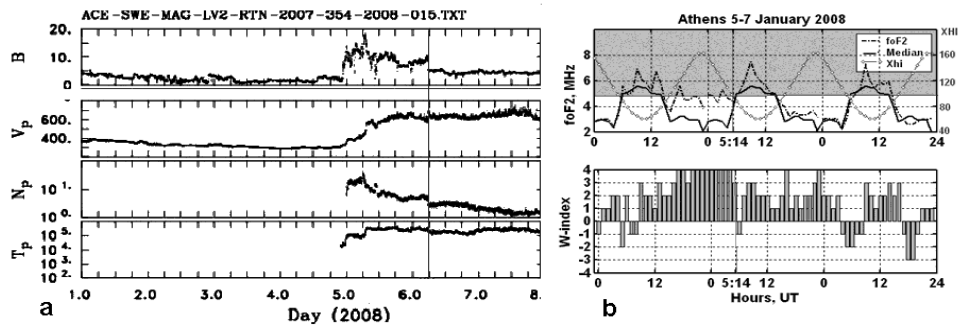

FIGURE 1. (a) Abrupt change of ACE IMF B-field, solar wind velocity Vp drop, proton lessened density Np and temperature Tp, on 6.01.2008 4.0 h UT (vertical line), $\Delta t = -1.2$ h prior the earthquake M6.2; (b) foF2 critical frequency (night/day) at Athens 5—7.01.2008 and ionospheric W-index at the solar night-to-day terminator passing EQ epicenter (5:14 h).

Figure 1 shows an example of congruent changes in the interplanetary space parameters and the ionospheric F2 layer critical frequency observed at Athens [38.4° N, 23.6°E] in the vicinity of epicenter [37.22°N, 22.69°E] of the earthquake (EQ) M6.2 occurred on 6 January, 2008, at 05:14:20 (hr, min, sec) UT. All solar wind and interplanetary parameters (Fig.1a) and the positive ionospheric index W = 4 [16] characterizing enhanced observed peak plasma density over the 27-days median quiet reference (Fig. 1b) show pre-earthquake disturbance during $\Delta t = -17$ h before EQ and their instant drop happened at $\Delta t = -1.2$ h prior to the EQ occurrence which illustrate solar wind — ionospheric — seismic associations.

Focused on investigations of the ionosphere precursors and post-event effects of the particular earthquakes or series of seismic events [7], a possible linkage of

the Earth's seismic activity with the long-term solar activity has not been paid due attention. Though it is difficult to distinguish between pure seismic precursors in the ionosphere from geomagnetic storms effects [11] the post-earthquake phenomena are well observed and found over the local areas of high seismic activity providing opportunity to make study of both temporal and spatial earthquake-ionosphere associations [14—15].

The long-term relation of the earthquakes of magnitude M = 5.0 to M = 10.0 with solar activity is investigated in the present study. We use monthly and annual data sets from the Advanced National Seismic System (ANSS) Catalogue for a period from 1964 (start at the solar minimum of the 20th solar cycle) up to the end of 2013 (near the peak of the 24th solar cycle). The composite global Catalogue of earthquakes is created by ANSS by merging the master earthquake catalogs from contributing ANSS member institutions and then removing duplicate events, or non-unique solutions for the same event. Total number of M5+ earthquakes for the selected period of 50 years is greater than 79000 events which provide a good database for the statistical analysis. Relevant monthly mean and annual mean sunspot numbers (SSN) are downloaded from the US National Geophysical Data Center, and the solar 10.7 cm radio flux (F10.7) is provided by Space Weather Canada service.

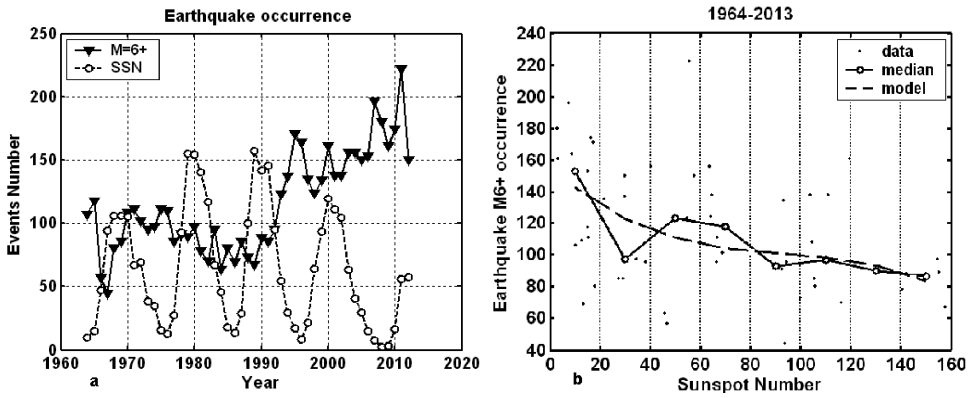

FIGURE 2. (a) Time series of annual number of earthquakes M6+ superimposed by the sunspot number SSN curve; (b) The annual number of M6+ EQs, their median derived at SSN bins (1 bin = 20 index units, i. u.) and model are plotted against SSN.

The annual number of earthquakes of magnitude M6+ and the annual SSN are plotted in Fig. 2a. The trend of the growing seismic activity during 25 recent years is seen therein. This period corresponds to combination of two recent 11-years solar cycles with two reverse directions of solar magnetic field. The signatures of the counter-phase variation of the earthquake occurrence and the sunspot numbers can be captured from Fig. 2b suggesting that seismic activity is enhanced towards the solar minimum.

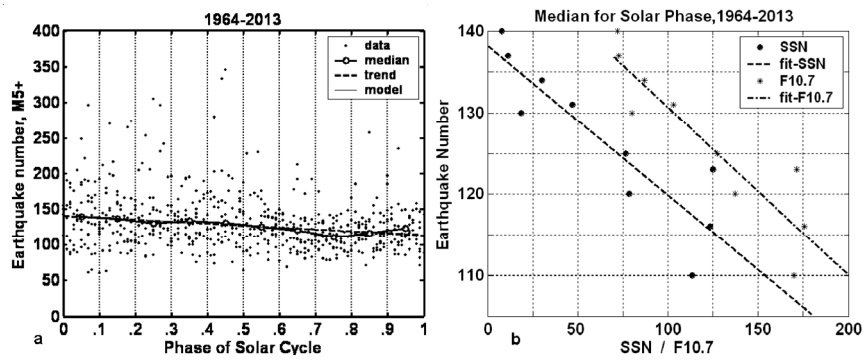

FIGURE 3. (a) Anti-correlation of monthly number of EQs M5+ with phase of solar cycle; (b) The median of EQs M5+ obtained in bins $\Delta\Phi$ is plotted against median SSN($\Delta\Phi$) and against median F10.7($\Delta\Phi$). All data points and results of least square fits for 1964—2013.

The anti-correlation of seismic activity with solar activity is obtained also by referring the monthly earthquake M5+ occurrence to the phase of the solar cycle [17]. Monthly number of EQs M5+ is plotted in Fig. 3a against the solar cycle phase, Φ, varying from $\Phi = 0$ for solar minimum to $\Phi = 1$ for solar maximum. The scatter exhibits influence of other factors in addition to the solar activity affecting the EQs occurrence. The median of *EQ* calculated in ten bins of $\Delta\Phi = 0.1$ varies in counter-phase with solar activity which means the EQ occurrence increased towards the solar minimum. This trend is clearly demonstrated in Fig. 3b where median of *EQ* occurrence is plotted against median of SSN obtained using the SSN in ten bins of $\Delta\Phi = 0.1$. The similar procedure is applied to produce median of *F10.7* at bins of $\Delta\Phi$ (Fig. 3b). Both Fig. 3a and Fig. 3b demonstrate trends of anti-correlation of seismic activity with characteristics of solar activity.

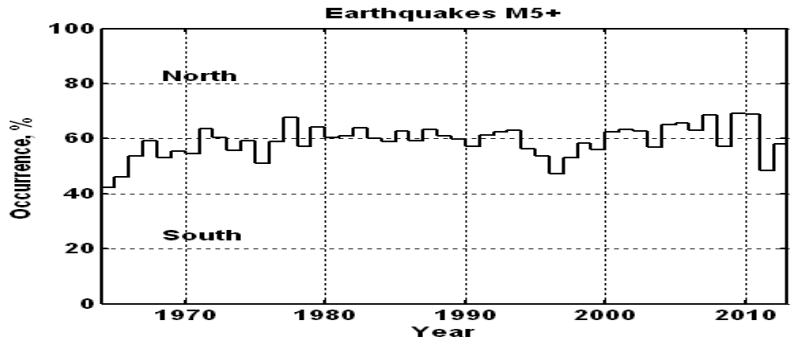

FIGURE 4. Annual percentage EQ M5+ occurrence in the North and South magnetic hemispheres.

The latitudinal/longitudinal variations of seismic activity are also analyzed with the ANSS Catalogue data. The coordinates of EQ M5+ epicenters have been separated by the magnetic equator for the North and South magnetic hemispheres and annual percentage of EQs M5+ in the North and South magnetic hemispheres are calculated (Fig. 4). Clear evidence of the long-term excess of M5+ events occurrence by 1.5 times is observed in the South magnetic hemisphere as compared with the North hemisphere.

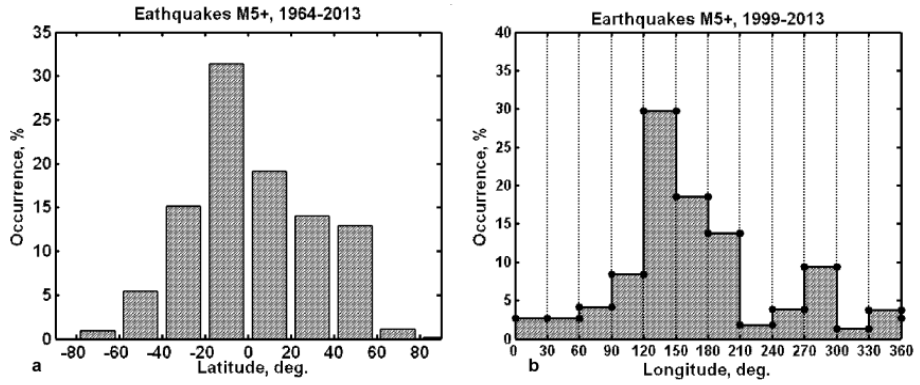

FIGURE 5. Percent of EQs number observed during 1964—2013: (a) in each bin of 20° of geographic latitude; (b) in each bin of 30° of geographic longitude.

The latitudinal distribution of EQ M5+ occurrence in the latitude bins of 20° averaged for 1964—2013 is plotted in Fig. 5a. Most of the EQs are found between 40°S and 60°N. The South equatorial zone [0:20°S] includes 30 % of all EQs (23,715 EQs from the total database of 79,051 events). The same percentage of 30 % of EQs happened to occur in the longitudinal zone [120:150°E] (Fig. 5b). Hence, the surface area on the Earth restrained by the latitudes range [0:20°S] and longitude range [120:150°E] presents zone of enhanced risk of earthquakes.

Clear evidence of the solar activity modulation of the earthquakes occurrence is demonstrated in the present study. The EQ occurrence varies in counter-phase with solar activity tending to increase towards the solar minimum. This trend is opposite to the upper atmosphere density and the ionosphere plasma density and total electron content which follow closely to the solar activity. When the solar activity is depressed at solar minimum the seismic activity become more effective and its contribution to the atmosphere and ionosphere characteristics strengthen. In view of the expected forthcoming low values of the SSN peak at the current 24th solar cycle [18] one could expect an enhanced earthquake activity for 2014—2020. The latitudinal and longitudinal distribution of the earthquakes indicates the zones of enhanced seismic activity at longitudes between 120° to 210°E and latitudes from 40°S to 60°N with greater earthquake occurrence in the South hemisphere equatorial region.

Catalogue of the Advanced National Seismic System (ANSS) is provided by the Northern California Earthquake Data Center (NCEDS) at *http://www.nceds.org/anss/anss-detail.html*. The sunspot number is provided by the US National Geophysical Data Center at *ftp://ftp.ngdc.noaa.gov/STP/space-weather/solar-data/solar-indices/sunspot-numbers/*. Solar F10.7 radio flux data are provided at *ftp://ftp.geolab.nrcan.gc.ca/data/solar_flux/*. Athens ionosonde data are provided by DIAS server *at http://hertz2.space.noa.gr:8080/*. ACE-SWEPAM data are provided at *http://www. srl. caltech. edu/*. This study is supported by the joint grant from RFBR 13-02-91370-CT_a and TUBITAK 112E568 project.

1. Gokhberg, M. B., V. A. Pilipenko, O. A. Pokhotelov. Satellite observation of the electromagnetic radiation above the epicenteral region of an incipient earthquake. *Dokl. Acad. Sci. USSR Earth Sci. Ser.*, Engl. Transl. 268 (1), 5—7, 1983.

2. Biagi, P. F., R. Piccolo, A. Ermini, S. Martellucci, C. Bellecci, M. Hayakawa, V. Capozzi, and S. P. Kingsley. Possible earthquake precursors revealed by LF radio signals, *Nat. Hazards Earth Syst. Sci*. **1**, 1/2, 99—104, doi:10.5194/nhess-1-99-2001, 2001.

3. Hayakawa, M., Y. Kasahara, T. Nakamura, Y. Hobara, A. Rozhnoi, M. Solovieva, and O. A. Molchanov. On the correlation between ionospheric perturbations as detected by subionospheric VLF/LF signals and earthquakes as characterized by seismic intensity, *J. Atmos. Sol.-Terr. Phys.***72**, 13, 982—987, DOI: 10.1016/j. jastp.2010.05.009, 2010.

4. Freund, F. Earthquake forewarning — A multidisciplinary challenge from the ground up to space. *Acta Geophysica,* **61**(4), 775—807, doi:10.2478/s11600-013-0130-4, 2013.

5. Pulinets, S. A. Physical mechanism of the vertical electric field generation over active tectonic faults. *Adv. Space Res.* 44, 767—773, 2009.

6. Harrison, R. G., K. L. Aplin, and M. J. Rycroft. Atmospheric electricity coupling between earthquake regions and the ionosphere, *J. Atmos. Sol.-Terr. Phys.* **72**, 5—6, 376—381, doi: 10.1016/j. jastp.2009.12.004, 2010.

7. Namgaladze, A. A., O. V. Zolotov, M. I. Karpov, Y. V. Romanovskaya. Manifestations of the earthquake preparations in the ionosphere total electron content variations, *Doklady Acad. Sci., Nat. Sci.* 4, 11, 848—855, doi: 10.4236/ns.2012.411113, 2012.

8. Liu, J. Y., Y. J. Chuo, S. J. Shan, Y. B. Tsai, S. A. Pulinets, S. B. Yu. Preearthquake-ionospheric anomalies registered by continuous GPS TEC. *Ann. Geophys.* 22, 1585—1593, 2004.

9. Pulinets, S. A., K. A. Boyarchuk. *Ionospheric Precursors of Earthquakes*. Springer, Berlin, 2004.

10. Zhao, B., M. Wang, T. Yu, W. Wan, J. Lei, L. Liu. Is an unusual large enhancement of ionospheric electron density linked with the 2008 great Wenchuan earthquake? *J. Geophys. Res.* 113, 1—6, 2008.

11. Karatay, S., F. Arikan, O. Arikan. Investigation of total electron content variability due to seismic and geomagnetic disturbances in the ionosphere, *Radio Sci.*, 45, RS5012, doi:10.1029/2009RS004313, 2010.

12. Komjathy, A., D. A. Galvan, P. Stephens, M. D. Butala, V. Akopian, B. Wilson, O. Verkhoglyadova, A. J. Mannucci, M. Hickey. Detecting ionospheric TEC perturbations caused by natural hazards using a global network of GPS receivers: The Tohoku case study. *Earth Planets Space*, 64, 1287—1294, doi:10.5047/eps.2012.08.003, 2013.

13. Le, H., L. Liu, J.-Y. Liu, B. Zhao, Y. Chen, W. Wan. The ionospheric anomalies prior to the M9.0 Tohoku-Oki earthquake. *J. Asian Earth Sciences,* **62**, 476—484, doi: 10.1016/j. jseaes.2012.10.034. 2013.

14. Pohunkov A. A., G. F. Tulinov, S. A. Pohunkov, V. V. Rybin. Investigation of seismic activity impact on the chemical composition of the upper ionosphere, *Heliogeophysical Research*, Issue 3, 90—98, 2013.

15. Rishbeth, H. F-region links with the lower atmosphere? *J. Atmos. Solar-Terr. Phys.,* 68, 469—478, doi:10.1016/j. jastp.2005.03.017, 2006.

16. Gulyaeva, T. L., I. Stanislawska, M. Tomasik. Ionospheric weather: Cloning missed foF2 observations for derivation of variability index. *Annales Geophysicae*, 26, 315—321, 2008.

17. Gulyaeva, T. L., I. Stanislawska, I. Derivation of a planetary ionospheric storm index. *Annales Geophysicae*, 26, 2645—2648, www.ann-geophys.net/26/2645/2008/, 2008.

18. Pesnell, W. D. Predictions of Solar Cycle 24, *Solar Phys.*, 252, 209—220, doi: 10.1007/s11207-008-9252-2, 2008.

D-5

Main Ionospheric Trough Model according to the Intercosmos-19 and CHAMP Data

Alexander T. Karpachev[1], Maksim V. Klimenko[2], Vladimir V. Klimenko[2]

[1] Pushkov Institute of Terrestrial Magnetism, Ionosphere and Radio Wave Propagation RAS, Moscow, Russia, e-mail: karp@izmiran.ru

[2] West Department of Pushkov Institute of Terrestrial Magnetism, Ionosphere and Radio Wave Propagation, RAS, Kaliningrad, Russia, email: maksim.klimenko@mail.ru

Median model of the position and shape of the main ionospheric trough (MIT) for the Northern and Southern hemispheres is created. For a period of high solar activity (1979—1981, $F_{10.7}$ = 150—250) the data from topside sounding onboard the Intercosmos-19 satellite (over 2000 passes in the subauroral ionosphere) were used. For low solar activity (2004—2009, F10.7 ≤ 140) the in-situ Ne measurements onboard the low-orbiting satellite CHAMP (~ 8000 passes) were used. The obtained analytical dependence for the MIT position describes more accurately its minimum position compared with other models as a function of local time (Figure 1) and longitude (Figure 2) [1].

Model of the MIT shape [3] is represented as a set of foF2 tables in the latitude range from 45° to 75° for 24 longitude intervals, 24 hours of Universal Time, maximum and minimum of solar activity with linear interpolation for intermediate levels of solar activity. The model is applicable to all longitudes of Northern and Southern hemispheres, nighttime conditions in the range of 18—06 LT, winter and equinoctial seasons and any level of solar activity, as well as for daytime winter

conditions, but only at low solar activity. In summer conditions MIT even at night-time is rare formed, therefore its effect on the sub-auroral ionosphere under these conditions is not considered. The model describes the mean monthly climatological state of the sub-auroral ionosphere for quiet geomagnetic conditions with Kp = 2.

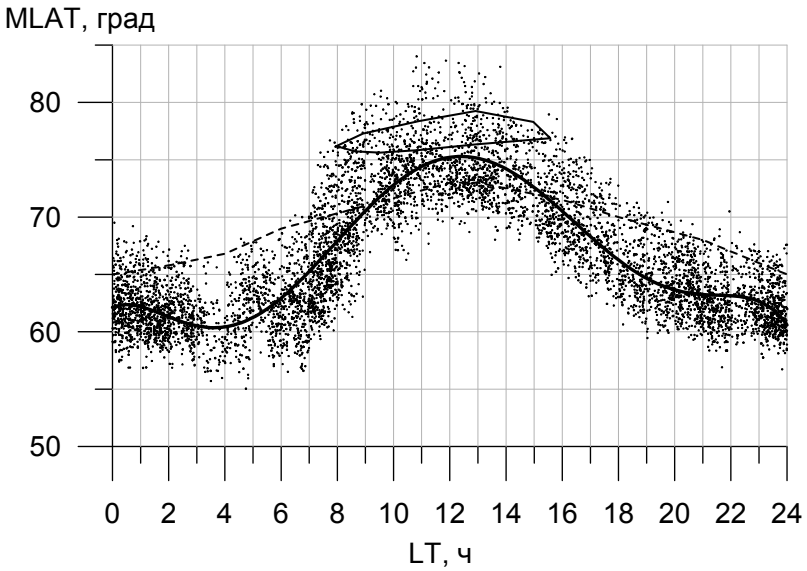

FIGURE 1. Ionospheric trough position changes in the course of local time. Points are the CHAMP data for the quiet winter conditions of low solar activity, solid curve is the trough average position, the dashed curve is the equatorial boundary position of diffuse auroral precipitation, closed loop is the area of the soft particles precipitation in the dayside cusp region [2].

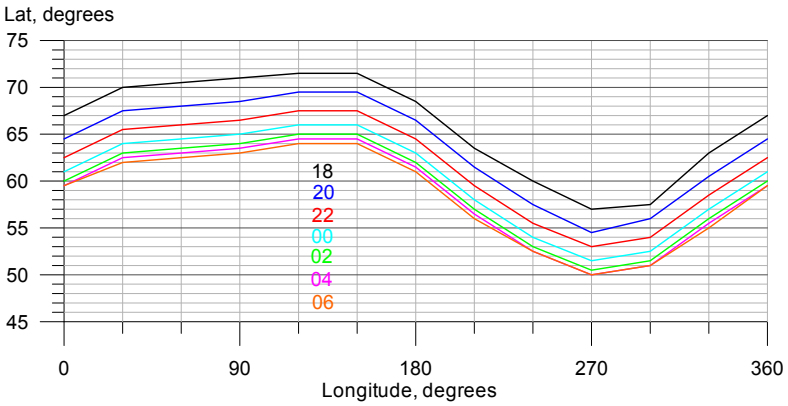

FIGURE 2. MIT position in the geographic coordinate system in Northern hemisphere for Kp = 2 for night-time (18—06 LT).

The MIT model is actually the median model of the sub-auroral ionosphere in the Northern and Southern hemipheres for winter and equinoctial conditions. The input parameters of the model are the number of the month of the year, UT and the index of solar activity. Figures 3 and 4 show the results obtained using the model of the main ionospheric trough.

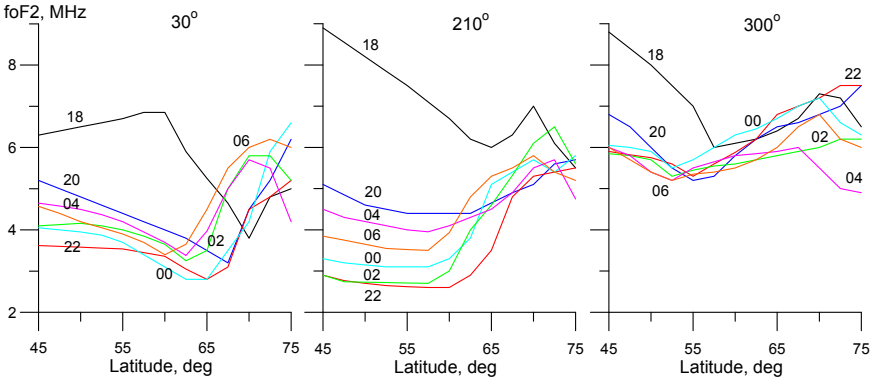

FIGURE 3. Latitudinal variations in foF2, obtained from the satellite Intercosmos-19 data for high solar activity for the night-time (18—06 LT) in three characteristic longitudinal sectors: European, Pacific and American.

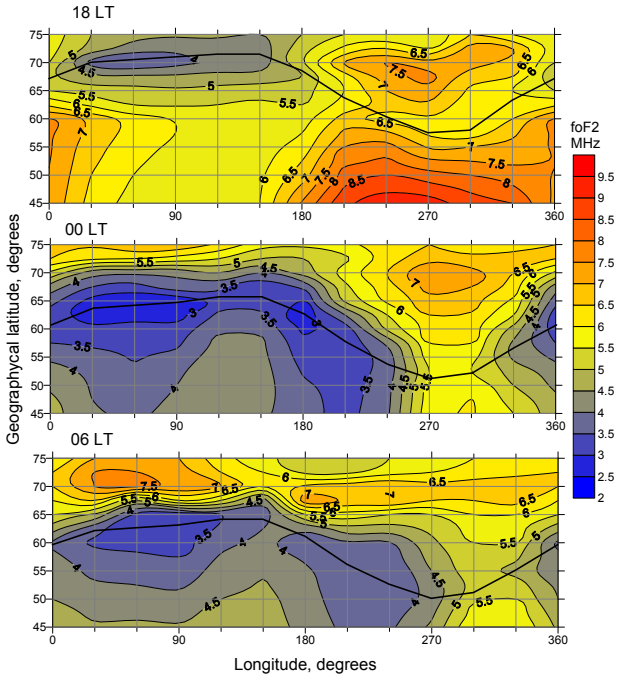

FIGURE 4. The foF2 variations in the MIT region for 18, 00 and 06 LT for winter conditions at high solar activity. Bold curves are the MIT minimum positions.

The MIT model is actually the median model of the sub-auroral ionosphere in the Northern and Southern hemipheres for winter and equinoctial conditions. The input parameters of the model are the number of the month of the year, UT and the index of solar activity.

This work was supported by RFBR Grant № 14-05-00788.

1. A. T. Karpachev, M. G. Deminov, V. V. Afonin, Model of the mid-latitude ionospheric trough on the base of Cosmos-900 and Intercosmos-19 satellites data. Adv. Space Res., 18, 221—230, 1996.

2. D. A. Hardy, M. S. Gussenhoven, E. Holeman, A statistical model of auroral electron precipitation. J. Geophys. Res., 90, 422—427, 1985.

3. A. T. Karpachev, The MIT shape dependence on longitude, altitude, season, local time, solar and geomagnetic activity. Geomagnetism and aeronomy. 43, 256—269, 2003.

D-6

Model Study of the Thermosphere Response to Perturbations Mesospheric Tides and Planetary Waves during Sudden Stratospheric Warming

Ivan Karpov[1,2], Fedor Bessarab[1,2], Yurij Korenkov[1], Maxim Klimenko[1], Vladimir Klimenko[1]

[1] West Department of Institute of Terrestrial Magnetism, Ionosphere and Radio Wave Propagation RAS, Kaliningrad, 236017, Russia
[2] I. Kant Baltic Federal University, Kaliningrad? 236041, Russia

The aim of this work is a theoretical study of the thermosphere response to the disturbance of tidal variations and planetary waves in the mesosphere due to the sudden stratospheric warming (SSW). In the model calculations used the global model of the upper atmosphere and ionosphere GSM TIP self-consistently describes the dynamics of neutral and charged components, as well as the dynamo electric fields and magnetospheric origin [1].

Calculations using the GSM TIP were made for conditions in January 2009 In January 2009 there was the SSW main phase is observed at 22—24.01.2009. The influence of mesospheric planetary waves and tides in the model GSM TIP is taken into account as boundary conditions at the lower boundary model 80km. The variations of the atmosphere on the lower boundary GSM TIP calculated for the period 1—30 January 2009 at model TIME GSM [2] taking into account the real variability of stratosphere and mesosphere.

The analysis of the results of GSM TIP calculations is aimed to selection of planetary and tidal variations in the parameters of the thermosphere using harmonic analysis of global distributions of the parameters during the simulated period. Global characteristics of tidal variations for each day were determined from the results of the calculations as follows:

$$F(r,\theta,\varphi,t,nd) = F_0(r,\theta,\varphi,nd) + \sum_n A_n(r,\theta,\varphi,nd)\cdot\exp(2\pi\cdot i\cdot n\cdot t/T) \quad (1)$$

r,θ,φ — height, colatitude and longitude, t — UT, nd — the number of days, $F(r,\theta,\varphi,t,nd)$ — calculated the global distribution of thermospheric parameter, $F_0(r,\theta,\varphi,nd)$ — the average daily value of the parameter, $A_n(r,\theta,\varphi,nd)$ — complex amplitude of the tidal variations with a period *T/n*, where *T = 24* hours, *n = 1, 2, 3.*

The spectral characteristics of tidal waves determined from the expansion of the tidal variations in the Fourier series in longitude.

$$B_{n,s}\left(r,\theta,nd\right) = \frac{1}{2\pi}\int_0^{2\pi} A_n\left(r,\theta,\varphi,nd\right)\cdot\exp\left(-is\varphi\right)d\varphi \quad (2)$$

$B_{n,s}(r,\theta,nd)$ — the complex amplitude of the tidal wave with period T / n and zonal wave number $s = 1, 2,3...$

The planetary waves parameters were determined from the Fourier expansion in longitude of daily mean parameters $F_0((r,\theta,\varphi,nd)$ from (1).

$$F_0\left(r,\theta,\varphi,nd\right) = \sum_s G_s\left(r,\theta,nd\right)\cdot\exp\left(is\varphi\right)$$

Where $G_s(r,\theta,nd)$ — the complex amplitude of the planetary harmonic with zonal number *s*.

The latitudinal distribution of zonal averaged mean temperature and zonal harmonics on height 80 km obtained in model calculations TIME GSM [2], for the simulation period are shown in Fig. 1. The structure of tidal variations at the height 80 km is characterized by significant zonal nonuniformity and day to day variability.

The example of day to day variability of solar migrating tidal waves is shown in fig. 2.

The global distributions of the thermospheric and ionospheric parameters taking into account variations at an altitude 80km (fig. 1,2) were calculated using the model GSM TIP for the period January 2—31.1.2009. The latitudinal distribution of the zonal averaged mean temperature and zonal harmonics with s = 1 over the simulated period shown in Fig. 3. As seen during the main phase of the SSW (January 20—24) appears at all altitudes in the thermosphere winter hemisphere at high latitudes. The mean temperature decreases at latitudes greater than 40^0. The

relative decreasing in mean temperature in this field decreases with increasing altitude and at altitudes of 250—300 km reaction to SSW is negligible. The latitudinal distributions of the zonal harmonics with s = 1 in the daily mean temperature (Fig. 3) in the thermosphere is significantly different from its structure at an altitude of 80 km (Fig. 1). The differences between latitudinal structures harmonics with s = 1 in temperature at the altitude of 80 km and higher altitudes connected with the fact that the mesospheric planetary waves do not penetrate into the thermosphere.

The change of latitudinal structure diurnal and semidiurnal tidal waves with height shown in Fig. 4.

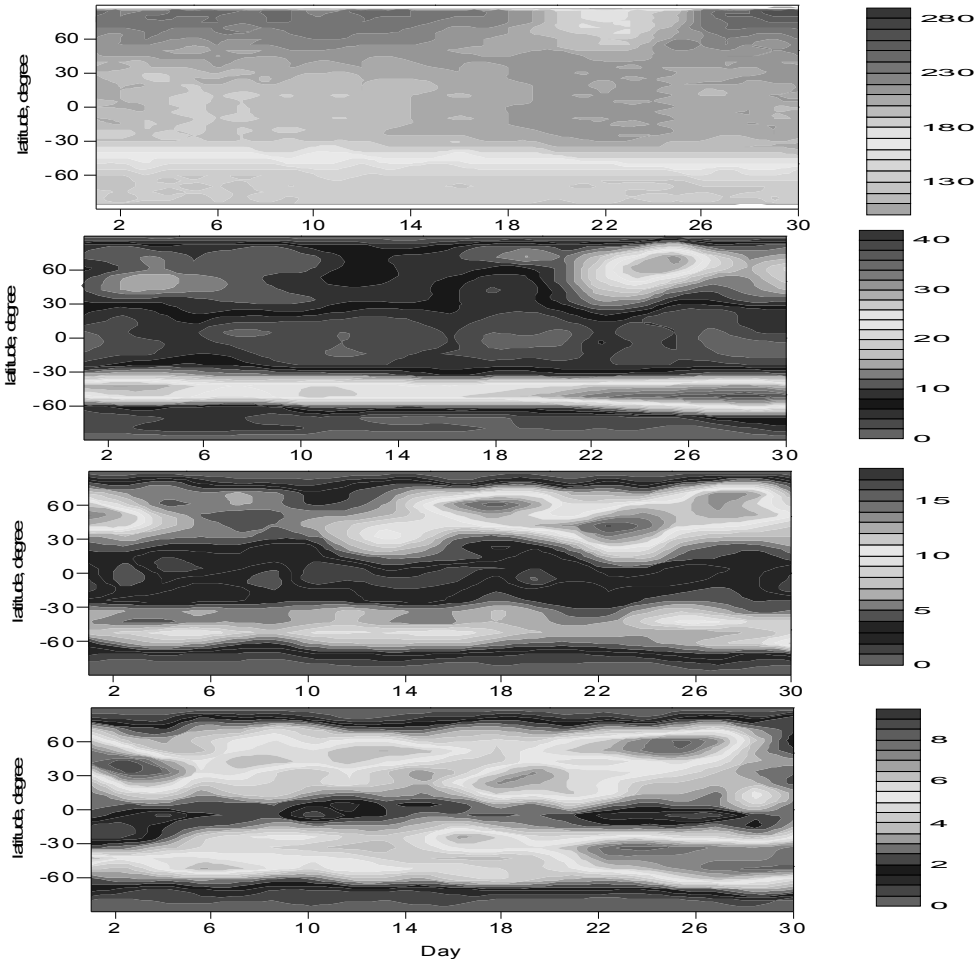

FIGURE 1. The latitudinal distributions of the amplitudes of zonal averaged mean temperature (s = 0 in (3)) and zonal harmonics with numbers s = 1, 2, 3. on the height 80 km during 2.01.-31.01.2009.

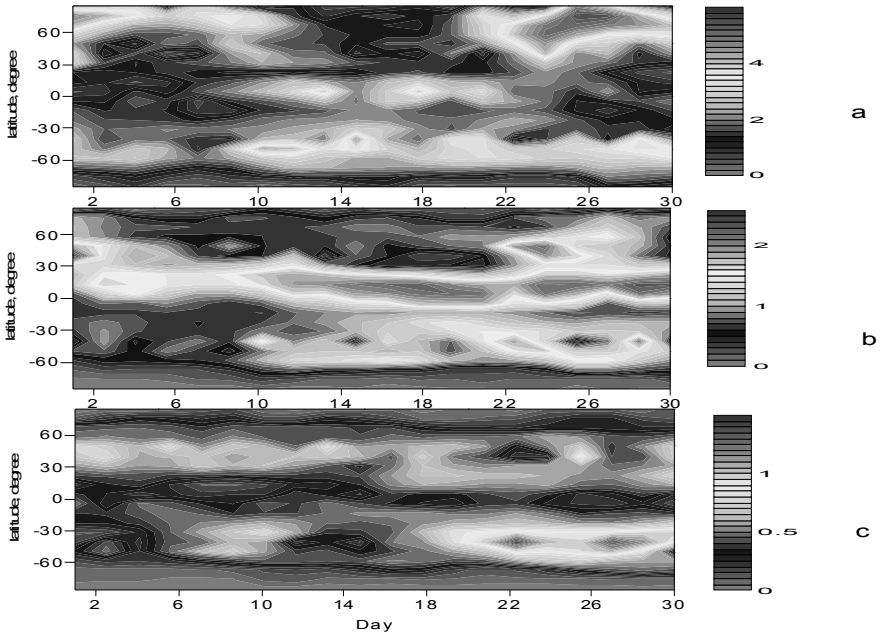

FIGURE 2. The latitudinal distributions of the amplitudes of solar migrating tidal waves diurnal (a), semidiurnal (b) and terdiurnal (c) on the height 80 km during 2.01.—31.01.2009.

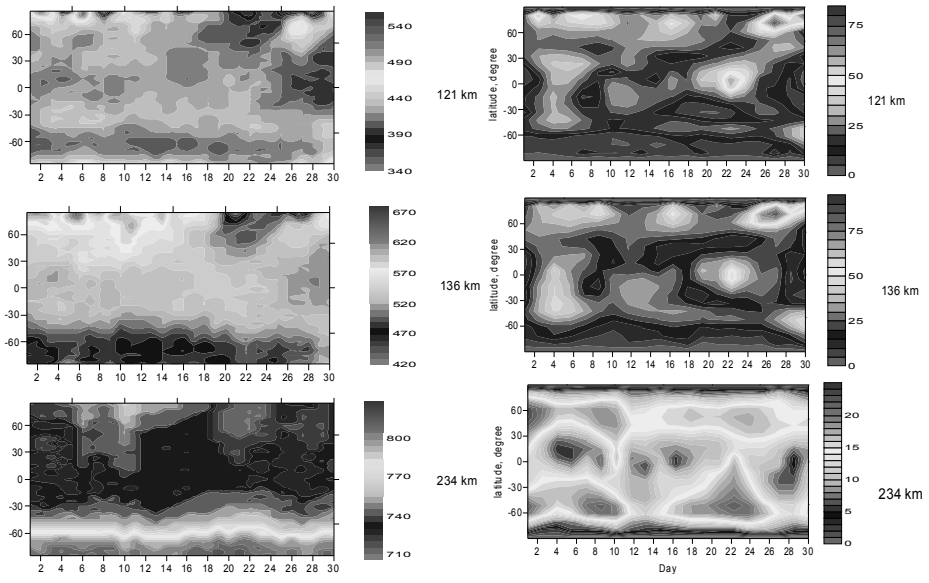

FIGURE 3. The latitudinal distributions of the zonal averaged mean temperature (left)and zonal harmonics with s = 1(right) on different heights during 2.01.—31.01.2009.

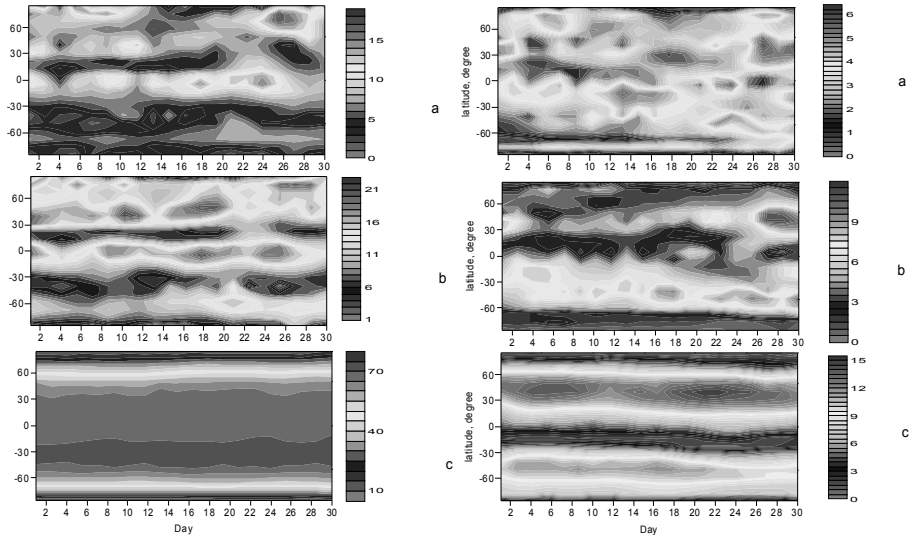

FIGURE 4. The latitudinal distributions of the solar diurnal (left) and semidiurnal (right) tidal waves on the height 121 km (a), 136km (b) and 234 km (c) during 2.01.—31.01.2009.

As seen from fig. 4 the structure of tidal waves strongly changes from day to day during the simulated period at altitudes of 80—140 km. The day to day changes of tidal waves amplitudes are insignificant in the upper thermosphere. Thus, calculations show that the characteristics of planetary and tidal waves in the upper thermosphere almost do not react to the passage of SSW.

The zonally averaged diurnal variations in ion O^+ concentration at the height 320 km (upper) and standard deviations from the mean values (bottom) for different days during modeling period are shown in fig. 5.

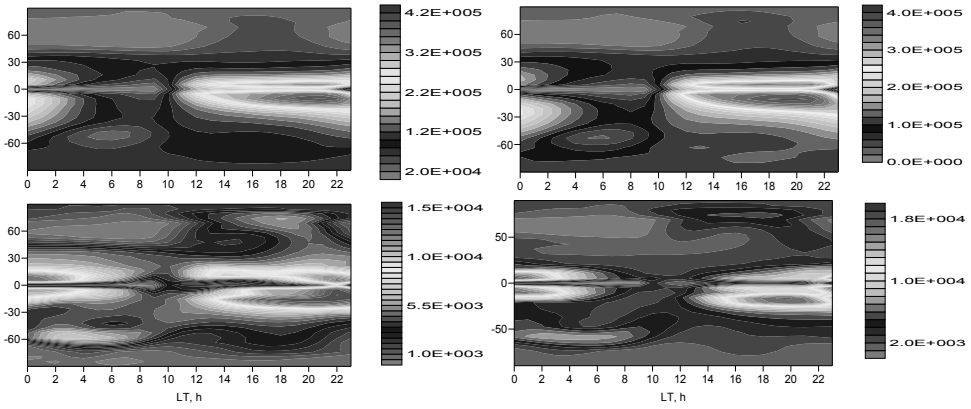

FIGURE 5. The zonal averaged diurnal variations ion O^+ concentration (upper) and standard deviations (lower) on the height 320 km 15.01.2009 (left) and 24.01.2009 (right).

As can be seen from fig.5 Significant changes in the structure of the diurnal variations of the ionosphere during the SSW does not arise. The standard deviations from the mean values do not exceed ~ 10 %.The amplitude of deviations not sufficient to explain the observed ionospheric effects during periods of SSW.

Thus, the results of the calculations show that

1. The mesospheric tides and planetary waves propagate into the thermosphere and can reach heights ~ 150 km.

2. The ionospheric disturbances initiated by mesospheric tides and planetary waves are small. The relative amplitudes iononsfere disturbances does not exceed 15 % in the calculation. The ionospheric effects observed during SSW periods reches 50 % and reach more.

3. The propagation of perturbations of mesospheric tides and planetary waves in the thermosphere is not a source of ionospheric disturbances during periods of SSW.

Acknowledgment The authors thank dr. H.-L. Liu for providing the results of calculations TIME GSM.

1. F. S. Bessarab, Yu. N. Korenkov, M. V. Klimenko, V. V. Klimenko, I. V. Karpov, K. G. Ratovsky, M. Chernigovskaya, *Modeling the effect of Sudden Stratospheric Warming with-in the thermosphere-ionosphere system*, Journal of Atmospheric and Solar-Terrestrial Physics, Elsevier, 2012, 90—91(December 2012), pp. 77—85, doi:10.1016/j.jastp.2012.09.005.

2. Richmond, A. D., E. C. Ridley, and R. G. Roble, A thermosphere/ionosphere general circulation model with coupled electrodynamics, Geophys. Res. Lett., 19, 601—604, 1992.

D-8

Development of the Model of HF Radio Wave Propagation in the Ionosphere

Daria S. Kotova[1], Maxim V. Klimenko[1], Vladimir V. Klimenko[1], and Veniamin E. Zakharov[2]

[1] West Department of Pushkov Institute of Terrestrial Magnetism, Ionosphere and Radio Wave Propagation RAS, Kaliningrad, 236017, Russia
[2] Immanuel Kant Baltic Federal University, Kaliningrad, 236041, Russia

Introduction. During the past decade, few studies of HF radio wave tracing have been performed using various numerical models of the ionosphere and radio wave propagation [1—5]. The undoubted merits of the results obtained in these studies are: (1) the model description of the of HF radio wave propagation in the vicinity of the main ionospheric trough [1—2]; (2) construction of the modeled oblique sounding ionograms with subsequent interpretation of observational iono-

grams [3—4]; (3) a model study of the main characteristics of oblique sounding ionograms [5]. However, these studies have some limitations. These investigations were carried out using either high-latitude ionospheric models, or ionosphere-plasmasphere models excluding the low-latitudinal region, i. e. they are not a global three-dimensional models and don't calculate self-consistently the electric field and the thermospheric and ionospheric parameters.

A distinctive feature of our research is to carry out the numerical calculations of HF radio wave traces in three-dimensional inhomogeneous anisotropic dispersed ionosphere. A distinctive feature of the used radio wave propagation model (RWP model), developed in the Kant BFU [6], is its complexity and universality. The model takes into account three-dimensional irregularity, anisotropy and dispersion of the medium of radio wave propagation. The model was developed for the case of complex geometrical optics and allows to investigate the dispersional distortion at LFM pulse propagation in the ionosphere.

RWP model. In the original state the numerical RWP model [6] was based on the decision of the eikonal equation by method of characteristics for each of the two normal modes in the geometrical optics approximation [7]. Solution is reduced to integration of system of six ray equations for the coordinates and moments:

$$\begin{cases} d\mathbf{r}/d\tau = \mathbf{p} - n\,dn/d\mathbf{p} \equiv \mathbf{s}(\mathbf{r},\mathbf{p}) \\ d\mathbf{p}/d\tau = n\,dn/d\mathbf{r} \end{cases}$$

where τ is integral parameter along each ray trajectory, **p** and **s** are pulse and beam vectors, respectively, **r** is radius vector of observations, n is refractive index.

The complex refractive indices of the ordinary and extraordinary wave at ionospheric heights from 60 up to 1000 km were calculated using the dielectric tensor of a cold plasma, which expression is given in [8]. The model allows us to obtain the differential wave absorption, expressed in dB/km for each of the two normal modes:

$$k = 8.68(\omega / c)\,\mathrm{Im}(n)\,,$$

where ω is the oscillation frequency, c is the speed of light. Integrated absorption (in dB) along each ray path on the interval length from σ_0 to σ equals

$$k_{Int} = \int_{\sigma_0}^{\sigma} k \cos\alpha d\sigma,$$

where α is the angle between the vectors **s** and **p**.

One example of the calculation results of radio paths obtained using this approach [9, 10] is shown in Figure 1. It shows the ray paths of the ordinary and extraordinary of wave modes and absorption of ordinary and extraordinary waves along each of the single hop pathes in dB. The summer solstice on June 22 was considered. Parameters required for the calculation of the refractive index specified using the IRI model [11].

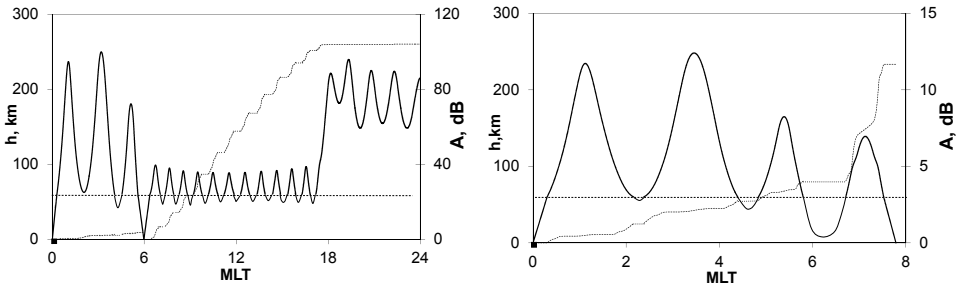

FIGURE 1. Model results of the trajectories and the integral absorption of HF radio waves in the ionosphere (f = 15 MHz, α = 5°, β = 90°, φ = 15°, 04:39 UT). The left graphs are for the ordinary wave, right graphs are for the extraordinary wave. α and β are the elevation angle and azimuth of the transmitter radiation, φ is the latitude of the transmitter, f is the frequency. The position of the transmitting station on the Earth surface pointed by the square.

The complex geometrical optics. RWP model has been extended to the case of complex geometrical optics with real ray paths [12]. Real character of the ray paths provides a choice of beam paths in the illuminated area, without getting into the geometric shadow.

The dispersion equation in the local approximation for each of two normal modes has the form:

$$H(\mathbf{p},\mathbf{r}) = \frac{1}{2}\left(\mathbf{p}^2 - n^2(\mathbf{r},\mathbf{l})\right) = 0, \tag{1}$$

where H is the Hamiltonian of the system, $\mathbf{p}$ is the complex momentum, n is the complex refractive index, $\mathbf{r}$ is the radius vector of the observation point, $\mathbf{l}$ is the complex vector orthogonal to the wave front, at that $\mathbf{p} = p\mathbf{l}$, p is a complex quantity of momentum, and so $p = n$.

For the real ray paths in addition to (1) we introduce the coupling equation

$$\operatorname{Im}\mathbf{r} = 0\,. \tag{2}$$

In generalized coordinates instead of equation (1) and (2) we have:

$$H(p_i, q_i) = 0\,, \tag{3}$$

$$\operatorname{Im}\ q_i = 0\,, \tag{4}$$

where $i = 1,2,3$ and p_i is the momentum conjugated to coordinate q_i.

The complete characteristic system of anisotropic media with real ray paths takes the form:

$$\frac{dq_i}{d\tau} = \mathrm{Re}\left(\frac{\partial H}{\partial p_i}\right)\left(1+\left(\frac{\mathrm{Im}\left(\partial H/\partial p_i\right)}{\mathrm{Re}\left(\partial H/\partial p_i\right)}\right)^2\right),$$

$$\frac{dp_i}{d\tau} = -\left(1\text{-}j\frac{\mathrm{Im}\left(\partial H/\partial p_i\right)}{\mathrm{Re}\left(\partial H/\partial p_i\right)}\right)\frac{\partial H}{\partial q_i}, \qquad (5)$$

$$\frac{d\psi}{d\tau} = \sum_{i=1}^{3}\frac{\partial\psi}{\partial q_i}\frac{dq_i}{d\tau} = \sum_{i=1}^{3} p_i\,\mathrm{Re}\left(\frac{\partial H}{\partial p_i}\right)\left(1+\left(\frac{\mathrm{Im}\left(\partial H/\partial p_i\right)}{\mathrm{Re}\left(\partial H/\partial p_i\right)}\right)^2\right),$$

where H is the Hamiltonian of the system, ψ is the eikonal, p_i is the momentum conjugated to coordinate q_i, τ is the independent variable, $d\tau_i$ is the differential of a complex function τ_i, $d\tau_i = d\tau + jd\tau_i^{'}$, which changes at the movement along each of the selected characteristics.

In the framework of a complex geometrical optics the solution of the characteristic system (5) allows to investigate self-consistently the mutual influence of the formation of the ray paths, absorption and irregularly structure of radio waves in the media with weak and strong absorption. The solution of this system does not require to solve the problem of analytic continuation of the refractive index into the region of complex values of the radius vector of the observation point. This is especially relevant at the numerical modeling of radio wave propagation in three-dimensional inhomogeneous media. Our consideration is limited to ray paths that remain in the illuminated region, without leaving to the caustic shadow. One of the applications can be a study of HF radio waves in the ionosphere.

Modeling of LFM signals in the ionosphere. In [13] a model of the RWP for the case of broadband signals in the HF band in the ionosphere was developed. It was used a dynamic representation of LFM signals in the form of a sequence of radio wave packets. We developed the numerical model of propagation of decameter radio signals with frequency modulated linearly (chirp or LFM signals). The model is designed to study the propagation of signals with different bandwidth and mean frequency of the spectrum in the three-dimensional inhomogeneous anisotropic ionosphere. In [14] we studied the dispersional distortion of LFM signals propagating in a three-dimensional inhomogeneous anisotropic ionosphere.

We have considered the chirp radiation by transmitting antenna

$$u(t) = 0, \quad t < 0, \quad t > \tau_{imp}, \; u(t) = A\exp\left(j\int_0^t(\omega_0 + \mu t)dt\right), \; 0 < t < \tau_{imp}, \qquad (6)$$

where A is the amplitude of the impulse, τ_{imp} is the duration of impulse starting at the moment $t = 0$, ω_0 and μ are the parameters of frequency modulation.

In an absorbing medium, on the part of the ray with the length σ from a point of radiation $\mathbf{r}_0$ to the observation point $\mathbf{r}$, the amplitude of the wave packet with the number ℓ reduced to the values

$$B_\ell(\mathbf{r}) = A\exp\left(-\frac{\omega_{\ell+1/2}}{c}\int_0^\sigma n_2(\mathbf{r},\omega_{\ell+1/2})\cos\alpha\, d\sigma\right), \tag{7}$$

where c is a speed of the light, $\alpha = \mathbf{p}\hat{}\,\mathbf{s}$ and $A = B_\ell(\mathbf{r}_0)$.

At the point $\mathbf{r}$ of the selected ray the propagation of wave packet with number ℓ excites the signal $u_\ell(t-\Delta t_{\ell g})$ where $\Delta t_{\ell g}$ is the time period of the group delay of the wave packet at the interval of the ray length σ from point $\mathbf{r}_0$ to point $\mathbf{r}$,

$$\Delta t_{\ell g} = \int_0^\sigma \frac{d\sigma}{u_{\ell g}}, \tag{8}$$

where $u_{\ell g}$ is the group velocity of wave packet,

$$u_{\ell g}(\mathbf{r},\omega_{\ell+1/2}) = \frac{c}{\left(n_1(\mathbf{r},\omega_{\ell+1/2}) + \dfrac{\omega_{\ell+1/2}}{2n_1(\mathbf{r},\omega_{\ell+1/2})}\left.\dfrac{\partial n_1^2}{\partial\omega}\right|_{\mathbf{r},\omega=\omega_{\ell+1/2}}\right)\cos\alpha} \tag{9}$$

At the effective duration Δt of each wave packet its length $\Delta\sigma$ varies at propagation in an inhomogeneous ionosphere along the corresponding ray path.

The instantaneous value of $\Delta\sigma$ for the wave packet with the boundary coordinates σ and $\sigma+\Delta\sigma$ along selected ray can be found by solving the equation

$$\Delta t = \int_\sigma^{\sigma+\Delta\sigma} \frac{d\sigma}{u_{\ell g}}, \tag{10}$$

at that for the medium with weak irregularity $\Delta\sigma \approx u_{\ell g}\Delta t$.

Because the ionospheric plasma dispersion the wave packets with different carrier frequencies have not only different group velocities, but also propagate along different ray paths. The LFM-pulse radiation is considered as a continuous sequence of wave packets with a duration Δt of each of them. On the duration of the chirp the integer number of $N = \tau_{imp}/\Delta t$ of discretization intervals is contained. The wave packet with number ℓ, where $\ell = 0,1,...,N-1$, have the central frequency of $\omega_{\ell+1/2} = \omega_0 + \mu(t_i + t_{i+1})/2$, where $t_i = \ell\Delta t$. Suppose that k is relative deviation in frequency modulation function at LFM-pulse duration $k = \mu\tau_{imp}/\omega_0$. If you specify $\omega_0 = 6\pi\cdot 10^6$ 1/s, $k = 3$, $\tau_{imp} = 10^{-4}$ s, and $\Delta t = 4\cdot 10^{-6}$ s, than LFM-pulse leads to radiation of $N = \tau_{imp}/\Delta t = 25$ wave packet.

The model can be used to study of the distortion of the LFM-pulses in an inhomogeneous anisotropic dispersed ionosphere. The model admits a generalization to other types of complex signals, for example the phase-shift keyed signals.

Model development to the case of using GSM TIP and IRI-2012 models as a medium model for radio wave propagation. Previously, to obtain a three-dimensional anisotropic medium of radio wave propagation we used empirical models of the ionosphere IRI [11] and the neutral atmosphere MSIS — Mass Spectrometer and Incoherent Scatter radar model [15]. At the last stage of model modification we obtained the ability to use the data of the dynamic environment model GSM TIP and empirical model IRI-2012 for calculation of the refractive index. An adaptation of RWP and GSM TIP models was a process of allocation of the propagation region and a three-dimensional interpolation from the nearest grid nodes at each step along the radio wave path. Therefore, we have to analyze the propagation of HF radio waves during two periods of geomagnetic storms on May 2—3, 2010 [16] and 26—29 September 2011 [17]. We examine the changes of radio wave paths and their attenuation in the high-, low- and mid-latitude ionosphere in quiet geomagnetic conditions and during geomagnetic storms. Figure 2 shows one example of the numerical results for the ordinary wave mode.

This work was supported by RFBR Grant № 14-05-00578.

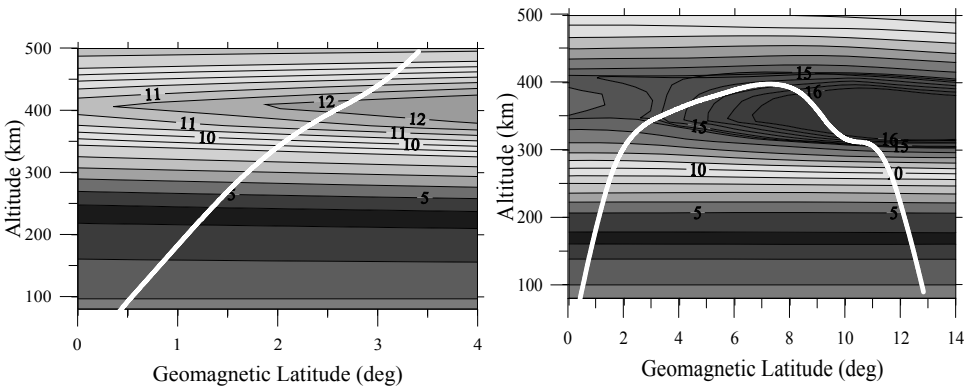

FIGURE 2. The numerical calculation results of trajectories (white lines) of HF radio waves in the ionosphere and the electron density contours along the path (f = 12.65 MHz, $\alpha = 60°$, $\beta = 0°$, $\varphi = 11.2°$ S, 16:00 UT) for IRI-2012 (at the left), and for GSM TIP (on the right).

References

1. M. Yu. Andreev, T. N. Lukicheva, V. S. Mingalev, *Model study of the effect of the main ionospheric trough on oblique HF radiowave propagation*, Geomagnetism and Aeronomy, Moscow, 2006, 46(1), pp. 94—100, doi:10.1134/S0016793206010105.

2. M. Yu. Andreev, G. I. Mingaleva, V. S. Mingalev, *Numerical simulation of the structure of the high-latitude ionospheric F region during meridional HF propagation*. Geomagnetism and Aeronomy, Moscow, 2007, 47(4), pp. 487—495, doi:10.1134/S0016793207040093.

3. M. Yu. Andreev, D. V. Blagoveshchensky, V. M. Vystavnoi et al., *Interpretation of experimental data on HF propagation on the St. Petersburg-Spitsbergen path*. Geomagnetism and Aeronomy, Moscow, 2007, 47(4), pp. 502—509, doi:10.1134/S0016793207040111.

4. D. V. Blagoveshchensky, M. Yu. Andreyev, V.S. Mingalev et al., *Physical and model interpretation of HF radio propagation on the St. Petersburg—Longyearbyen (Svalbard) path,* Advances in Space Research, Oxford, 2009, 43(12), pp. 1974—1985, doi:10.1016/j. asr.2009.01.030.

5. G. V. Kotovich, V. P. Grozov, A. G. Kim et al., *Application of the theoretical reference ionosphere model for calculating HF-radiowave propagation characteristics*. Geomagnetism and Aeronomy, Moscow, 2010, 50(4), pp. 504—508, doi:10.1134/S0016793210040110.

6. V. E. Zakharov, A. A. Cherniak*, Numerical model of radio paths of HF radio waves in the ionosphere*, I. Kant BFU News, Kaliningrad, 2007, No. 3, pp. 36—40. (in Russian)

7. Yu. A. Kravtsov, Yu. I. Orlov, *Geometrical Optics of Inhomogeneous Media*, Berlin, 1990, p. 312.

8. B. E. Brunelli, A. A. Namgaladze, *Physics of the Ionosphere*, Moscow, 1988, p. 527.

9. V. E. Zakharov, A. A. Cherniak, *Formation of multi-hop traces and absorption of HFradio waves in the 3D inhomogeneous ionosphere,* I. Kant BFU News, Kaliningrad, 2008, No. 4, pp. 51—55. (in Russian).

10. V. E. Zakharov, Ye. V. Bakhar, *Influence of the height of the transmitter on the formation of the HF radio wave traces in the ionosphere,* I. Kant BFU News, Kaliningrad, 2009, No. 4, pp. 58—64 (in Russian).

11. D. Bilitza, *International reference ionosphere 2000*, Radio Sci., Washington, 2001, 36(2), pp. 261—275.

12. V. E. Zakharov, D. S. Kotova, *Model of HF radio wave propagation in the ionosphere in the approach of complex geometrical optics*, Collection of Reports XXIII Russian Scientific Conference, Yoshkar-Ola, 2011, V. 3, pp. 340—342 (in Russian).

13. V. E. Zakharov, D. S. Kotova, *Modeling of the broadband signal distortion in the ionosphere*, «Radiotekhnika» (Radioengineering), Moscow, 2013, №2, pp. 87—90 (in Russian).

14. V. E. Zakharov, D. S. Kotova, *Investigation of distortions of the chirp signals in the neighborhood of critical frequencies of ionospheric plasma,* I. Kant BFU News, Kaliningrad, 2013, No. 4, pp. 34—38. (in Russian).

15. A. E. Hedin, *Extension of the MSIS thermospheric model into the middle and lower atmosphere*, J. Geophys. Res., United States, 1991, 96(A1), pp. 1159—1172.

16. D. S. Kotova, M. V. Klimenko, V. V. Klimenko, V. E. Zakharov, *Ionospheric response to the geomagnetic storm on May 2, 2010 and its effect on HF radio wave propagation in the high-latitude ionosphere*, Proc. XXXVI Annual Seminar "Physics of Auroral Phenomena", Apatity: PGI KSC RAS, 2013, pp. 174—177 (in Russian).

17. D. S. Kotova, M. V. Klimenko, V. V. Klimenko, V. E. Zakharov, *Mathematical modeling of HF radio wave propagation through three-dimensional inhomogeneous ionosphere*, XIII Young Scientists' Conference "Interaction of fields and radiation with matter", Irkutsk, 2013, pp. 242—244. (in Russian).

The Study of F-scatter with DPS-4 Ionosonde

E. V. Nepomnyashchaya, V.A Panchenko, V. I. Rozhdestvenskaya, V. A. Telegin

Pushkov Institute of Terrestrial Magnetism, Ionosphere, and Radio Wave Propagation
142190 Moscow Troitsk. Russia

It is well known that, although the basic mechanisms of F-spread have been studied for decades, the regional features in the behavior of the ionospheric parameters and their relation to solar activity still remain an important scientific and applied problem.

To analyze the spatial and temporal statistical characteristics, it will be sufficient to use a simplified two-level classification: index S =0 for the quiet ionosphere and index S=1 for the cases when $\Delta f \geq 0.25$ MHz.

According to [1], the probability of occurrence of the night-time F-spread in winter at Moscow (55.5^0N, 37.3^0E, geomagnetic latitude —50^0) may reach 90 % at the minimum and does not exceed 40 % at the maximum of the solar activity cycle. Fig.1 illustrates the results obtained in the Moscow area in the period close to the maximum of cycle 21 (from 1979 to January 1980) by ground-based (AIS, IZMIRAN) and satellite (IK-19) observations [2].

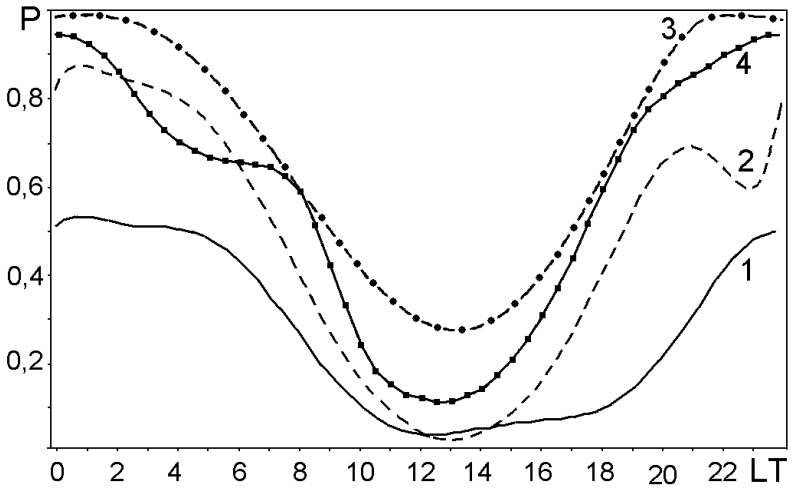

FIGURE 1. Diurnal variation in the probability of F-spread occurrence: 1) in winter 1979—1980 (ground-based AIS data); 2) in winter 1979—1980 (IK-19 orbital data); 3) in January 2012 (DPS-4 data); and 4) in January 2013(DPS-4 data).

Curve 1 in Fig. 1 represents ground-based measurements made with the AIS ionosonde. The F-spread probability at night is equal to ≈ 0.4, i. e., similar to the value reported in [3]. On the other hand, the probability inferred from the IK-19 satellite data in the same period of winter 1979—1981 (activity maximum) differs significantly, the nighttime value being about twice as high (see curve 2 in Fig. 2) [2]. Comparing both results, one can suggest that the difference may be explained, partly, by different hardware characteristics of the ground-based and orbital ionosondes and the noise level on ionograms and, partly, by larger variability of the upper ionosphere compared the regions below F-maximum.

F-spread data for the period 1979—1980 were obtained with an AIS-type ionsonde. This is a classical analog pulsed ionosonde characterized by continuous frequency tuning, small dynamic range of the recorded signal, and recording on photographic film. Acquisition of a new, DPS-4 digisonde at IZMIRAN gave us an opportunity to return to this issue.

One must bear in mind that the hardware characteristics of DPS-4 and AIS differ greatly. A distinctive feature of the digital ionosonde DPS-4 is its low power. However, special signal processing techniques ensure a sufficiently high signal-to-noise ratio and a large dynamic range of the recorded signal. Its important difference from AIS is a discrete, usually at 50 kHz steps, frequency tuning. Along with issuing ionograms, DPS-4 can automatically restore the electron density profile, and, optionally, plot the power distribution of the reflected wave according to the arrival angles and measure the drift velocity of the ionospheric plasma.

Fig. 2a presents a DPS-4 ionogram with the signs of F-spread obtained in the nighttime at the Moscow station. The red branch is the ordinary component coming from the zenith; the green branch is the extraordinary component, and the rest is the side view. The color-direction scale is given on the right of Fig. 2a. The legend on the left provides the layer parameters determined automatically.

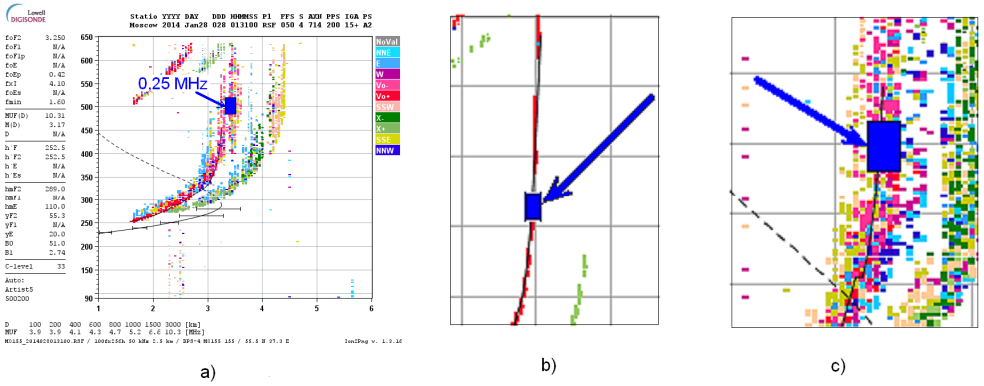

FIGURE 2. a) A DPS-4 ionogram with F-spread manifestations; b) F-spread is absent c) F-spread is present.

The method used to reveal the presence or absence of F-spread is illustrated in Figs. 2a and 2b. It was chosen for the sake of simplicity and for the convenience of comparison with the earlier data obtained at IZMIRAN.

We also selected DPS-4 ionograms similar to those presented in Fig. 2 for the winter period at the maximum of cycle 24. Using DPS-4 data, we estimated the probability of occurrence of F-spread in January 2012 (curve 3 in Fig. 1) and in January 2013 (curve 4 in Fig. 1). In both cases, the broadening $\Delta f \geq 0.25$ MHz was considered to be a criterion of F-spread (see Figs. 2b and 2c)

Similar estimates were obtained for the summer periods of 1980 and 2013. The results are represented in Fig. 3. The vertical bars show the error estimate.

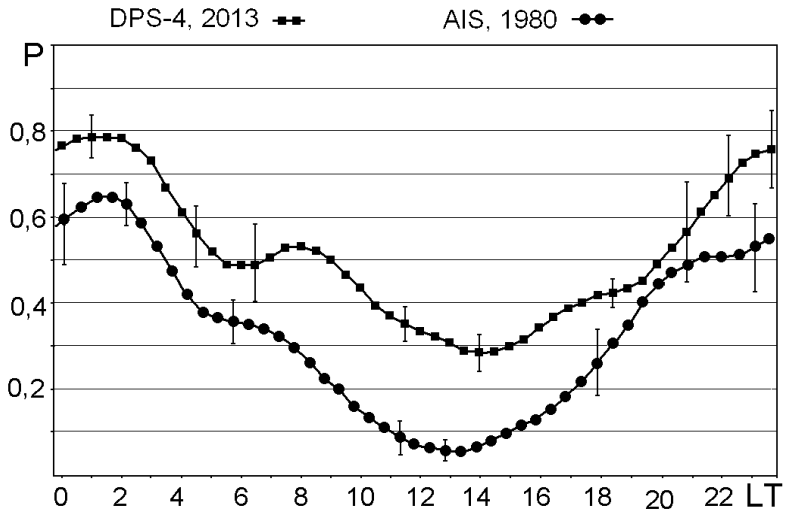

FIGURE 3. Diurnal variation in the probability of F-spread occurrence in summer 1980 (AIS data) and in summer 2013 (DPS data).

The comparison of Fig. 1 and Fig. 2 corresponding to different solar maxima (1979—1980 and 2012—2013) shows that, qualitatively, the curves for different cycles are very much alike, and F-spread occurrences correlate very well in spite of the use of different equipment.

Nevertheless, it can be noted that the occurrence rate of F-spread on DPS-4 ionograms is sometimes significantly higher than obtained earlier from AIS data.

The difference in the F-spread occurrence rates on ground-based ionograms for 1979—80 and 2012—2013 may be due to two factors. First, the maximum of the current cycle 24 (2012—2013) is pronounced weaker than the maximum of cycle 21 (1979—1980). Different levels of solar activity cannot fully account for the quantitative difference, because, according to our data, even in the period of minimum of 1976—1977 the probability of F-spread did not approach unity. The second factor

responsible for the discrepancy is the difference in the AIS and DPS-4 hardware characteristics. The AIS ionosondes are characterized by a small dynamic range of the recorded signal. They produce film ionograms, which do not display all the scattered signals, but only those whose power is higher than the threshold value. Thus, the relatively weak scattered signals cannot be detected, and the trace on ionogram turns out to be narrow. When signals are processed and recorded digitally with DPS-4 digisonde, the dynamic range is significantly larger. The detection threshold for DPS-4 is usually lower than for AIS and other stations of the same type. The lower is the detection threshold, the more are the extension and frequency range of the trace seen on the ionogram. Hence, the occasions when the trace width exceeds 0.25 MHz and F-spread is recorded are more frequent. Besides, the discrete frequency tuning of DPS-4 with a 50 kHz step also contributes to the apparent width of the trace. This change of characteristics in the process of updating the ionosondes must be taken into account when comparing data obtained in different periods.

1. Antonov A.M., Nepomnyashchaya E.V., Fatkullin M.N. F-spread in the daytime low-latitude ionosphere, *Geomagn. Aeron.,* 1987, v. 27, №5, p.831—833.

2. Karpachev A.T., Telegin V.A. F-spread study based on the topside sounding ionospheric data obtained from the "Interkosmos 19": and "Kosmos-1809", ГР №01200302876, №02200604293, 2005, 27 P.

3. Gershman B.N., Kazimirovsky E.S., Kokourov V.D., Chernobrovkina N.A. F-spread phenomenon in the ionosphere, Moscow, Nauka, 1984, 140 p.

D-10

The Estimations of Ionospheric Total Electron Content by GLONASS Measurements

Irk Shagimuratov, Nadezda Tepenitsyna,
Iurii Cherniak, Aleksandr Radievsky, Luisa Koltunenko,
Galina Yakimova

WD IZMIRAN, Kaliningrad, prospect Pobedy, 41, Russia

Absrtact. The comparative analysis of the ionospheric total electron content (TEC) estimations based on dual-frequency measurements of signals delays of the GLONASS and GPS navigation satellites systems is presented. The difference and similarity of diurnal variations of TEC obtained with GLONASS/GPS are discussed.

Introduction

With fulfillment of global satellite navigation system — GLONASS were open the new possibility for global monitoring of the ionosphere. The GLONASS satellites are located in middle circular orbit at 19,100 km altitude with a period of 11 hours and 15 minutes. In contrast with the 55 degree GPS satellites orbit inclination the GLONASS' orbit have a 64.8 degree inclination that makes GLONASS signals especially suited for the high latitude ionosphere to study. The GLONASS constellation operates in three orbital planes, with 8 evenly spaced satellites on each. A fully operational constellation with global coverage consists of 24 satellites. The GPS constellation operates in six orbital planes, with 4 evenly spaced satellites on each. Every GPS satellite transmits the navigation signals on two fixed frequencies: L1 (1575MHz), L2 (1227MHz). Each GLONASS satellite transmits signals on two owned frequencies which are formed wit the specific rule.

Methodolodgy

The permanent navigation networks provide the GLONASS observations as well as GPS that available as code and phase measurements in the RINEX format. It is allows to use of the same algorithms for processing of measurements from both systems.

The differential dual-frequency GLONASS/GPS measurements are used for the estimation of the ionospheric TEC. The relation between code P_1, P_2 [m] measurements and TEC can express as [1]

$$\Delta P = P_2 - P_1 = \frac{STEC}{M} + A_p, \tag{1}$$

where P_1, P_2 [m] — code measurements of signals on L_1, L_2;

M — scaling factor that converts units of distance to TEC units [electron/m^2];

A_p — differential instrumental group delays of the receiver and satellite hardware (instrumental biases).

STEC — integral TEC along the line-of-sight between the satellite and receiver.

For phase measurements the equation is very similar:

$$\Delta\Phi_{[m]} = \Phi_1 - \Phi_2 = \frac{STEC}{M} + A_p + \left(N_1 \cdot \lambda_1 - N_2 \cdot \lambda_2\right) = \frac{STEC}{M} + A_\Phi,$$

where N_1, N_2 — the carrier phase ambiguities;

λ_1, λ_2 — are the carrier phase wave lengths.

So the TEC obtained from GLONASS/GPS measurements is relative. To obtain absolute value of the ionospheric TEC instrumental biases must be removed. These instrumental biases are the main source of error at the estimation of TEC using GLONASS/GPS data.

When TEC estimated from GLONASS/GPS observations, the ionosphere was approximated by a spherical shell on a fixed height of 400 km above the Earth's surface. A simple geometric factor was used to convert the slant TEC into a vertical one. To reduce the influence of the horizontal gradients only signals of the satellites with lowest elevation angle 20^0 involved into analysis. The phase ambiguities were removed by fitting phase measurements to the code data collected along an individual satellite pass. After pre-processing, the phase measurements contained an instrumental bias only. The biases were determined for each station using GPS measurements of all satellite passes over a given site in a 24-hour period. The diurnal variations of TEC over a site and the biases for all satellites were estimated simultaneously. At all stations, before the technique was run, the instrumental biases were removed in all satellite passes. Using this procedure, an absolute line of sight TEC for all satellite-receiver paths was calculated.

Results

In the most approaches the ionosphere is represent by a spherical layer with finite small thickness, neglecting horizontal gradients in TEC distribution. For reconstruction of diurnal variations of TEC we used model of TEC. The TEC was approximated as a function of local time (LT) and the difference between the receiver latitude and the latitude of the subionospheric point (sp) along satellite passes (Δφ). The diurnal variation of TEC is expressed as a series of harmonic terms:

$$TEC = a_0 + \sum_{i=1}^{6} a_i \cos is + \sum_{i=1}^{6} b_i \sin is + c_1 \Delta\varphi + c_2 \Delta\varphi s + c_3 \Delta\varphi^2$$

$$s = \pi(LT - 14)/12$$

The diurnal variation of TEC is formed using TEC measurements of all satellite passes observed over individual station on 24 hour interval. It demonstrates Fig. 1 where the diurnal variations of TEC over mid-latitude station of Kaliningrad (54.42°N, 20.27°E) and high-latitude one of Kiruna (67.74 °N, 21.06 °E) are shown.

The example on Fig. 1 are presented the comparison of the diurnal variations of GLONASS (dash line) and GPS (solid line) TEC for quiet (09 December 2013) and disturbed (09 December 2013) geomagnetic conditions. It is observed the common agreement between behavior of diurnal variations for both system. Nevertheless the some difference take place. It can be explained due to of the GLONASS satellites inclination is higher than GPS the difference depend on latitude.

During quiet conditions the difference between GLONASS and GPS TEC are estimated less than 1 TECU (1 TECU = 10^{16} el/m2). As it was expected the TEC value at mid-latitudes is obviously more than at high-latitudes. The values and sign of GLONASS/GPS TEC difference varied during the day. It can be explained by differ satellite configuration of both system which changes during day. This can be illustrated by Fig. 2 where the map of subionospheric satellite traces over Kaliningrad station for 09—12 and 18—21UT intervals is presented.

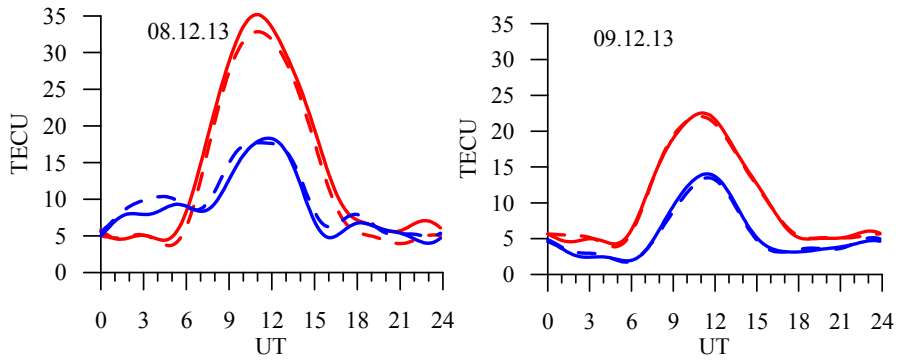

FIGURE 1. The diurnal variations of GLONASS(dash) and GPS (solid)TEC over station of Kaliningrad (red line) and of Kiruna (blue line) for quiet (09 December 2013) and disturbed (08 December 2013) days

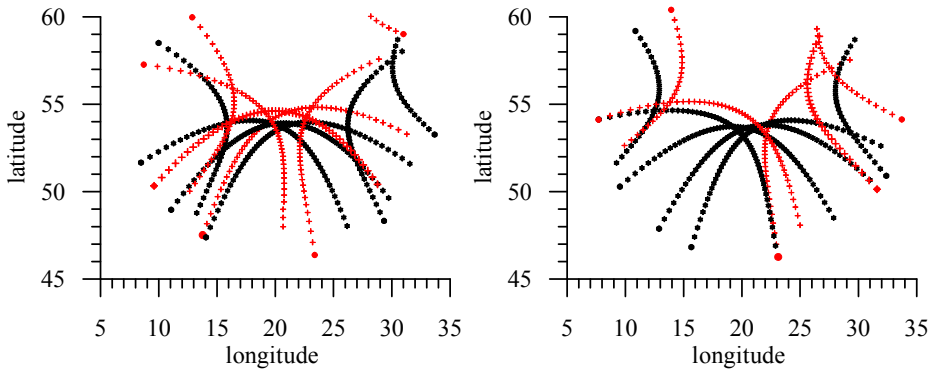

FIGURE 2. Map GLONASS/GPS satellite traces in the ionosphere on 09—12UT (left panel) and 18—21UT (write)

The maps demonstrate the area of the ionosphere affected on radio signal delays from which the electron content information is extracted. As seen on Fig2 the area for both system is some differ and this configuration permanently changed during the day. That lead to caused difference of GLONASS/GPS TEC estimations. The difference is more expressed at high latitudes. On the average the values of GLONASS TEC is lower than GPS one.

As mentioned above the diurnal TEC variations is formed using measurements along all satellite passes observed over station on 24 hour interval. The Fig.3 is presented the map of the satellite traces in the ionosphere on 24 hour interval over Kiruna and Kaliningrad stations. The picture shows the ionospheric area from which the TEC measurements were collected for the diurnal variation of TEC over station to form. One can see that the ionospheric area is some differed for GLONASS and GPS. The essential distinction took place on high latitudes. It is reason what is why the GONASS/GPS TEC can be differed with one another.

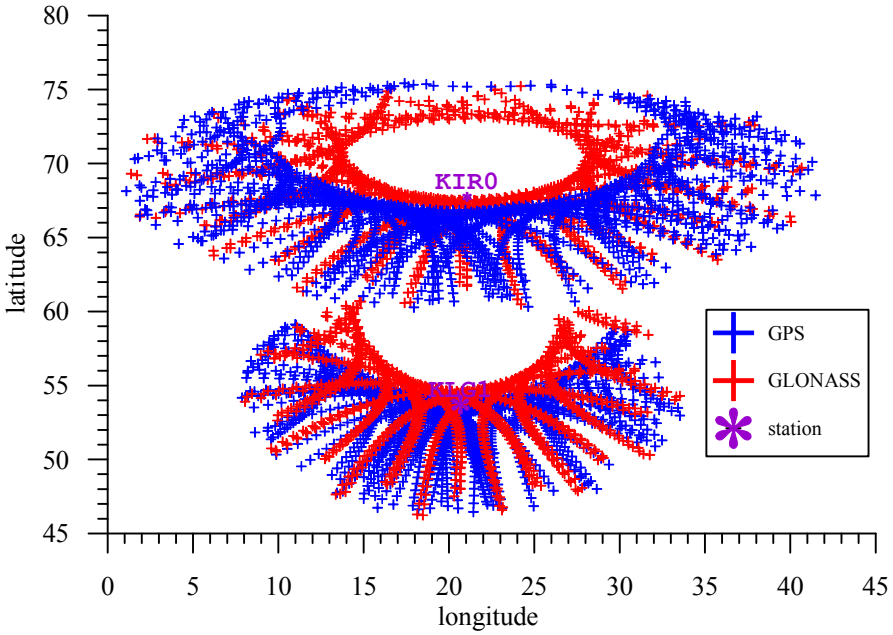

FIGURE 3. Map GLONASS/GPS satellite traces in the ionosphere on 24 hour interval.

It should be emphasized that GPS satellites have inclination less than GLONASS, so at high latitudes the satellites are observed at low elevations in contrast to middle latitudes. Undoubtedly that at lower elevations the influence horizontal TEC gradients essentially increased and that lead to rise of the distinction of TEC values between TEC estimation based on both system measurements.

During geomagnetic storms the TEC gradients are essentially increased in the ionosphere [2]. In such cases the accuracy of determining of instrumental biases is worsen and in consequence the absolute TEC can estimated with some ambiguity. On the Fig.1 the diurnal TEC variations over middle and high latitudes during storm 9 December 2013 are shown. Over Kaliningrad station the strong day time positive effect took place. The difference between GLONASS and GPS TEC values has been increase relative to quiet day. As a whole the estimated value of GPS TEC was less than GPS one. At high latitude during storm the diurnal variation of TEC was essentially changed and the difference GLONASS/GPS TEC increased. It is appeared influence

In Fig.4 is presented the statistic GLONASS/GPS TEC measurements for mid- and high-latitude stations. The picture shows high correlation between TEC values estimated from GLONASS and GPS observations. The TEC dispersion has been increased at low TEC values that corresponded night conditions. At high latitudes GONASS TEC is ordinary less than GPS one. This is happened due to GLONASS satellites have higher inclination that GPS. The GLONASS navigation satellite signals provide to probe the ionosphere at higher latitudes than GPS.

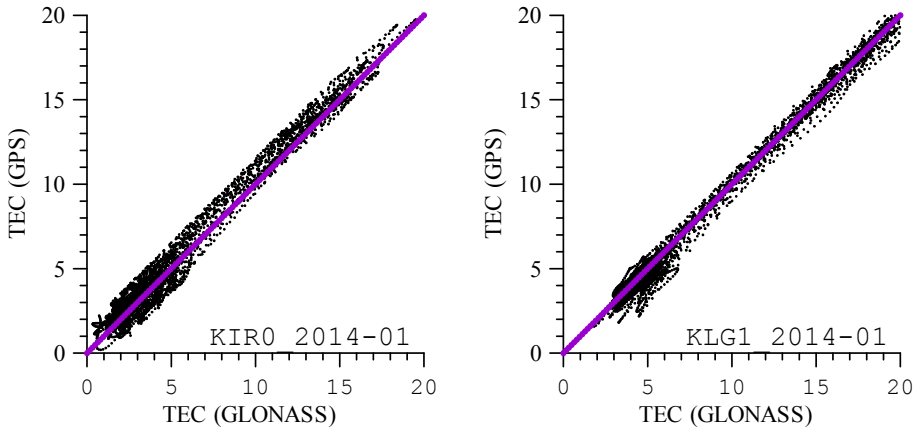

FIGURE 4. The comparison of scatterplots between GLONASS and GPS values of TEC during January 2014

Summary

The GLONASS navigation satellite system orbits have a 64.8 degree inclination that makes them signals especially suited for the sounding of the high latitude ionosphere. At latitudes low than 55ºN the difference between GLONASS and GPS TEC estimates raised due to distinction of satellite constellation of both system, but this difference do not exceed 1.0 TECU. At higher latitudes the GPS TEC values overestimate GLONASS derived TEC, this difference can reach 2—3 TECU. It is necessary to take notice that are high correlation between TEC values using GLONASS and GPS measurements when of the same algorithms for processing of measurements from both systems were used.

Aknowledgements

The work was supported by RFFI, grant 14-07-00512 and by RAS Presiduim Program N 22.

References

1. Shagimuratov I.I., Yu.V. Chernyak, I.E. Zakharenkova, G.A. Yakimova. Use of Total Electron Content Maps for Analysis of Spatial—Temporal Structures of the Ionosphere. / Russian Journal of Physical Chemistry B, Vol. 7, No. 5, 2013, p. 656.

2. Shagimuratov I.I., Baran L.W., The structure of mid- and high-latitude ionosphere during September 1999 storm event obtained from GPS observations // *Ann. Geophys*., V20, N1, pp. 655—660, 2002.

Ionosphere Response to Spacecraft Engine Exhaust Jets Effects

Vitaly V. Khakhinov, Sergey S. Alsatkin, Dmitri S. Kushnarev,
Valentin P. Lebedev, and Konstantin G. Ratovsky

Institute of Solar-Terrestrial Physics Siberian Branch of Russian Academy of Sciences,
P. O. Box 291, Irkutsk, 664033, Russia

Active space experiments (ASEs) in the near-Earth outer space play an important role for investigations of ionosphere response to influences of various origins. To study some ionosphere response (e. g., formation, evolution, and dynamics of small- and medium-scale irregularities in the ionosphere), we can use the controllable influence of spacecraft's liquid propellant engines (LPEs) exhaust jets on space plasma.

Studying artificial ionospheric response to spacecraft engine exhaust jets effects is the objective of "Radar-Progress" ASEs carried out with transport spacecraft (TSC) "Progress" and the Irkutsk incoherent scatter radar (IISR) [e. g., 1—7].

Since 2007, Central Research Institute of Machine Building and Institute of Solar-Terrestrial Physics have been conducting "Radar-Progress" ASEs (prior to 2010, the experiment was called "Plasma-Progress") for studying spatial-timporal characteristics of ionospheric disturbances generated by "Progress" TSC LPEs. TSC is involved in ASE in the free flight mode at 350—410 km altitudes, after the cargo delivery mission to the International Space Station (ISS) is completed.

The main facility for the diagnostics of these disturbances is IISR [8]. IISR is a monostatic pulse radar station with frequency scanning of antenna pattern. Frequency range is 154—162 MHz, pulse power is 2.5 MW, pulse repetition frequency is 24 Hz, pulse duration ranges from 100 to 1000 μs. Radar digital control and acquisition system allows us to control antenna pattern and record the full form of received signal in real time during each cycle of sounding. IISR software allows us to obtain the electron density height profile (*Ne(h)*) at 120—1200 km heights.

The distinctive feature of our ASEs is small mass of exhaust products (2—11 kg). Studying ionospheric plasma response to ejection of small amounts of exhausts is of great interest. We study formation, evolution, and dynamic behavior of the ionospheric disturbances generated artificially at a given time and place. ASE results play a major role in developing theoretical and mathematical models of the LPE exhaust jets and its interaction with the ionosphere, as well as in checking the iono-

spheric models themselves. ASE sessions were conducted at known orbital conditions such as helio-geophysical conditions, and location and orientation of TSC in orbit.

During the flyby through the main IISR beam, one of two LPE is being activated. LPE are 8 orientation and mooring engines or 1 approach and correction engine (ACE). The total fuel consumption rate for 8 orientation and mooring engines is 376 g/s; and that for ACE is 1 kg/s.

Type and duration of the LPE operation vary in each session (from 5 to 11 s), as well as the start local time and direction of exhaust jets. The duration of TSC flyby through the radar beam is 15—20 s. To conduct the experiment, we selected the following options of the direction of exhaust jets:

— towards the IISR beam ('towards IISR');

— along the TSC motion ('braking');

— against the TSC motion ('acceleration');

— northward, in the plane of the TSC local horizon ('northward').

Note that the 'towards IISR' direction is practically along the geomagnetic field lines, whereas other directions are across the field.

The first ASE session (September 2007) revealed dramatic effects of exhaust jets on ionospheric plasma. When the exhaust jet was directed 'towards IISR' and the burned fuel consumption was 5.1 kg, a region of decreased (down to 40 %) electron density was formed (a 'hole' extending from the TSC altitude down to 250 km). The following years 2008 and 2009 were the years of the prolonged solar minimum. This led to the decrease in the background electron density, and the detection of weak ionospheric disturbances was limited by the IISR technical capabilities. Later experiments in 2010 were carried out at higher solar-activity level, and, consequently, at higher background *Ne*. These experiments confirm the previous conclusion that delectability of artificial irregularities depends on background *Ne*. Figure 1 shows *Ne(h)* profiles for the experiment of 1 September 2010 when ACE exhaust stream was directed northward. Dashed curve corresponds to the conditions observed 5 min before burning, thick solid curve is *Ne(h)* ~ 5 min after, and thin solid curve is *Ne(h)* ~ 10 min after. The largest depletion was ~ 28 %, about 10 min after burning. Figure 2 presents the results of the experiment of 4 September 2010 (the largest depletion was ~ 12 %, about 10 min after burning) in the same way. Thin solid horizontal line corresponds to the TSC altitude.

The sessions conducted in April and September 2010 confirmed the dependence of the disturbance delectability not only on background *Ne(h)*, but also on the LPE power. That is why only ACE was used during the last ASE sessions.

As an additional radio physical facility, a DPS-4 Digisonde was involved. To detect ionospheric disturbances caused by the TSC LPE run, we analyzed the following Digisonde data:

1) sky maps;

2) the peak electron density (N_mF2) behavior;

3) vertical sounding ionograms.

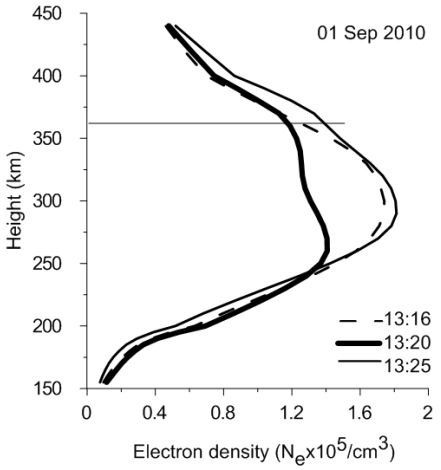

FIGURE 1. *Ne(h)* during the experiment on 1 Sep 2010. ACE runs northward at 13:20:02 UT. Amount of fuel was 7.5 kg, 364 km TSC orbit altitude.

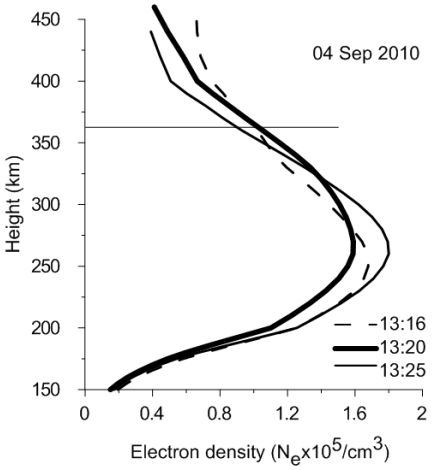

FIGURE 2. *Ne(h)* during the experiment on 4 Sep 2010. ACE runs northward at 12:59:30 UT. Amount of fuel was 7.44 kg, 363 km TSC orbit altitude.

The sky map is a map showing the locations of reflection points. Figure 3 shows the sky map obtained on 20 September 2007 from 20:21:41 to 20:50:38 UT. The white and black circles show the reflection points observed before and after the ACE run, correspondingly. Thick solid line shows the TSC trajectory with the ACE running. Before the ACE start the reflection points are close to north-south direction. This pattern is typical for southward traveling ionospheric disturbances of auroral origin. After the ACE start the reflection points are observed in the southwest sector, i. e. in the TSC trajectory sector. The effect can be explained by the reflection of sounding radio waves from the disturbances generated by the ACE run. The wide spread of the points can be associated with the interference of the disturbances of anthropogenous and natural origins.

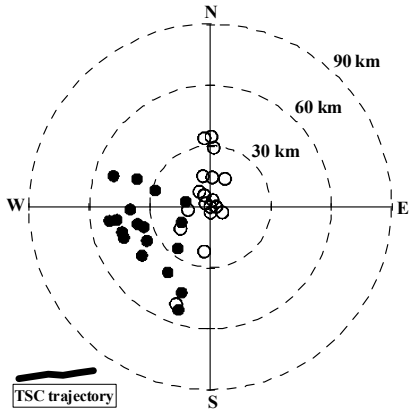

FIGURE 3. The sky map obtained on Sep 20, 2007 from 20:21:41 to 20:50:38 UT.

The first IISR observations showed that the LPE run can be followed by negative N_mF2 disturbances. We have developed the method of detecting the ionospheric effect caused by LPE run. The N_mF2 disturbances (ΔN_mF2) were calculated as the relative differences between observed N_mF2 and 31-day median N_mF2 values.

The criteria of ionospheric response detection were the following: (1) the minimum in ΔN_mF2 variations was observed after the LPE start time; (2) the delay between the LPE start time and the ΔN_mF2 minimum time were less than 45 minutes; and (3) the ΔN_mF2 disturbance amplitude were more than 5%. The method showed that the ionospheric effect was detected in ~50% of all the cases, and more often the effect was observed in the cases of the "to ISR" direction. The method did not reveal any dependence of detecting the ionospheric effect on N_mF2 and peak height values.

In 2011—2013, we conducted 6 ASE sessions, including 17 measurement cases. Directions of LPE injection jets, time and duration of ACE burns were various. Sounding pulse parameters and IISR acquisition system settings were not changed. Figure 4—6 show the 2011—2013 results. The difference between *Ne(h)* profiles obtained before and after burning does not exceed statistical uncertainty, and, hence, the engine exhaust jet effect is undistinguishable.

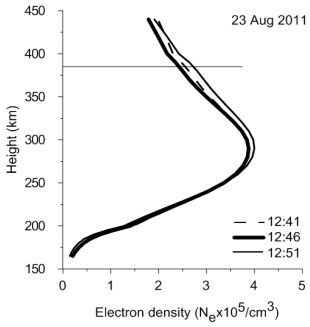

FIGURE 4. *Ne(h)* during the experiment on 23 Aug 2011. ACE runs 'braking' at 11:46:17 UT. Amount of fuel was 9.0 kg, 384 km TSC orbit altitude.

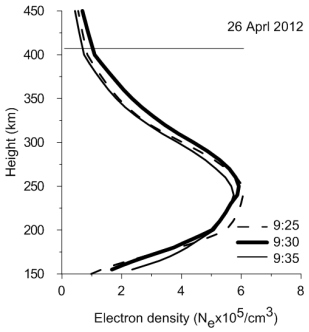

FIGURE 5. *Ne(h)* during the experiment on 26 April 2012. ACE runs 'towards IISR' at 09:27:52 UT. Amount of fuel was 9.0 kg, 407 km TSC orbit altitude.

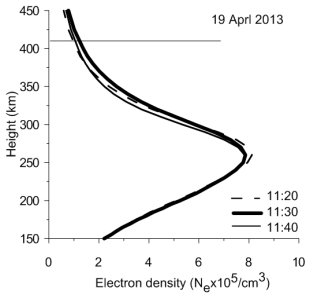

FIGURE 6. *Ne(h)* during the experiment on 19 April 2013. ACE runs 'towards IISR' at 11:29:24 UT. Amount of fuel was 9.0 kg, 410 km TSC orbit altitude.

The 2007—2013 experiments allowed us to analyze main factors affecting the conditions of the 'Radar- Progress' experiment. We found a parameter which varied throughout the experiment series and which has never been taken into account before. This factor is the TSC orbit altitude. Over the last 3 years, the ISS altitude was lifted in order to reduce the delivery time of crews and cargoes. Together with the ISS orbit, the "Progress" orbit was also lifted and, the height of the engine exhaust jets was increased, respectively. Thin solid horizontal line in Fig. 4—6 shows the TSC orbit altitude. Figure 7 shows the lift of the average TSC 'Progress' orbit altitude (from 340 km (2007) to 410.5 km (June 2013)) over the past 6 years. At the same time, the peak height of *Ne* varied from 250 to 350 km (315 km during the session on 20 September 2007 and 300 km during the session on 16 June 2013). During the latest experiment series, ACE thus burned at heights where the electron density was 1.5—2 times lower than at the peak height of *Ne*.

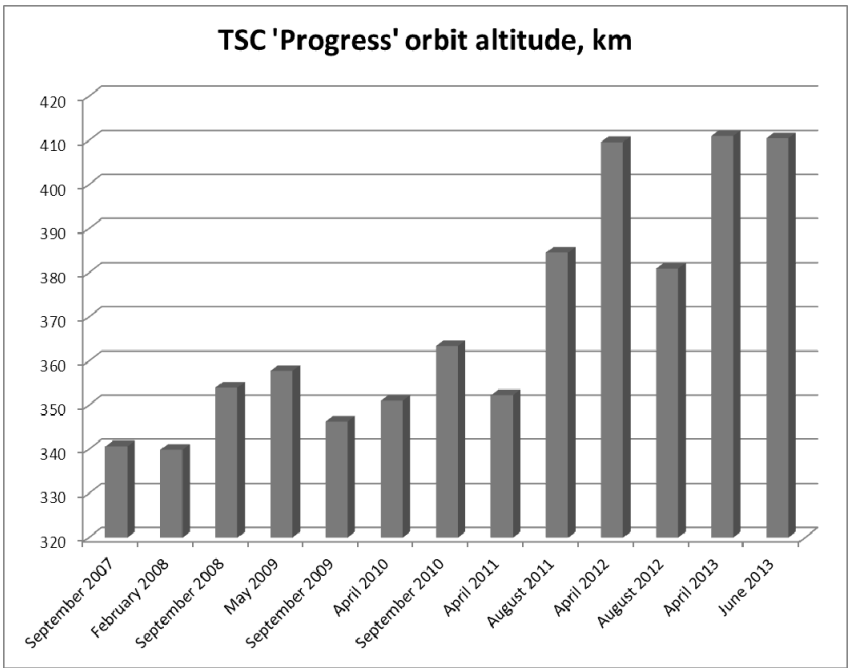

FIGURE 7. TSC "Progress" orbit altitude (2007—2013).

It should also be noted that only a part of IISR beam can be filled with TSC emission products, since the TSC "Progress" trajectory does not usually coincide with the ground IISR beam projection. Under these conditions, the TSC emission effect is weakened. Therefore, the electron density depletion was insignificant despite the relatively large burned fuel consumption.

The main results of this paper are the following. The experiment sessions in 2011—2013 showed rather weak effects of engine exhaust jet on ionospheric plasma. The difference between electron density profiles obtained before and after burning does not exceed statistical uncertainty, and the engine exhaust jet effect is undistinguishable. Delectability and disturbance parameters depend on the TSC "Progress" orbit altitude, burned fuel consumption, IISR beam direction, heliogeophysical conditions, and exhaust jet direction relative to the TSC velocity and the geomagnetic field. The most important factor affecting the "Radar-Progress" experiment is the TSC "Progress" orbit altitude. To confirm this hypothesis, it is necessary to reduce the altitude down to peak heights of electron density (250—350 km) in further experiments.

Results of this study were obtained at unique facilities of the common use centre "Angara". The study has been supported by the grant 13-05-00456-a and 13-02-00957-a of the Russian Foundation for Basic Research.

1. V. P. Lebedev, V. V. Khakhinov, F. F. Gabdullin, A. G. Korsun, E. M. Tverdokhlebova, E. A. Laletina, A. I. Manzhaley, *Studying the characteristics of the plasma environment at low-orbiting space vehicles by radar methods*, Cosmonautics and Rocket Engineering, v. 50 (1), 2008, pp. 51—60.

2. B. G. Shpynev, V. V. Khakhinov, A. V. Medvedev, A. P. Potekhin, V. P. Lebedev, E. M. Tverdokhlebova, A. I. Manzheley, *Ionospheric perturbation associated with the "Plasma-Progress" experiment at Irkutsk*, Proc. XXIX URSI GA, 2008, GP2—05.3.

3. A. P. Potekhin, V. V. Khakhinov, A. V. Medvedev., D. S. Kushnarev, V. P. Lebedev, B. G. Shpynev, *"Active space experiments with the use of the transport spacecraft "Progress" and Irkutsk IS Radar*, PIERS Proc., 2009, pp.223—227.

4. V. Khakhinov, A. Potekhin, B. Shpynev, S. Alsatkin, K. Ratovsky, V. Lebedev, D. Kushnarev, *Results of Complex Radiosounding of Ionospheric Disturbances Generated by the Transport Spacecraft "PROGRESS" Onboard Thrusters*, Proc. XXX URSI GA, 2011, HP2.15.

5. V. V. Khakhinov, B. G. Shpynev, V. P. Lebedev, D. S. Kushnarev, S. S. Alsatkin, D. S. Khabituev, *Radiosounding of ionospheric disturbances generated by exhaust streams of the transport spacecraft "Progress" engines*, PIERS Proc., 2012, pp. 1168—1171.

6. V. V. Khakhinov, A. P. Potekhin, V. P. Lebedev, B. G. Shpynev, S. S. Alsatkin, E. M. Tverdokhlebova, M. Yu. Kurshakov, A. I. Manzheley, N. I. Timofeyeva, *Remote sensing of ionospheric disturbances generated spacecraft engines exhaust jets*, Electromagnetic Methods of Environmental Studies, 2012, pp. 99—101.

7. B. S. Borisov, F. F. Gabdullin, V. I. Garkusha, A. G. Korsun, M. Yu. Kurshakov, V. A. Strashinskiy, E. M. Tverdokhlebova, V. V. Khakhinov, *Radiophysical characteristics of low-orbit spacecraft plasma environment revealed by space experiments*, Nelineinyi mir (Nonlinear World), V. 10, 2012, pp. 700—709.

8. V. V. Khakhinov, V. A. Lebedev, A. V. Medvedev, K. G. Ratovsky, *Capabilities of the Irkutsk incoherent scattering radar for space debris studies*, 5th European Conf. on Space Debris Proc. Darmstadt, Germany. ESA SP-672.

Trajectory Approach to the Schrödinger Equation, Precession of the Electron's Spin in an Atom

Nina Sotina

Lomonosov Moscow State University, recently lives in USA, c/o Neptune Station, P. O. Box 245085, Brooklyn, NY, 11224, USA.

1. Quantum Mechanics as a physical model.

The "mathematical formalism of quantum mechanics" describes many observations very well, but there are heated discussions among scientists about its physical interpretation. The various interpretations offer different approaches to the issues that arise, which include *the wave function collapse,* paradoxes *such as EPR*, and *etc.* This situation creates a lack of clarity in the formulations and definitions of quantum mechanics as a physical model.

Followers of the Copenhagen interpretation (which is the most widely accepted one) insist on the point of view that physics is the science which rests solely with measurements. In the Copenhagen interpretation joint probability of noncommuting operators cannot be used because direct measurement experiments cannot be conducted. However, it should be noted, that even proponents of the Copenhagen interpretation have difficulty explaining the results of experiments with essentially quantum effects (e. g., teleportation of polarization of the photon). In the context of the experiments the problem of interpretation of the quantum formalism is further aggravated: it is necessary to assume that**, although some properties of reality exist before measurements only potentially, however, there is a correlation between them**. If one assumes that quantum objects have a priori properties corresponding to noncommuting operators, either negative probabilities, or «hidden variables» should be introduced in quantum physics.

Historically, the issue of incompleteness in the description of physical reality by quantum mechanics was put forward by Einstein, Podolsky, and Rosen in 1935 (the EPR-paradox). They proposed the existence of «hidden variables», that is such properties of elementary particles that allow a quantum system's consistency with the deterministic theory of elementary particles. However, in about 30 years Bell advanced his famous inequalities. It followed from the violation thereof in quantum theory that the hidden variables, might be either "nonlocal", or a field of a special type wherein disturbances can spread at speeds greater than the speed of light.

2. Quantum Potential Approach by D. Bohm and its critical analysis.

D. Bohm was a proponent of the causal interpretation of quantum theory and, therefore, the existence of hidden variables. In 1952 he published two articles [1] in which an alternative to the Copenhagen interpretation was proposed, based on the notion of a particle acted on by a new kind of field that give rise to what was called "a quantum potential". Bohm assumed that an elementary particle that has a definite coordinate $\vec{r}(x, y, z)$ is moving along a definite trajectory with a definite velocity $\vec{V}(\vec{r}, t)$. He represented $\Psi(\vec{r}, t)$ in the following complex form

$$\Psi(\vec{r}, t) = A(\vec{r}, t) \exp\left(i S / \hbar\right) \tag{1}$$

Bohm substituted it into the Schrödinger equation for a single particle

$$i\hbar \frac{\partial \Psi(\vec{r}, t)}{\partial t} = -\frac{\hbar^2}{2m} \Delta \Psi(\vec{r}, t) + U(\vec{r}, t) \Psi(\vec{r}, t) \tag{2}$$

separated real and imaginary parts and obtained two equations: **1)** an equation for the probability density A^2

$$-\frac{\hbar}{2m} \frac{\partial A}{\partial t} = 2(\nabla A)(\nabla S) + A \Delta S \tag{3}$$

and **2)** Hamilton-Jacobi equation, containing not only the classical potential U, but also the quantum potential U_Q:

$$U_Q = -\hbar^2 \Delta A / 2 m A \tag{4}$$

$$\frac{\partial S}{\partial t} + \frac{(\nabla S)^2}{2m} + U + U_Q = 0 \tag{5}$$

The following condition must be added to the above equations:

$$\int |\Psi|^2 d\tau = \int A^2 d\tau \,. \tag{6}$$

The integral is taken over the entire volume of configuration space.

The Hamilton-Jacobi equation (5) defines an ensemble of particle trajectories. For any particle passing the point $\vec{r}$, the velocity vector $\vec{V}(\vec{r}, t)$ is given by

$$\vec{V}(\vec{r}, t) = \nabla S / m \tag{7}$$

Since the force on a particle now depends on function $A(\vec{r}, t)$, evaluated at an actual location of the particle, D. Bohm made a conclusion that the wave function of an individual particle is a mathematical representation of an objectively real field ("Ψ-field"). He interpreted U_Q in terms of the quantum information and nonlocally. He wrote: "*The quantum potential U_Q is different in many ways from*

classical potentials. The first key difference is that multiplication of the wave function by a constant does not change the quantum potential.... This means that its effects ***do not necessary fall off with the distance****.... The quantum information potential has the new feature of* ***nonlocality,*** *implying an instantaneous connection between distant particles*" [2].

Bohm understood A^2 as the probability distribution of particles in a statistical ensemble of similar systems. Experiments, however, show that the wave property is characteristic of each individual elementary particle. Based on these experiments the model of a quantum particle, which has both corpuscular and wave properties, was adopted. V. A. Katel'nikov proved in [3] that even if we stay within the framework of this model, we can obtain the equations for possible trajectories of a particle and velocities of this particle on the trajectories of the same form as equations (8) — (10). Note, that **under any trajectory approach one** assumes that a particle has a priori properties corresponding to noncommuting operators and hence **suggests the existence of hidden variables.**

Bohm and his followers arrived at the erroneous conclusion that U_Q is of the order of $\hbar^2$. They assumed, that in the classical limit $\hbar \to 0$ Eq. (10) becomes simple Hamilton-Jacobi equation [this incorrect statement can be even found in some textbooks]. **The Bohm's reasoning about nonlocality was also incorrect**. Now let us justify our statement.

As is known the time-independent Schrödinger equation has the form

$$(\hbar^2 / 2m)\Delta\psi(\vec{r}) + (\varepsilon - U)\psi(\vec{r}) = 0 \tag{8}$$

Substituting Eq. (1) into Eq. (8) we obtain the modified Hamilton-Jacobi equation (10) in the form

$$\frac{1}{2}mV^2 + U + U_Q = \varepsilon \tag{9}$$

If in Eq. (9) and Eq. (3) A, V and ε are calculated from the same solution of the Schrödinger equation then these equations become identities. For example, in the case of a hydrogen atom Eq. (9) leads to the identity

$$U_Q \equiv \varepsilon_n - (1/2)m_e V^2 + e^2 / r \tag{10}$$

where ε_n is the Bohr's energy level, m_e, e are the mass and the charge of an electron, and V is velocity calculated from Eq. (7). **Identity (10) demonstrates that the quantum potential is not small and is a function of r.**

Identity (10) can be proved by direct calculations of U_Q and V from the solutions of the Schrödinger equation in the case of a hydrogen atom by symbolic manipulations. As is known these solutions can be written in the form

$$\psi(r, \vartheta, \varphi) = A_{nlk}(r, \vartheta)\exp(ik\varphi).$$

Given $A_{nlk}(r,\vartheta)$, one can obtain the velocity and the trajectory of the electron's motion, as well as the quantum potential U_Q. The phase of the wave function can be written as $S/\hbar = k\varphi$, where $k = 0, \pm 1, \pm 2, ..., \pm l$. By substituting the above expression into the formula (7) for the velocity of the electron one obtain

$$\vec{V} = (\hbar k / m_e)\nabla\varphi = (\hbar k / m_e r \sin\vartheta)\vec{i}_\varphi \tag{11}$$

For $k \neq 0$ the electron travels along a circular orbit with the center on an axis, which passes through the original.

3. Derivation of the Schrödinger Equation from the theory of stability.

In 1931, N. G. Chetaev, the expert in the theory of stability, published an article [4] in which he assumed that the time-independent Schrödinger equation under condition (6) extracts from all the solutions of the Hamilton-Jacobi equation only those that satisfy the condition for stability. However, Chetaev did not obtain the Schrödinger equation exactly because he made the wrong assumption that U_Q is the potential energy of small disturbing forces. Below we give our derivation of the Schrödinger equation taking as a basis the same approach as Chetaev, but correcting his mistake. We introduce an unknown potential Φ in the Hamilton-Jacobi equation, which is the operator dependent on a trajectory. Operator Φ equals to the known function U_Q defined by Eq. (4) on the trajectories that are obtained under the classical approach to the Schrödinger equation.

The motion integral of a material particle extended with the additional potential Φ has form

$$mV^2/2 + U + \Phi = \varepsilon \tag{12}$$

Consider now the motion of a particle that it would have under the same initial conditions as in an unperturbed motion if the small disturbing forces with potential energy W are present. Eq. (12) in this case takes the form:

$$mV^2/2 + U + \Phi + W = \varepsilon \tag{13}$$

Let us call a collection of trajectories of a particle with the same energy ε and having different initial conditions a *trajectory packet*. Introduce the function

$$\psi(\vec{r}) = A(\vec{r})\exp\left(iS/\hbar\right) \tag{14}$$

where A^2 is the density of the trajectories and $S(\vec{r})$ is related to the particle's velocity by Eq. (7). Chetaev suggested that the influence of the perturbing forces on a trajectory packet at an arbitrary point of configuration space is proportional to the density of trajectories at that point. For the packet consisting of stable trajectories this influence must be minimal. That is, the disturbing forces produce minimum perturbation on the ensemble, if the following relationships

$$\int W \psi \psi^* d\tau \Rightarrow \min, \qquad \int \psi \psi^* d\tau = 1 \tag{15}$$

are satisfied. The integral is taken over the entire volume of configuration space. Substituting W from Eq. (13) into Eq. (15), we obtain the following variational problem

$$\delta \int F \, d\tau \equiv \delta \int \left(\frac{mV^2}{2} + U + \Phi - \varepsilon\right) \psi \psi^* d\tau = 0 \tag{16}$$

Functions $S(\vec{r})$ and $A(r)$ realize extrema of the definite integral (16), if they satisfy the system of two Euler—Lagrange equations. The first equation is:

$$\frac{\partial}{\partial x}\left(\frac{\partial F}{\partial S'_x}\right) + \frac{\partial}{\partial y}\left(\frac{\partial F}{\partial S'_y}\right) + \frac{\partial}{\partial z}\left(\frac{\partial F}{\partial S'_z}\right) - \frac{\partial F}{\partial S} = 0 \tag{17}$$

The second equation can obtained from Eq. (17), if in the latter we substitute S with A . Taking into account that U , ε and Φ do not change under variation of S , Eq. (17) takes the form

$$2\,(\nabla A)\,(\nabla S) + A \Delta S = 0 \tag{18}$$

Eq. (18) coincides exactly with Eq. (8) (for a stationary case). If we assume that operator Φ satisfies condition

$$\frac{\hbar^2}{2m}\frac{\Delta A}{A} = \left(A'_x \frac{\partial \Phi}{\partial A'_x} + \ldots\right) + \frac{A}{2}\left[\frac{\partial}{\partial x}\left(\frac{\partial \Phi}{\partial A'_x}\right) + \ldots\right] - \frac{A}{2}\frac{\partial \Phi}{\partial A} - \Phi \equiv \Pi - \Phi \tag{19}$$

on the trajectories, that are solutions of the varational problem, then the second Euler—Lagrange equation coincides exactly with Eq. (9). Since the set of solutions of Eq. (9) is a subset of solutions of Eq. (12), $\Pi = 0$ on the trajectories that are obtained from the trajectory approach to the Schrödinger equation. System of two equations (18) and (9) along with substitution (14) are equivalent to the time-independent Schrödinger equation.

Thus, **the Schrödinger equation** along with conditions (6) and $\Pi = 0$ **extracts from all the solutions of the Hamilton-Jacobi equation** (12), that contains two potentials: the classical potential U and an unknown potential Φ (which is the operator dependent on a trajectory), **only those solutions that satisfy the necessary conditions for stability**. **Among these solutions** (even within the same packet) **there can be "extra" solutions that do not satisfy the sufficient conditions of stability and, therefore, are not realized in nature.**

4. Precession of the electron's spin in an atom.

The mysterious potential Φ is obviously a mathematical representation of the physical properties of «hidden variables». Below, we will make an attempt to understand at least to some extend these properties.

In some cases the equation of motion of the object's center of mass and the equation of motion about the center of mass may not be independent, and because of that they cannot be analyzed separately. In such cases Hamilton's principal function as well as the generalized integral of motion depend on variables corresponding to both rotational and translational motion. If we search only for the motions for which (1) the energy of motion of the center of mass is equal to zero, and (2) the motion with respect to the center of mass reduces to the fast precessional motion (for example, the precession of the electron's spin), then we arrive to the generalized integral of motion (9) which was obtained from the Schrödinger equation. We demonstrate this procedure now for the case of **a hydrogen atom.**

We set $\sin\vartheta = 1$ in the formula for the velocity of the electron (11) and substitute this formula into identity (10); then, we substitute the resulting expression for U_Q into Eq. (9). Eq. (9) for a hydrogen atom can be represented in the form

$$\frac{m_e V^2}{2} - \frac{\hbar^2 k^2}{2 m_e r^2} + \varepsilon_n = \varepsilon \tag{20}$$

In Eq. (20) along with the term that characterizes the energy of the center of mass, which is equal to zero for the solutions of the Schrödinger equation, there is an extra term ε_n associated with the motion with respect to the center of mass. It can be rigorously proved that such extra term appears in the case of the fast precessional motion with a small precession angle. For the precession of the electron's spin this term is $|\varepsilon_n| = \hbar\omega_e / 2$.

If in the quantum vacuum the electron's motion creates a structure (a quasi-particle) having spin $\hbar$, then from the law of conservation of the angular momentum the following equality holds

$$|\varepsilon_n| = \hbar\omega_e / 2 = \omega_p \cdot \hbar \tag{26}$$

where ω_p is the angular frequency of the vacuum structure's spin precession [5]. Under this approach frequencies of the quasi-particle's spin precession ω_p equal to the natural frequencies of an atom.

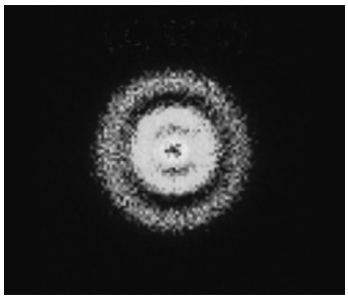

Note, that in Eq. (20) we limit our derivations to the cases of the motions along circular orbits with the center at the origin ($\sin\vartheta = 1$), even though Eq. (20) is valid for any circle with the center on z axis. Since the motion on these trajectories satisfies only the necessary condition for stability, among these trajectories there might be "extra" trajectories that are not stable. Intuitively it is clear that the best candidates of being stable are the motions with the center at the origin. The picture of a hydrogen atom, obtained with a quantum utilizing the photoionization method (Institute AMOLF, The Netherlands) can be considered as a partial proof of the above reasoning.

Note that among all orbits with the center at the origin there are Bohr orbits. For the Bohr orbits ($r = r_B$) Eq. (9) can be represented in the following form $(1/2)m_e V^2 - e^2 / r_B + \varepsilon_n - \varepsilon_k = \varepsilon_n$. The quantum potential in this case equals the energy of precessional motion: $U_Q = \varepsilon_n - \varepsilon_k$

Conclusion. The approach presented above gives us a mathematical base with which to suggest that the spin of the electron is precessing in an atom. It also opens a new direction to the study of the nature of hidden variables.

Acknowledgments. I would like to thank Nadia Lvov and Vladimir Bychkov for valuable comments.

References

1. D. Bohm, Phys. Rev., 85 (2), 1952, pp. 166—193.
2. D. Bohm & B. J. Hiley, Foundations of Physics, 14 (3), 1984, pp. 255—274.
3. V. A. Kotel'nikov, Phys. — Usp., 52, 2009, pp. 185—190.
4. N. G. Chetaev, *Stability of Motion. Proceedings in Analitical Mechanics,* Moscow, 1962, pp. 245—249 [in Russian].
5. N. Sotina, *Reports of the 16th RCCNT&BL, Dagomys, June 2009*, Moscow, 2010, pp. 172—177 [in Russian].

E-2

Reaction of Associative Ionization $N + O \rightarrow NO^+ + e^-$ in Slow Collisions of Atoms

Georgy K. Ozerov[1], Sergey O. Adamson[2], Nikolay S. Malyshev[1], Gennady V. Golubkov[1], Maxim G. Golubkov[1]

[1] N. N. Semenov Institute of Chemical Physics, Russian Academy of Sciences, Kosygin str 4, Moscow 117977, Russian Federation
[2] Department of Chemistry, M. V. Lomonosov Moscow State University, 119991,Moscow 1, GSP-1, 1—3 Leninskiye Gory, Russian Federation

Introduction

The reaction of associative ionization (AI) of nitrogen and oxygen atoms

$$N^{**} + O \rightarrow NO^{**} \rightarrow NO^+(^1\Sigma^+) + e^-, \quad (1)$$

is one of the most important processes in the E and D layers of terrestrial ionosphere responsible for low-temperature plasma charge formation during the periods

of enhanced solar activity [1]. The reaction (1) passes through the stage of intermediate Rydberg complex NO^{**} formation. This is multichannel process since it follows with participation of Rydberg, dissociative and valence states of the system under consideration.

Most model theoretical studies of the AI process have been carried out without regard for the set of quasi-crossings, which are inspissated before the potential curve of quasimolecule exits trough the boundary of molecular ion continuum. Attempts to take them into account within the framework of traditional approaches based on an individual consideration of each quasi-crossing failed for highly excited states [2]. In this connection, a diffusion approach to the process of collision ionization of excited atoms was developed, according to which the diffusion along the energy states of quasimolecule occurs in elementary collision event [3]. Nevertheless, the most convenient theoretical method for the investigation of the dynamics of AI reaction currently is the multichannel quantum defect theory (MQDT). Thus, the first time the resonance structure of differential and total cross sections for the endothermic reaction (1) were obtained by MQDT in [4].

In this paper the partial and total cross sections as well as the temperature dependence of the rate constant for the reaction of AI of nitrogen and oxygen atoms were calculated in the framework of MQDT. The potential energy curves and nonadiabatic coupling function which were calculated (or constructed) by the method of configuration interaction with a set of initial configurations were used to construct the functions of quantum defect. The results were compared with existing experimental data.

Integral variant of MQDT. General equations of the theory

Let us use MQDT [5] in presenting of the formal theory of scattering of $X + Y^*$ atoms with the transition to the final $e^- + XY^+$ state of the system. Hamiltonian of the system under consideration in atomic units ($\hbar = m_e = e = 1$) can be represented in form:

$$\mathbf{H} = \mathbf{H}_0 + \mathbf{V}, \tag{2}$$

$$\mathbf{H}_0 = -\frac{1}{2}\Delta_r - \frac{1}{r} + \mathrm{H}_q, \tag{3}$$

where $-\frac{1}{2}\Delta_r$ is the kinetic energy operator of weakly bounded electron, **r** is its coordinate relative to the center of mass of positively charged molecular ion core XY^+, $\mathbf{H}_q$ is the molecular Hamiltonian depending on the coordinate set $\{\mathbf{x}\}$ of the internal core electrons, $q = \{v, N\}$ is the set of vibrational *v* and rotational *N* quantum numbers of the ionic core. The zero-order Hamiltonian $\mathbf{H}_0$ is chosen in such a way that all interactions in dissociative $X + Y$ configurations are taken into ac-

count exactly, while for the scattering $e^- + XY^+$ channel the Coulomb part of interaction $V^C = -\frac{1}{r}$ is contained only. Thus in the total Hamiltonian (2) operator $\mathbf{V} = \mathbf{V}^{nC} + \mathbf{V}^{CI}$ includes a non-Coulomb interaction $\mathbf{V}^{nC}$ of the electron with the ionic core and interaction $\mathbf{V}^{CI}$ between $e^- + XY^+$ and $X + Y^*$ configurations, which is responsible for the nonadiabatic transitions between them.

Solution of the AI problem is reduced to the definition of the T-operator of collisions, which satisfies the system of rearranged Lippmann-Schwinger equations [5], i. e.

$$\mathbf{T} = \mathbf{t} + \mathbf{t}\,(\mathbf{G} - \mathbf{G}_0)\,\mathbf{T}, \tag{4}$$

$$\mathbf{t} = \mathbf{V} + \mathbf{V}\mathbf{G}_0\mathbf{t}, \tag{5}$$

where $\mathbf{G} = (E - \mathbf{H}_0)^{-1}$ is Green's operator with switched off interaction $\mathbf{V}$, $\mathbf{G_0}$ is an operator weakly depended on the total energy E. Let's denote the basic functions of the Hamiltonian $\mathbf{H}_0$ as $|q\rangle$ for the $e^- + XY^+$ and $|\beta\rangle$ for the dissociative states.

The Green's operator $\mathbf{G}$ in (7) is represented by the contributions of noninteracting $e^- + XY^+$ and $X + Y^*$ configurations and has the form

$$G(E) = \sum_i |i\rangle G^C(E - E_i)\langle i| + \frac{1}{\pi}\sum_\beta \int \frac{|\beta\rangle\langle\beta|}{E - E_\beta + i\gamma}\, dE_\beta. \tag{6}$$

Here E_i and $|i\rangle$ are excitation energies and corresponding wavefunctions of the ion core XY^+, respectively, G^C is Green's function describing electron motion in a Coulomb field. In spherical harmonic representation it can be written as

$$G^C(\mathbf{r}, \mathbf{r}', \varepsilon) = \sum_{lm} Y^*_{lm}\left(\frac{\mathbf{r}}{r}\right) G^C_l(r, r', \varepsilon) Y_{lm}\left(\frac{\mathbf{r}'}{r'}\right), \tag{7}$$

where $Y_{lm}\left(\frac{\mathbf{r}}{r}\right)$ is the spherical function, and ε is the electron energy. Important is the possibility of separating the radial Coulomb Green's function into parts strongly and weakly dependent on the energy [5], i. e.

$$G^C_l(r, r', \varepsilon) = \operatorname{ctg}\pi\nu(\varepsilon)\,|\varphi_{\varepsilon l}(r)\rangle\langle\varphi_{\varepsilon l}(r')| + g(r, r', \varepsilon). \tag{8}$$

The first term in (8) at $\varepsilon < 0$ corresponds the position of the Coulomb levels $\nu(\varepsilon) = 1/\sqrt{-2\varepsilon}$ and is expressed in terms of regular at zero Coulomb wavefunctions $\varphi_{\varepsilon l}(r)$ normalized as

$$\langle\varphi_{\varepsilon l}(r)|\varphi_{\varepsilon' l}(r)\rangle = \pi\delta(\varepsilon - \varepsilon'). \tag{9}$$

Excluding the smooth on energy real part from (8) we can obtain

$$\mathbf{G}_0(E) = \sum_{i,lm} |i\rangle Y_{lm}^*\left(\frac{\mathbf{r}}{r}\right) g_l(r,r',E-E_i) Y_{lm}\left(\frac{\mathbf{r}'}{r'}\right)\langle i| + \frac{1}{\pi}\sum_{\beta} P\int \frac{|\beta\rangle\langle\beta|}{E-E_\beta} dE_\beta, \quad (10)$$

where P means the principal value of the integral, we have the following expression for the collision **T**-operator:

$$\mathbf{T} = \mathbf{t} + \mathbf{t}\left\{\sum_q |q\rangle\langle q| \operatorname{ctg}\left[\frac{\pi}{\sqrt{-2\varepsilon_q}}\right] - i\sum_{\beta}|\beta\rangle\langle\beta|\right\}\mathbf{T}. \quad (11)$$

Here $\varepsilon_q = E - E_q$ is the electron energy in the q channel of motion, E_q is the energy of vibrational and rotational excitation of ion core. In open Rydberg channels, where $\varepsilon_q \geq 0$, the functions should be replaced by $\operatorname{ctg}\left[\pi/\sqrt{-2\varepsilon_q}\right] \to -i$. Because of linearity and separability of the kernel, integral equation (11) can be reduced to a system of linear algebraic equations for the elements of **T**-matrix, in which dissociative channels are considered along with the scattering channels. Moreover, the strong nonadiabatic coupling of the electronic and nuclear motions responsible for formation a heterogeneous continuum of intermediate Rydberg states interacting with the decaying dissociative terms is taken into account consistently [6]. These important properties follow from the formal scattering theory and automatically provide a unitarity of **S**-matrix on an arbitrary basis set.

Basis states and elements of reaction t-matrix

The basis wavefunctions $|q\rangle$ of the Rydberg configuration in the laboratory coordinate system with consideration of the vibrational and rotational motion of the nuclei are

$$|q\rangle = |JMlN\,v\rangle = \varphi_{\varepsilon_v l}(r)\varphi_i(\mathbf{x})\chi_v^J(R)\Phi_{lN}^{JM}\left(\frac{\mathbf{r}}{r},\frac{\mathbf{R}}{R}\right), \quad (12)$$

where φ_i is the electronic wave function of the ion, $\{\mathbf{x}\}$ is the set of coordinates of the inner electrons, and $\chi_v^J(R)$ — is the vibrational wavefunction of the ion. The total angular wavefunction $\Phi_{lN}^{JM}\left(\frac{\mathbf{r}}{r},\frac{\mathbf{R}}{R}\right)$ of the system is defined in the representation with total angular momentum *J,* its projection *M*, momentum of rotational motion of nuclei *N,* so that in the case of *LS*-coupling the σ-configuration for ion XY^+ takes the form

$$\Phi_{lN}^{JM}\left(\frac{\mathbf{r}}{r},\frac{\mathbf{R}}{R}\right)=\sum_{m}Y_{lm}\left(\frac{\mathbf{r}}{r}\right)Y_{N,M-n}\left(\frac{\mathbf{R}}{R}\right)\left(l\,N\,m\,M-n\,|\,J\,M\right),\qquad(13)$$

where $\left(l\,N\,m\,M-n\,|\,J\,M\right)$ are vector addition coefficients.

In the dissociative configuration $X+Y^{*}$ the electrons are fast enough, so their motion is quantized in the field of the fixed nuclei and is described in the adiabatic approximation. To calculate the configuration interaction matrix elements it is necessary to expand the channel wave functions (12) into the adiabatic basis, i.e. to change in the coordinate system associated with the molecule, in which the projection Λ of the electron angular momentum on the molecular axis is fixed.

The states of diatomic molecules in this basis are classified according to the values of J and Λ. Angular momentum l of the electron here in general is not preserved. The total wave function in the adiabatic approximation is a superposition of the channel basis functions

$$\left|JM\rho\Lambda v\right\rangle=\sum_{l}a_{l\rho}^{J\Lambda}\left|JMl\Lambda v\right\rangle,\qquad(14)$$

where ρ is the quantum number that specifies the effective angular momentum of the electron in accordance with the largest coefficient of the expansion $a_{l\rho}^{J\Lambda}$. Quite similarly are defined the wave functions of the dissociative configuration $\left|\beta\right\rangle$.

To calculate the elements $t_{lNv,l'N'v'}^{J}$ and $t_{lNv,l'\beta\Lambda}^{J}$ in the system of equations (4)-(5) responsible for nonadiabatic rovibronic and configuration transitions, it is convenient to introduce the auxiliary operator

$$\bar{\mathbf{t}}=\mathbf{V}+\frac{1}{\pi}\sum_{q}P\int\mathbf{V}\frac{\left|q\right\rangle\left\langle q\right|}{E-E_{q}-\varepsilon}\bar{\mathbf{t}}\,d\varepsilon,\qquad(15)$$

which describes the interaction of the electron with the ion core in an isolated Rydberg configuration $e^{-}+XY^{+}$. Electron parts of matrix elements of the $\bar{\mathbf{t}}$ operator in the mixed basis (14) are diagonal in respect to ρ and Λ and are expressed via R-depended diabatic quantum defects $\bar{\mu}_{\rho\Lambda}$ as

$$\bar{t}_{\rho\Lambda,\rho'\Lambda'}^{J}(R)=-\mathrm{tg}\,\pi\,\bar{\mu}_{\rho\Lambda}(R)\,\delta_{\rho\rho'}\,\delta_{\Lambda\Lambda'}.\qquad(16)$$

As long as the adiabatic basis $\left|JMl\Lambda v\right\rangle$ is related to channel basis (14) through the unitary transformation [7] as

$$\left|JMl\Lambda v\right\rangle=\sum_{N}U_{N\Lambda}^{Jl}\left|JMlNv\right\rangle,\qquad(17)$$

For the $\bar{t}^J_{lNv,l'N'v'}$ elements we have

$$\bar{t}^J_{lNv,l'N'v'} = -\sum_{\rho\Lambda} a^{J\Lambda}_{l\rho} U^{Jl}_{N\Lambda} \left\langle \chi^J_v \middle| \operatorname{tg} \pi\mu_{\rho\Lambda}(R) \middle| \chi^J_{v'} \right\rangle a^{J\Lambda}_{\rho l'} U^{Jl'}_{\Lambda N'}, \tag{18}$$

where $U^{Jl}_{N\Lambda}$ is the Fano rotation submatrix. Based on the pattern of Rydberg terms and the information about the adiabatic wavefunctions (14) as a basis, one can define by (18) a complete set of matrix elements $\bar{\mathbf{t}}$ -operator.

According to (5) and (16) the reaction matrix **t** satisfies the equation:

$$\mathbf{t} = \bar{\mathbf{t}} + \bar{\mathbf{t}} \frac{1}{\pi} \sum_{\beta} P \int \frac{|\beta\Lambda\rangle\langle\beta\Lambda|}{E - E_\beta} \mathbf{t}\, dE_\beta . \tag{19}$$

From this equation with regard to the smallness of the configuration coupling one can obtain the following expressions for the matrix elements:

$$t^J_{lNv,l'N'v'} = \bar{t}^J_{lNv,l'N'v'} + \frac{1}{\pi} \sum_{\beta} P \int \frac{V^{CI}_{lNv,\beta\Lambda} V^{CI}_{\beta\Lambda,l'N'v'}}{E - E_\beta} dE_\beta , \tag{20}$$

$$\begin{aligned} t^J_{lNv,\beta\Lambda} = V^{CI}_{lNv,\beta\Lambda} &+ \frac{1}{\pi} \sum_{l'N'v'} P \int \frac{\bar{t}^J_{lNv,l'N'v'} V^{CI}_{l'N'v',\beta\Lambda}}{E - E_\beta} dE_\beta \\ &+ \frac{1}{\pi} \sum_{\beta' \neq \beta, \Lambda'} P \int \frac{\bar{t}^J_{lNv,\beta'\Lambda'} V^{CI}_{\beta'\Lambda',\beta\Lambda}}{E - E_\beta} dE_\beta , \end{aligned} \tag{21}$$

$$t^J_{\beta\Lambda,\beta'\Lambda'} = V^{CI}_{\beta\Lambda,\beta'\Lambda'} . \tag{22}$$

The values of configuration interaction V^{CI} are determined by specific peculiarities of the quasimolecule electron structure and typically are small in comparison with unity. The elements $t^J_{lNv,l'N'v'}$ in (20) consist of two terms, where the first one refers to the interaction with the ion core, whereas the second one to the mixing of Rydberg series with the dissociative continuum. The coupling between Rydberg and dissociative channels (21) is defined similarly. Direct coupling among dissociative channels play leading role in inelastic transitions. Since the diagonal elements $t^J_{\beta\Lambda,\beta\Lambda}$, which describe elastic scattering in the initial dissociative channels, are of second order of magnitude of configuration interaction, and therefore they are omitted here.

The potential energy curves of excited states of *NO* molecule

In the present work the potential energy curves and one-electrion properties calculations were pefrormed in framework of the internally contracted multireference configuration interaction (MRCISD) and Davidson-corrected multireference configuration interaction (MRCISD + Q) methods [8—11], implemented in MOLPRO package [12]. Given in the region R ≤ 2.5 a. u. excited doublet states (e. g., $^2\Phi$, $^2\Delta$ and $^2\Sigma^-$ symmetries),) reveals autoionizing character, to construct MRCI wave functions the orbitals obtained in RHF for the $X^1\Sigma^+$ state of the ion NO^+ were used. One electron basis set was generated by augmenting 6—311G ++(3df,3dp) basis set [13—15] with diffusive s- and p-type functions. In the basis set the functions with ζ_s = 0.0203 and ζ_p = 0.0203 were included at the nitrogen atom and with ζ_s = 0.0278 and ζ_p = 0.0278 type were did at oxygen atom, respectively. MRCI calculations were performed with frozen 1s and single and double excited from 2s orbitals.

In MCSCF calculations orbitals 5σ-7σ, 1π-3π [3330] were used to construct the active space. To reduce computational cost the selection procedure to produce the effective model Hamiltonian was utilized [16—17]. The preliminary calculations shows that the selection cutoff value ω ≤ 0.01 is sufficient to evaluate the energies differences (T_e) and equilibrium internuclear distances (R_e) of the 1—$2^2\Pi$, 1,$2^2\Sigma^+$ as well as the dipole moment of the ground state and the moment of transition between $X^2\Pi$-1,$2^2\Sigma^+$ states. All calculations were carried out with the cutoff ω = 0.005. And for estimating electronic matrix elements of the nonadiabatic coupling the finite difference three point method with the step 0.002 a. u. was used.

The diabatic potential energy curves for the ground state of ion NO^+, first Rydberg state corresponding to the $p\pi^2\Pi\left(X^2\Sigma^+\right)$ series of intermediate complex, and dissociative excited states of *NO* molecule are presented in Fig. 1. The dependencies for the $A'^2\Sigma^+$ and $I^2\Sigma^+$ states are taken from works [18] и [19], respectively.

To describe the reaction (1) is sufficient to consider the five dissociative states $A'^2\Sigma^+$, $I^2\Sigma^+$, $B^2\Pi$, $L^2\Pi$, and $B'^2\Delta$, because configuration interaction for the state $L'^2\Phi$ is small, and its contribution can be neglected. The state $A'^2\Sigma^+$ interacts with the Rydberg $p\sigma$ series, the $I^2\Sigma^+$ state couplings with $s\sigma$ and $d\sigma$ series, state $B'^2\Delta$ interacts with $d\delta$ series, and $B^2\Pi$ and $L^2\Pi$ with $p\pi$ series.

The configuration $A'^2\Sigma^+$ correlating with the ground states of atoms $N(^4S)+O(^3P)$ is populated due to nonadiabatic transition from the state $I^2\Sigma^+$. Since at considered energy range the Rydberg series with vibrational quantum number v > 10 make a negligible contribution to the total cross section of the reaction (1), we can restrict ourselves to the Morse potential when describing ion NO^+ [4].

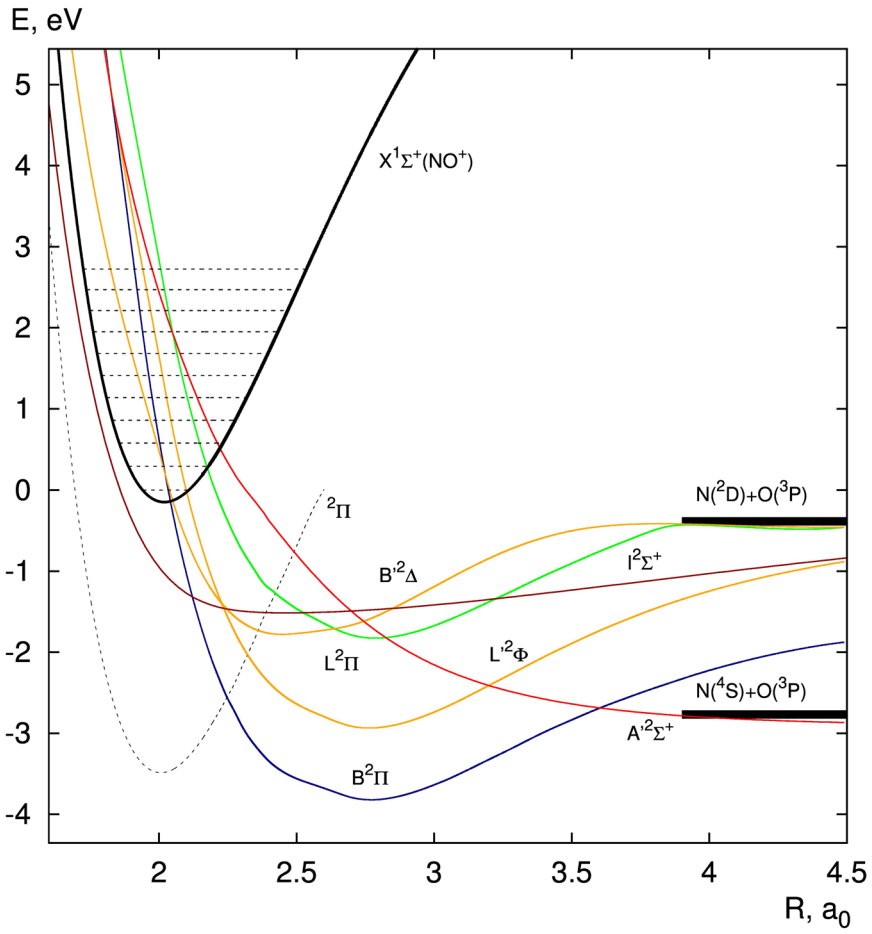

FIGURE 1. Dependencies of diabatic potential energy curves of NO molecule on internuclear distance R. Energies are measured from the ground state of the ion $NO^+(X^1\Sigma^+)$. The $I^2\Sigma^+$, $B^2\Pi$, $L^2\Pi$, $B'^2\Delta$, and $L'^2\Phi$ terms converge to a limit of separated atoms limit $N(^2D)+O(^3P)$ with an energy $E=-0.38$ eV. The $A'^2\Sigma^+$ term correlates with the limit of ground state atoms $N(^4S)+O(^3P)$ with an energy $E=-2.76$ eV. The dotted line depicts the first Rydberg $p\pi\ ^2\Pi\left(X^1\Sigma^+\right)$- state of *NO* molecule.

The matrix elements of electron coupling of Rydberg and dissociative states are presented in Fig. 2. By virtue of data represented in Fig. 2 it should be noted that main contribution is caused by couplings of Rydberg $p\pi$-series with Π- states and $d\delta$-series with $B'^2\Delta$ state.

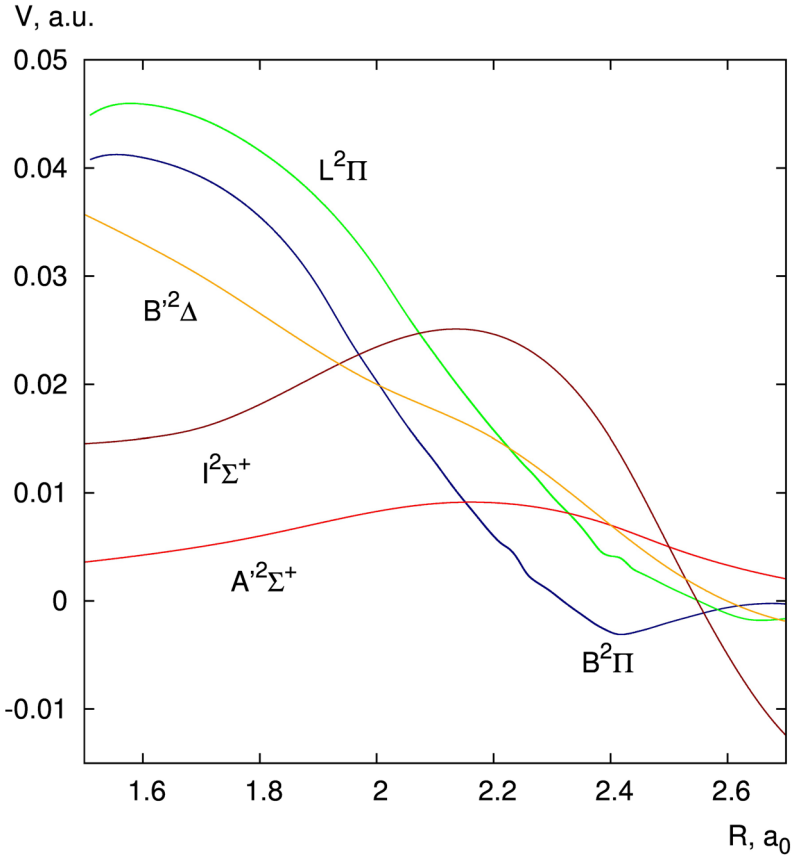

FIGURE 2. Dependencies of electronic matrix elements of configuration interaction V of the Rydberg and dissociative states on the internuclear distance R.

Quantum defects of *NO* molecule

Adiabatic quantum defects as functions of internuclear distance R for Rydberg $p\pi$ -series were recovered by the data of diabatic potential energy curves

$U_{l\lambda}(R)$ for the first Rydberg $p\pi\ ^2\Pi(X^1\Sigma^+)$ state and $U_{ion}(R)$ for ion $X^1\Sigma^+$ state with using the relation

$$\mu_{nl\lambda}(R) = n - \frac{1}{\sqrt{2(U_{ion}(R) - U_{l\lambda}(R))}}, \tag{23}$$

where l and λ are the angular momentum of the Rydberg electron and its projection on the internuclear axis. The results are presented in Fig. 3.

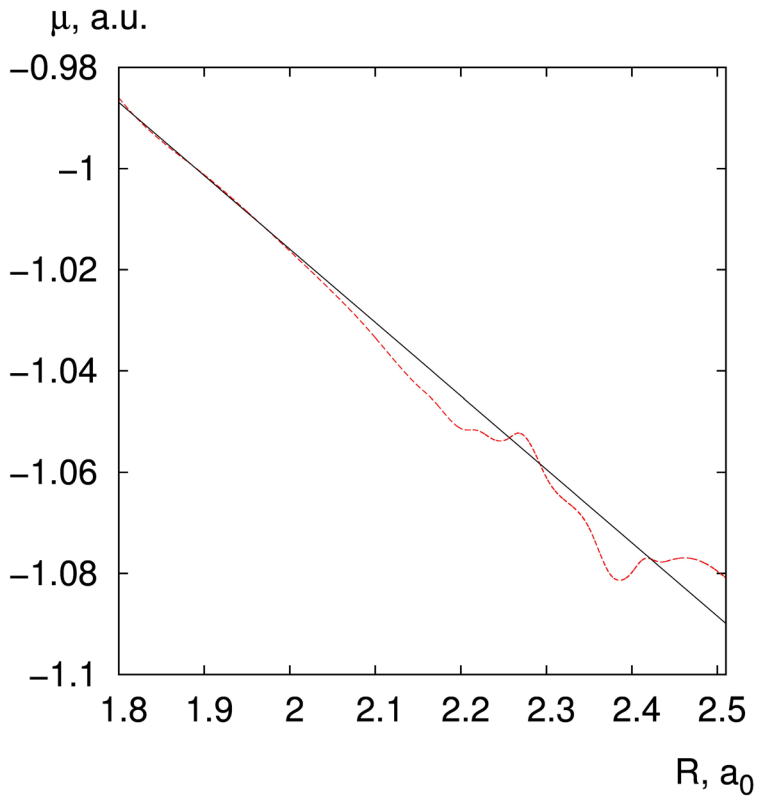

FIGURE 3. Adiabatic quantum defect of Rydberg $p\pi$ series as function of internuclear distance R. Red dotted line is referred to calculation (23), black full line represents linear interpolation.

The quantum defect data for the other series were taken from the works [9—11], where the linear interpolation for the quantum defect functions was assumed

$$\mu(R) = \mu(R_e^+) + \left.\frac{d\mu(R)}{dR}\right|_{R_e^+} (R - R_e^+), \tag{24}$$

where $R_e^+ = 2.0195\, a_0$ is the equilibrium distance of the NO^+ ground state.

The data on adiabatic quantum defects which were used in our calculations are represented in Table 1.

Partial and total cross sections of AI reaction $N + O \to NO^+ + e^-$

As an example, let us consider the case of an endothermic reaction

$$N(^2D) + O(^3P) \to NO^{**} \to NO(^1\Sigma^+) + e^- . \tag{25}$$

Therefore, one can ignore the nonadiabatic coupling with the rotational motion in the intermediate Rydberg complex NO^{**}, fix the direction of the molecular axis in determining the **T**-operator, and average over the orientations at the final stage of the calculation. As a result, the total cross section of the reaction may be written as [23]:

$$\sigma_{AI}(E) = \frac{2\pi}{M_c} \sum_{\beta} \frac{g_\beta}{E + E_\beta} \left[\sum_{\substack{v=0 \\ j=0}}^{\infty} (2j+1) \left\langle \left| T^j_{\beta v} \right|^2 \right\rangle \right], \tag{26}$$

where M_c is the reduced mass of colliding atoms, E is the total energy of the system measured from the reaction threshold E_β, j is angular momentum of the relative motion of the nuclei, g_β is the statistical weight of the dissociative β - channel. Since near the ionization threshold the matrix elements $T^j_{\beta v}$ do not depend on j, they can be taken out of the sum, and finally the expression for the total cross section of the reaction can be presented in the form:

$$\sigma_{AI}(E) = 4\pi E \sum_{\beta} \frac{g_\beta R_\beta^2}{E + E_\beta} \left\langle \left| T^j_{\beta v} \right|^2 \right\rangle, \tag{27}$$

where R_β is the intersection point of ion and dissociative β -terms.

TABLE 1. The values of adiabatic quantum defects and their first derivatives for Rydberg series of the NO^{**} molecule.

Rydberg series	$\mu(R_e^+)$	$\mu'_R(R_e^+)$
$s\sigma\ I^2\Sigma^+$	1.123 [20]	0.035 [20]
$d\sigma\ I^2\Sigma^+$	– 0.058 [20]	– 0.052 [20]
$p\sigma\ A'^2\Sigma^+$	0.641 [21]	0.12 [21]
$d\delta\ B'^2\Delta$	0.041 [22]	– 0.029 [22]

In accordance with the general rules, the convergence of two atoms $N(^2D)$ and $O(^3P)$ should correlate with the nine valence states with the spin of 1/2, the spin weight of which is equal to 1/3. These states include: three nondegenerate states (two $^2\Sigma^+$ and one $^2\Sigma^-$) and six doubly degenerate states (respectively, three $^2\Pi$, two $^2\Delta$ and one $^2\Phi$), the statistical weights of which are $g_\beta = s_\beta / 45$, where s_β is the degeneracy.

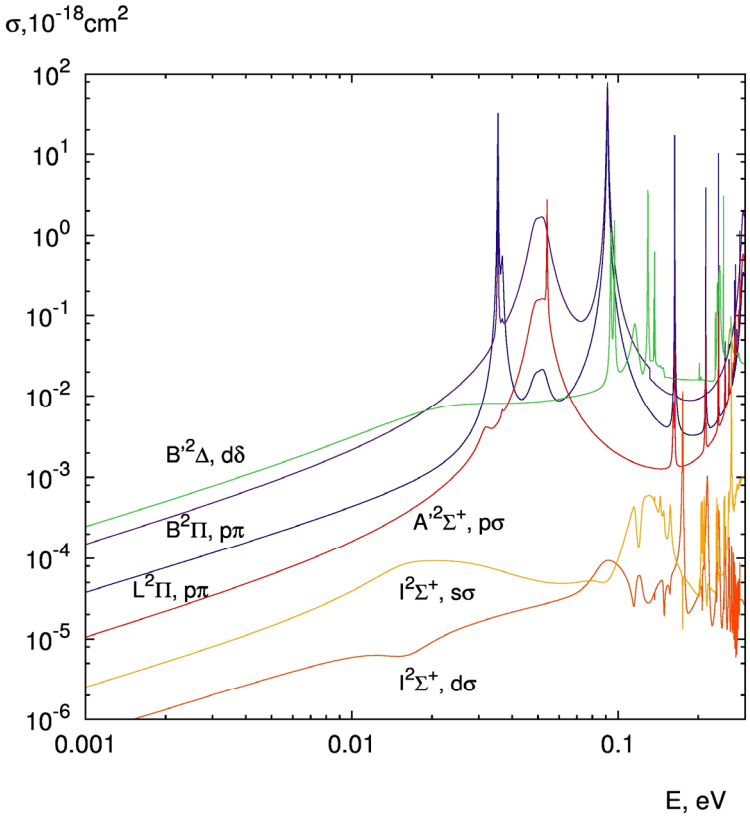

FIGURE 4. Partial cross sections of the reaction (25) with respect to the kinetic energy of the colliding atoms for different dissociative channels.

The dependencies of partial cross section of reaction (25) on threshold energy E at the range of 0—0.3 eV are shown in Fig.4 In the calculation scheme 11 vibrational states with $v = 0 - 10$ were included. These cross sections have a pronounced resonance structure, which is formed as a result of a multi-channel interaction among autoionization states of the intermediate complex NO^{**} and dissociative β-continua. According to data presented in Fig.4, it can be assumed that dissociative states $A'^2\Sigma^+$, $B^2\Pi$, $L^2\Pi$, and $B'^2\Delta$ make the main contribution to the total cross section. The contribution of $I^2\Sigma^+$ state should be neglected.

The energy dependence of the total cross section for reaction (25) is presented in Fig.5. The results are compared with the experimental data [24] obtained in the merged beam technique. The total cross section is characterized by the presence of step jumps when crossing the threshold of each open channel. Such behavior, according to [25], is reproduced by averaging the expression (26) over the Rydberg resonances and agrees well with the experimental data.

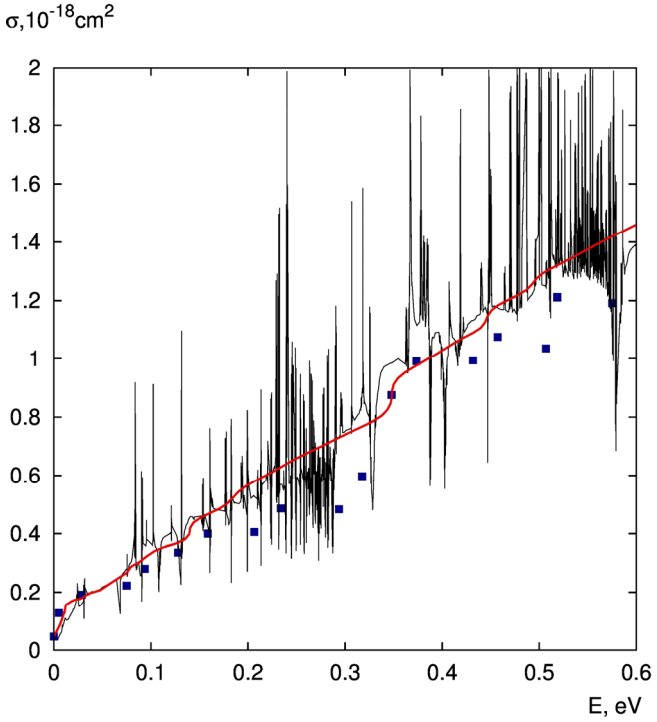

FIGURE 5. Total cross section of the reaction (25) with respect to energy E, which is measured from ground state of ion $NO^+(X^1\Sigma^+)$. Black solid line represents calculations with using the relation (25), dark-blue squares are the experimental data [24], and red solid line corresponds to early calculations of [25].

The rate constant of the AI reaction $N+O\rightarrow NO^+ + e^-$

The temperature dependence of the reaction (25) rate constant is obtained as a result of thermodynamic averaging of the total reaction cross section over reagent states, i. e.

$$k_{AI}(T) = \sqrt{\frac{8}{\pi M_c T^3}} \int_0^\infty \sigma(E) \exp\left(-\frac{E}{T}\right) E\, dE\,, \tag{28}$$

where T is the translational temperature of the colliding atoms. The resulting rate constant is calculated using (28) and is shown in Fig.6.

This dependence for $T < 1000$ K can be interpolated by the expression:

$$k_{AI}(T) = 4.747 \cdot 10^{-13} \exp\left(-0.01432 / T\right) \text{ cm}^3/\text{sec} \tag{29}$$

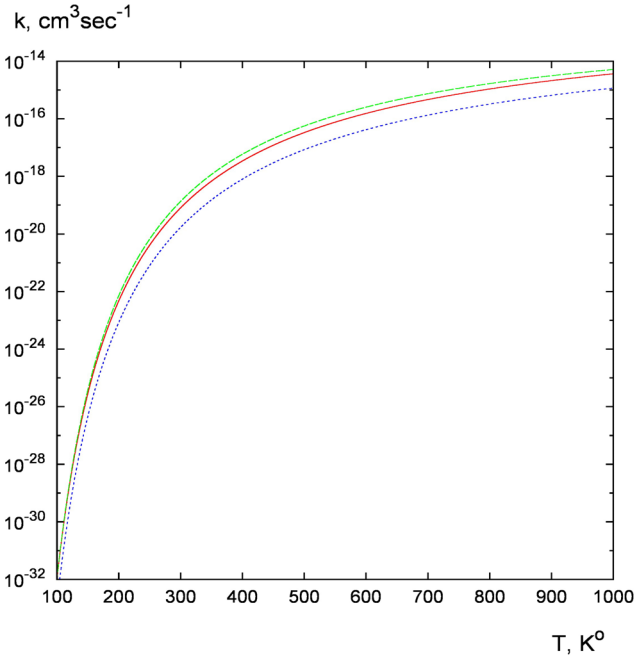

FIGURE 6. Temperature dependencies of the rate constants of reaction (25). Red solid line is the calculation performed by the formula (28), green dashed line is the interpolation for $T < 1000$ K calculated by formula (29), blue dots is the interpolation (30) for $T > 4000$ K taken from Ref. [4].

The interpolation of (28), which should be used in the case of higher temperatures $T > 4000$ K has the form [4]

$$k_{AI}(T) = 8.378 \cdot 10^{-11} T^{1/2} (0.01396 + 2T) \exp\left(-0.01439 / T\right) \text{ cm}^3/\text{sec}, \quad (30)$$

and also is present in Fig. 6. The value of temperature in (29) and (30) should be taken in Kelvins.

Conclusion

In the present work the reaction of associative ionization of nitrogen and oxygen atoms was studied in the case of slow atom collisions in the framework of MQDT. The calculation of the diabatic potential energy curves of the excited states of *NO* molecule was carried out. The dependencies of the partial and total cross sections of the reaction (25) on the energy of the colliding atoms were calculated. It is shown that the main contribution to the total cross section make the dissociative $A'^2\Sigma^+$, $B^2\Pi$, $L^2\Pi$, and $B'^2\Delta$ states. The calculated total cross section of AI reaction has good agreement with the experimental data. The temperature dependence of the rate constant was defined at the temperature range $100 \text{ K} \le T \le 1000$ K. The

obtained data may be useful for calculating the tiered kinetics of population of highly excited Rydberg states in the photoionization plasma formed in the upper terrestrial atmosphere by the action of light flux coming from solar flares [1].

References

1. Golubkov G.V., Golubkov M.G., Manzhelii M.I. Microwave and IR Radiation of the Upper Atmosphere during Periods of Enhanced Solar Activity. *Doklady Physics.* V. 57. N. 2. P. 461—464 (2012)

2. Golubkov G.V., Devdariani A.Z. Associative Ionization in Slow Collisions of Atoms. *Russian Journal of Physical Chemistry B.* V. 5. N. 6. P. 892—906 (2011).

3. Devdariani A.Z., Klyucharev A.N., Penkin A.P., Sebyakin Yu.N. Diffusion approach to collisional ionization of the excited atoms. *Optics and Spectroscopy*. V. 64. N. 3. P. 706—709 (1988).

4. Golubkov G.V., Ozerov G.K. The Near-Threshold Associative Ionization $N(^2D)+O(^3P) \rightarrow NO^{**}(X^1\Sigma^+) + e^-$ Reaction. *Doklady Physics.* V. 59. N. 3. P. 122—125 (2014).

5. Golubkov G.V., Ivanov G.K. Rydberg states of atoms and molecules and the processes with their participation. Moscow: URSS, 2001.

6. Golubkov G.V., Ivanov G.K., Golubkov M.G. Nonadiabatic effects in dissociative recombination of electrons with hydrogen molecular ions. *Chemical Physics Reports.* V. 15. N. 4. P. 503—513 (1996)

7. Golubkov M.G., Golubkov G.V., Ivanov G.K. Low-temperature dissociative recombination of electrons with H_2^+, HD^+, and D_2^+ molecular ions. *Journal of Physics B: Atomic, Molecular and Optical Physics.* V. 30. N. 23. P. 5511—5534 (1997).

8. Werner H.-J., Knowles P.J. An efficient internally contracted multiconfiguration-reference configuration interaction. *The Journal of Chemical Physics.* V. 89. N. 9. P. 5803—5814 (1988).

9. Knowles P.J., Werner H.-J. An efficient method for the evaluation of coupling coefficients in configuration interaction calculation. *Chemical Physics Letters.* V. 145. N. 6. P. 514—522 (1988).

10. Knowles P.J., Werner H.-J. Internally contracted multiconfiguration-reference configuration interaction calculations for excited states. *Theoretica Chimica Acta.* V. 84. N. 1—2. P. 95—103 (1992).

11. Langhoff S.R., Davidson E.R. Configuration interaction calculations on the nitrogen molecule. *International Journal of Quantum Chemistry.* V.8. N. 1. P. 61—72 (1974).

12. Werner H.-J., Knowles P.J., Knizia G., Manby F. R., Schütz M., et. al. MOLPRO, version 2010.1, a package of *ab initio* programs (http://www. molpro. net).

13. Krishnan R., Binkley J.S., Seeger R., Pople J.A. Self-consistent molecular orbital methods. XX. A basis set for correlated wave functions. *The Journal of Chemical Physics.* V. 72. N. 1. P. 650—654 (1980).

14. Frisch M.J., Pople J.A., Binkley J.S. Self-consistent molecular orbital methods. 25. Supplementary functions for Gaussian basis sets. *The Journal of Chemical Physics.* V. 80. N. 7. P. 3265—3269 (1984).

15. Clark T., Chandrasekhar J., Spitznagel G.W., Schleyer P.V.R. Efficient diffuse function-augmented basis sets for anion calculations. III. The 3—21+G basis set for first-row elements, Li-F. *Journal of Computational Chemistry.* V. 4. N. 3. P. 294—301 (1983).

16. Langhoff S.R., Bauschlicher C.W. Jr., Partridge H. Theoretical study of NO γ system. *The Journal of Chemical Physics.* V. 89. N. 8. P. 4909—4917 (1988).

17. Sheehy J.A., Bauschlicher C.W. Jr., Langhoff S.R., Partridge H. Theoretical study of the nitric oxide ε and 11000 Å bands. *Chemical Physics Letters.* V. 225. N. 1—3. P. 221—228 (1994).

18. Sun H., Nakamura H. Theoretical study of the dissociative recombination of NO^+ with slow electrons. *The Journal of Chemical Physics.* V. 93. N. 9. P. 6491—6501 (1990).

19. Meischer E. The $I^2\Sigma^+$ state of the NO molecule. *Journal of Molecular Spectroscopy.* V. 69. N. 2. P. 281—293 (1978).

20. Bardsley J.N. Dissociative recombination of electrons with NO^+ ions. *Planetary and Space Science.* V. 31. N. 6. P. 667—670 (1983).

21. Nakashima K., Nakamura H., Achiba Y., Kimura K. Autoionization mechanism of the NO molecule: Calculation of quantum defect and theoretical analysis of multiphoton ionization experiment. *The Journal of Chemical Physics.* V. 91. N. 3. P. 1603—1610 (1989).

22. Raoult M. A unified treatment of $^2\Pi$-$^2\Pi$ Rydberg-valence state interactions in NO. *The Journal of Chemical Physics.* V. 87. N. 8. P. 4736—4761 (1987).

23. Golubkov G.V., Ivanov G.K. Near-threshold associative ionization reactions of atoms. *Journal of Physics B: Atomic, Molecular and Optical Physics.* V. 21. N. 11. P. 2049—2062 (1988).

24. Ringer G., Gentry W.R. A merged molecular beam study of the endoergic associative ionization. *The Journal of Chemical Physics.* V. 71. N. 4. P. 1902—1909 (1979).

25. Golubkov M.G., Ivanov G.K. Near-threshold associative ionization of atoms. *Journal of Physics B: Atomic, Molecular and Optical Physics.* V. 21. N. 11. P. 2049—2064 (1988).

E-3

Calculation of the Lowest ^{1}S Helium Resonance Using the Stabilization Method

A. A. Preobrazhenskaya[1], D. D. Kharlampidi[1], A. I. Dementiev[1], S. O. Adamson[2]

[1] *Chair of Inorganic Chemistry, Department of Chemistry, Moscow State Pedagogical University, Nesvizhskii per, 3, Moscow 119021, Russia*

[2] *Laboratory of Molecular Structure and Quantum Mechanics, Department of Chemistry, Lomonosov Moscow State University, Leninskie Gory, 1, Moscow 119991, Russia*

Recently the stabilization technique based on the modification of the initial Hamiltonian by external potential

$$V_s(R_0, V_0) = \begin{cases} 0, & r_i \le R_0 \\ \sum_i V_0(1 - R_0/r_i), & r_i > R_0 \end{cases}, \quad (1)$$

where R_0, V_0 are independent parameters and i=1,2 — index of electron, has been used to calculate the lowest ^{1}S resonances of H^- [1]. Now, this technique is applied to the energy and width estimation of the lowest ^{1}S helium resonances.

The computational scheme on the first step includes the variational solution of the Schrödinger equation

$$\left[\hat{H}_{el}(1,2)+\sum_{i=1}^{2}V_0(1-R_0/r_i)-E(R_0,V_0)\right]\Phi(1,2)=0\,, \tag{2}$$

where $\hat{H}_{el}(1,2)$ — the non-relativistic Hamiltonian of the helium atom and $\Phi(1,2)$ — the two-electron wave function. Then the resonance energy and width are estimated using the first derivative of the phase shift function $\delta_0(E(R_0,V_0))$. On the intermediate step the phase shift function is calculated applying the wave function continuity condition at $r=R_0$:

$$tan\left[\delta_0\left(E(R_0,V_0)\right)\right]=\frac{W(r)d\sin(\varsigma(k_1r))/dr-\sin(\varsigma(k_1r))}{\cos(\varsigma(k_1r))-W(r)d\cos(\varsigma(k_1r))/dr}\,, \tag{3}$$

where

$$W(r)=r\left[\frac{2|k_2|r}{f(r)}\frac{df(r)}{dr}+1+l-|k_2|r\right]^{-1},$$

$$f(r)=U(l+1-\eta,2l+2,2|k_2|r),$$

$$\eta=m_e(Ze^2+V_0R_0)/|k_2|\hbar^2\,,\ \varsigma(k_1r)=k_1r-\nu\ln(2k_1r)-l\pi/2+\arg(\Gamma(l+1+i\nu))\,,$$

$$\nu=-m_eZe^2/k_1\hbar^2\,,$$

e — elementary charge. In the previous formulas Z = 1 a.u. and variables k_1, k_2 define the wave numbers of the internal and external intervals: $k_1=\sqrt{2m_eE(R_0,V_0)/\hbar^2}$ and $k_2=-i\sqrt{2m_e(V_0-E(R_0,V_0))/\hbar^2}$, $\mathrm{Re}(k_2)=0$.

The energy and width of the lowest resonance were evaluated as an example of the described above stabilization procedure. The wave function consisting of internal and external parts was used in the calculations. The internal part included a full set of the configuration state functions (CSF) constructed from the 9s8p7d set of single-particle functions and external — a set of single-excitations with respect to internal part spanned by the set of 18s18p18d single-particle functions. All details concerning the wave function construction and variational calculations can be found elsewhere [1]. The stabilization procedure was carried out for R_0 = 7.0 ÷ 25.0 a.u. at V_0=4.0 a.u. (Table 1). For comparison, the energy and width of the resonance were calculated also using the complex scaling method. These results are in a good agreement with the independent ones (Table. 2).

TABLE 1. Average[a] resonance energy (E_{res}) and width (Γ) obtained for the lowest helium ^{1}S resonance using the stabilization method and the average errors (*10^5). E_{res} values are given with respect to the ground state of He^+. All values are given in atomic units.

R_0	E_{res}	ΔE_{res}	Γ	ΔΓ
8.7	1.22230	2	0.00485	3
12.7	1.22215	5	0.00459	9
16	1.22211	17	0.00454	33

[a] Averaging over the $1.6 \le b \le 3.8$ (scaling factor) values. See details in Ref. [1].

TABLE 2. Energy (E_{res}) and width (Γ) for the lowest helium ^{1}S resonance. E_{res} values are given with respect to the ground state of He^+. All values are given in atomic units.

Method	E_{res}	Γ	Reference
Stabilization	1.22217	0.004549	[2]
Stabilization	1.22216	0.004503	[3]
Stabilization	1.2235	–	[4]
Complex scaling	1.2221494	0.0045528	[5]
Complex scaling	1.22219	0.004576	Present results

Financial support by Russian Foundation for Basic Research (grant No. 12-03-00821) is acknowledged.

1. S.O. Adamson, D.D. Kharlampidi and A.I. Dementiev, *Prog. Theor. Chem. Phys*. 27, 2013, pp. 101—118.
2. S. Kar and Y. K. Ho, *Chem. Phys. Lett.* 402, 2005, pp. 544—548.
3. A. Ghoshal and Y. K. Ho, *J. Phys. B.* 42, 2009, p. 075002.
4. Y. Sajeev, *Chem. Phys. Lett.* 587**,** 2013, pp. 105—112.
5. P. R. Kaprálová-Žďánská and J. Šmydke, *J. Chem. Phys*. 138, 2013, p. 024105.

E-4

Mechanisms of Reactions of Copper Complexes with Alkyl Radicals

Ekaterina M. Zubanova[1], Elena N. Golubeva[2], and Georgii M. Zhidomirov[1,2]

[1] Chemistry Department, Lomonosov Moscow State University, 119991, Moscow, Russia
[2] Boreskov Institute of Catalysis (BIC), SO RAN, Novosibirsk, 630090, Russia

Alkyl radicals may form in atmosphere by influence of radiation. They decay reacting with transient metal complexes and transform to diamagnetic products. Such reactions of organic radicals and copper compounds also appear to be stages

of copper-catalyzed processes, such as controlled/"living" radical polymerization, atom transfer addition of halohydrocarbons to olefins (Kharash reaction), radical cyclizations, metathesis of C-Cl bond, etc. These processes include similar redox stages with partition of metal complexes and organic radicals. There are two principal mechanisms of reactions between metal complexes and alkyl radicals. First, which is termed as electron transfer, assumes formation of organometallic intermediates via addition of radical to metal ion. These intermediates may transform to more stable products and, supposedly, transformation of copper organic intermediates occurs with formation of cationic organic fragment. Another mechanism includes concerted one-step process with ligand transfer from complex to radical. The mechanism depends on many factors, especially, ligand nature, metal valence, radical structure, nuclearity of metal complex, and solvent. Generally, the ligand transfer is typical for halide and pseudohalide copper(II) complexes, but the possibility of other processes should not be excluded, especially for bi- and polynuclear species. Reactions between copper(II) complexes with oxygen containing ligands, such as acetates, triflates, and alkyl radicals are assumed to occur through the formation of organocuprates [1].

In present work reactions between different copper complexes with a number of radicals were studied in the scope of density functional theory. To define the influence of the nuclearity we have studied structure of potential energy surfaces (PES) in the systems of mononuclear and binuclear copper(II) chlorides $CuCl_4^{2-}\ldots CH_3$, $(N(CH_3)_4)_2CuCl_4\ldots CH_3^{\bullet}$ and $Cu_2Cl_6^{2-}\ldots CH_3^{\bullet}$, $(N(CH_3)_4)_2Cu_2Cl_6\ldots CH_3^{\bullet}$ [2,3]. In the systems which include mononuclear species only processes of chlorine transfer were found as reactions. The products of chlorine transfer from mononuclear copper(II) chlorides by methyl radical are copper(I) chlorocomplexes and methylchloride. Stationary points corresponding to $CuCH_3Cl_4^{2-}$ and $(N(CH_3)_4)_2CuCl_4CH_3$ exist on the PES, but the addition of methyl radical to copper(II) chlorides in not the way of their formation. In systems $Cu_2Cl_6^{2-\cdots}CH_3^{\bullet}$ and $(N(CH_3)_4)_2Cu_2Cl_6^{\cdots}CH_3^{\bullet}$ both processes of chlorine transfer (terminal and bridge) and formation of organocuprates $Cu_2Cl_6CH_3^{2-}$ and $(N(CH_3)_4)_2Cu_2Cl_6CH_3$ were found. Products of ligand transfer in these cases are heterovalent copper chlorides $Cu_2Cl_5^{2-}$ and CH_3Cl. Reactions of formation of $Cu_2Cl_6CH_3^{2-}$ and $(N(CH_3)_4)_2Cu_2Cl_6CH_3$ were obtained to be spontaneous; besides, these complexes may transform to products of ligand transfer mechanism — heterovalent copper chloride complexes and methylchloride with an activation barrier about 30—40 kJ/mol. This path — concerted CH_3Cl elimination is accompanied by increasing the charge on alkyl radical. In the Fig. 1 the PES of the system $Cu_2Cl_6^{2-}\ldots CH_3^{\bullet}$ is presented. Points TS1 and TS2 correspond to transition states of terminal and chlorine detachment from $Cu_2Cl_6^{2-}$, respectively, points P1 and P2 — to products of this detachment weak complexes between CH_3Cl and heterovalent complexes $Cu_2Cl_5^{2-}$. The C1 and C2 are weak complexes between $Cu_2Cl_6^{2-}$ and $CH_3^{\bullet}$ radical, oriented to terminal and bridge chlorine detachment, respectively. Complex P3 corresponds to organocuprate $Cu_2Cl_6CH_3^{2-}$, and TS3 is transition state between organocuprate and weak complex $Cu_2Cl_5^{2-} \ldots CH_3Cl$. All energies were calculated at PBE0(BS)/def2-tzvp level assuming zero-point energy corrections.

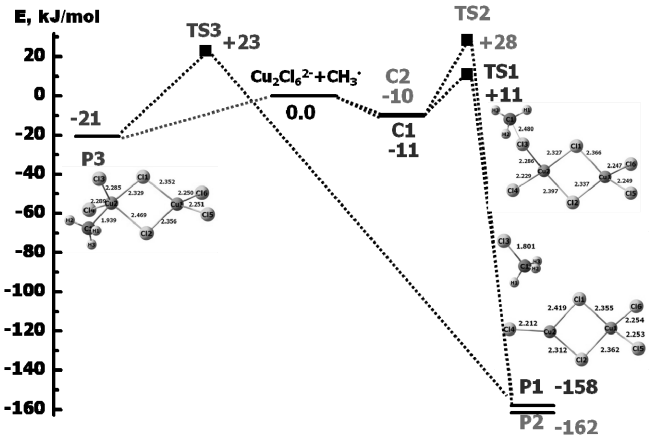

FIGURE 1. PES in system the $Cu_2Cl_6^{2-}…CH_3^{\bullet}$.

Another systems studied are neutral copper(II) acetate complexes and alkyl radicals. In system $Cu(OAc)_2$ and $CH_3^{\bullet}$ two barrier reactions were found: formation of organocuprates and addition of methyl fragment to ligand (an analogue of ligand transfer process in such system). Optimized geometric structures of copper(II) acetate and copper-methyl acetate complexes are presented in the Fig. 2. The reaction of $CuCH_3(OAc)_2$ formation is energetically more favorable than formation of $Cu(OAc)(O(CH_3)Ac)$. Complex $CuCH_3(OAc)_2$ also could transform through barrier to products of ligand transfer mechanism. So, our calculations confirm experimental date on influence of ligand to nature on mechanism reactions between copper complexes and alkyl radicals.

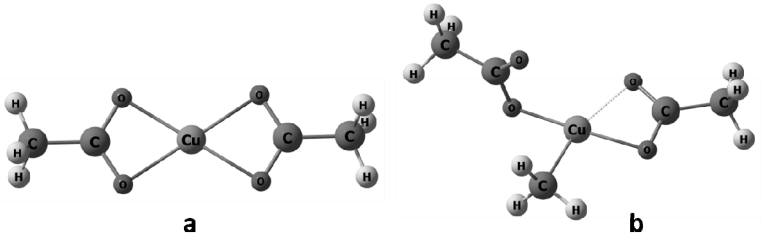

FIGURE 2. Geometric structures of $Cu(OAc)_2$ (a) and $CuCH_3(OAc)_2$ (b).

Quantum-chemical calculations were performed using resources of Supercomputing Center of Lomonosov Moscow State University. The research was partially supported by RFBR Grants 13-03-00420a and 12-03-33104mol_a_ved.

1. J. K. Kochi, *Acc. Chem. Res.*, 1974, 7, 351— 360.
2. E. N. Golubeva, E. M. Zubanova, G.M. Zhidomirov, *J. Phys. Org. Chem.,* 2013, 26, 724—729.
3. E. M. Zubanova, E.N. Golubeva, G.M. Zhidomirov, *Organometallics*, 2014, 33, 121—128.

Physic-chemistry Properties Intermolecular Complexes H_3O^+ — M and H_2O — M and their Participation in the Atmospheric Processes

Y. V. Zaika, G. I. Kobzev

Orenburg State University, RF

By the method DFT-D / 6—311G** to calculated the equilibrium geometry structure, electronic and spin characteristics of complexes H_2O — M and H_3O^+ — M, M = N_2, O_2, CO_2, NO_2, SO_2, H_2S (Fig. 1).

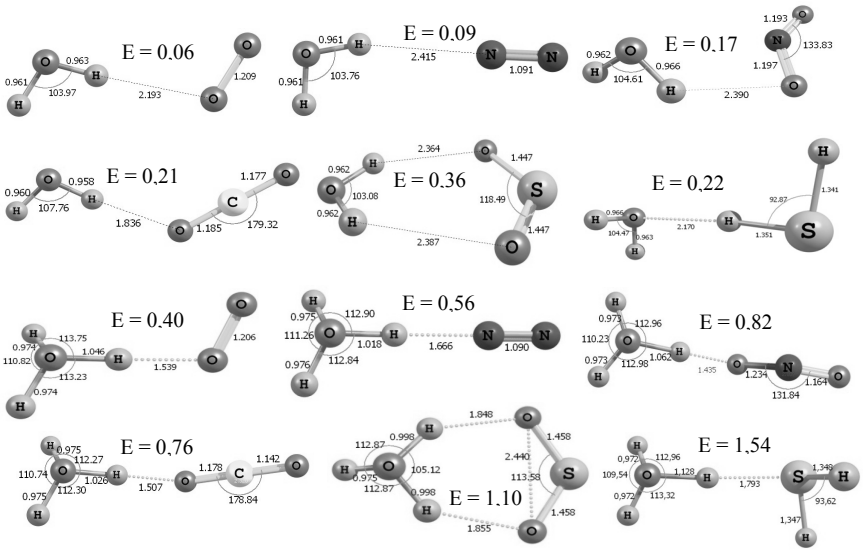

FIGURE 1. The geometry and energy break intermolecular complexes H_2O — M and H_3O^+ — M, M = N_2, O_2, CO_2, NO_2, SO_2, H_2S.

By the method SA-MCSCF/6—311G** to evaluated the energies of excited states, points allowed and forbidden transitions. On the basis of eigenvectors obtained by the DFT-D method to calculate vibrational spectra and thermodynamic parameters (ΔH, ΔG, ΔS), equilibrium constants (K_p, K_c) and their concentration on the different altitudes. To analyze the charge of concentration atmospheric intermolecular complexes H_3O^+ — M and H_2O — M at different temperatures.

To revealed that, complexes containing H_3O^+ are more resistant that complexes with H_2O.

Supra-molecular Structure and Spin Diffusion of Fluoroplastics Studied by NMR

Tatiana P Kulagina[1], Grigorii E. Karnaukh[1], Lev P. Smirnov[1], Mikhail A. Smirnov[1], Vyacheslav M. Buznik[2]

[1] Institute of Problems of Chemical Physics RAS, Semenov prospect, 1, Chernogolovka, Moscow region, 142432, Russia
[2] Metallurgy and materials science institute RAS, Leninskii prospect, 49, Moscow, 119991, Russia

The main efforts of researchers are now directed on development of the new polymeric composite materials (PCM), by introduction of additives of other polymers in it, in whole or in part incompatible thermodynamic with initial polymer. In particular, powders polytetrafluoroethylene (PTFE) find application in a number of branches, as materials for antifrictional, antiwear, hydrophobic, tire-tread and biocompatible coverings. The area and efficiency of their application in many respects are defined by the sizes and morphology of particles of powder which, in turn, depend on a way of their receiving [1—4]. In most cases powders PTFE are obtained from the tetrafluoroethylene (C_2F_4) monomer gaseous phase at ultra-violet radiation and presence of various initiators.

At studying partial — crystalline polymers usually much attention is given to crystallinity degree on which depend durability, elasticity, elasticity and biodegradability of a material. There are several methods for determination of crystallinity degree, however these methods are difficult and give only approximate data.

Application of the NMR techniques to investigation of a supra-molecular structure in BPS provided unique information about the features of their supramolecular and topological structures and the mechanisms of thermal and thermomechanical degradation. The NMR-relaxation represents a universal method of studying of structure and molecular dynamics in polymers. In particular, the NMR method is applied to definition of crystallinity degree of polymers [3, 4].

In this work the theory of line shape NMR in the heterogeneous polymeric systems (HPS) is offered. On the basis of this theory the method of definition of crystallinity degree (or part of the organic filler added in system) HPS by experimental signals NMR is developed.

In the offered theory a signal of free induction decay (FID) G(t) from HPS is the sum of signals from crystal (or filler, containing magnetic nuclear) G_{cr} *(t)* and amorphous (polymeric) G_m *(t)* phases of the sample:

$$G(t) = (1 - p)G_{\mathrm{m}}(t) + pG_{\mathrm{cr}}(t), \tag{1}$$

where p is the crystallinity degree.

The line shape $F(\omega)$ is defined by transformation of Fourie from (1) and have been done by expression:

$$F(\omega) = p[F_{\mathrm{cr}}(\omega) - F_{\mathrm{m}}(\omega)] + F_{\mathrm{m}}(\omega), \tag{2}$$

where $F(\omega) = \sqrt{\frac{2}{\pi}} \int_0^\infty G(t)\cos(\omega t)\,dt$, $F_{cr}(\omega)$, $F_m(\omega)$ are contributions to the line shape from crystal and amorphous phase of the sample.

The formula (2) shows that the spectrum area S (integrated intensity of absorption) is equal to:

$$S = \mathrm{p}(S_{\mathrm{cr}} - S_{\mathrm{m}}) + S_{\mathrm{m}}, \tag{3}$$

where S_{cr} is the spectrum area of crystal phase, and S_m — is the spectrum area of amorphous phass of HPS.

It follows from the equation (3), that the spectrum area S depends linearly on the crystallinity degree p. If the area of crystal S_{cr} and amorphous S_m phases are known it is possible to construct a universal straight line of dependence S on p. However it is usually impossible to separate the amorphous and the crystal phases of HPS and it is necessary to compare the theoretical and experimental spectra for crystalliniti degree determination.

Numerical calculation FID $G(t)$ is carried out with the help of the general kinetic theory of magnetic dipoles [5]. The kinetic equations were obtained for the partial densities of magnetic dipoles (polarizations of layers) $\sigma^{\beta}(h, t)$, where $\beta = x, y, z$, which are formed by the spins of the system located at time t in the same longitudinal local field h.

$$\frac{d\sigma^x}{dt} = -\left(\omega + \frac{3h}{2}\right)\sigma^y - \left(\frac{3}{2} - \alpha\right)\left(h\sigma_0^y + \sigma_1^y - h\sigma^y\right) + \frac{\sigma_0^x - \sigma^x}{\tau_\perp} - \frac{\sigma^x}{T_\perp} \tag{4}$$

$$\frac{d\sigma^y}{dt} = \left(\omega + \frac{3h}{2}\right)\sigma^x + \left(\frac{3}{2} - \alpha\right)\left(h\sigma_0^x + \sigma_1^x - h\sigma^x\right) - \omega_1\sigma^z + \frac{\sigma_0^y - \sigma^y}{\tau_\perp} - \frac{\sigma^y}{T_\perp} \tag{5}$$

$$\frac{d\sigma^z}{dt} = \omega_1\sigma^y + \frac{1}{\tau_\parallel}\left(\sigma_0^z + \frac{h\sigma_1^z}{\langle h^2\rangle} - \sigma^z\right) + \frac{\sigma_{eq}^z - \sigma^z}{T_{\parallel Z}} - \frac{h\sigma_1^z}{\langle h^2\rangle T_{\parallel d}} \tag{6}$$

where ω is the off-set of magnetic field, ω_1 is the amplitude of arbitrary saturating field, $1/\tau_\perp$ is the rate of change of the transverse polarization of the layer in the course of spectral diffusion; $1/\tau_\parallel$ is the rate of establishment of equilibrium in the

spin system; $1/T_{\perp}$ and $1/T_{\|}$ are the rates of the transverse and longitudinal relaxation, $T_{\|Z}$ and $T_{\|d}$ are the times of longitudinal spin-lattice relaxation of the Zeeman and dipole reservoirs, respectively. The parameter (*3/2 – α*) characterizes the non averaged isotropic part of the dipole — dipole interaction (DDI) and exchange of polarization between layers.

In deriving the equations (4—6), we took into account both the regular processes, defined by interaction Hamiltonian (the precession of the dipoles in the external fields and the dipole fields created by the neighboring dipoles and polarization transfer) and the random process of spectral diffusion $D/D_0 \sim \tau_0/\tau_{\perp}$, which reflects the random variation of the longitudinal local field under the influence of spin exchange and thermal atomic motion. In the equations (4—6) the following designations are entered:

$$\sigma_0^{\beta} = \int_{-\infty}^{\infty} \sigma(h,t)g(h)dh, \ \sigma_1^{\beta} = \int_{-\infty}^{\infty} \sigma(h,t)hg(h)dh \tag{7}$$

where $\sigma_0^{\beta}(t)$, $\sigma_1^{\beta}(t)$ are the polarizations of Zeeman and dipole reservoirs, respectively; $g(h)$ is an even function of longitudinal distribution of local fields in dense spin systems, $g(h) = g(-h)$,

The decision of system of the equations (4—6) is obtained for a line shape $F(\omega)$. All calculations were performed for the case where $g(h)$ was the Gaussian function of distribution of longitudinal local fields:

$$g(h) = \frac{1}{\sqrt{2\pi\langle h^2\rangle}} \exp\left[-\frac{h^2}{2\langle h^2\rangle}\right], \tag{8}$$

where $\langle h^2\rangle = \int_{-\infty}^{\infty} h^2 g(h)\,dh$, $\langle h^2\rangle = \frac{4}{9}M_{2cr}$, M_{2cr} is the second moment of the crystal phase of line shape.

The steady state solution to equations (4—6) was obtained for the line shape function $F(\omega)$:

$$F(\omega) = \frac{\sigma_0^y(\omega)}{\sigma_{eq}^z}, \tag{9}$$

where σ_{eq}^z is the longitudinal equilibrium polarization.

Note that, for developed molecular motions, the isotropic part of the spin exchange term does not contribute to the observed signal, and, therefore, the kinetics of the polarization of the spin system can be considered only in longitudinal local fields [5]. In this case, at $\alpha = 3/2$, equations (4—6) are applicable to describing the amorphous phase, since the terms of the equations describing spin exchange disappear.

Now development of energy saving technologies of manufacturing products from PTFE is currently underway. Special attention is focused on processing of ultra disperse powders PTFE in the solid phase. For a choice of a temperature mode of processing of PTFE in a solid state it is necessary to know the temperature of phase transitions. For this aim it is necessary to study supra-molecular structure and relaxation properties of this materials.

Definition of change of supra-molecular structure of samples of PTFE from crystal (rigid) to amorphous (mobile) at temperature increase is carried out on the basis of developed before the theory spectra NMR in solid state [2, 3].

^{19}F NMR measurements were taken in a field of 9.4T at a frequency of 400 MHz on a Bruker AVANCE 400 spectrometer while changing the temperature from 230 to 343 K for four samples. The FID was recorded with a delay of 20 μs after a 90° pulse with a width of 2μs, the number of measurements was 8 to 32 depending on the measurement temperature.

In this work comparison of theoretical and experimental line shapes NMR at various temperatures is carried out. When comparing the second moment of line shape for the crystal phase $G_{cr}(t)$ at a temperature – 40 ^{o}C was defined: $M_2 = 2.2 \cdot 10^8$ s^2, $\alpha = 0.8$, $p = 1$. At temperature increase amorphous phase $G_m(t)$ was calculated with the same value M_2 at $\alpha = 3/2$. In calculations parameters of degree of crystallinity p and characteristic time of spin diffusion was varied: $2 \cdot 10^{-5}$ s $< \tau_\perp < 8 \cdot 10^{-5}$s. At low temperature ($\tau_\perp = 2 \cdot 10^{-5}$s) line shape is wide, has two extremums ("camel back") that is characteristic for crystals. At temperature increase line shape is narrowed and transformed into a Gaussian form at high temperature ($\tau_\perp = 8 \cdot 10^{5}$s).

In Fig. 1 the dependence of the spectrum area on temperature calculated from experiments for four samples obtained by various technological methods [1] is presented.

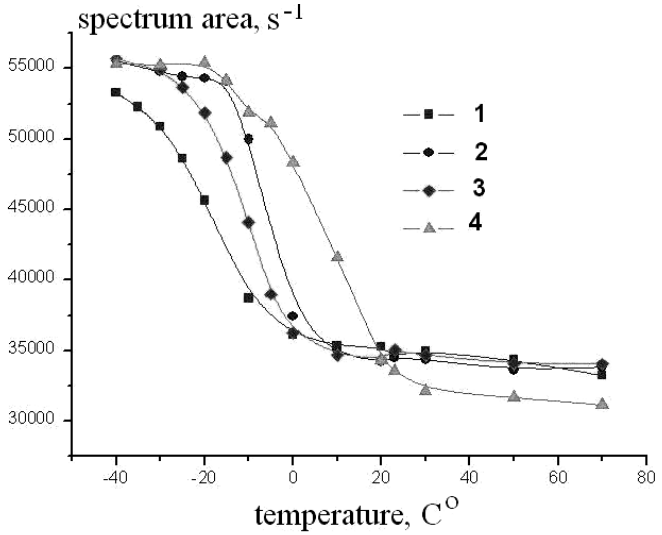

FIGURE 1. Experimental dependence of the spectrum area on temperature for four samples of PTFE powder.

As well as in work [4], from comparison of theoretical and experimental signals of a nuclear magnetic resonance degree of crystallinity is defined and universal linear dependence of degree of crystallinity p on the spectrum area is received The values p obtained from experimental signals at various temperature which well coincide with theoretical dependence are given in Fig. 2.

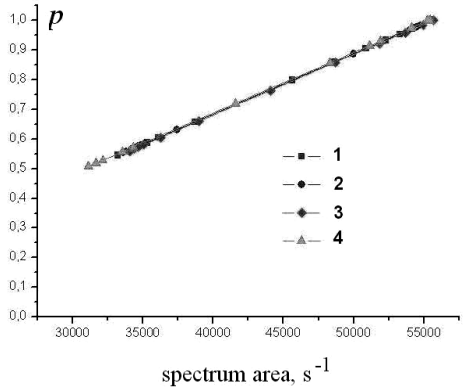

FIGURE2. The universal dependence of degree of crystallinity on spectrum area.

This dependence is applicable for definition of degree of crystallinity in all samples of PTFE, at any temperature from -40^{o}C до 70^{o}C. For all samples at temperature increase change of supramolecular structure from crystal to partial and crystal is established.

From comparison of the theory and experiment values of time of spin diffusion which are connected with coefficient of spin diffusion are received D: $D/D_0 \sim \tau_0/\tau_\perp$ (D_0, τ_0 — are the equilibrium constants). In Fig. 3 dependence the coefficient of spin diffusion on the inverse temperature which has a pronounced break is presented and qualitatively corresponds to theoretical and experimental dependences of $S(T)$ (Fig. 1) and p (T). The obtained dependence of lnD (1/T) allows to determine the range of phase transitions. In studied samples phase transition happens at the maintenance of an amorphous phase of 20 %, at p = 0.8.

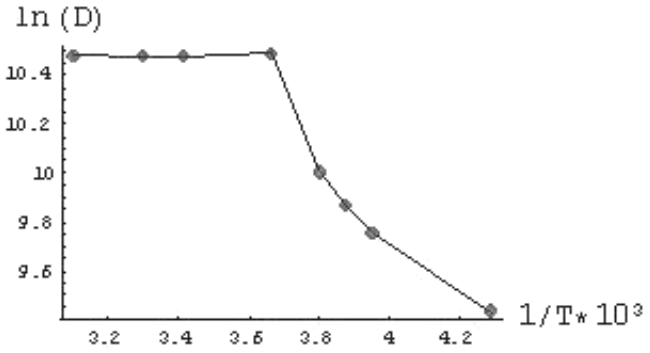

FIGURE 3. The dependence of coefficient of spin diffusion on inverse temperature.

The analysis of dependences of degree of crystallinity and coefficient of spin diffusion from temperature allows to define optimum conditions of receiving and application of materials on the basis of fluoroplastics.

1. V.M. Buznik, Yu.E. Vopilov, V.K. Ivanov *et. al., Pespektivnie materiali (Russian)*, 2012, N 4, pp. 44—52.

2. T.P. Kulagina, P.S. Manikin, G.T. Karnaukh, L.P. Smirnov, *Doklady Physical Chemistry, Part 2*, 2010, v. 431, pp. 67—71.

3. T.P. Kulagina, P.S. Manikin, G.T. Karnaukh, L.P. Smirnov, *Russian journal of Physical Chemistry B*, 2011, v: 5, N:4, pp. 674—680.

4. T.P. Kulagina, O.M. Vyaselev, D.V. Pugachev, A.M. Stolin, *Doklady Physical Chemistry, Part 2*, 2012, v. 443, pp. 63—66.

5. B.N. Provotorov, T.P. Kulagina, G.E. Karnaukh, *J. Experim. and Theor. Phys.,* 1998, v. 86, pp. 527—533.

M-2

Chitosan Nanocomposites with Metal Ions and Nanoparticles

Timofei E. Grigoriev[1], Roman D. Varganov[1], Irina A. Romanova[1], Vladimir S. Yamshikov[2] and Sergey N. Chvalun[1]

[1] National Research Centre "Kurchatov Institute", Akademika Kurchatova pl. 1, Moscow, 123182, Russia
[2] Faculty of Physics at M.V. Lomonosov Moscow State University, Leninskie Gory, Moscow, 119991, Russia

Chitosan is a natural copolymer of glucosamine and N-acetylglucosamine. Much attention has been focused on the preparation of chitosan-metal materials because of their potential biomedical applications. Chitosan is biocompatible polymer allowing its use in various medical applications such as wound coverage, implantation and injection. Chitosan is metabolized by human enzymes (especially lysozyme) and is considered as biodegradable.

Systematic study of the metal ion-chitosan interactions and the process of metal nanoparticles growth inside polymer matrix will give an opportunity to fabricate different biocompatible polymeric and composite materials with specified structure and properties.

In the present work behavior of Ag ions in chitosan solutions with different concentration, molecular weight of chitosan and deacetylation degree of chitosan was investigated systematically. Influence of external parameters (pH, temperature) on polymer — metal ion interaction was investigated. Composite chitosan based materials with incorporated Ag were made in forms of sponges and films. Influence of solution conditions on nanoparticle growth was investigated.

Investigation of molecular mechanism of Ag reduction by chitosan was carried out using IR spectroscopy. Measurements were made on the chitosan films and sponges made from acetic acid chitosan solutions containing $AgNO_3$. The Ag nanoparticle formation controlled by surface plasmon resonance in UV-Vis spectra of solutions.

D. Wei et al. [1] supposed two stage mechanism of Ag reduction in chitosan solution:

1) Ag ion coordination on the amino groups of polymer

$$R\text{-}NH_2 + H^+ \rightleftharpoons R\text{-}NH_3^+$$

$$R\text{-}NH_2 + Ag^+ \rightarrow R\text{-}NH_2Ag^+$$

$$R\text{-}NH_3^+ + Ag^+ \rightarrow R\text{-}NH_2Ag^+ + H^+$$

$$R\text{-}NH_2Ag^+ + H_2O \rightarrow AgOH + R\text{-}NH_3^+$$

2) metal-polymer complex formation following Ag_2O formation

$$2AgOH \rightleftharpoons 2Ag^+ + 2OH^- \rightleftharpoons Ag_2O + H_2O$$

$$Ag_2O + R'CH_2OH \rightarrow R'CHO + 2Ag + 2H_2O$$

$$Ag_2O + R'CHO \rightarrow R'COO^- + 2Ag + 2H_2O$$

In the Fig. 1 one can see IR spectra of the chitosan film with and without silver nanoparticles. We supposed two types of binding sites on the chitosan molecules corresponding to amino and hydroxyl groups. Peak position and intensity analysis are difficult in the 3000—3600 cm^{-1} region. But Fig. 1 reveal shift in 1550 and 1630 cm^{-1} lines of amino groups of chitosan. Also Ag-chitosan interaction followed by increase in C-H interaction (corresponding to 1370 cm^{-1} line). 820 cm^{-1} line shows Ag-O bonds formation and confirm the suggested [1] mechanism of Ag reduction in chitosan solution. Ag_2O formation also revealled during WAXS measurements.

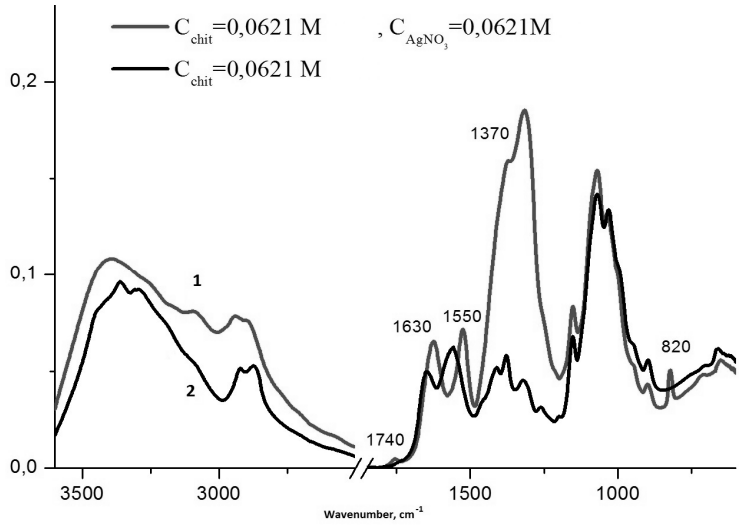

FIGURE 1. FTIR spectra of chitosan film with (1) and without (2) Ag nanoparticles.

Structure of metal-chitosan composite materials was investigated by electron microscopy. On the Fig. 2 and 3 one can see SEM images of chitosan sponges with (Fig. 3) and without (Fig. 2) Ag nanoparticles.

All of the composite materials showed improved biological activity.

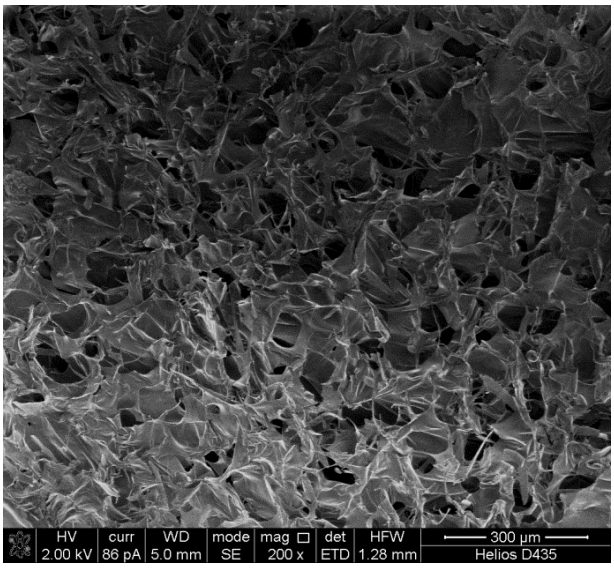

FIGURE 2. SEM image of chitosan sponge without Ag nanoparticles.

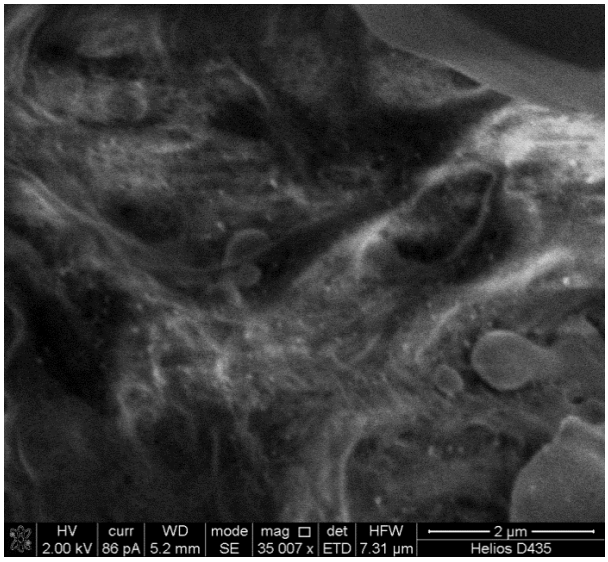

FIGURE 3. SEM image ot chitosan sponge containing Ag nanoparticles.

1. Dongwei Wei, Yongzhong Ye, Xueping Jia, Chao Yuan, Weiping Qian, *Carbohydrate Research*, 345 (2010) 74—81.

Properties of Nitroxide Biradicals: Quantum-Chemical Calculations and the Experiment

Oleg I. Gromov[1], Elena N. Golubeva[1], Victor N. Khrustalev[2], Evgeniy N. Degtyarev[3], Alexander A. Dubinsky[3], and Alexander I. Kokorin[3]

[1] Chemistry Department, M. V. Lomonosov Moscow State University, Moscow, 119991, Russia
[2] A. N. Nesmeyanov Institut of Organoelement Compounds RAS, Moscow, 119991, Russia
[3] Department of Kinetics and Catalysis, N. Semenov Institute of Chemical Physics RAS, Moscow, 119991, Russia

Free radical interactions are very important for understanding environmental processes, and biradicals are convenient class of compounds to model some of these interactions. Much effort is applied to the biradicals investigation both experimentally and theoretically [1,2,3]. The theoretical description needs reliable structural data that might be to some extent gained from such experimental methods such as X-ray diffraction. Another convenient source of structural data is quantum-chemical calculation. Therefore, extensive evaluation of modern computational techniques is needed for solving this problem. In present work we focus our attention on calculations of geometry of rigid nitroxide biradicals with polyacetylene bridges [4] using Density Functional Theory (DFT).

Computational details

Geometries of nitroxide biradicals in the triplet state were calculated at UKS/B3LYP/ level with cc-PVDZ basis set [5]. Open-shell singlet state geometries were calculated in the Broken Symmetry approximation [6,7] at the same level of theory and were found to match triplet state equilibrium geometries. Distances $R_{NO\text{-}NO}$ were calculated as a distance between centers of N—O bonds. Zero field splitting values D were also calculated at UKS/B3LYP/cc-PVDZ level neglecting a spin-orbit part. Spin-spin part was calculated on the basis of unrestricted natural orbitals [8]. Calculations were performed using ORCA 2.9.1 program package [9].

Results and Discussion

Biradicals studied include two 1-oxyl-2,2,6,6-tetramethyl-3,4-ene-piperidine rings and bridges containing acetylene or *p*-phenyl groups. To evaluate mutual orientation of nitroxide rings a θ angle is introduced (Fig. 1).

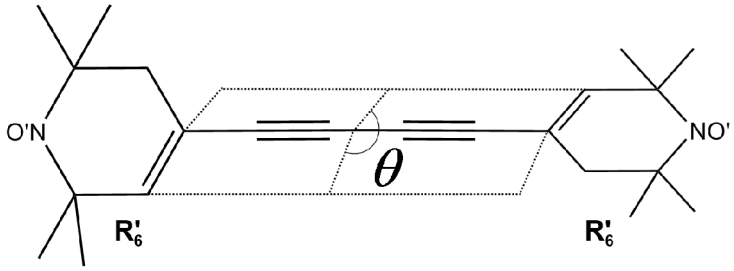

FIGURE 1. Structure of acetylene-bridged nitroxide biradical.

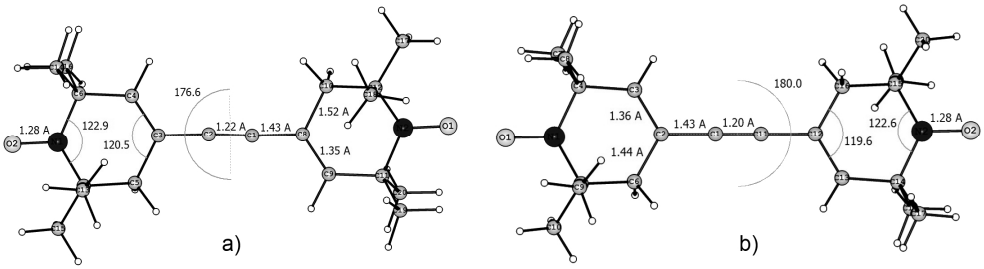

FIGURE 2. Calculated on UKS/B3LYP/cc-PVDZ level (a) and the X-ray analysis based [10] (b) R'$_6$-C ≡ C-R'$_6$ geometry.

Calculations reveal almost identical N-O bond lengths of 1.28 A in the whole series of biradicals studied (Figs. 2—4). In the case of R'$_6$-C ≡ C-R'$_6$, this result is in a good agreement with the experimental data (FIG. 2), though for R'$_6$-(C≡C)$_2$-R'$_6$ biradical experimental N-O bond length is slightly longer (FIG. 3). This might be attributed to the intermolecular interactions in the crystal.

Mutual orientation of nitroxide rings in crystals in both R'$_6$-C≡C-R'$_6$ and R'$_6$-(C≡C)$_2$-R'$_6$ biradicals is characterized by the angle θ almost equal to 180°. DFT calculations showed a slightly smaller angle value. The only exception is the R'$_6$-R'$_6$ biradical, which exhibits θ = 166° due to intramolecular steric effects. The rotation barriers around the main molecular axis for several biradicals were shown not exceeding 8 kJ/mol [12]. Thus, deviations of calculated θ-angles from experimental θ-angles can be assigned to the intermolecular interactions in crystals in comparison with biradical solutions.

Calculated lengths of triple acetylene bonds in the bridge are in the error limit within 0.02 Å, while single carbon-carbon bond lengths in the nitroxide rings, predicted by DFT modeling, may differ from the experimental up to 0.08 Å (Fig 2). It should be noted that for the whole set of biradicals, DFT calculations predict similar results, whereas the experimental data for R'$_6$-C≡C-R'$_6$ biradical differ from those for R'$_6$-(C≡C)$_2$-R'$_6$ biradical.

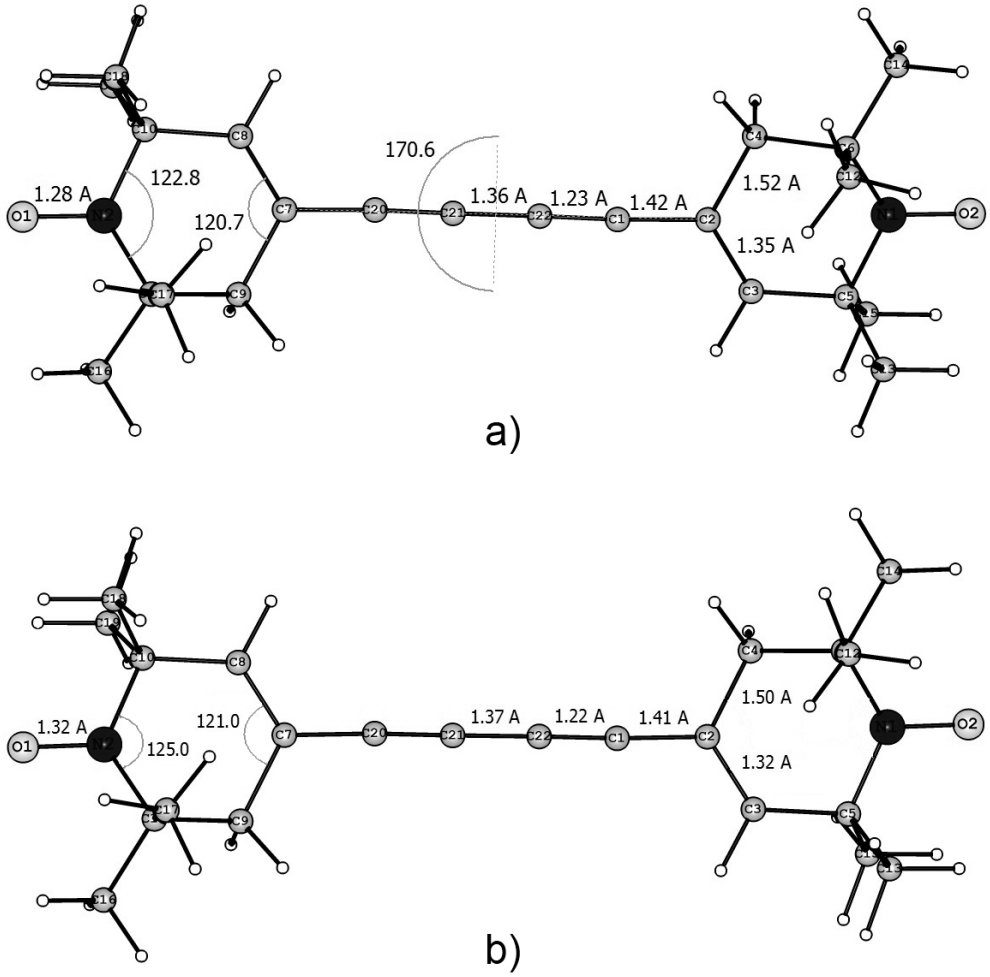

FIGURE 3. Calculated on UKS/B3LYP/cc-PVDZ level (a) and the X-ray analysis based [11] (b) R'_6-$(C{\equiv}C)_2$-R'_6 geometry.

Calculated $R_{NO\text{-}NO}$ distances are also in good agreement with experimental ones (TABLE 1). Small deviations are not exceed 0.1 Å, are in the error limit of calculations and of experimental values of C-C-C, N-C-C and C-N-C angles, and on accumulation of deviations in the acetylene carbon — carbon bonds in long-chain biradicals. Appropriate values of $R_{NO\text{-}NO}$ allow calculating the zero field splitting parameters D, which are also in a good agreement with experimental (TABLE 1).

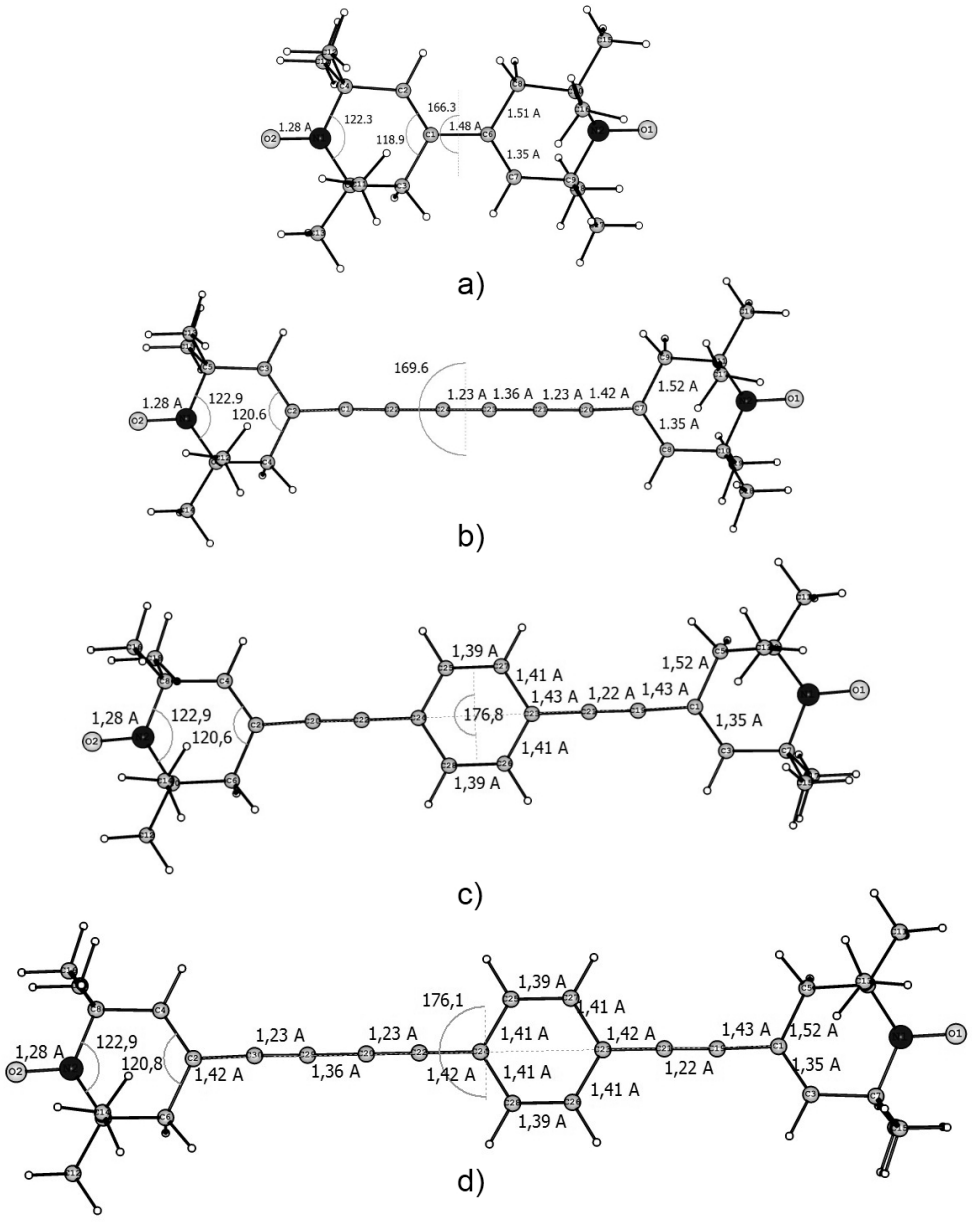

FIGURE 4. Calculated on UKS/B3LYP/cc-PVDZ level geometry of R'$_6$-R'$_6$ (a) R'$_6$-(C≡C)$_3$-R'$_6$ (b), R'$_6$-C≡C-Ph-C≡C-R'$_6$ (c) and R'$_6$-C≡C-Ph-(C≡C)$_2$-R'$_6$ (c).

TABLE 1. Calculated on UKS/B3LYP/cc-PVDZ level and experimental distances $R_{NO\text{-}NO}$ and zero field splitting values D for the acetylene-bridged biradicals.

Biradical	$R_{NO\text{-}NO}^{B3LYP}$, Å	D^{B3LYP}, G	$R_{NO\text{-}NO}^{exp}$, Å	D^{exp}, G
R'_6-R'_6	8.50	45.3	8.6 [10]	43.7
R'_6-C≡C-R'_6	11.04	22.8	11.12 [10]	20.2
R'_6-$(C\equiv C)_2$-R'_6	13.62	11.9	13.7 [11]	10.8
R'_6-$(C\equiv C)_3$-R'_6	16.20	7.0	16.3	6.4
R'_6-C≡C-Ph-C≡C-R'_6	17.94	5.1	17.9 [10]	5.0
R'_6-C≡C-Ph-$(C\equiv C)_2$-R'_6	20.52	3.4	—	—

Previously, the intramolecular electron spin exchange integral values $|J|$ of these biradicals dissolved in toluene solutions have been experimentally measured from the electron paramagnetic resonance (EPR) spectra,13]. It was interesting to compare these values with appropriate parameters of the same biradicals. The results obtained are shown in Fig. 5, where $|J|$ values are given as $|J/a|$, e. g., in units of the corresponding hyperfine splitting (hfs) constants a [14]. One can see that the experimental curve has a good linear fitting in co-ordinates $\ln|J/a|$ — $R_{NO\text{-}NO}$ (Fig. 5).

Classical quantum chemistry predicts that in the case of direct spin exchange in vacuum, i. e., when spin exchange is realized via straight overlapping of the molecular wave functions, the value of $|J|$ has to decrease approximately tenfold with each one Å of the distance between unpaired electrons. Much less pronounceable experimental dependence of $|J/a|$ on $R_{NO\text{-}NO}$ allows us to suggest the efficient role of the bridge in the effective spin exchange coupling between radical centers in structurally rigid nitroxide biradicals.

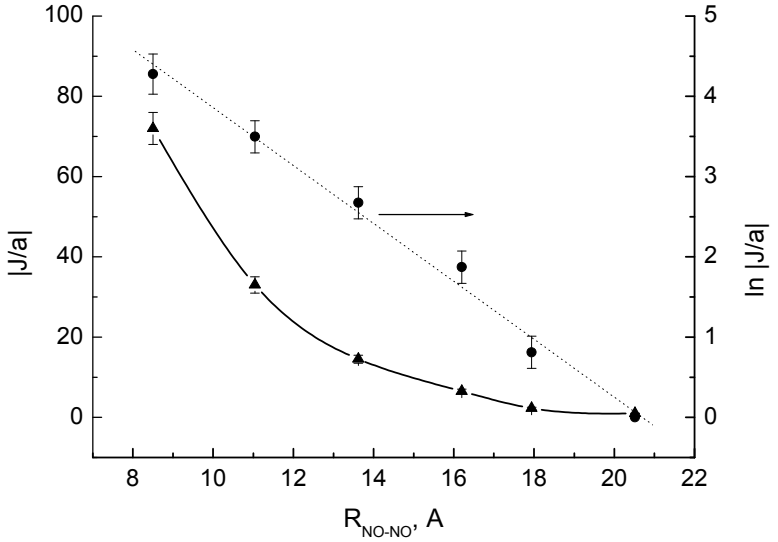

FIGURE 5. Experimentally measured values of the exchange integral $|J/a|$ *vs*. calculated distances $R_{NO\text{-}NO}$. (c).

Conclusion

DFT calculation at UKS/B3LYP/cc-PVDZ level allows obtaining correct structural information on acetylene-bridged nitroxide biradicals. Calculated geometries are in a good agreement with the experimental data, though distances $R_{NO\text{-}NO}$ are slightly longer than experimental ones. However, such distance dependent parameters as zero-field splitting constant D, can be calculated with a rather good agreement with those experimentally measured. The experimental dependence of the exchange integral value $|J|$ on the distance $R_{NO\text{-}NO}$ is not so strong as is predicted by the quantum chemical theory in case of through-space interaction.

The research is partially supported by RFBR Grant 12-03-00623-a.

Calculations were performed using resources of the Supercomputing Center of Lomonosov Moscow State University [15].

1. M. Abe, *Chem. Rev.*, 2013, v. 113, 7011—7088.

2. A. I. Kokorin, B. Mladenova, E. N. Golubeva and G. Grampp, *Appl. Magn. Reson.*, 2011, v. 41, pp. 353—362.

3. A. I. Kokorin, V. N. Khrustalev, E. N. Golubeva, *Appl. Magn. Reson.*, 2014, v. 45 (in press).

4. A. I. Kokorin, *Appl. Magn. Reson.*, 2004, v. 26, pp. 253—274.

5. T. H. Dunning, Jr., *J. Chem. Phys.*, 1989, v. 90, pp. 1007—1023.

6. L. Noodleman, *J. Chem. Phys.*, 1981, v. 74, pp. 5737—5743.

7. L. Noodleman and E. R. Davidson, *Chem. Phys.*, 1986, v. 109, pp. 131—143.

8. F. Neese, *J. Chem. Phys.*, 2007, v. 127, p. 164112.

9. F. Neese, *The ORCA program system*, Wiley Interdiscip. Rev., Comput. Mol. Sci., 2012, v. 2, pp. 73—78.

10. A. I. Kokorin and V. N. Khrustalev, unpublished results.

11. R. P. Shibaeva and L. P. Rozenberg, *Zh. Strukt. Khimii*., 1975, v. 16, pp. 258—261.

12. A. I. Kokorin, E. N. Golubeva, B. Y. Mladenova, V. A. Tran, T. Ka´lai, K. Hideg and G. Grampp, *Appl Magn Reson.*, 2013, v. 44, pp.1041—1051.

13. A. I. Kokorin, V. V. Pavlikov and A. B. Shapiro, *Proc. Acad. Sci. USSR, Doklady Phys. Chem.*, 1980, v. 253, pp. 525—527.

14. V. N. Parmon, A. I. Kokorin and G. M. Zhidomirov, *Stable Biradicals*, Nauka, Moscow, 1980.

15. Vl. V. Voevodin, S. A. Zhumatiy, S. I. Sobolev, A. S. Antonov, P. A. Bryzgalov, D. A. Nikitenko, K. S. Stefanov and Vad. V. Voevodin, *Practice of "Lomonosov" Supercomputer* Open Systems Publ., Moscow, 2012, no. 7 [http://www.osp.ru/os/2012/07/13017641/].

Gas-sensitive Properties of Poly-para-xylylene Based Thin Composite Films Containing Ti and TiO_2 Nanoparticles

Alexey Yu. Khnykov[1], Sergey A. Zavyalov[2,3], Evgeny I. Grigoriev[2,3], Valentina V. Zakharova[2] and Sergey N. Chvalun[3]

[1] Enikolopov Institute of Synthetic Polymeric Materials of RAS, Profsoyuznaya Str, 70, Moscow, 117393, Russian Federation
[2] Karpov Institute of Physical Chemistry, Vorontsovo Pole Str, 10, Moscow, 105064, Russian Federation
[3] National Research Center "Kurchatov Institute", Academica Kurchatova Sq, 1, Moscow, 123182, Russian Federation

The problem of testing of atmosphere composition is very actual now in solving many tasks such as environmental monitoring, industrial waste inspection, checkup of food freshness, search of drugs, explosives, toxic agents etc. Existing semiconductor gas sensor have too high operating temperature, bad selectivity, bad reproducibility of results and can be regenerated with difficulty [1]. Piezoresonance gas-sensing devices can measure the concentration of narrow range of gases and have very short life duration [2]. So it is necessary to work out the new models of gas sensors. During the recent two decades such new type of materials as polymer nanocomposites attracts significant attention of researchers because of the specific properties of these materials [3]. The employment of nanostructural materials as a sensitive layer of gas sensors makes it possible to improve most of operating characteristics of these devices [4]. Recent investigations have shown that the nanocomposites in which metal or semiconductor nanoparticles are diffused in poly-p-xylylene matrix exhibit very high sensitivity to a few gases and vapors [5—9]. This report is devoted to influence of water, ethanol, propylbenzene, benzene and toluene vapors upon the electrophysical properties of thin (thickness about 1 μm) films made of nanocomposites poly-p-xylylene/titanium(titanium oxide).

The films under study was prepared by VDP-synthesis [10, 11]. The samples with the filler volumetric content of 7, 8, and 12 % was investigated.

Voltage-current curves of the samples at direct voltage at different partial pressures of some vapors was obtained for finding out the character of the conductance dependence on the composition of atmosphere. Curves had the ohmic character. The result was obtained that the DC-conductance of the films under consideration goes up till 6 orders of magnitude when the concentration of high-polar molecules (H_2O, C_2H_5OH) in the air increases. The measurements had also shown that the presence of low-polar ($CH_3C_6H_5$) or nonpolar (C_6H_6) molecules in the atmosphere doesn't exert any impact on the DC-conductivity.

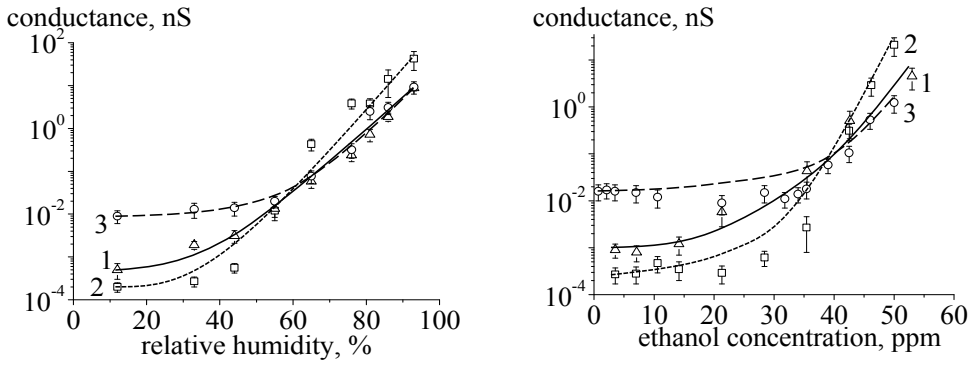

a *b*

FIGURE 1. Dependences of titanium-containing samples conductivity on relative humidity (a) and ethanol concentration in the air (b). Curves 1, 2 and 3 correspond to nanocomposite containing 7, 8 and 12 vol.% of filler respectively.

The molecules of propylbenzene have the intermediate between two above cases value of dipole moment and have the effect of intermediate character on the conductance, i. e. the small increase of it. So, the dipolar moment of adsorbate molecule is important for sensor effect. The described phenomenon may be explained as follows: the adsorbed molecules modify the value of surface dipole moment at nanoparticle/polymer interface, thereby changing the vacuum levels shift at the interface and this in turn alters the electron work function from nanoparticle into polymer matrix. Therefore the conductance also modifies. The sample, containing the quantity of filler near percolation threshold, is the most sensitive because in this case the conductivity under adsorption changes not only quantitatively but also qualitatively, i. e. the charge transport mechanism gradually alters from activated tunneling between nanoparticles and traps to the current through continuous cluster of nanoparticles.

The observation of behavior of nanocomposite DC-conductance at gas adsorption doesn't allow to solve a problem of selectivity, i. e. we can't find out what gas namely has provoked the change of conductance. So it arouse interest if the measurements of samples complex impedance (or complex dielectric permittivity) at different frequencies of alternating voltage in the atmospheres of different compositions may get over this difficulty. To this purpose the frequency dependences of capacity and the conductance of the nanocomposite samples at alternating voltage was obtained. The curves of capacity versus frequency was approximated by the Debye law using the least-squares method (regression method).

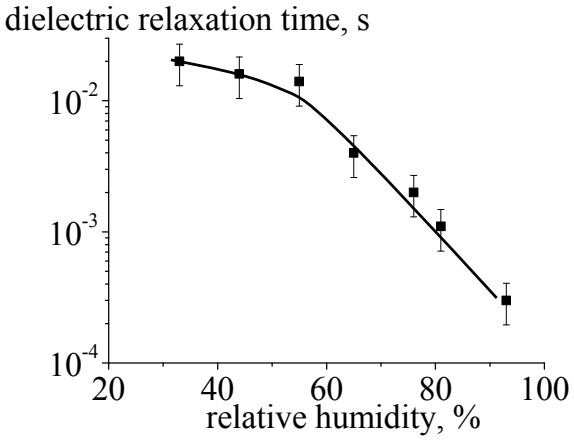

FIGURE 2. The dependence of dielectric relaxation time on the air humidity for sample containing 8 vol.% of titanium oxide.

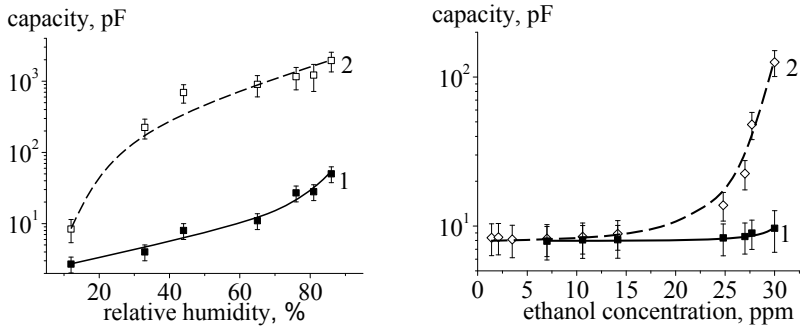

a *b*

FIGURE 3. a) humidity dependence of 1-capacity corresponding high-frequency dielectric permittivity, 2-capacity corresponding low-frequency permittivity of sample containing 8 vol.% of titanium oxide; b) the dependence of: 1-high frequency capacity, and 2-low-frequency capacity on the ethanol concentration in the air for sample containing 12 vol.% of titanium.

The values of capacities corresponding low-frequency permittivities and high-frequency permittivities (capacity is proportional to the permittivity) and the effective values of dielectric relaxation time was derived from the curves. It was turned out that the above quantities significantly depend on the concentration of polar molecules in the air (Fig. 2, 3).

The values of complex dielectric permettivities in the air of zero humidity was obtained using impedance spectrometer for the composite film containing 8 vol.% of titanium oxide. The frequency dependence of complex dielectric modulus was calculated from this data. The values of reciprocal complex capacity in the air with humidity of 33 % was calculated from measured real capacity and AC-resistance of the identical sample. According this data the godographs of dielectric modulus and reciprocal complex capacity was plotted for humidities of 0 % and 33 % respectively. The numeral approximation of this data by the law of Cole-Cole (1) was carried out and the values of the ratio $\varepsilon_0/\varepsilon_\infty$ (ε_0 — low-frequency dielectric permittivity, ε_∞ — high-frequency dielectric permittivity), α (parameter of relaxation time spread) and τ (effective relaxation time) were obtained. The calculations had given the following values of parameters: for humidity equal to 0 % $\varepsilon_0/\varepsilon_\infty = 4.2 \cdot 10^7$, $\alpha = 6 \cdot 10^{-2}$, $\tau = 5.2 \cdot 10^4$ s, for humidity equal to 33 % $\varepsilon_0/\varepsilon_\infty = 1.53 \cdot 10^3$, $\alpha = 2.3 \cdot 10^{-2}$, $\tau = 1.9 \cdot 10^{-2}$ s. The differences can be explain as follows. In the systems under study three mechanisms of dielectric relaxation with characteristic times of different orders of magnitude act. The most rapid relaxation is given rise by the orientation of physically adsorbed polar molecules (relaxation time about hundredth parts of second or smaller). More sluggish process — recharge of surface states formed by the particles chemisorbed on interface between filler and polymer matrix (relaxation time between tenth parts of second and tens of seconds). And the slowest relaxation — process being due to the phenomena of Maxwell-Wagner or volume polarization with characteristic time of tens of second or greater. There are no adsorbed molecules or their parts on the nanoparticles in the dry air, therefore the third relaxation mechanism is dominated, so the ratio of $\varepsilon_0/\varepsilon_\infty$ is greater than for the humid air for which the fast polarization contributes to the common dielectric response. The same reason provokes the fact that average relaxation time for dry air is much more than for moist atmosphere. The process of Maxwell-Wagner in our samples is equivalent to one in the system of huge quantity of different resistors and capacitors connected in a random way. That is why the distribution width of relaxation times for this phenomena is significant. The formation of third phase doesn't occur at the humidity of 33 %, therefore adsorption doesn't change the structure of composite, so volume polarization passes in the humid air in the same way as for dry one. At the same time the relative distribution width of relaxation times for the recharge of surface states is less than for Maxwell-Wagner processes. That is why the parameter α, characterizing the relative distribution width for humid air is less than for dry one. The set of four values: ε_0, ε_∞, α, τ is unique for given concentrations of given gases collection in the atmosphere surrounding the composite film. Therefore the measurement of this values set allows us to solve a problem of selectivity, i. e. to determine the composition of gas medium.

$$\varepsilon = \varepsilon_\infty + \frac{\varepsilon_0 - \varepsilon_\infty}{1 + (i\omega\tau)^{1-\alpha}} \qquad (1)$$

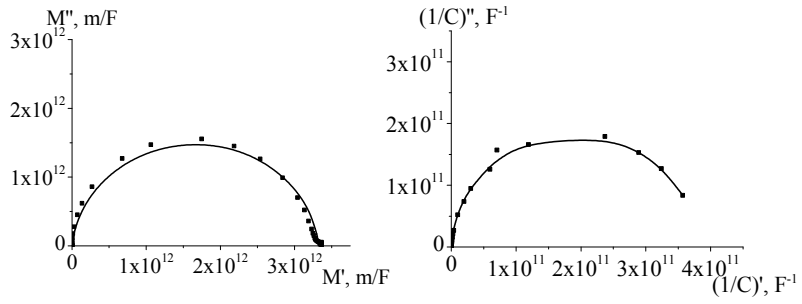

a *b*

FIGURE 4. The godographs of complex dielectric modulus and reciprocal complex capacity in the air with humidity of 0 % (a) and 33 % (b) respectively for the sample containing 8 vol.% of titanium oxide.

Along with the above measurements the investigations of the time dependence of the current after application of the positive or negative voltage step were carried out. In the case of positive step the current firstly spiked in a short space of time and then decreased tending to a limit. This process after initial peak can be conditionally approximated by the sum of constant and the decreasing exponent (Fig. 5). The result was obtained that the time constant of this exponent depends on the air composition. In the case of negative step the current decayed with the course of time. This time dependence can be conditionally approximated by the damped exponential curve with a certain effective time constant. Time constant decreased as the humidity increased (Fig. 6a). This fact can be explain as follows: the more humidity the more contribution of fast relaxation of surface states recharge comparing with the contribution of slow Maxwell-Wagner processes in the common relaxation process.

Therefore the effective relaxation time decreases as the water vapor concentration rises. The above time dependence of current can be approximated by the sum of constant and two decreasing exponents with different time constants (Fig. 5). The ratio of pre-exponential factor of "fast" exponent to pre-exponential factor of "slow" exponent characterizes the relative contributions of fast and slow relaxation processes. It can be seen on the Fig. 6b, that this ratio increases as the humidity increases, which corresponds to the growth of the relative part of interfacial states recharge in the common relaxation.

The above stated information indicates that the new types of selective gas sensors may be worked out, using parameters of frequency dependence of capacity and the parameters of the time dependence of current after application of voltage steps for the thin nanostructured PPX/metal(semiconductor) films as a sensitive parameters.

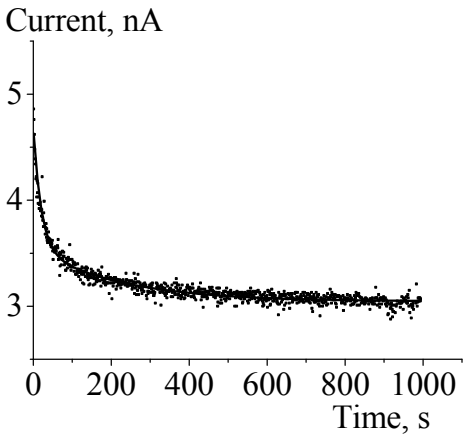

FIGURE 5. The time dependence of current after application of voltage step to the nanocomposite sample containing 12 vol.% of titanium.

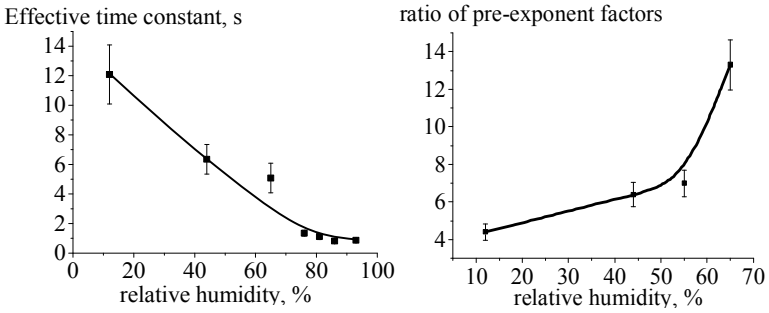

a *b*

FIGURE 6. a) The dependence of the effective time constant of the current decay after voltage switch off, b) ratio of the pre-exponent factors of the "quick" and "slow" damped exponential curves in the approximation of the time dependence of current after application of the positive voltage step.

Supported by RFBR 14-03-00890.

1. *Полупроводниковые* сенсоры в физико-химических исследованиях / И. А. Мясников, [и др.]. М. : Наука, 1991. 330 с.

2. Development of QCM Trimethylamine Sensor Based on Water Soluble Polyaniline / L. Guang [et al.] // Sensors (Peterborough, NH). 2007. V. 7. № 10. P. 2378—2388.

3. Godovski, D. Yu. Electron behavior and magnetic properties of polymer-nanocomposites/ D. Yu. Godovski // Advances in polymer science. 1995. V. 119. P. 79—122.

4. Jimenes-Cadena, G. Gas sensors based on nanostructured materials / G. Jimenes-Cadena, J. Riu, F. X. Rius // Analyst.. 2007. V. 132. № 11. P. 1083—1099.

5. Preliminary Study of the Interaction of Metal Nanoparticle-containing Poly-p-xylylene films With Ammonia / G.B. Sergeev [et al] // Analytical Communications. 1997. V. 34. №4. P. 113—114.

6. *Влияние* света и адсорбции газов на электропроводность наногетерогенных металл-полимерных материалов / Г.Н. Герасимов [и др.] // Химическая Физика. 1998. Т. 17. №6. С. 168—173.

7. Sensor Properties, Photoconductivity and Dielectric Behaviour of Poly-p-Xylylene Films Containing Semiconductor Nanocrystals / L.I. Trakhtenberg [et al.] // Israel Science and Technology. 1999. V. 1. №3. P. 34—42.

8. *Хныков А.Ю.* Газочувствительные свойства тонкоплёночных нанокомпозитов на основе поли-п-ксилилена с низким содержанием палладия / А.Ю. Хныков, С.А. Завьялов, С.Н. Чвалун // Высокомолекулярные соединения А. 2002. Т. 44. №10, С. 1858—1861.

9. *Хныков А.Ю., Завьялов С.А., Григорьев Е.И., Чвалун С.Н.* Электрофизические свойства нанокомпозитов на основе поли-пара-ксилилена с наночастицами меди // Высокомолекулярные соединения А. 2006. Т. 48. №11. С. 1968—1976.

10. *Озерин С.А.* Синтез, структура и свойства гибридных нанокомпозитов на основе серебра, сульфида свинца и поли-п-ксилилена дис. … канд. физ.-мат. наук : 02.00.06: защищена 06.10.2005 / Озерин Сергей Александрович. М., 2005. 127 с.

11. *Григорьев А.Е.* Фотопроводящие и сенсорные свойства поли-п-ксилиленовых плёнок, содержащих наночастицы металла: дис. … канд. физ.-мат. наук: защищена 11.10.99 / Григорьев Алексей Евгеньевич. М., 1999. 123 с.

M-7

Properties of Nanostructured Metal Oxide Catalysts Studied by Various Physical Methods

Alexander I. Kokorin[1], Tatjana V. Sviridova[2], and Dmitry V. Sviridov[2]

[1] Semenov Institute of Chemical Physics, Russian Academy of Sciences, Moscow, Russia
[2] Chemistry Department, Belarusian State University, 220030 Minsk, Belarus

In the last decades, the mixed oxides of molybdenum and vanadium have attracted much interest as one of the most prospective catalyst for oxidation of hydrocarbons [1, 2] and sulfured organics [3] by molecular oxygen. However, the elaboration of the effective Mo-V oxide catalysts well adapted to the specific chemical reactions provides a problem due to a diversity of binary oxides which can be formed in the V_2O_5-MoO_3 system depending on the synthetic route used and the possibility of realization of different oxidation mechanisms, the role of which varies with temperature. Thus, in the low-temperature range (200—300 ºC), the singlet oxygen generated at the active sites of the mixed oxide catalyst appears to be involved in the oxidation [4]. In this paper, the role of structural features of molybdenum-vanadium nanocatalyst in the formation of its oxidation properties is discussed.

The dispersion of nanostructured oxide V_2O_5:MoO_3 was synthesized by solvothermal method described elsewhere [5]. As the precursors, vanadic and molybdic acids obtained via ion exchange technique (by acidification of $(NH_4)_6Mo_7O_{24}$ and NH_4VO_3 aqueous solutions on resin) were used. Freshly prepared solutions of oxoacids were mixed in the amounts corresponding to the mole ratio of V:Mo = 1:1 and incubated at 100 ºC for 5 h. The resultant mixed oxide V_2O_5:MoO_3 was then separated by centrifugation. The SEM micrograph given in Fig. 1a evidences that thus obtained oxide dispersion has non-compact layered structure with lamellas built of small aggregates. According to the XRD analysis, the size of crystallites forming these aggregates is below 50 nm.

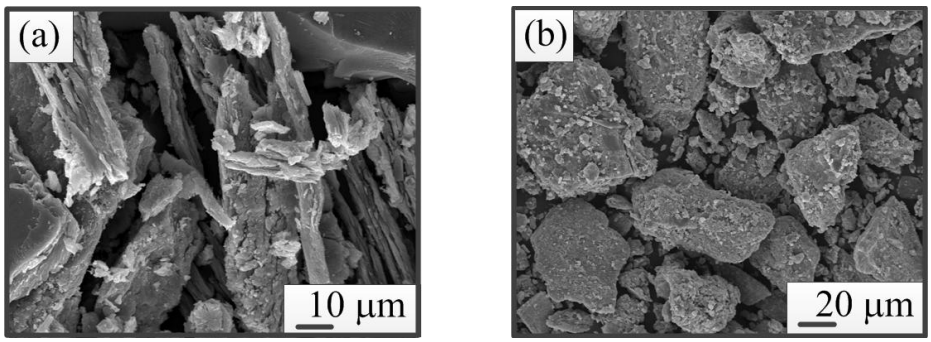

FIGURE 1. SEM images showing the general morphology of V_2O_5:MoO_3 particles: (a) freshly prepared, (b) annealed at 400 ºC.

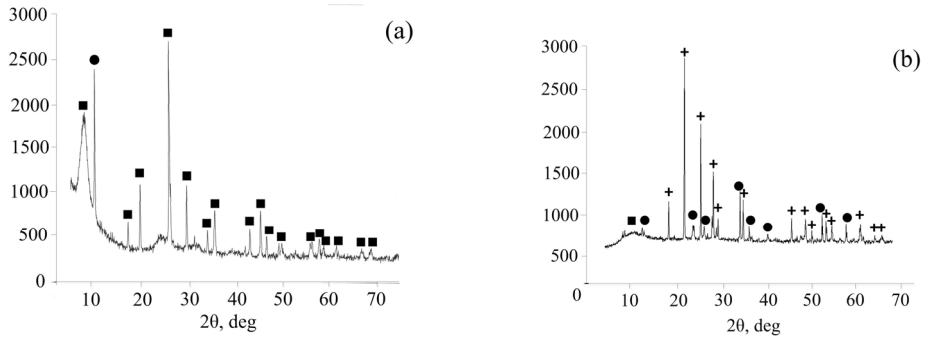

FIGURE 2. The XRD patterns of V_2O_5:MoO_3 catalyst: (a) freshly prepared, (b) annealed at 400 C. (●) hexogonal MoO_3; (■) xerogel V_2O_5; (+) monoclinic $V_{3.6}Mo_{2.4}O_{16}$.

The XRD patterns given in Fig. 2 evidence that thermally stimulated polycondensation of molybdic and vanadic acids yields a xerogel of hydrated V_2O_5 in which some of V^{5+} sites are substituted by Mo^{6+} ions, this xerogel also containing an admixture of hexagonal molybdenum trioxide. The low-energy shift of IR band at 1009.6 and 470.0 cm^{-1} (Fig. 3), which correspond, respectively, to ν(V = O) and

δ(V-O) vibrations, also provides an evidence that substitution occurs in xerogel under solvathermal conditions. As the result, the solid solution isomorphous to vanadium oxide xerogel is formed, this xerogel containing large amount of bound water as evidenced be IR spectroscopy (Fig. 3); the excess of molybdenum oxide which is not enter into xerogel exhibiting crystallization forming individual hexagonal phase.

Very close ionization potentials inherent in V^{5+} and Mo^{6+} ions facilitates their substitution in the xerogel matrix, the latter process being accompanied with transition of corresponding number of vanadium ions into V(IV) state to stabilize Mo^{6+} ions.

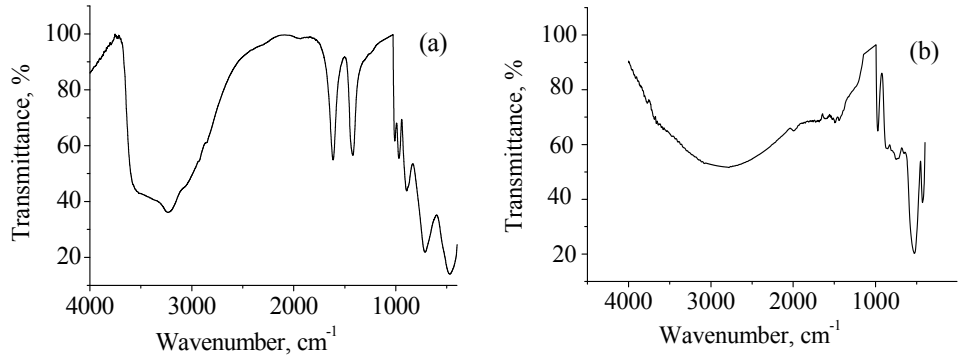

FIGURE 3. The IR spectra of V_2O_5:MoO_3 catalyst: (a) freshly prepared, (b) annealed at 400 ºC.

The paramagnetic centers V(IV) arising in the xerogel matrix were studied with ESR technique at 77 K; the ESR spectrum of $VOSO_4$ was also recorded for comparison. It is seen from Fig. 4 that the ESR spectrum of V_2O_5:MoO_3 represents a superposition of anisotropic singlet line (corresponds to the associates of paramagnetic centers) with multicomponent spectrum from isolated V(IV) ions. It should be noted that the number of isolated centers generated in V_2O_5:MoO_3 during synthesis exceeds the number of V(IV) centers typical of microcrystalline molybdenum-vanadium oxides obtained by thermal decomposition of co-precipitated ammonium molybdates and vanadates [4].

Since V_2O_5:MoO_3 catalysts normally operate at elevated temperatures, the effect of thermal treatment on structural and morphological features of solvathermally-derived molybdenum-vanadium oxides was investigated.

It is seen from SEM micrograph given in Fig.1b that heating results in the disruption of the lamellar structure of the mixed oxide yielding sintered aggregates ca. 20 μm in size which are built from mach smaller particles ca. 500 nm in size. The XRD pattern given in Fig. 2 provides an evidence that along with V_2O_5 xerogel-based solid solution and hexagonal MoO_3, the monoclinic phase $V_{3.6}Mo_{2.4}O_{16}$ is detected after heat treatment. The partial conversion of xerogel into monoclinic binary oxide is accompanied with dehydration of the sample that manifests itself in the IR spectrum as the degradation of the bands corresponding to vibrations of OH groups(Fig. 3).

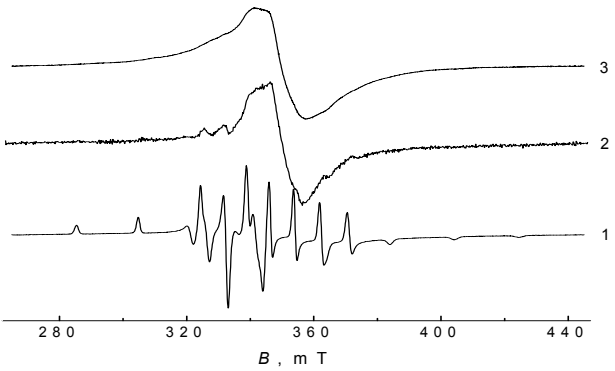

FIGURE 4. The ESR spectra at 77 K of V_2O_5:MoO_3 catalyst: *2* — freshly prepared, *3* — annealed at 400ºC. *1* is a frozen 0.005 M aqueous-ethanol solution $VOSO_4$.

The ESR measurements indicate that the content of paramagnetic V(IV) centers exhibits rather slight increase upon annealing (Fig. 4). The concentration of unassociated centers decreasing upon annealing, while the amount of associated vanadyl-like centers in the nanocrystalline V_2O_5:MoO_3 samples obtained in the work increases. The parameters of ESR spectrum of heated nanostructured V_2O_5:MoO_3 ($A_{||}$ = 173—184 mT) are lower than that of microcrystalline V_2O_5:MoO_3 that points to the reinforcement of V = O bond in the nanostructured mixed oxide as compared to microcrystalline samples.

TABLE 1 The efficiency of benzene and thiophene oxidation by molecular oxygen at V_2O_5:MoO_3 catalysts at 250 ºC.

V_2O_5:MoO_3 sample	Conversion degree, %	
	Benzene	Thiophene
Freshly prepared	0.7	31.0
Annealed at 400 C	0.5	41.0

It is seen from Table 1 that calcination of V_2O_5:MoO_3 mixed oxide improves its catalytic activity towards oxidation of thiophene that amounts 40 %, while the activity towards oxidation of benzene does not exceed 1 %. Low rate of benzene oxidation, which is ca. 20 times less than that in the case of microcrystalline V_2O_5:MoO_3 catalyst derived via thermal decomposition of corresponding salts, can be attributed to high strength of V = O bond (widely accepted as an active site for catalytic oxidation process [1, 6]). On the other hand, the pronounced activity towards oxidation of sulfured organics is due to the high concentration of VO(II) centers in the lattice of xerogel-based solid solution.

The obtained results allow a conclusion that in the case of V_2O_5:MoO_3 mixed oxides there exist two independent catalytic systems: (i) solid solutions responsible

for activity of the catalyst towards oxidation of hydrocarbons and (ii) vanadyl-like redox centers responsible for oxidation of sulfide groups. By tailoring the structural features of V_2O_5:MoO_3 oxide through choosing of the proper synthetic rout and synthetic conditions, it is possible to adjust its catalytic properties by changing the contribution of these two mechanisms. Thus, for example, the nanostructured V_2O_5:MoO_3 oxide opens new avenues in the development of effective industrial and environmental systems for catalytic elimination of sulfured compounds capable to operate at low temperatures (below 200—250 ºC).

Acknowledgement. This work was supported by the Russian Foundation for Basic Research and the Basic Research Foundation of Belarus.

1. A. Satsuma, A. Hattori, K. Mizutani, A. Furuta, A. Miyamoto, T. Hattori, Y. Murakami, *J. Phys. Chem.,* 1989, V. 93, pp. 1484—1490.

2. P. A. Vakhrushin, T. V. Sviridova, M. V. Vishnetskaya, D. V. Sviridov, A. I. Kokorin, *Russian Journal of Physical Chemistry B*, 2012, Vol. 6, No. 6, pp. 711—715.

3. T. V. Sviridova, A. A. Antonova, E. V. Boikov, M. V. Vishnetskaya, D. V. Sviridov, A. I. Kokorin*, Russian Journal of Physical Chemistry B,* 2013, Vol. 7, No. 2, pp. 118—122.

4. A. I. Kokorin, A. I. Kulak, I. S. Tomski, Yu. N. Rufov, *Russ. J. Phys. Chem. B,* 2013, Vol. 7, No 3, pp. 255—261.

5. T. V. Sviridova, L. I. Stepanova, D. V. Sviridov. *Molybdenum: Characteristics, Production and Applications*. Eds. Ortiz M., Herrera T. Nova Sci. Publ., New York, 2012, pp. 147—179.

6. E. V. Boikov, T. V. Sviridova, M. V. Vishnetskaya, D. V. Sviridov, A. I. Kokorin, *Russ. J. Phys. Chem. B*, 2013, Vol. 7, No 3, pp. 251—254.

Stable Heterogeneous Plasmoid in Swirl Flow

Klimov A., Grigorenko A., Efimov A., Kazansky P.,
Polyakov L., Sidorenko M., Tolkunov B.

Institute for High Temperature RAS, Izhorskaya 13, bld. 2, Moscow 127415, Russia

Swirl flow control and a vortex control near a flying vehicle realized by a non-equilibrium plasma formation (plasmoid) is the important key task in a plasma aerodynamics today. Experimental results obtained during this study can be used in aviation and the plasma-assisted combustion [1—6].

Physical properties of a longitudinal plasmoid created by the capacity coupled high-frequency discharge in the high-speed swirl flow are studied in our works [1—6] in detail. Measurement of a power budget in this HF plasmoid in swirl flow is a very important for an aluminium- hydrogen power generation [4] and extra power production [1—8, 10]. This work is a continuation of the previous one [6].

Remind that the artificial stable microwave (MW) plasmoid was obtained by Kapitsa P. in the swirl gas flow namely [7]. This MW plasmoid had unusual physical properties close to the observed properties of a *natural ball lightning*. What was the role of a swirl flow in the stable plasmoid creation in his experiment? The answer to this question has not been given in his theoretical model and has been left for further investigations. Now this question is studied in our work in detail.

The experimental setup was described in the previous work [6]. General view of this set up is shown in the Fig. 1. Plasma — vortex reactor (PVR) is made of a quartz tube with a diameter 60 mm. A swirl gas flow (or a non-swirl one) is created both by a tangential gas injector and an axial gas injector in this reactor. The swirl flow in PVR is excited and heated by the combined discharge (HF+DC). A mass flow rate is measured in this experiment. The testing gases used in this set up are the followings: — air, nitrogen, argon, water steam and their mixtures. Argon-water steam mixture (10:1) is used also. This mixture is used to obtain dissociated *hydrogen* in the argon plasma and to study of their interaction with metal clusters. The typical parameters of a pulsed repetitive HF generator used in this work are the following: a maximal output pulsed voltage is ~ 60kV, a pulsed HF power is ~ 1÷10 kW, a HF frequency is F_{HF} ~ 0.3—10 MHz, a pulse repetitive frequency is $F_{P1} = 10 \div 10^4$ Hz, pulse duration is $T_p = 10\mu s \div 100ms$. The typical parameters of the high — current pulse repetitive discharge are the following: a pulse current is up to 100 Amp, a pulse duration is 1—100 μs, and a pulse repetitive frequency is $F_{P2} = 10 \div 10^4$ Hz. Typical parameters of the non-equilibrium continuous DC discharge are the following: a current ~ 1—2 Amp, a mean power 1—2 kW.

It was mentioned in our previous work [6] that an extra heat release in the PVR can be connected with LENR (low energy nuclear reactions) in the heterogeneous cluster plasmoid. In order to study this question in detail it is necessary to measure the X-radiation from this plasmoid [7, 9, 11]. The wave range of this X-radiation is within 100÷10000 eV. A spectrometer X-123 is used to measure the X-radiation from the heterogeneous plasmoid in the swirl flow. The typical X-spectra are shown in the Fig. 2.

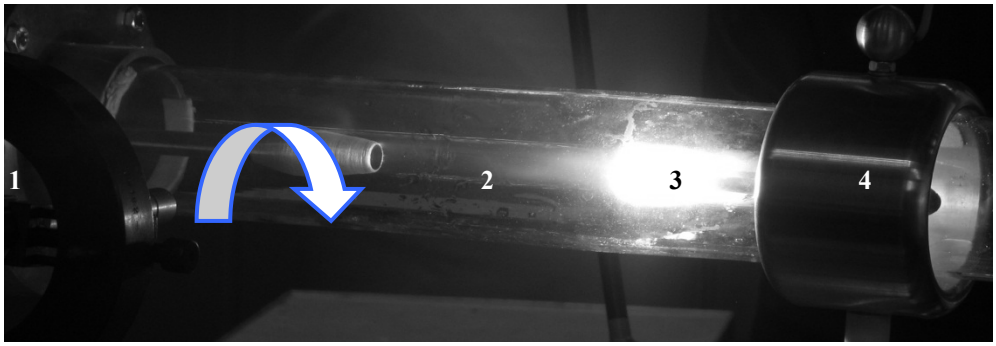

FIGURE 1. Heterogeneous plasma created by pulsed repetitive combined discharge in swirl flow. Gas mixture Ar: H_20 = 10:1. Axial velocity V_x is closed tangential velocity V_t: $V_x \sim V_t \sim 30$m/s, $P_{st} \sim 1.5$ Bar. *1* — swirl generator, *2* — water steam injector, *3* — erosive metal clusters, *4* — cathode.

It was revealed that

1. The intensive X-radiation (Fig. 2) is created by the heterogeneous plasmoid (3, Fig.1) namely. This radiation is absent in the diffuse plasma (2, Fig. 1). Remember that the heterogeneous plasmoid is created by the combined discharge in the following gas mixture: Ar: water steam ~ 10: 1. Dissociated hydrogen is intensively created by the diffuse plasma in this regime (2, Fig. 1). Recorded optical spectra proved this conclusion.
2. There are some maxima in the recorded spectra. The first main maximum is located near $\lambda_1 \sim 1.3$ keV. The second maximum is located at $\lambda_2 \sim 4.6$ keV.
3. The X-spectra are recorded behind a reactor nozzle also. Note that an electric discharge is absent in this region but excited hydride metal clusters existed in the swirl flow (drifted away by this flow). So, these excited and charged cluster particles are responsible for the X- radiation generation namely. Our suggestion is connected with an important role of LENR on X-radiation generation by the cluster particles [9].
4. An intensity of X-radiation is controlled by a polarity of the erosive (or evaporated) electrode. The maximal intensity of the X-radiation is measured near the cathode electrode. A positive hydrogen ion flux (protons) bombarded its surface in this regime.

5. It is revealed that the maximal extra energy release is measured in the PVR at the maximal X-radiation intensity.

6. The X-radiation is absent in the swirl plasmoid without the water steam injection at the same electric discharge and the argon flow parameters.

7. The X-spectra of decaying plasma flow behind the nozzle are changed dramatically with respect to the one in the heterogeneous plasmoid. There is only one maximum (pike) in this regime only.

Summarizing all obtained experimental results one can suppose that the X- radiation is connected with a metal hydride cluster creation near the erosive electrode (see bright erosion plasma (3) in the Fig. 1. So, the theoretical model considered in the work [9] can be used to clear a physical mechanism of an extra energy release in our experiment.

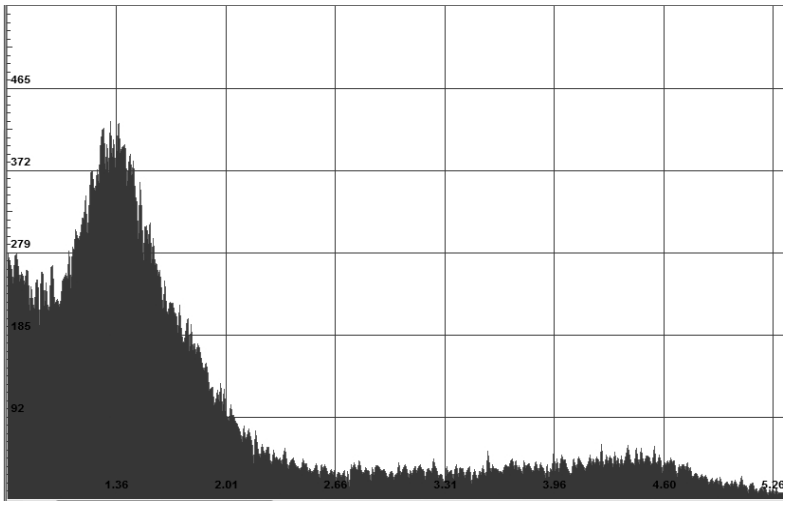

FIGURE 2. X-radiation from the heterogeneous plasma in the PVR. The combined discharge (DC+HF), a mean power — 500W, the hot electrode —cathode.

Optical spectra are recorded in the heterogeneous plasma in the swirl flow in our experimental setup PVR. The typical spectra are shown in the Figure 3. One can see lines of the excited argon atom ArI, excited hydrogen atom HI (Hα, Hβ), optical lines of atom MoI, hydroxyl radical OH in these spectra. There is a considerable continuous spectrum of molybdenum cluster particles in the figure 3. It is important to note that an intensity of the hydrogen optical lines is decreased in this regime considerably. This result may be connected with a strong interaction of hydrogen atoms and ions with cluster particles and molybdenum hydrides creation. An electron temperature estimated by processing of the optical lines of MoI and ArI is about $T_e \sim 6000$—7000 K. Plank's temperature estimated by the continuous cluster spectrum is about $T_b \sim 2000$ K. Rotational temperature estimated by the molecular band AlO is about $T_R \sim 2300$ K (aluminum electrodes are used in this experiment). So, it is revealed that there is the non-equilibrium heterogeneous plasma in the swirl flow with $T_e >> T_b, T_R$

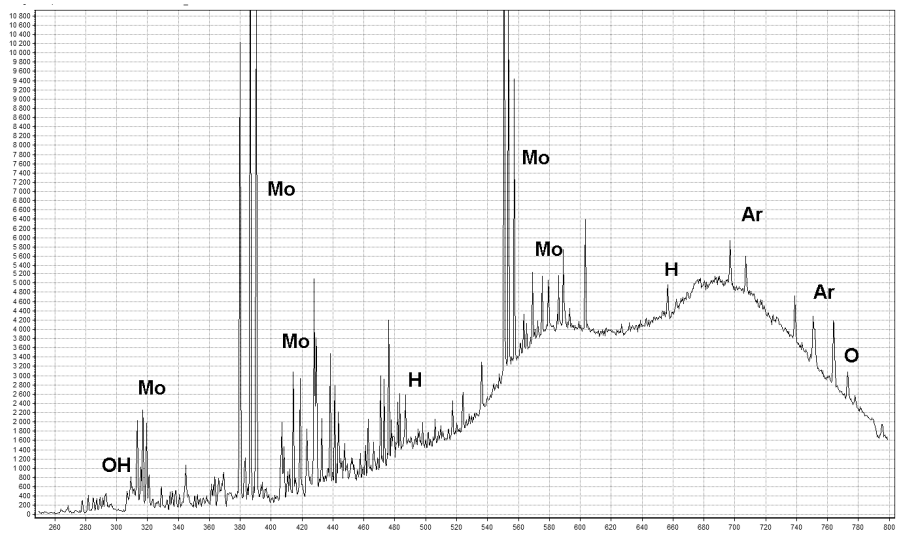

FIGURE 2. Optical spectrum of the heterogeneous plasma in the swirl flow. PVR, near cathode electrode, $T_e \sim 6350$K, $T_b \sim 1800$K.

Conclusion

1. Parameters of the heterogeneous non-equilibrium plasma are measured in the experimental set up PVR. An electronic temperature estimated by processing of the optical spectra is about $T_e \sim 6000$—7000 K. Plank's temperature estimated by the continuous cluster spectrum is about $T_b \sim 2000$ K. A rotational temperature estimated by the molecular band of AlO is about $T_R \sim 2300$ K (aluminum electrodes are used in the experiment). So, it is revealed that there is non-equilibrium heterogeneous plasma in the swirl flow: $T_e >> T_b, T_R$. According our opinion plasma-chemical kinetics *in cluster plasmoid* may be connected with *extra energy release in the PVR* [1, 6] (see, for example, [9, 14, 15]).

2. It is revealed that the heterogeneous non-equilibrium H_2O-Ar plasma is an intensive source of soft X- radiation with 1—10 keV quantum energy. This result correlates with the one obtained in the work [7].

3. It is revealed that there is a self — organization oscillation regime created by the DC discharge in H_2O-Ar plasma.

The work is supported by the Limited liability corporation "New Inflow". We thank Mr. V. Avdeychik, Mr. O. Grebenkin, prof. F. Zaitsev, and prof. N. Magnitskii for interest to this work and fruitful discussions.

1. Klimov A., Calorimetric Measurements in plasma vortex, Proc. 14th Conf. on Cold Nuclear Transmutation and Ball Lightning, Dagomys, Sept. 19—26, 2006, pp. 246—253.

2. Klimov A., Moralev I., et. al., Longitudinal Vortex Plasmoid Created by Capacity HF Discharge, AIAA Paper, Proc. 46th AIAA Conf. Reno NV, 7—11 Jan 2008, pp. 1—11.

3. A. I. Klimov, Vortex Plasmoids Created by High_Frequency Discharges, Atmosphere and Ionosphere: Dynamics, Processes, Monitoring (Springer, Berlin, 2012), pp. 251—273.

4. Klimov A., Bityurin V., Grigorenko A., et. al., Plasma- Assisted Combustion of Heterogeneous Fuel in High Speed Airflow, Proc. 6th TChPPA Workshop, 8—12 May 2008, St.- Petersburg, Russia, pp.1—15.

5. Klimov A., Bityurin V., Grigorenko A., et. al., Study of a Longitudinal Plasmoid Created by Capacity Coupled HF Discharge in Vortex Airflow, AIAA Paper 2009—1046, 47th AIAA Aerospace Sciences Meeting, 5—8 January 2009, Orlando, Florida, 2009, pp. 1—12.

6. Klimov A., Evstigneev N., Moralev I., et. al., Vortex Control by Combined Electric Discharge Plasma, AIAA Paper 2013—1046, 51th AIAA Aerospace Sciences Meeting, Dallas, Texas, 2013, pp. 1—15.

7. Kapitsa PL (1969) Free plasma filament in high frequency field at high pressure. Zhur Exp Teoret 515 Fiz 57(6): pp. 1801—1866.

8. Evstigneev N. Solution of 3D Non-Viscous Compressible Gas Equations on Unstructured Meshes Using the Distributed Computing Approach // Numerical Methods and Programming, Research Computing Center Moscow State University, V8, pp. 252—264. 2007.

9. A. Widom, L. Larsen, Ultra Low Momentum Neutron Catalyzed Nuclear Reactions on Metallic Hydride Surfaces, Eur. Phys. J. C (2006), pp. 1—5.

10. N. M. Evstigneev, F. S. Zaitsev, A. I. Klimov, N. A. Magnitskii, and O. I. Ryabkov, Mathematical Modeling of Energy Release in a Plasma Vortex Reactor, Doklady Mathematics, 2013, Vol. 87, No. 3, pp. 354—356.

11. R. L. Mills, The Grand Unified Theory of Classical Physics, Vol. 1: Atomic Physics (Black Light Power, Granbury, 2010), pp. 1—1238.

12. K. Tacibana, Excitation of, $1s_4$, $1s_3$ and $1s_2$ levels of argon by low — energy electrons. Physical review A, V.34, N. 2, 1986, pp. 1007—1015.

13. J. A. Blauer, G. R. Nickerson, A survey of vibrational relaxation data for processes important to $C0_2$-N_2-H_2O infrared plume radiation. Technical Report AFRPL-TR-73—57.

14. A. Emelianov, A. Eremin, V. Fortov, et. al., Quantum phenomena in ignition and detonation at elevated density, Phys. Rev. Lett. 109, Issue 14, 05 Oct 2012, pp. 25—54.

P-2

New Cases of Observation of High Energy Ball Lightning

Anatoly I. Nikitin, Tamara F. Nikitina and Alexander M. Velichko

Talrose Institute for Energy Problems of Chemical Physics, Russian Academy of Sciences, Moscow, 117829, Russia

The most mysterious property of ball lightning is its ability to accumulate a great amount of energy in the limited volume. As the first documentary case of high energy ball lightning observation one may consider the publication in the newspaper ”The Daily Mail (London)” on November, 5th, 1936 a letter to the editor named ”A thunderstorm mystery” [1, P. 7]: ” Sir, during a thunderstorm I saw a large, red hot ball come down from the sky. It struck our house, cut the telephone wires, burnt the window frame, and then buried itself in a tub of water which was

underneath. The water boiled for some minutes afterwards, but when it was cool enough for me to search I could find nothing in it". Dorstone, Hereford. W. Morris. Assuming that mass of water in the tub was 18 kg, it was heated up to 100^0C and a mass 1.8 kg was evaporated, energy of "English" ball lightning was estimated as 10 MJ, and the energy density as $\rho_E = 1.9 \cdot 10^{10}$ J/m^3 [2].

A "natural experiment", described by Mr. Morris, was not single. In August, 1962 in Ukraine near the town of Perechin a ball lightning the size of tennis ball fell in a trough with water for cattle. The water was almost completely boiled away from the trough, the cooked frogs laid at the bottom. The size of the trough was 0.3×2.5 m, depth of water layer was 15 cm [3, P. 106]. Accepting that mass of water in the trough was m_1 = 112.5 kg, mass of the evaporated water was m_2 = 100 kg, and water heating occurred from 10^0C to 100^0C, we find, that energy, transferred to water by ball lightning, was equal to 269 MJ. The volume of a tennis ball 6 cm in diameter is equal to 113 cm^3, from here the energy density of the "Ukrainian" ball lightning was $\rho_U = 2.38 \cdot 10^{12}$ J/m^3. Next important event occurred in July, 1972 in Hungary [4]. At midday during a break in the presence of numerous factory workers a brightly shining ball the size of soccer ball fell in a pit with 120 litres of water. All the water has evaporated. For heating of 120 litres of water by 80^0C and its evaporation the energy 311 MJ is necessary. Accepting the diameter of the ball equal to 25 cm, we find the energy density of the "Hungarian" ball lightning $\rho_H = 3.8 \cdot 10^{10}$ J/m^3. Thus, it is necessary to regard the cases, when the energy of ball lightning has been measured with the help of "water calorimeter", as the reliable facts. Below we will describe two new cases of estimation of energy of ball lightning.

New cases of observation of ball lightning in Russia.

1. A ball lightning on the Ucha River.

Here is the story of the participant of event engineer Nikolay Fyodorovich Ignatov that has occurred in July, 1964 on the river Ucha near the platform Mamontovka in the Pushkin district of the Moscow Region. The story-teller was 20 years old then.

"At that time I was the student of technical school of communication. At 4 o'clock in the morning I fished on the river Ucha. The sun has not rise yet, weather was clear, there was no rain this morning and overnight. In the place of fishing the width of the river was 20—30 metres. I had a simple reed fishing-rod with an ordinary line and hook. Before the described event I have caught 5—6 roaches which I held in the 10 l Gi pail. The pail was half-filled with water. I felt that fish had eaten a worm from a hook. I took out a line with an empty hook from water and when I was carrying the hook, hanging on the line, above the water's edge (the hook was about 1 metre above the ground), the shining ball with a diameter about 5 centimetres suddenly "clung" to it. I did not notice from where the ball had arrived. The weight of a sinker with the hook when the ball had stuck to it did not increase. I don't remember the colour of the ball, it was shining slightly brighter than a luminescent lamp, and its light did not blind eyes. The ball contour was accurate. I was confused and slowly lowered the hook with the ball, hanging on it, into the pail with the caught fish. At once the water began to hiss and gurgle, as it happens, when the heated stone is thrown into it. Water was boiling for some more minutes.

The fish was cooked so as it had been boiled too long: it had been skinned, scaled and gutted. At boiling a dense steam rose from water. The hook, tied to the line, had disappeared. The line remained untouched, it became only slightly shorter. In fear from the uncertainty of what had occurred, I upset the remains of the water with fish on the ground and came to a hostel with the empty pail. When I told my companions about the incident, they did not believe me: they decided that I had caught nothing and I was justifying myself for it. I had to go and show them the boiled fish on the ground. ”

Let's estimate the energy which was brought by ball lightning into the pail with the caught fish. The capacity of a standard pail, made from Gi, we will accept equal to 10 l. There was in it m_w = 5 kg of water and m_f = 0.9 kg of roach (6 fishes with an average weight 150 g). The initial temperature of water we will accept equal to 20 ^{0}C. Let the specific heat capacity of fish is equal to specific heat capacity of water c = 4.2 kJ/kg·K. The energy, spent for water heating by $\Delta\theta = 80\ ^0$C before boiling, is $Q_w = c\,(m_w + m_f)\Delta\theta$ = 1.98 MJ. It is necessary to add to this result the heat Q_p, spent for heating of the pail with mass m_p = 1 kg on $\Delta\theta = 80^0$C. A specific heat capacity of a steel is c_s = 0.46 kJ/kg·K, therefore $Q_p = c_s m_p \Delta\theta$ = 36.8 kJ. As a result we obtain that energy of the "Moscow" ball lightning appeared equal to $Q_M = Q_w + Q_p$ = 2 MJ. It is the lower estimate of energy. The eyewitness spoke about a production of steam at water boiling, on what, naturally, the part of energy of ball lightning was spent. But, because data about the quantity of the evaporated water is not available, we can tell nothing about amount of this additional energy. The volume of a ball of diameter 5 cm is equal to 65 cm^3, from here we find, that the energy density in the ball lightning was not less than $\rho_M = 3\cdot10^{10}$ J/m^3. As we see, this figure is well coordinated with the values of energy density of "English" ($\rho_E = 1.9\cdot10^{10}$ J/m^3) and "Hungarian" ($\rho_H = 3.8\cdot10^{10}$ J/m^3) ball lightning. Apparently, the fishing hook has disappeared because of action on it of the high-frequency electromagnetic field, radiated by ball lightning. The observers repeatedly informed about disappearance of metal subjects (rings, bracelets, etc.) after their meeting with ball lightning [3—6]. It is probably that water heating also occurred because of the action of this electromagnetic radiation on it.

Behind Nikolay Fyodorovich at a distance 215 m from him there was the electrified railroad along which every 5—10 minutes the freight and passenger trains were passing. According to the eyewitness, there was not a thunder-storm at this time. Therefore the possibility is not excluded that the ball lightning was created in an electric arch at a locomotive slip ring. Because this happened behind the back of the story-teller, he could not see the formation and approaching to him of the shining ball. In the literature there are the descriptions of cases of occurrence of ball lightning at breaking of contacts of electric power plants, including a trolley line. On June, 18th, 1981 the inhabitant of Odessa T. B. Borodina observed an unusual picture: ”When the trolleybus was turning at intersection, its bow came off. It hit wires a few times, causing short-term short circuits, there was a crash, and sparks flew down. Suddenly the round bright ball 15—20 centimetres in diameter, in colour and brightness reminding an electric welding arch, separated from a lump of sparks. The ball crossed a road at a height of trolleybus wires, fell on wires of an opposite trolleybus line and began to move ahead along them with a speed, a little

larger, than before. The wires were fixed on the lamp posts. As the ball was passing under the lamps, they flashed by turns. So the ball flew past 3 or 4 lamps" [7, P. 107]. Trolleybuses are fed with a direct current with strength 200 A at voltage 500—750 V. Thus, if to assume, that ball lightning formation lasted about one second, its energy could be from 100 to 140 kJ. In the Soviet Union electric trains were fed with a direct current at voltage 3300 V. A power of electric locomotive was equal to 4.4 MW, and a power of the motor car of electric train was 0.88 MW. Thus, energy of ball lightning, equal to 2 MJ, could be received from an arch between a contact wire and a slip ring, lasting 0.45—2.3 seconds.

2. Ball lightning in Buryatia.

On May, 27th, 2013 at 15 o'clock of local time ball lightning destroyed a house in the outskirts of village Mogsokhon of Kizhinginsky district of Buryatia [8]. According to the stories of eyewitnesses of the event, "that day nothing indicated the tragedy. The usual rain began, but suddenly a thunder struck of such force, that passers-by and the cattle, being at this time in the street, crouched with horror and fled their several ways. A minute later after that the bright shining ball descended from the sky and forced its way into the house of the Bayan Sandanov's family through a roof. Then there was a deafening explosion inside the house. A housewife, the spouse of the Bayan, cleaning the kitchen after a dinner, was in the house during the explosion. Found under pieces of a fallen wall she was seriously bruised and partially lost her hearing. The suffered woman was hospitalized, now she has recovered her health. After the explosion the house is in a critical state: doors and windows were smashed and thrown away at a large distance, the wall part fell, and a roof was partially destroyed (see Fig. 1). Because of the explosion of ball lightning in many neighbouring houses the electric appliances were destroyed".

FIGURE 1. The look of the destroyed house [8].

Let's try to estimate the energy of the ball lightning, which exploded in the house. We will carry out estimation on the basis of definition of mass of trinitrotoluene, which explosion leads to the consequences similar to that, which occurred in the village Mogsokhon. According to a demolition guide [9, P. 125], for the destruction of a flat package of logs the weight C (in grams) of a contact charge (directly located on the object to be undermined) is defined with the formula:

$$C = kF, \tag{1}$$

where F is the area of cross-section of a package (cm^2), and the factor k is defined by the kind and the condition of wood. For a dry pine or a spruce $k = 1$. Let us accept a height of the wall, which fell out of the house, equal to $H = 3$ m. This wall is constructed out of 13 logs, from here we find a thickness of a log $d = 23$ cm and the cross-section of package $F = Hd = 6900$ cm^2. From the formula (1) at $k = 1$ we find $C = 6.9$ kg of trotyl. A heat of trotyl explosion is equal to 4 MJ/kg, so the energy, contained in 6.9 kg trotyl, is equal to 28 MJ. If blasting is carried out by a charge which is at a distance r (m) from a wooden wall, the weight of charge C(kg) may be found from the formula [9, P. 127]:

$$C = 30kdr^2. \tag{2}$$

Here d (m) is a thickness of a log. If the charge is in the centre of a room of the size 4×4 m^2, at $r = 2.2$ m and $d = 0.23$ m $C = 33$ kg trinitrotoluol, that is equivalent to energy 132 MJ. In the description of the event nothing is said about the size of ball lightning. If to accept it equal to diameter of "average" ball lightning $D = 30$ cm, then the energy density of the "Buryat" ball lightning ρ_B will be from $2.1 \cdot 10^9$ J/m^3 to $9.3 \cdot 10^9$ J/m^3. These figures are the same order, as values of energy density of highly energetic ball lightning, about which it was spoken above.

All that allows to say that ball lightning is the dangerous natural phenomenon. This conclusion is not coordinated with the opinion of some researchers, who speak about insignificant danger of ball lightning. For example, Stenhoff [1, P. 94] considers it as non-dangerous object, and all destructions, ascribed to it, explains by the action of usual linear lightning.

We thank Dr. V. I. Kulikov for useful discussion of results of ball lightning explosion.

1. M. Stenhoff, *Ball Lightning. An Unsolved Problem in Atmospheric Physics*, New York, Kluwer/Plenum, 1999.

2. B. L. Goodlet, *Lightning*, IEE Journal, London. V. 81, p. 1.

3. I. Imyanitov and D. Tikhiy, *Beyond Boundary of Science Laws*, Moscow, Atomizdat, 1980.

4. G. Egely, *Analysis of Hungarian Ball Lightning Observations*, In: Progress in Ball Lightning Research. Ed. A. G. Keul. Proc. VIZOTUM. The Vizotum Project, Salzburg, Austria, 1993.

5. W. Brand, *Der Kugelblitz: Probleme der Kosmischen Physik*, V. II and III. Hamburg, H. Grand, 1923.

6. V.L. Bychkov, A.I. Nikitin and G.C. Dijkhuis, *Ball Lightning Investigations*, In: The Atmosphere and Ionosphere. Dynamics, Processes and Monitoring. Eds. V.L. Bychkov, G.V. Golubkov, A.I. Nikitin. Dordrecht, Springer, 2010, pp. 201—373.
7. A.I. Grigoriev, *Ball Lightning*, Yaroslavl, YarGU Publisher, 2006.
8. B. Ts. Dugarov, *An accident in Mogsokhon, http://arigus-tv.ru/news/item/50247/*
9. *A Management on Blasting Works*, Moscow, Military Publishing House of the USSR Ministry of Defence, 1963.

P-3

A Photograph of the Unusual Discharge of Lightning

Anatoly I. Nikitin, Tamara F. Nikitina and Alexander M. Velichko

Talrose Institute for Energy Problems of Chemical Physics, Russian Academy of Sciences, Moscow, 117829, Russia

Bead lightning and ball lightning are rare atmospheric phenomena encountered during thunderstorms [1, 2]. Documentary records (photos or video films), confirming their existence, are even more rare. Usually the bead lightning in a photo looks as a bright strip of a linear lightning disrupted by regular non-luminous intervals. Here we show a photo of unusual discharges of lightning, reminding bead lightning. In our opinion such discharges have been photographed for the first time. Channels of the unusual discharges of lightning contain from one to three bright parallel dash lines. Estimates are made confirming our guess that linear lightning leaders may represent waveguides where standing waves of radio frequencies (with wavelengths about 2 metres) are formed up resulting in the unusual form of the discharges.

The picture in Fig. 1 was made during a thunderstorm on January, 31st, 2013 on Northern Cyprus in the settlement of Iskele located between the cities Famagusta and Bogaz. The author of the picture, Julia Karabanova, at approximately 23 hours 30 minutes of local time came out onto a balcony of the house she was staying in to photograph the moon looking through the clouds. 1—2 seconds after the moment when she pressed the shutter button, a lightning flashed, and almost simultaneously with it she heard a deafening crack. The woman even thought that she had caused the lightning by pressing the button. The brightness of the light flash was so large that the woman was frightened, that she could be blinded or burned. A camera "Olympus FE170" operating in an auto mode was used. The size of the image is 2816 × 2112 pixels, colour representation is sRGB, colour depth is 24. The lens focal length was 6 mm, aperture F/3.1, exposition 4 seconds. The sensitivity of the CCD-matrix was 320 ISO. This camera features digital image stabilization mode

allowing compensating of trembling of the lens axis within several degrees. However at large displacements of the lens axis this system doesn't work. The author of the picture said that after the flash she had run to the dark room holding the camera in front of her. There were no light sources on her way which could be caught by her camera. In the photo except the trace, starting from the place where the moon was seen between the clouds, there were several less bright traces, looking like dash lines.

FIGURE 1. A lightning photographed 31st January 2013 on Northern Cyprus.

Fig. 2 is the increased fragments of the left and the central parts of the picture. For convenience let us number the brightest traces in Fig. 1 sequentially from left to right, with figures from 1 to 5. The soft trace 1 (see also Fig. 2a) looks like a straight dashed line with the relation of length of a bright part to length of a non-luminous part, approximately equal to 2. The trace 2 looks like a slightly curved dashed line with the relation of length of a bright part to length of a non-luminous part also equal to 2. If we accept thickness of trace 1 to be equal to one arbitrary unit, then thickness of trace 2 will be equal to 5 units, and thickness of trace 3 to 17 units. One can see in Fig. 2a that trace 3 represents 4 parallel dotted lines with thickness of one unit, with spacing between the lines equal to 2 arbitrary units. We notice that the whole channel 3 is shining, and the relation of the width of the bright part of the channel to the width of its dark part in this trace is approximately equal to 1. The thickness of trace 4 (see Fig. 2b) is 1.5 times more than the thickness of trace 3, in

the arbitrary units it is equal to 26. This trace has no dotted structure. Trace 5 consists of three parallel dashed lines with the thickness of 2 arbitrary units, with separations, respectively, equal to 9.6 and 5.5 arbitrary units. The ratio of the length of the bright part to the length of the non-luminous part in trace 5 is approximately equal to 1.5. The length of strokes in trace 5 decreases from the bottom part of the photo to the top, it is possible to explain this by perspective, the trace reflecting the change of the direction of propagation of the lightning from vertical to horizontal one (from the observer). Using the program ImageJ we found, that the brightnesses of traces, consecutively from 1 to 5, correspond approximately as 1:1:3:5:1.

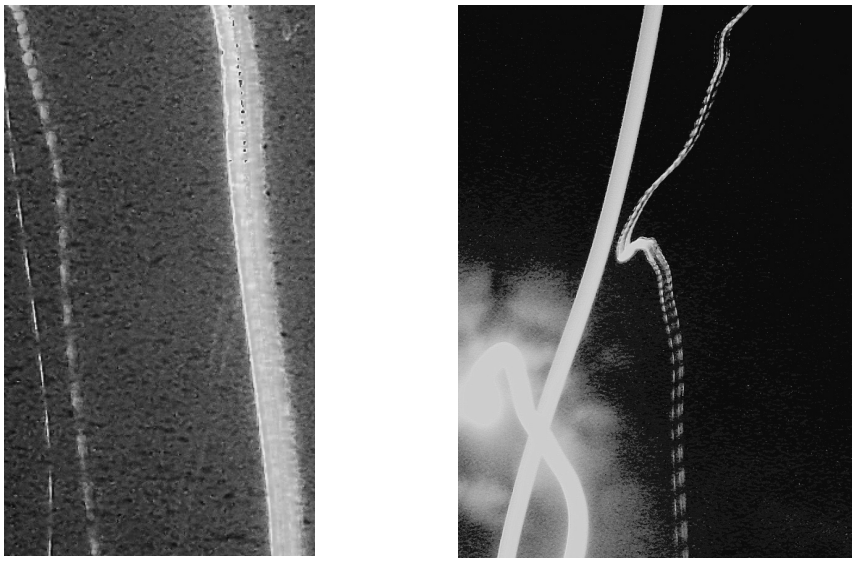

a *b*

FIGURE 2. (a) The enlarged left part of Figure 1. (b) The enlarged central part of Figure 1.

Now let's try to answer a question: what events were imprinted by the camera of the photographer? According to her story the things could work out the following way. After pressing the shutter button of the camera the computer calculated the desired time of exposure (4 seconds) and the exposition of the image sensor began. It lasted long enough for the details of the clouds lighted with the moon to be developed in the frame. 1—2 seconds after the beginning of the exposure a few shining channels (traces 1—3 and 5) appeared in the field of view of the camera. These channels (or one of them) led to a bright flash before the woman's eyes and a loud crash. It made her instinctively shift the camera axis, at first up, and then down. After it she ran into the room, where the light was switched off. When the camera moved this way the image of the moon drew a continuous trace 4. Since there were no light sources at the path of the axis of the camera lens after the moment, when the image of the moon went out of the camera field of view, no addi-

tional images appeared in the frame. Thus we could consider the trace 4 to be left by the moon image, and the traces 1—3 and 5 were left by really existing extended light sources. They may represent an unusual kind of lightning which can be related to the class of bead lightning [1]. The common opinion about the nature of bead lightning is not formed up yet. The majority of researchers consider that the reason of formation of a bead lightning may be compression of the discharge channel by the magnetic field generated by the lightning's current (pinch-effect) [3]. However, the pinch-effect begins to play an appreciable role only at high currents 0.5—1 MA [4]. Usually such high currents do not happen in lightning discharges (maximum current of a positive lightning does not exceed 200—300 кА) [5]. Therefore the question about the nature of the formation of discontinuous shining traces (and, in general, about the nature of bead lightning) remains open.

Let's try to find the reason of occurrence of the observed dotted channels. We will assume that these channels are traces, laid by the leader of lightning, through which the current of the return stroke, however, has not passed. It is known that the leader represents a thin channel, through which a current of a few amperes flows, and this channel is surrounded by a plasma cover. Diameter of this cover is about one metre [6]. Temperature is maximal in the channel centre (that supports its high conductivity), and it decreases along the radius of the channel. Since pressure P is the same in all parts of the channel (it is approximately equal to the atmospheric pressure), according to law $P = nk_BT$, gas density n (and, accordingly, the electrons' density n_e) in the channel centre, where temperature T is high, should be less, than in peripheral parts of the channel. (Here k_B is Boltzmann constant). The dielectric permeability of plasma ε_p (a square of the refraction index N_p) in terms of system CGSE is [7]:

$$\varepsilon_p = N_p^2 = 1 - \frac{\omega_p^2}{\omega^2} = 1 - \frac{4\pi n_e e^2}{m\omega^2}. \qquad (1)$$

Here $\omega_p = (\frac{4\pi n_e e^2}{m})^{1/2}$ is the plasma frequency, n_e is the electron gas density, e is the electron charge, m is the electron mass, ω is circular frequency of the wave, propagating in plasma. As only the waves with frequency $\omega > \omega_p$ can propagate through plasma, the refraction index of plasma N_p is less than unit, and it decreases with increase of electron gas density n_e. Thus, in the centre of the leader channel, where the electron gas density is low, the refraction index N_p will be higher than in the channel periphery. It is known from the optics that if light propagates from an optically more dense N_d environment to a less dense N_i environment (refraction index $N_d > N_i$), a creation of conditions for total internal reflection becomes possible [8]. In an optically transparent rod (a light waveguide), when the refraction index of its core is higher than the refraction index on its border, light can propagate, reflecting from the light guide borders. Similar conditions for propagation of radio-

waves can be developed also in "a plasma waveguide", formed by a lightning leader channel. The maximum length of the wave E_{01}, the electric vector of which is directed along the waveguide axis and which can propagate inside a circular waveguide of radius a, is defined by the formula [9]:

$$\lambda_0 = \frac{2\pi a}{\nu_{01}} = 2.615a. \qquad (2)$$

Here ν_{01} is the first root of the equation for the Bessel function $J_0(x) = 0$. For the waveguide of radius $a = 1$ m, $\lambda_0 = 2.615$ m and $\omega = 7.2 \cdot 10^8$ s^{-1} the frequency ω must be higher than plasma frequency $\omega_p = 5.642 \cdot 10^4 \sqrt{n_e}$ [10]. This will be possible, if the electron gas density $n_e > 1.628 \cdot 10^8$ cm^{-3}. According to estimations, the charge of a unit length of the leader channel cover can be equal to $l_q = 3 \cdot 10^{-7}$ C/cm [6]. At the cover diameter $D = 100$ cm the charge density in it is $\rho_q = 4l_q/\pi D^2 = 3.82 \cdot 10^{-11}$ C/cm^3. This corresponds to electron gas density $n_e = \rho_q/e = 2.38 \cdot 10^8$ cm^{-3}.

We see that in a plasma waveguide, formed by a leader channel, radio-waves with a wave length about $\lambda = 2$ m can propagate. Let the length of a leader channel be $L_c = 6$ km, and the time of existence of a current in the channel be $t_{ch} = 10^{-2}$ c [6]. Time of passing of the wave along the length of the channel can be estimated as $\tau_w = L_c/c = 2 \cdot 10^{-5}$ s. (Here c is velocity of light). If the wave is reflected from the channel ends, then in time $t_{ch} = 10^{-2}$ s it can make $2.5 \cdot 10^6$ passages along its length. Thus a standing wave may be formed, for instance E_{01n}, in loops of which conditions for excitation of air molecules may be created. The length of this wave is approximately equal to 2 m, the order of this value coincides with the length of luminous strokes inside the channels. In channels 5 and 3 with three and four parallel strokes, presumably, waves of modes E_{02n} and E_{12n} may propagate.

The hypothesis stated here allows obtaining only a general idea about the occurrence of periodic structure in the leader channel of a positive lightning. Undoubtedly, this hypothesis calls for a discussion and further development. To be fair, it is necessary to notice, that the idea that radio-waves can propagate through a lightning channel, was proposed earlier [1]. However, the authors of this idea spoke about the channel of a return stroke of lightning and about the possibility of radio-waves influence on pinch-effect. Here we speak about processes in the channel of a leader, through which a current of the main discharge has not passed.

We thank J. I. Karabanova for permission to use the photography of lightning and A. Yu. Karabanov for discussion and help in processing of the photo.

1. J. D. Barry, *Ball Lightning and Bead Lightning*, Plenum, New York, 1980.
2. M. Stenhoff, *Ball Lightning. An Unsolved Problem in Atmospheric Physics*, Kluwer/Plenum, New York, 1999.
3. M. A. Uman, *Bead Lightning and the Pinch Effect*, Journal of Atmospheric and Terrestrial Physics, 1962, V. 24, pp. 43—45.
4. B. E. Mejerovich, *The Channel of a Strong Current*, Open Company FIMA, Moscow, 1999.
5. M. A. Uman, *The Lightning Discharge*, Academic Press, Orlando, Florida, 1987.

6. E. M. Bazeljan and Yu. P. Raizer, *Physics of Lightning and Protection from Lightning*, Fizmatlit, Moscow, 2001.
7. D. A. Frank-Kamentsky, *Lectures on Physics of Plasma*, Atomizdat, Moscow, 1968.
8. G. S. Landsberg, *Optics*, Fizmatlit, Moscow, 2003.
9. V. I. Kalinin and G. M. Gershtein, *Introduction to Radio Physics*, Publishing House of the Technical and Theoretical Literature, Moscow, 1957.
10. B. M. Smirnov, *Properties of Gas-Discharge Plasma*, Publishing House of Polytechnical University, St.-Petersburg, 2010.

P-4

Luminous Regions under the Capillary Discharge Interaction to Metallic Foils

Dmitri L. Kirko, Alexander S. Savjolov, Igor D. Egorov

National Research Nuclear University MEPhI, Kashirskoe shosse 31, Moscow 115409, Russia

During a channel lightning formation near the Earth's surface a metallic thing smelting and a ball lightning origin may be observed. In some experiments with the capillary discharge the luminous regions (LR) (dimensions 1—3 mm) from the discharge flying and during 0,1—3 s existing were registered [1,2].

In this work the experimental devise contains the discharger to the power source connected up and the support from organic glass, on which a metallic foil was placed. The power source has the capacitor battery (charge voltage 200—250 V B, energy 100—250 J). The discharge current was 100—150 A and pulse duration 6—10 ms. During the discharger switching on the capillary discharge torch interacted to a metallic foil (material: aluminum, cupper, brass).

An interaction process of capillary discharge torch with metallic foils was fixed by camera Nikon 1G (time resolution 1 ms). This plasma radiation was researched with the help of spectrometer Ava Spec 2048 (spectral region 200—1000 nm, distribution 0,3 nm). At the final interaction stage the origin of luminous regions (LR) from near the capillary region starting were observed. LR has a near ball form (Fig. 1), mean dimensions were 0,5—2 mm, and lifetime 0,01—0,5 s. LR quantity was 1—5 at one shot. A motion trajectory had near to a parabolic form usually. A LR

FIGURE 1. Photo of luminous regions (time duration 1 ms).

transference in space had length to 0,5 m. A radiation color was white with little dark blue hue. Sometimes around main LR white color luminescence at filming frames little white-grey loop or blue halo were.

At a bar (metallic or dialectical things) striking LR finished it existence. During to a horizon dialectical plane falling LR elastic reflections to 2—5 quantity were observed. At a paper using a strike place were fixed. At the final stage of LR existence the next processes are observed: 1) gradual LR diameter decreasing and fluent going out, 2) LR disintegration to some more little fragments and it more rapid going out, 3) sudden LR going out. The observed luminescence has a good formed stable structure. The LR cover has elastic properties at a strike and many reflections from dialectical surfaces appearing.

1. R. F. Avramenko, B. I. Bachtin, V. I. Nikolaeva, L. P. Poskacheeva, N. N. Shirokov, Journal Techn. Physics, 12, 57 (1990).

2. S. E. Emelin, V. S. Semenov, V. L. Bychkov, N. K. Belisheva, A. P. Kovshik, Journal Techn. Physics, 3, 19 (1997).

P-5

Luminescence in Liquid Nitrogen under the Influence of Impulsive Discharge

Dmitri L. Kirko, Alexander S. Savjolov, Igor D. Egorov

National Research Nuclear University MEPhI, Kashirskoe shosse 31, Moscow 115409, Russia

A ball lightning appears usually at a humid air condition. In experiments of discharges in water the luminous regions (LR) origin were discovered [1]. At an impulsive discharge interaction with cryogenic liquids (nitrogen, oxygen) a weak volume luminescence appeared [2], so LR (ball and irregular) formation in liquid nitrogen and argon with dimensions 0,1—1 cm and lifetime 10—40 s [3, 4] were observed.

In these experiments liquid nitrogen in a thin wall vessel was located, and impulsive discharge (capillary, arc) near liquid surface was placed. For shooting film and photo made camera Nikon 1G (time resolution 1 ms) was used. After the discharge switching on a volume luminescence in liquid nitrogen was observed that decreased rapidly. Then in liquid nitrogen volume luminous regions (LR) (Fig. 1) with a ball form and so with stretching and irregular forms were appeared. The LR dimensions 0,1—1 cm in volumes $2 \cdot 10^2$—$5 \cdot 10^3$ cm^3 were. The lifetime in region 10—40 s was. A luminescence color dark blue, blue, violet, rarely yellow was. LR may move mainly in liquid nitrogen volume under a boiling liquid flow influence.

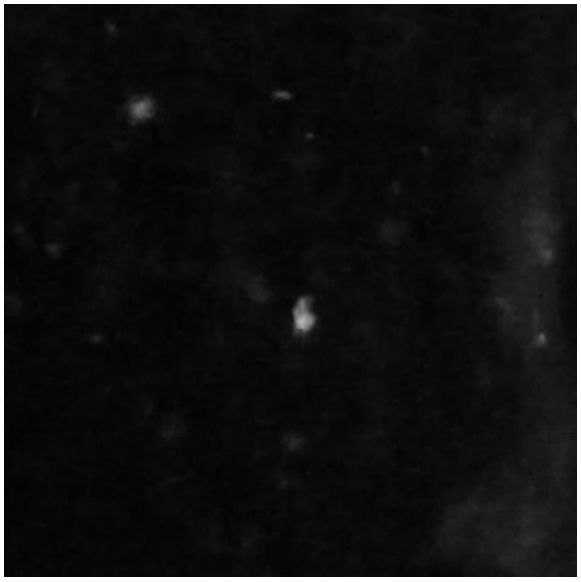

FIGURE 1. Photo of luminous regions (time duration 1 ms).

The determination of conditions at a ball luminous region origin acting is the important fact of research. It was determined that the presence of ultraviolet radiation in range 300—360 nm in a discharge exciting is the significant fact. This exiting process has a threshold and appears at the value radiation energy $E \approx 12$ mJ (impulse duration $\Delta t = 7$—9 ms) exceeding. Material and volume value of liquid nitrogen vessel are the other important parameters. The best results in aluminum vessels were obtained that perhaps deal with high aluminum reflecting properties for ultraviolet radiation. At a liquid nitrogen volume increasing effect amplification is a common tendency. It was fixed a little metallic part influence (dimensions 0,05—0,5 mm) in liquid nitrogen to a LR origin. These metallic parts may act as original condensation centers during a LR origin. The layer near vessel bottom is the main region of LR formation. Probably luminous regions form independence field structures in favorable conditions of cryogenic liquid existing. The research of liquid air and liquids with boiling temperature near normal conditions represents the interest.

1. P. I. Golubnichiy, V. M. Gromenko, V. M. Krutov, Journal Techn. Physics, 1, 183 (1990).

2. G. J. Minkoff, *Frozen free radicals*, Interscience Publishers Inc., N. Y., 1960.

3. D. L. Kirko, A. S. Savjolov, V. A. Kadetov, Journal Techn. Physics Letters, 10, 78 (1995).

4. D. L. Kirko, A. S. Savjolov, Proc. X Intern. Conf. "Wave electr. hydrodyn. of conduct. liquid" (4—8 July, 2013), Yaroslavl, Russia, pp. 96—99.

On Hydrodynamic Analogy of Electromagnetic Waves

Vladimir L. Bychkov

Physical department M. V. Lomonoisov Moscow state university, Moscow, 119991, Russia

Introduction

We represent a continuation of [1], devoted to investigation of analogies between equations of hydrodynamics and electrodynamics. In [1] were obtained equations analogical to Maxwell equations but without a displacement current. So they required additional analysis from the point of view of derivation of wave equations [2]. At that main equations connecting hydrodynamic and electrodynamic equations were the acceleration of a flow $\frac{\partial \vec{v}'}{\partial t} = \overline{E}$, an electric field strength, and its curl $rot\,\vec{v}' = -\overline{B}$, magnetic induction ($\vec{v}'$ -is a velocity of the flow, t — time). In this work we derive wave equations from the hydrodynamic equations for a compressing viscous one atomic gas (fluid) that represents "a physical vacuum" in modern terms, which was proposed in D. I. Mendeleev work [3] and argued by N. Tesla [4].

Wave equations

Let us consider weak disturbances of the fluid as is customary in hydrodynamics and get equations for the hydrodynamic disturbances and waves [5—7]. At analysis we start from the conservation laws with a source [7]. Thus the continuity equation with the source has a form:

$$\frac{\partial \rho}{\partial t} + div\ (\rho \cdot \overline{V}) = m; \tag{1}$$

and the momentum equation is

$$\frac{\partial \overline{V}}{\partial t} + (\overline{V} \cdot \nabla)\ \overline{V} + \frac{1}{\rho} grad\ p + \frac{1}{\rho} \cdot \overline{V} \cdot m = \nu \Delta \overline{V} \tag{2}$$

Here ν is a coefficient of the physical viscosity, introduced here for accounting of the momentum dissipation, ρ is the density of the fluid, p is a pressure in the fluid, $\overline{V}$ is a velocity of the fluid.

Let us consider (1), (2), and assume that the disturbance of following parameters takes place under an action of a disturbance of some source $m = m_0 + m'$, i. e. of a density $\rho = \rho_0 + \rho'$, of a velocity $\bar{v} = \bar{v}_0 + \bar{v}'$ and of a pressure $p = p_0 + p'$.

Here $\rho_0 = const$, $\bar{v}_0 = const$, $p_0 = const$, and $\rho_0 >> \rho'$, $\bar{v}_0 >> \bar{v}'$, $p_0 >> p'$ $m_0 >> m'$

Then one can transform (1) to

$$\frac{\partial \rho'}{\partial t} + \bar{v}_0 grad (\rho') + \rho_0 div \bar{v}' = m'. \tag{3}$$

At expansion of (3) we introduce a velocity of a sound [5, 7]

$$\frac{grad\ p'}{grad\ \rho'}\Big|_{\rho=\rho_0} = c^2$$

$$\frac{\partial \bar{v}'}{\partial t} + (\bar{v}_0 \cdot \nabla)\bar{v}' + \frac{c^2}{\rho_0} grad \rho' + \frac{1}{\rho_0} \cdot \bar{v}_0 \cdot m' + \frac{1}{\rho_0} \cdot \bar{v}' \cdot m = \nu \Delta \bar{v}'. \tag{4}$$

Let us take *grad* of (3) and differentiate (4) over *t*

$$\frac{\partial\, grad\ \rho'}{\partial t} + \rho_0 grad\ div\, \bar{v}' = grad\ m'$$

$$\frac{\partial^2 \bar{v}'}{\partial t^2} + (\bar{v}_0 \cdot \nabla)\frac{\partial}{\partial t}\bar{v}' + \frac{\partial}{\partial t}\left(\frac{c^2}{\rho_0} grad\ \rho'\right) + \frac{1}{\rho_0} \cdot \bar{v}_0 \cdot \frac{\partial}{\partial t} m' + \frac{1}{\rho_0} \cdot \frac{\partial}{\partial t}\bar{v}' \cdot m = \nu \Delta \frac{\partial}{\partial t}\bar{v}'$$

From where

$$\frac{\partial^2 \bar{v}'}{\partial t^2} + \bar{v}_0 \cdot div \frac{\partial}{\partial t}\bar{v}' - c^2\ grad\ div\, \bar{v}' + \frac{c^2}{\rho_0} grad\ m' + \frac{\bar{v}_0}{\rho_0} \cdot \frac{\partial}{\partial t} m' + \frac{m}{\rho_0} \cdot \frac{\partial \bar{v}'}{\partial t} = \nu \Delta \frac{\partial}{\partial t}\bar{v}'$$

or

$$\frac{\partial^2 \bar{v}'}{\partial t^2} - c^2 \nabla^2 \bar{v}' - c^2 \cdot rotrot\ \bar{v}' = \nu \Delta \frac{\partial}{\partial t}\bar{v}' - \frac{c^2}{\rho_0} grad\ m' - \frac{\bar{v}_0}{\rho_0} \cdot \frac{\partial m'}{\partial t} - \frac{m}{\rho_0} \cdot \frac{\partial \bar{v}'}{\partial t} - \bar{v}_0 \cdot div \frac{\partial \bar{v}'}{\partial t} \tag{5}$$

Main summands in (5) to the right prove to be $\nu \Delta \frac{\partial}{\partial t}\bar{v}'$, $\frac{\bar{v}_0}{\rho_0} \cdot \frac{\partial m'}{\partial t}$ and $\frac{c^2}{\rho_0} grad\ m'$, so (5) transforms to

$$\frac{\partial^2 \bar{v}'}{\partial t^2} - c^2 \nabla^2 \bar{v}' - c^2 \cdot rotrot\, \bar{v}' = \nu \Delta \frac{\partial}{\partial t}\bar{v}' - \frac{c^2}{\rho_0} grad\ m' - \frac{\bar{v}_0}{\rho_0} \cdot \frac{\partial m'}{\partial t}.$$

Usually a term $c^2 \cdot rotrot\,\bar{v}'$ is considered as of the second order of smallness and is disregarded, and from (5) one obtains equations for a propagation of longitudinal waves in gases or in fluids. Let us consider the general case. So we consider a propagation of the disturbance at a distance greater than a size of the source and assume that one can disregard an action of the source in a far zone, then

$$\frac{\partial^2 \bar{v}'}{\partial t^2} - c^2 \nabla^2 \bar{v}' - c^2 \cdot rotrot\,\bar{v}' = \nu\Delta \frac{\partial}{\partial t}\bar{v}', \tag{6}$$

This equation represents a generalization of the wave equation. At $c^2 \nabla^2 \bar{v}' >> c^2 \cdot rotrot\,\bar{v}'$ one has

$$\frac{\partial^2 \bar{v}'}{\partial t^2} - c^2 \nabla^2 \bar{v}' = 0$$

In a one dimension case one has wave solutions, if $\vec{v}' = \vec{v}_0' \cdot \sin(x - ct)$, and $\frac{\partial \vec{v}'}{\partial t} = \bar{E}$ [1]; one of them is

$$\bar{E} = \bar{E}_0 \cdot \cos(x - ct)$$

If a vector of a disturbance is vorticle than one gets a following equation at far distance from the source

$$\frac{\partial^2 \bar{v}'}{\partial t^2} - c^2 \cdot rot\,rot\,\bar{v}' = 0, \tag{7}$$

Since in this case [1]

$$rot\,\bar{v}' = -\bar{B},$$

then one gets

$$\frac{\partial \bar{E}}{\partial t} + c^2 \cdot rot\,\bar{B}' = 0,$$

And together with the equation

$$\frac{\partial \bar{B}}{\partial t} = -rot\,\bar{E}$$

one comes to the Laplace equation

$$\frac{\partial^2 \quad B}{\partial \quad t^2} + \quad c^2 \cdot \nabla^2 B = 0, \tag{8}$$

which has a solution $B = B(r,\theta,ct)$ in a cylindrical coordinate system, i. e. indeed a transversal flow of the physical vacuum

$$B = B(r,\theta,ct) = J_n(mr)\left(c_1 \exp(mct) + c_2 \exp(-mct)\right)\left(c_3 \cos(n\theta) + c_4 \sin(n\theta)\right),$$

Which definite solutions are determined by the boundary conditions.

Let us consider again a pair of derived equations in the case of the disturbance vorticle vector

$$\frac{\partial \overline{E}}{\partial t} = -c^2 \cdot rot \overline{B} \tag{9}$$

$$\frac{\partial \overline{B}}{\partial t} = -rot\,\overline{E}$$

They are principally different from the Maxwell's equations for wave by the sign minus in (9) to the right. Only at opposite sign one can get the wave equation for the magnetic and electric fields of the type

$$\frac{\partial^2 \overline{B}'}{\partial t^2} - c^2 \nabla^2 \overline{B} = 0.$$

Namely they describe a propagation of the longitudinal wave.

From (5) at $c^2 \nabla^2 \overline{v}' >> c^2 \cdot rotrot\,\overline{v}'$ one obtains an equation

$$\frac{\partial^2 \overline{v}'}{\partial t^2} - c^2 \nabla^2 \overline{v}' = \nu \nabla(\nabla \frac{\partial}{\partial t}\overline{v}') - \overline{v}_0 \cdot div \frac{\partial}{\partial t}\overline{v}', \tag{10}$$

describing the longitudinal waves with friction. The reason for a decay of the electromagnetic waves is not explained in the classical electrodynamics.

Conclusions

Basing on the hydrodynamic equations for a fluid with a source in the acoustic approach we have obtained analogues of Maxwell's equations for electromagnetic waves. They describe a propagation of a disturbance's wave over a gas with a speed equal to the speed of a sound in the gas. In electrodynamics it is the speed of light. The equations describe a propagation of the waves having generally both longitudinal and cross-section components. The transversal solutions are possible only at the transversal disturbances, that in the electrodynamics generally speaking is caused by nothing. About the existence of the longitudinal, instead of the transversal waves also spoke N. Tesla [4] when he criticized Hertz conclusions from the theory and experiments, and approved, that Hertz was mistaken at treatment of the experimental results obtained with a help of the primitive equipment, and in under-

standing of the propagation medium. If there are longitudinal waves the physical vacuum reminds an atomic gas. The same approved D.I. Mendeleyev [3] when identified that the medium which we in the given case name «a physical vacuum», with one-atomic, inert gas. Therefore all constructions of a firm Ether with rigid structure are erroneous. If there are longitudinal waves the physical vacuum reminds a gas. N. Tesla's and D.I. Mendeleyev's conclusions also prove an application of the hydrodynamics equations (Navier-Stokes or Euler) for one-nuclear viscous ideal gas.

1. Bychkov V.L. To electrodynamic and hydrodynamic analogy. AIS-2012. "Atmosphere, Ionosphere, Safety" Kaliningrad. June 24—30. 2012. Section P. P. 30—31.
2. Sommerfeld A. Mechanics of deformable media. Inostannaya Literatura Pulishers. Moscow -Leningrad. 1950.
3. Mendeleev D.I., "*Peridical law"*, Moscow: AS USSR publishers. 1958. P. 470.
4. Safer M. Nikola Tesla. Moscow. Yauza. EKSMO. 2007.
5. Loitsyanski L.G., "*Mechanics of liquids and gases"*. Moscow-Leningrad: Gos. Izd. Tekch. — Teoretich. Literat. 1953.
6. Kochin N.E., Kibel I.A., Rose N.V., "Theoretical Hydromechanics". Vol. 1. Moscow: Gos. Izd. Fiz. Mat. Lit. 1963.
7. Vallander S.V. *"Lectures on Hydro-aero-mechanic",* Leningrad: Len. State. Univ. Publishers. 1978.

P-7

Ball Lightning with a Case Filled by a Vapor

Vladimir L. Bychkov

Physical department M.V. Lomonoisov Moscow state university, Moscow, 119991, Russia

Introduction

A model of Ball Lightning with a case made of melted material and filled by an evaporated gas has been presented. It is natural generalization of a theory presented in [1, 2] where BL was considered as an object with a solid or melted cover filled by a powder material of reduction oxides (for example Si appearing at SiO_2 reaction with organic materials, C, H [3]) appearing at linear lightning impact to the earth. This powder at later stages combusts at interaction with oxygen penetrating the cover, this leads to destruction of BL and release of energy of Si combustion. Undertaken experiments [3] have shown an appearance of fireballs in discharge

conditions in specially designed tubes filled by basalt (which contains Si). These objects lived portions of a second being of several mm in a diameter. Their life finished with an explosion what, as if, confirmed the theory of [2]. An analysis of the objects showed that their inside structure consisted of pores and cavities as if a vaporizing processes took place inside them. This result leads us to a new analysis of works [4—7] and creation of a developed model including a role of vapor inside BL.

To explosions of artificial BL

In researches of artificial BL several cases when the obtained luminescent objects blew up [4, 5, 7] are known. In [4, 5] sometimes remained «shells» — pieces of a solid cover. Sometimes at explosions of metal wires in cells with water [6] took place a formation of thin-walled hollow spheres. As a rule experiments occurred in conditions, when the material (for example basalt cotton wool or a titanic foil) was in some container in which there took place a formation of a plasma and insertion of energy into the substance. At that the analysis of the remainders, showed that these objects have an external firm environment, and their internal part consists of a porous substance. It specified the process of boiling which took place inside of the objects. The gas pressure P_{at} inside of the experimental volume was much greater than the atmospheric one (for example, $P_{at} \geq 3 \cdot 10^5$ Pa [4]). Later there took place an emission of these objects through a special hole out of the volume into air of atmospheric pressure. After that an explosion of these objects took place [4] when they were moving in air

This phenomenon can be described from a point of view of the sphere energy balance as of the created material melt in plasma conditions. We consider a balance of the gas pressure in an experimental volume, surface tension P_{Lap} and pressure of a vapor that was generated at heating of a material inside the created sphere:

$$P_{at} + P_{Lap} = P_{gas} \tag{1}$$

where

$$P_{Lap} = \frac{2 \cdot \alpha}{r} \tag{2}$$

α is a coefficient of a surface tension of melted material, r is a radius of the sphere;

$$P_{gas} = \frac{(M - a \cdot 4 \cdot \pi \cdot r^2 \cdot \rho) \cdot R\,T}{\mu \cdot 4/3 \cdot \pi \cdot (r-a)^3} \tag{3}$$

gaseous pressure defined by the Mendeleev-Clapeyron equation, M is the mass of the vapor, a is the thickness of the case, ρ is the density of the case, R — universal gas constant, μ — molecular weight of the gas. By (3) we take into account that a part of the vapor can be deposited on a case's wall in a form of a film and to effectively decrease the vapor pressure to the case.

Estimates for the experiment show that the gas pressure in the experimental volume was $P_{at} \approx 3 \cdot 10^5$ Pa at a start of the experiment. The surface pressure of the silicon α(mN/m) = 840(± 45) − 0.19(± 0.09)(T(K)−1685) [8], this gives the value α(mN/m) ≈ 790 at a temperature close to a boiling temperature of Silicon (T = 1950 K [9]). The sphere's radius was r ≈ 2 mm, and a thickness of the case was $a \approx 100$ μm. This shows that the balance of pressure inside the sphere and in the experimental set up at the beginning of the experiment $P_{at} \approx P_{gas}$. At the object emission into air the pressure balance inside and outside of the sphere (4) was violated and $P_{at} << P_{gas}$, and the sphere becomes broken by the vapor's pressure inside it.

To natural Ball lightning

Linear lightning impact to different materials —organic and inorganic and their mixtures (for example- soil) leads to creation of long-lived luminescent objects. So an idea of BL creation at the linear lightning impact to materials is reasonable. From this point of view BL can be created even at the linear lightning impact to ice in clouds: in this case some weak lightning discharge can create bubbles filled by the water vapor, the same result can be achieved at the linear lightning impact to wood, pieces of metal and so on. But in difference to the explosion of metallic spheres BL carry non-compensated electric charge which seriously changes the situation. So the consideration of BL existence one has to include the Coulomb and the polarization influences [1] on the balance of pressure inside and outside of BL. In the following chapter we will consider Si-based BL since during last years silicon BL [3] became very popular (we have already marked that BL can consist of any melting material). Here we consider a sphere filled by vapors of melted material and covered by some case made of the oxide of the melted material or some film created at BL formation (for example a film of ice).

Pressure balance in natural ball lightning

Let us apply obtained above information for the development of the model [1, 2]. We consider an unipolarly charged, which has an excess of charges of one sign. In this case it is easy to explain many observations with discharges from a BL surface and also BL damaging impact to people and objects.

Let a pressure caused by the polarization of the case acts the BL surface [10, 11] compressing it to the center, pressure of the Coulomb rejection of the same name charges inside the case of BL, external pressure of an atmosphere and pressure of the gases inside the case. So P_{pol} is a pressure of the polarization forces [10, 11] when a dipole layer is created on a dielectric case:

$$P_{pol} = \frac{2 \sigma \cdot q \cdot a}{4 \cdot \pi \cdot \varepsilon_0 \cdot r^3}, \quad (4)$$

here a is the case thickness, σ-is a charge of the surface unit, q-is a charge of the sphere. For Si and H_2O σ proves to be of the same value about σ = 1.6 Кл/м^2 [8, 9]. ε_0 is the dielectric constant, r is a radius of the sphere.

A pressure of the Coulomb charges rejection acting the case P_C is defined by the following equation [1]:

$$P_C = \frac{q^2}{2 \cdot (4\pi)^2 \cdot r^4 \, \varepsilon_a \, \varepsilon_0}, \tag{5}$$

ε_a — is a dielectric constant of air.

Let us write down an equation of the pressure balance. The equation has a form

$$P_{at} + \ P_{pol} + P_{Lap} = P_C \ + \ P_{gas} \, . \tag{6}$$

Let us not consider the surface tension and pressure rise due to chemical processes inside the case. The latter assumption is connected with the fact that no oxidizer can get inside the case at BL origination. We see that this case is different from the case considered in the previous section. It is evident that different conditions are realized at different values of charge, temperature inside the sphere, its size and so on. For example in highly charged BL one has from (6)

$$\frac{q^2}{2 \cdot (4\pi)^2 \cdot r^4 \ \ \varepsilon_a \ \ \varepsilon_0} = \frac{2 \ \ \sigma \ \cdot q \cdot a}{4 \cdot \pi \cdot \varepsilon_a \cdot \varepsilon_0 \cdot r^3}, \tag{7}$$

or $q = 16 \pi \sigma \cdot r \cdot a$, from which one can find a connection between BL radius and a thickness of its case. For example $a \approx 1.2 \cdot 10^{-4}$ m at $q = 10^{-2}$ C and r = 1 m.

The similar case is realized at $a \geq M /(\cdot 4 \cdot \pi \cdot R^2 \cdot \rho)$, when it is possible to disregard the vapor pressure inside the sphere, when practically all the vapor transforms into the vapor film.

When BL charge decreases at, so called, leaking off the charges [1] the term P_{gas} becomes the main in (6) and an explosion takes place due to vapor pressure inside the case. The case can also collapse at decrease of charges and cooling of the vapor.

Ball Lightning energy

Let us calculate BL energy accounting heating its material up to vaporization and following oxidation under the oxygen impact. For example, we consider BL origination at linear lightning stroke into a soil and transferring electric energy and charge at it [3,2]. BL appears in some area inside the soil, at that its case is formed of melted SiO_2, and BL is filled with a vapor of Si.

For estimation of energy transferred by the linear lightning to the soil consisting of Si let us use a standard equation for heat leading to evaporation of a solid substance:

$$\boldsymbol{Q = c_1 m (T_{melt} - T_{init}) + L \cdot m + c_2 m \cdot (T_{boil} - T_{melt}) + \lambda \cdot m,} \tag{8}$$

Here m is a mass of heated material, c_1 is a specific thermal capacity of the material in the solid state; c_2 is a specific thermal capacity of the material in the liquid state; T_{init} is the initial temperature of the material (20° C); T_{melt} — temperature of the material melting, T_{boil} — temperature of the material boiling; λ is specific temperature of melting (for Si $\lambda = 1.78 \cdot 10^6$ J/kg [10]); L is a specific heat of vaporization. Melting temperature of Si $T_{melt} = 1400°$ C [9]. The specific heat for Si $c_1 = 0.84$ kJ/(kg K)). Then c_1 m $(T_{melt} - T_{init}) = 0.92 \cdot 10^6$ J/kg [12]. For estimates of vaporization let us take data [13] для SiO_2 $T_{boil} = 1950$ K. Heat capacity of Si let us take as for quartz [12] at 1000 and we get $c_2 \cdot m \cdot (T_{boil} - T_{melt}) = 1.34 \cdot 10^6$ J/ kg. For L we take enthalpy of vapor forming for Si [13] $\Delta H^0 = 2.86\ 10^7$ J/ kg. One can see that not all the parameters are well established, nevertheless they can give a value of the effect. Putting all of them in (9) we get a following formula for BL specific heat energy

$$Q/m = c_1 \cdot (T_{melt} - T_{init}) + c_2 \cdot (T_{boil} - T_{melt}) + \lambda + L \approx 3.26 \cdot 10^7 \text{ J/ kg}$$

Heat release at Si combustion in air is estimated [2] as $q = 0.88 \cdot 10^7$ J/ kg, i. e. it is about 27 % from the energy inputted by the linear lightning to the material. At that it can be released after the destruction of the sphere when oxygen will easily come into the fuel – Si. Evidently this is the estimate from above since some part of the material will not be oxidized. The total specific energy can be estimated as

$$Q_{term+chem}/m \leq 4.1 \cdot 10^7 \text{ J/ kg.}$$

Let us apply this data to the observed BL. The description of, so called, Khabarovsk case was published in [14]. "The BL in Khabarovsk during a strong rain…Then over a cinema building… there appeared a fireball of bright orange color in of 1.5 m diameter about. Sparks were strewed from it. Then BL has started to descend, it has passed to the earth surface through branches of trees, for an instant it has flashed over a site of soil and again has risen upwards. Strong explosion was heard, it became dark and silent. In total BL existed about one minute. Despite the water considerable quantity on the soil and the torrential rain, in the zone in diameter of ~ 1,5 m and depth of 20—25 cm the soil was charred and fused. The total volume of the zone filled with the slag, was about of 0,4 m^3. Estimations of released by BL energy made by the authors of [14] taking into account heating of the ground and the evaporation of the moisture being in it had appeared to be $W \approx 1.1 \cdot 10^9$ J".

Let us estimate a minimal energy of BL going to heating of a soil, at that we consider energy of Vaporized BL material and write down an equation of heat balance of a vapor which goes to heating of the soil to melting temperature

$$m_v \cdot (c_2 (T_{boil} - T_{melt}) + L + q) = (m_s - m_v) \cdot c_1 (T_{melt} - T_{init}),$$

here m_v is a mass of the vapor, m_s is the mass of the soil after its mixing with the vapor. From this equation follows that in order BL could release energy about of 10^9 J it is necessary that the linear lightning would melt and vaporize about 9.3 kg of the soil.

Ball Lightning charge

Basing on results of [1] let us estimate a charge of BL with a weight about of 9.3 kg, which was flying at a height of 20 m (building in the Khabarovsk case). Here we are making a supposition that BL was thrown out of a region of Earth where the linear lightning stroked the soil as in [3,2]. At that we suppose that BL was ejected from the soil under a pressure of gases released in the soil under impact of the linear lightning. An equation describing an indifferent equilibrium of a sphere at a height x has a form [10,11]

$$q_{suef} E_{ext} = m_{sph} \cdot g + \frac{q_{surf}^2}{16 \pi x^2 \varepsilon \varepsilon_0}, \tag{9}$$

where g is gravitation constant, $\varepsilon = 10$ is dielectric permeability of a soil, ε_0 is the vacuum constant, respectively, q_{surf} is electric charge of BL (here we consider that BL and earth surface have electric charge of the same sign). and E_{ext} is an external electric field acting BL. From (10) one can determine a level of the minimal electric field at which this equilibrium is possible:

$$E_{ext}^2 = 4mg/(16 \pi x^2 \varepsilon \varepsilon_0), \tag{10}$$

and a minimal value of BL's electric charge

$$q_{surf} = 4 \cdot x \sqrt{mg\pi \varepsilon \varepsilon_0}. \tag{11}$$

Inserting known values of parameters and BL mass one can get a following value of the electric field $E_{ext} \approx 1.43 \cdot 10^4$ V/m and BL charge $q_{surf} \approx 1.3 \cdot 10^{-2}$ C. In [1] is shown that a pulsating electric field is realized at such parameters in an area with the radius r_a, at which the electric field value on the BL surface decreases to the air breakdown field E_{br}, so it is possible to determine a possible radius of air excitation by BL, which can be considered by observers for the radius of BL

$$E_{br} = \frac{q_{surf}^2}{4 \pi r_a \varepsilon_a \varepsilon_0}, \tag{12}$$

Here ε_a is the dielectric constant of air. Using the equation (12) and air breakdown field value $E_{br} = 3 \cdot 10^6$ V/m one can obtain the following estimate of possible observable BL radius $r_a \approx 0.5$ m in the considered case at the observed by the witnesses one $r_a \approx 0.75$ m. Obtained values one can consider as satisfactory accounting a multitude of made assumptions.

Conclusions

We have presented a developed model of BL with accounting of energy of vapor inside BL. This energy proved to be much higher than those of combusting BL. This model allows more realistically consider the observation of [14]. Concerning experimental modeling, our investigations indicate that it is necessary to realize a uniporlarly charged BL. Experiments [3,4] showed that it is impossible to realize it in conditions of glow, pulsed and arc discharges due to the plasma quasi-neutrality. Most probably for obtaining of BL one has to use corona and Tesla devices or even electron or beams where the uniporlarly plasma regions can be formed.

1. V.L. Bychkov, A.I. Nikitin, G.C. Dijkhuis, Ball Lightning Investigations. In: V.L. Bychkov, G.V. Golubkov, A.I. Nikitin (eds.) The atmosphere and ionosphere. Dynamics, Processes, and Monitoring. Springer, Dordrecht, 2010, P. 201—373.

2. V.L. Bychkov, Artificial and Natural Fireballs as Combustion Objects. IEEE Transactions on Plasma Science 2010. V.38 P.3289—3290.

3. Abrahamson J., Dinniss J.: Ball lightning caused by oxidation of nanoparticle networks from normal lightning strikes on soil. Nature. **403**, 519—521 (2000).

4. S. Emelin, V. Bychkov, A. Astafiev, A. Kovshik, A. Pirozersky, Plasma combustion nature of artificial ball lightning. IEEE Transactions on Plasma Science 2012. V. 40, P. 3162—3165

5. S.E. Emelin, V.S. Semenov, V.L. Bychkov et. al. Some objects formed in the interaction of electrical discharges with metals and polymers. Tech. Phys. 1997. V. 42, N. 3, P. 269—277.

6. L.I. Urutskoev, V.L. Bychkov, V.I. Liksonov, Yu.P. Dontsov, Luminous objects in experiments with exploding foils. Ibidem. P.23. Abstracts of 7-th Intern. Sympos. on Ball lightning (ISBL2001). July 26—29, 2001, University of Missouri St. Louis. P. 14.

7. K.L. Corum, J.F. Corum. Tesla's production of electric fireballs. Tesla Coil. Builder's Association News. 8. (3), 13—18. 1989

8. N. Eustathopoulos *http://www.sciencedirect.com/science/article/pii/ S002202481300119X — aff1*, B. Drevet. Surface tension of liquid silicon: High or low value? Journal of Crystal Growth. V. 371, 15 May 2013, P. 77—83.

9. Reference book of physical values. Ed. I.K. Kikoin Atomizdat. Moscow. 1975.

10. A.I. Nikitin, *An electrical capacitor as the element of the power core of ball lightning*, Electrical Technology Russia, 1998, №4, pp. 70—85.

11. A.I. Nikitin, *The dynamic capacitor model of ball lightning*, Proc. 6th Int. Symp. on Ball Lightning (ISBL99), 1999, Antwerp, Belgium, pp. 91—95.

12. J. Shelby Structure and technology of glass. Mir. Moscow. 2006.

13. E.K Kazenas, Yu.V. Tsvetkov. Thermodynamics of oxides vaporization. URSS. Moscow. 2008.

14. M.T. Dmitriev, B.I. Bakhtin, B.I. Martynov: Thermal factor of ball lightning. Zhur. Tech. Fiz. **51,** N. 12. 2567—2572 (1981).

15. A.I. Nikitin, T.F. Nikitina and A.M. Velichko, *Analysis of video filmed June 3, 2009 in town Dolgoprudny, Russia,* Proceedings of 10th International conference: Wave electrodynamics of conducting liquid. Long-lived plasma objects and poorly investigated forms of natural electric discharges in atmosphere, 2013, Yaroslavl, Russia, pp. 149—165.

On Ball Lightning Formation by Soliton Waves

Geert C. Dijkhuis

Convectron NV, Rotterdam, the Netherlands. icblchair@kpnmail.nl

Abstract. A Chinese research team has recently reported spectra of natural ball lightning (BL) [1]. A cloud-to-ground lightning stroke in Gansu Province, Northwestern China, formed BL at 0.9 km distance from film cameras equipped with slitless spectrographs. The ball moved horizontally with speed about 8.6 m/s. Successive colors purple, orange, white and red appear during its luminous lifetime of 1.64 s. Its spectral lines reveal radiation from soil elements. Remarkably, in the stable stage the light intensity persistently oscillated at frequency 99.4 Hz, nearly at the second harmonic of 50 Hz as frequency on nearby high-voltage (35 kV) power lines.

Similar luck fell to French colleagues observing thunderstorms in the volcano chain of central France [2]. After some inactivity, the storm reached superheated air masses rising above the city of Clermont-Ferrand. Then in 20 minutes, 21 "superbolt" impacts occurred, emerging directly from the thundercloud anvil. At the sixteenth impact an intense, almost spherical ball of light formed close to ground level, which remained visible for 1.4 second, see Figure 1.

The observers monitored the storm from a distance of about 11 km. They estimated the initial halo size as 12 to 16 m across. About a second later, the halo size had shrunk to 4 to 5 m. Careful inspection found no evidence of damage in the impact area, a hill top at 690 m altitude with little vegetation and without nearby power lines, transformers or other man-made structures. Throughout its short existence the bright halo of light remained static, disappearing exactly where it was formed.

For atmospheric electricity including space charge, (split-)quaternion calculus solves the Maxwell equations in real matrix form [3, 4]. In non-linear plasma regimes, the matrix method opens a shortcut route to soliton wave solutions of the non-linear Schrödinger (NLS) equation [5]. We obtain soliton solutions travelling as helical waves to a channel head that balloons into a sphere. Calculation of ball lightning formation as in Fig. 1 needs tubular waves on a lightning channel smoothly joined to spherical waves on the lightning ball. As kinematic solutions, NLS solitons conserve their total number and energy, as ideal gas molecules do in a micro-canonical ensemble.

We express complex 2×2 matrices for soliton waves in ref. 5 as real 4×4 split-quaternion matrices in non-linear plasma regimes. Matching solitonic wave profiles with pure quaternions we obtain characteristics of chiral soliton waves propagating smoothly across the borderline joining channel and sphere. The hyperbolic secant profiles of Cartesian solitons turn into analogous expressions for cylindrical and spherical coordinates. Multi-soliton solutions result from profiles normalized for finite domains. Characteristic curves smoothly join chiral surface waves propagating along flaring tube and chopped sphere as shown in Fig. 2.

FIGURE 1. Photo of ball lightning formed by a "superbolt" stroke in France.

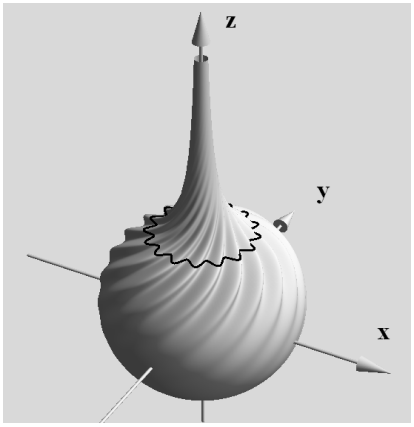

FIGURE 2. Characteristics for soliton waves balloon channel end into sphere.

The common borderline reduces to a wavy circle given by:

$$\{x,y,z\} = \{\rho\cos\varphi\ ,\ \rho\sin\varphi\ ,\ 1\} \qquad (1a)$$

$$\rho = 0.5 + 0.05\cos 16\varphi\ \ ,\ \ 0 < \varphi < 2\pi \qquad (1b)$$

as planar harmonic curve resolved into sixteen wave crests winding the *z*-axis. The sphere radius serves as natural reference length along the *z*-axis in this particular solution. The general soliton solution has free parameters for wave unit counts and reference ranges on either side of the borderline. It marks our quaternion method as a flexible tool for wave front calculation in atmospheric electromagnetics connected with formation of ball lightning.

References

1. J. Cen, P. Yuan and S. Xue, *Observation of the optical and spectral characteristics of ball lightning*. Phys. Rev. Lett. 112, 035001, 24 January 2014.

2. R. Piccoli, *Ball lightning observed after a "superbolt" impact during an exceptional thunderstorm*. Int. Journ. Unconventional Electromagnetics and Plasmas (UEP), Vol. 5, GRP, New Delhi, India, 2013

3. G.C. Dijkhuis, *On 3D potential field solutions for atmospheric charge distributions.* PIERS Online,Vol. 6, No. 4, pp. 300—306, 2010.*piers.org/piersonline/piers.php?volume=6&number=4&page=300*

4. G.C. Dijkhuis, *On chiral wave front calculation for atmospheric electromagnetics*. Int. Journ. Unconventional Electromagnetics and Plasmas (UEP), Vol. 5, General Research Publications, New Delhi, India, 2013.

5.Y. Ben-Aryeh, *Soliton solutions of non-linear Schrödinger [NLS] and Korteweg-de Vries [KdV] equations related to zero curvature in the x,t plane.arxiv.org/ftp/arxiv/papers/1111/1111.5226.pdf*

Simple Method of Doppler Ionospheric Observations

Vladimir T. Polyakov

Department of Telecommunications of the Russian New University (RosNOU),
Radio str., 22, Moscow, 195005 Russia

Among the passive methods of ionosphere monitoring the Doppler method occupies a special place. It allows, receiving signals from the remote broadcast, and possibly other stations, to estimate the overall character of the propagation. By reflection spectra near the signal carrier frequency it is possible to estimate the state of ionospheric layers, their disturbances, vertical movements, and other dynamic processes.

Doppler frequency shift of the signal reflected from the moving layers of the ionosphere, usually small and range from fractions to several Hz. This requires increased frequency stability of master oscillator at the transmitting side and the oscillators in receiver.

The relative instability of the radio transmitters carrier frequency usually best 10^{-8}, which gives 0.1 Hz on 10 MHz, and they may well be used as a reference. Instability of tuning frequency in receivers is usually much more. Often that is the main obstacle to the widespread use of the Doppler method.

Ionosphere is not confined to the slow movement of the layers. This turbulent environment in which the winds blow (by some estimates up to 500 m/s), gives rise to vortices and other large- and small-scale inhomogeneities. Fluctuations in the electron density inevitably lead to a change in the reflection coefficient and the place from which the signal is reflected. Because of this rapid change both the amplitude and phase of the reflected signal is occurs. As a result, instead of a pure sinusoidal signal sent to the ionosphere, we get a complex pseudo noise signal with blurred spectrum.

This is most clearly manifested in the "Aurora" — reflection of VHF radio signals from a region of enhanced ionization in the polar ionosphere. Instead musical telegraph signal we hear parcels (dots and dashes) pure noise. The effect is manifested in normal conditions on HF, but here it is much less — the signal bandwidth extends at best to share, often down to a few, and only sometimes up to tens of hertz.

The essence of the method consists of the simultaneous reception of signals of two or more stations with a radio with an amplitude (AM) detector. He highlights the difference beat frequency between the carrier frequencies. Grid frequency radio HF multiple of 5 kHz, so the beat frequency can be 5, 10, 15, etc. kHz.

Spectral analysis of the difference signal the computer performs. Proved to be very convenient program Spectran, created by Italian radio amateurs I2PHD and IK2CZL and distributed for free. The program digitizes the sound signal from the microphone or line input of computer sound card, and performs the Fourier transform. In view of the program displays the instantaneous spectrum signal and spectrum composed of a sequence of instantaneous spectra. Sampling frequency, the frequency resolution of the spectrogram and the duration ("waterfall" speed) set by the user. Program provides automatic capture and storage spectrograms.

Frequency stability of the difference signal in this method is determined solely by the stability of carrier frequencies of radio stations, and does not depend on the stability of the receiver heterodyne. The only requirement — that the selected carrier frequency did not exceed the bandwidth limits of receiver.

As an example for comparison in FIG. 1 shows the spectrum of AM signal aviation beacon adopted ground-wave and not having ionospheric distortion. Frequency of modulation (vertical axis) is 1000 Hz, the frame duration of about 20 seconds (speed is set such that it was possible to read telegraph signal).

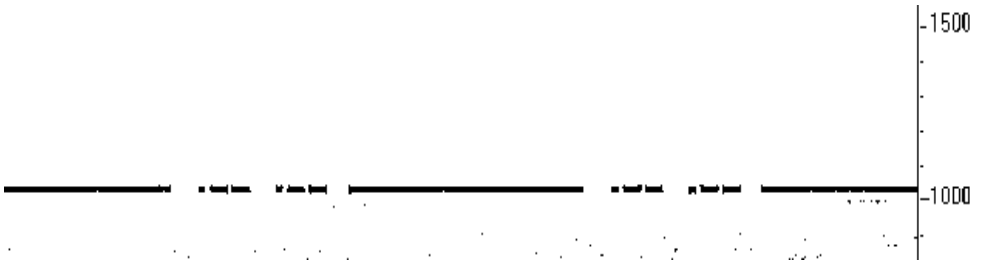

FIGURE 1.

Ionospheric observations by this method were used laptop Compaq Evo600c and receiver Degen DE1103 with telescopic whip or a small wire antenna. Both have an internal battery power supply, fit in a small briefcase and weigh no more than 2—3 kg. Equipment is portable and quite suitable for radio expeditions.

The disadvantage of the method is that the recorded total ionospheric distortion of both received signals. It is eliminated if one of the signals coming from the local station. However, selection of relevant stations operating on adjacent frequencies can be a problem.

Sensitivity is very high. Due to the high frequency resolution (typically better than 0.1 Hz) can record signals of AM stations, the transmission of which is not even heard. An example of such record showed in FIG. 2. In Moscow was received the "Voice of Russia" from Vladivostok at the frequency 12 030 kHz. Support served a much more powerful signal "Radio Liberty" at a frequency of 12025 kHz. Only it was heard. Recorded 06.05.2013 at 16... 16:30 Moscow Time (MSK). The duration of this and subsequent spectrograms is 30 minutes.

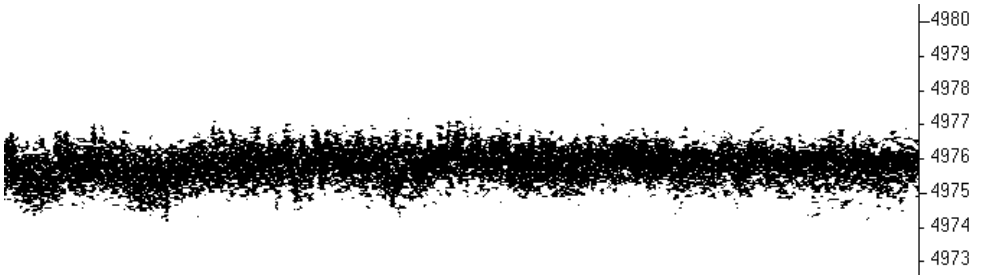

FIGURE 2.

Frequency periodic oscillations, caused by ionospheric waves with a period of about 4 minutes are clearly visible at the beginning and middle of the frame, and about 1 minute at the end. Significant 'blurring' or broadening of the spectrum is visible a bandwidth of more than 1 Hz.

In some cases, there are long gravity waves in the ionosphere with a period of half an hour or more. An example of such a recording made 15.06.2013 at 21:20—21:50 MSK is given in Fig. 3. It was received China Radio International (CRI) from Urumqi at the frequency 7260 kHz. The second station was Radio Belarus on 7255 kHz. Interestingly, the Chinese were louder than the neighboring Belarusians.

FIGURE 3.

Sudden short (1.5 min) perturbation is seen in the middle of the frame. General broadening of the spectral line reaches 2 Hz, the amplitude of the Doppler shift of the long wave — 1 Hz. It's pretty typical for a relatively low frequency (7 MHz), evening and night time.

A more detailed study of the spectra with respect to the near and distant stations showed that the spectrum near stations expands more than that, apparently, is due to close their vertical drop waves on the ionosphere. This effect is particularly strongly manifested when the signal is "Radio Russia" from Taldom (75 km north of Moscow) in the village Springs (33 km south-east of Moscow) at a frequency of 13 665 kHz. Ground wave at a distance of 100 km almost is absent, and the signal came by ionospheric wave at nearly vertical incidence on the ionosphere.

In these experiments, has been found possible to observe reflections from aircraft flying over a large number of the Moscow region. At a wavelength of 20 m and a speed of the aircraft 200—250 m/s (720—900 km/h), the Doppler shift can be as high as 10—15 Hz. Traces of the aircraft can be seen in FIG. 4 in the form of oblique lines, upward and downward from the main track, distorted by ionosphere. In the middle of the frame can be seen as ionospheric disturbance lasting about 2 minutes, possibly caused by a meteorite.

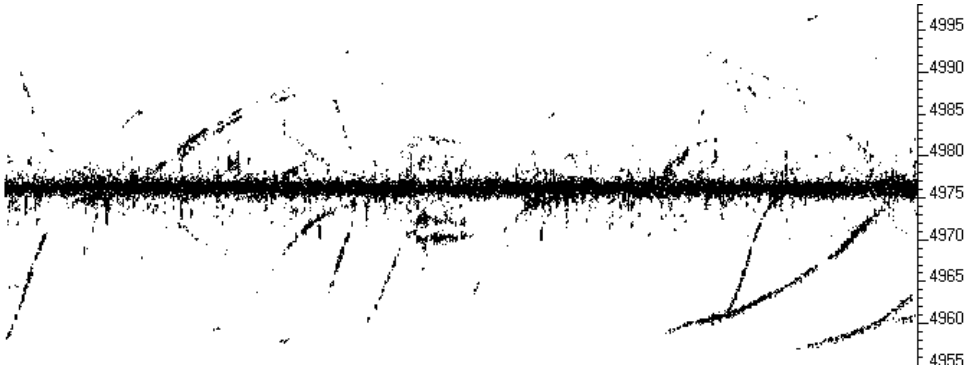

FIGURE 4.

Of particular interest is the observation of ionospheric disturbances during work of heating facilities. Experiments were hindered by the lack of information about the exact time of heating, and it is not always possible to find the desired radio signal which passes through the heating region. Nevertheless, some observations managed to hold.

During the summer session of heating facility in Tromso 19.06.2013 was received station EWTN (Vandiver, USA) at a frequency of 11520 kHz. With a power of 250 kW, it sends a signal to the east, in the direction of Europe and North Africa. Support served signal Grigoriopol (Moldova) at a frequency of 11510 kHz. She could hear perfectly, while Vandiver held weakly, with fading and understood only a few words. Of course, the transatlantic trace is quite far from northern Norway, but it is unknown what impact extends distance heating. Announced time of stand 9—13 UT, spectrum recorded from 9:13 to 9:43 UT (Fig. 5).

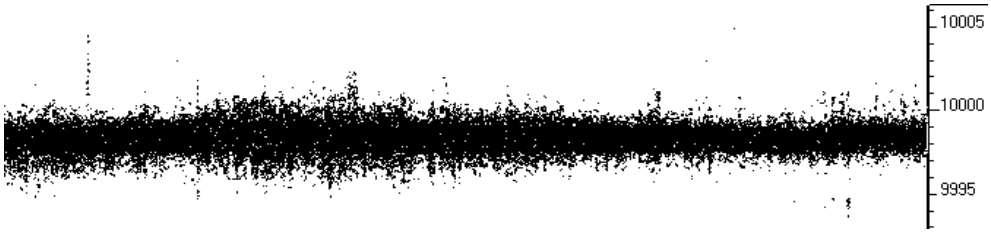

FIGURE 5.

On the color image of Spectran are clearly visible several separate tracks. Unfortunately, in black and white they are not visible. Surprised lower track — he as from the local transmitter, and is not subject to slow Doppler frequency shifts. It can be an "ionospheric mirror". Rapid fluctuations and fadings still were. More frequent was short and broadband impulses that go beyond the limits of the scale. Broadening of the spectrum at 8 minute of recording due presumably artificial ionospheric irregularities associated with the stand work.

In conclusion, the author expresses the hope that the above method will help to make massive Doppler ionospheric investigations.

S-2

The Impact of a Focused Gamma Pulse on the Aircraft Electronic Equipment

A. Chudnovskiy

Open Joint-stock Company "Research-and-Production Corporation "Precision System and Instruments" Isc2004@mail.ru

At present, there are narrowly focused emitters of gamma rays with energies of 300 MeV. Such emitters can pose a threat to the operation of electronic equipment spacecraft.

The process of generation of a focused flux of gamma rays is similar to X-ray physics. The target is used as anode, and as the electrons — their flow at the exit aperture of the linear accelerator. The angular divergence of the gamma ray beam $\theta = E0/E\gamma$ where $E_0 = 0.5$ MeV — electron rest energy, E_γ — energy gamma photon. Since the energy of gamma rays does not exceed the energy of an electron at the output of the electron accelerator E_e, so for the electron energy of 500 MeV angular divergence θ will be 10—3 radians, with generation efficiency of 5—10 %. The duration of the beam of gamma rays is a few microseconds, and the follow-up period of beams is tens and hundreds of Hz. Electrons, emitted from the aperture of the accelerator, are simulated with operating frequency of magnetron 1—10 GHz. Electrons themselves are spatially concentrated at approximately one tenth the wavelength of the magnetron. When the pump frequency of magnetron equal to 3 GHz, the duration of the beam T = 2 microseconds contains about 600 trains of gamma rays with the duration of each train $\Delta t = 0{,}033$ ns.

We show that this emitter is the perfect device for destruction of electronic equipment. Electron-positron pairs are born in the propagation of gamma rays with high energy. Having travelled the long distance, the energy of gamma rays drops to

energies where the probability of the Compton effect increases. In the absorption of gamma rays in a metal housing of the electronic equipment, the electromagnetic pulse is generated inside with electric field intensity ~ $(\Delta t)^{-2}$, and the electromotive force produced in a closed loop ~ $(\Delta t)^{-3}$. Then at the pump frequency of magnetron f_0 similar to 10 GHz the EHV ~ $(10\ f_0)^3$ can be generated.

We proceed to quantitative assessment. Let the average electron beam current be 5 mA. The duration of the emitted pulse Δt = 1 ms, pulse repetition frequency F = 10 Hz, the maximum energy of gamma rays E_γ = 600 MeV, linear accelerator pump frequency *f* = 10 GHz. The number of electrons per second at the output of the linear accelerator $N_e = 3\ 10^{16}$ pieces. With an efficiency of target = 0.33, the total number of gamma rays per second is equal to $N_\gamma = 10^{16}$ pcs./sec. The energy of born gamma photons will lbe in the range from 10 to 600 MeV. Taking the width of the energy spectrum of gamma rays into account, the energy range Eγ = 500 ± 100 MeV has total $N_\gamma = 10^{15}$ pcs./sec. 10 trains are born in 1 second. The train of pulses lasting for 1 second contains 103 gamma rays. The duration of one pulse is 10^{-11}sec, each pulse contains $\delta N_\gamma = 10^{11}$ pcs. gamma rays.

Let's consider the propagation of high-energy gamma quants in the air. During the propagation gamma photon creates an electron-positron pair: electron energy with E' and a positron with energy E". For the gamma quant energy $E >> m_e c^2$ the mean free path will be μ = 230 m before the birth of the electron-positron pair with E′ = 10—50 МэВ [1]. The full loss of the gamma quant energy is reached at distances L = (E/2E′) μ and is respectively equal to 12 km for E′ = 10 MeV and 3km for E′ = 33 MeV when the gamma radiation travels along the Earth's surface.

Let's take a look at the example when the gamma emitter is at the h height. The radiation is oriented vertically. In this case one act run length (before the birth of the first pair) will be:

$$\mu(h) = \mu \exp(h/H), \qquad (1)$$

where h — is the distance from the Earth's surface; H = 8 km scale height of the atmosphere.

Let's estimate maximum distance L, on which the gamma quant energy is completely lost:

$$L = \int_0^{E/2E'} \mu\, dn \exp[(n\mu + h)/H] = H\,[\exp(h/H)][\exp(\mu E/2HE') - 1]. \qquad (2)$$

Table 1 shows the height R, providing the initial energy loss of 1 GeV gamma rays from 1 GeV down to 40 MeV for various energies E' at E = 1 GeV.

TABLE 1.

h [km]	0	4	8	16	24
L [km]/ E′=10 MeV	33	54	89	240	656
L [km]/ E′=33 MeV	12	19	32	87	238

High energy gamma quants create an electron-positron pairs in air, then: the beam divergence is not increased; gamma quants energy falls to 20—40 MeV at distances R. The flux density of a single pulse of gamma quants ρ_γ at distances R is ρ_γ [pcs/m^2] = $\delta N_\gamma (\theta R^2)^{-1} = 10^8 R^{-2}$, where R — distance to target in km.

We now estimate the electromagnetic pulse induced in the body of the radio-electronic equipment (REA). Let the absorption of gamma quants and electrons born in the REA housing be μ_γ and μ_e. We can now estimate the total number of produced electrons penetrating into the body of the electronics (REA)

$$n_e = \rho_\gamma (E_\gamma/E_e)\, \mu_\gamma (1 - \mu_e).$$

Since the mean free path of gamma quants with energy of 30 MeV in Al is 16 cm, and the electrons with energy of 3 MeV — 2 cm, so with a REA body thickness of 3—5 mm μ_γ = 0,025, and $(1 - \mu_e) = 1$. Taking the number of absorbed electrons into account in the housing of REA, the area S in the REA body for one pulse is equal to:

$$n_e = 2{,}5\ 10^8\ S\ R^{-2}\ [км]\ \eta(t) - \eta(t - \Delta t) \qquad (3)$$

Estimation (3) is obtained for a magnetron pump frequency 1 GHz, clock frequency F = 10Hz, the amount of gamma pulse trains 10^3, a pulse duration of 10^{-11}s with a total number of gamma rays in a single pulse $\delta N_\gamma = 10^{11}$, injector current = = 0.16 mA.

The dipole radiation of the electromagnetic pulse for the time structure of gamma quants (3) will be done as follows. Inside the REA body the electromagnetic charge $q = e\, n_e(t)$ is born, where e is the electron charge, with dipole moment $d(t) = q\, l$, where L is the REA body thickness. The dipole moment produces the following electrical field component intensity $E = d''(t)\ (4\pi\varepsilon_0\ c^2\ l/2)^{-1}$, where ε_0 — electrical permittivity of free space, c — the speed of light. Believing $d''(t) = d(t)\ (\Delta t)^{-2}$ for E we get the following estimation

$$E[В/м] = 1{,}2\ 10^8\ e\ S\ R^{-2}\ l\ [4\pi\varepsilon_0\ c^2\ l/2\ (\Delta t)^{-2}]^{-1} = 2\ 10^6\ R^{-2} \qquad (4)$$

The radiation (4) contains from the 4 quasi periods with length of each 2,5 10^{-12} sec. The magnetic component of the radiation has the intensity $H[э] = 6\ 10^3\ R^{-2}$. The induced voltage U from the magnetic component of the radiation for the area $\Delta S = 10^{-4}$m^2 and the area of the REA body S = 0,0225 m^2 (15 × 15 cm) is

$$U[В] = 4\mu_0\ (\Delta S)\ H\ (\Delta t)^{-1} = 3\ 10^6\ R^{-2} \qquad (5)$$

The induced voltage will be 20 V for the 100 km distance between correspondents, that is enough for microchip destruction with 3,3 V supply voltage. Modern accelerators allow to increase injector current to 10mA and to clock frequency to 10 GHz. For this case the destruction of space onboard electronic devices is possible from distances up to 2000 km with induced voltage 7,5 KV for the heights of the radiator equal to 16 km. If the radiator is ground-based, the destruction of the onboard space electronics is available on heights up to 300 km.

Planned Set Of Experiments To Be Performed At International Space Station

Leonid S. Chudnovsky[1], Vladislav S. Chudnovsky[1], Yuriy P. Vain[1], Konstantin S. Mozgov[1], Sergey I. Rensky[1], Sergey A. Panov[1], Nikolay A. Korshunov[1], Vyacheslav A. Shuvalov[2]

[1] Open Joint stock Company "Research-and-Production Corporation "Precision Systems and Instruments" (OJC "RPC "PSI") 53 Aviamotornaya str., Moscow, 111024 Russian Federation
[2] Federal State Unitary Enterprise "Central Research Institute of Machine Building" (FGUP TSNIIMASH) 4, Pionerskaya str., Korolev, Moscow Region, 141070 Russian Federation

Set of experiments on detection of ionizing, optical and radio-frequency radiation of lightning discharge is planned to be performed in 2015—2017. X-rays spectrum time history under solar flares will be studied, and scanning of electromagnetic radiation in millimeter wavelength range will be performed.

Lightning discharge investigation is directed on development of lightning discharge selection algorithms: cloud-to-cloud, cloud-to-Earth and discharges in upper atmosphere.

Lightning discharge optical radiation is detected by an optical radiometer with ± 10° antenna beam width in 0,35—1,2 μm wavelength range, digitized with 1 MHz sampling and written into the data storage device. Data from the storage device will be processed for the purpose of debugging of selection algorithms for lightning discharge radiation; for propagation path distortion analysis using mathematical method of integral functions [1].

Optical detection channel involves high-sensitive optical radiometer with a narrow beam width of ± 2°, designed for turbulent spectrum investigation of Earth background radiation under air-mass transport. Additionally, level of Earth background optical radiation itself is to be estimated.

Electromagnetic radiation detector operates at three frequencies: 35, 75 and 100 MHz. Detected data are stored in the storage device with the period of sampling 0,125 μs. Based on the stored data the arrival time of electromagnetic radiation is refined. Lightning discharge spectrum is also refined, total electron concentration along the propagation path is estimated. Noise data registered in the three spectrum ranges are also investigated.

Processing of lightning discharge optical and radio-frequency radiation data allows to refine the accuracy of measurement method of optical radiation arrival time [2].

Ionizing radiation is detected for γ-quant energy of 0,5—100 MeV. X-rays radiation spectrum is studied for energy range of 1—20 keV. Block is targeted for study of background radiation and intensity of cosmic-ray shower and solar flares.

Electromagnetic scanner of millimeter wavelength range is designed for Earth surface analysis at this range.

1. L. Chudnovsky. Speech signal recovery, distorted by the propagation path / Problems of criminalistics examination of video and audio recordings. Scientific collected papers of National research and development institute of court expertise. Moscow, 1990.

2. L. Chudnovsky, I. GroznovIncrease of accuracy of definition of time of arrival a priori a unknown signal in systems with the limited pass band // I International Conference «Atmosphere, Ionosphere, Safety». Book of Abstracts. Kaliningrad: I. Kant State University Press, 208, P. 217.

S-4

Trace Distortion Corerection

L. Chudnovskiy

Open Joint-stock Company "Research-and-Production Corporation "Precision System and Instruments»

Signals from the source, having travelled through different traces are being registered in dimensional-delivered monitoring systems. Some changes transforming the signal from the source to some standard trace have to be made to identify the received signals. This procedure can be realized as, for example, the inverted filtration problem.

Nowadays methods of the attributes regularization, gomomorf vision (known as the kepstral method for the phase-minimum functions [1, 3, 5]), etc. are being used for the solvation of the inverted filtration problem. Each of these methods has its own features and the borders of use. So the regularization method is used to show the signal from the source, distorted by the passed trace with length of the pulse characteristics shorter than the initial source length. The attribute method (coordinates of the zeroes of the Fourier figure of the signals are located in the complex plane of frequencies) is being well used in the solvation of the inverse problems, when the length of the signal from the source and path pulse characteristics are similar. Kepstral method lets the periodical quasi-delta functional signal propagation path restoration from the source with the repeat frequency lower than the lowest mode frequency of the travelled path. The problem, mentioned above can also be solved with the use of the attribute method.

Presumably the attribute method is the most effective from the methods mentioned above in the inverted problem solvation. There are known examples of use of that method in electromagnetic pulse and seismical acoustic signals [2, 4, 6]. Method was successfully used as for determined as well as for quasi-stationer signal (random processes) [2]. The researches, who use this method, face some severities. The first one is the bound of use the method in case of the artificial truncation of the signal (finitization) in time for further analysis. The second one says, that the process is purely computational when the finite signal is pictured as some set of points in the frequency complex plane (zeroes of the Fourier figure of the finite original signal). The third one is the process of analysis itself, when the achieved sets of the points in the complex plane need to be divided in the trace and signal ones.

Further we'll take a look at the dependency between the dislocation of the zeroes of the Fourier figure (attributes) of the registered finite signal and it's time shape. Achieved evaluations in spaces L_1 and L_2 allow us to ease the attribute coordinates factorization process to path and signal type. The simple algorithm of the inverted problem solvation via attribute method will be observed further. In this algorithm the coordinates of the attributes are not evaluated (it requires too many computational procedures), and the process of the signal restoration itself is being reduced to the Viner's filtration problem.

Let's take a look at the algorithm of the signal processing using the attribute method. Let's observe some signal realizations, having traveled through different paths. Then we overlay the maps of the attribute coordinates (of the same signal having traveled through different paths). Those attributes with matching attributes are taken as the signals for the original signal restoration, travelling through free space [4]. We must point, that the additive noise influence, uneven signal sweep of the recording equipment the in time, existence of the harmonic distortion lead to some dispersion in the signal's attribute coordinates in it's realization.

Let's analyze the energy and time shape distortion of the signal, caused by the attribute coordinates variation. Further it will be shown that these variation cause the appearance of the new additive signal.

Here is the mathematical setting of the attribute method. Let's take a look at the finite segment f(t) of the infinite signal $f_и(t)$:

$$f(t) = f_и(t)[\eta(t) - \eta(t - T)] \quad (1)$$

where: $\eta(t)$ — unit function; T — finitization time interval.

Let's suppose that spectral density of this signal is the entire function of the first order like T:

$$F(\omega) = A\, e^{-i\omega B} \prod_k (\omega - \omega_k) \quad (2)$$

where: A, B — amplitude and time shift of the signal;

$\omega_k = Re\omega_k + iIm\omega_k$ — coordinates of the zeroes of the Fourier figure (attributes), evaluated from the condition

$$\int_0^T f(t)\, e^{-i\omega t}\, dt = 0.$$

We can restore signal f(t) up to the amplitude A and time shift B if the coordinates of the attributes are known. If A and B are not meaningful parameters of the signal analysis, the equation (2) can be showed as following:

$$F(\omega) = \prod_{k,\,n} (\omega - i\mathrm{Im}\omega_k)^{ak} (\omega - \omega_k)^{an} (\omega - \omega_n^*)^{an} = f_n(\omega)\, f_k(\omega) \qquad (3)$$

where: ak, an — zero multiplicities; ω_k — imaginary axis zero coordinates; ω_n — complex conjugate zero coordinates.

Let's confine with the case of aliquant roots $a_k = a_n = 1$. As it is stated in equation (3), we have two opportunities of the attribute's coordinates offset. Let's take a look at the attribute coordinates offset in ω_n, when

$$\omega_n^{\text{воз}} = \omega_n + \delta\omega_n = \mathrm{Re}\omega_n + i\mathrm{Im}\omega_n + \mathrm{Re}\delta\omega_n + i\mathrm{Im}\delta\omega_n \qquad (4)$$

The attributes offset leads to the appearance of the additive signal in spectral area

$$F_{\text{воз}}(\omega) = F(\omega) + \delta F(\omega) \qquad (5)$$

$$\delta F(\omega) = 2F(\omega)\, \chi(\omega)\{\,|\,\delta\omega_n\,|\,|\,\omega_n\,| + i\mathrm{Jm}\delta\omega_n\} \qquad (6)$$

$$\chi(\omega) = (-\omega^2 + \omega_n\omega_n^* - 2i\omega\, \mathrm{Jm}\omega_n)^{-1} \qquad (7)$$

In time area the signal is being ranked in the following way:

$$\Delta f(t) = -\alpha[\,|\,\delta\omega_n\,|\,|\,\omega_n\,| + \mathrm{Im}\delta\omega_n(d/dt)][f(t) \circ \chi(t)] \qquad (8)$$

where ○ — convolution operation; χ(t) — filter pulse characteristic (7).

Pulse characteristic χ(t) differs for $\mathrm{Im}\omega_n > 0$ and $\mathrm{Im}\omega_n < 0$:

$$\chi_+(t) = \eta(t)\, (\mathrm{Re}\omega_n)^{-1} \exp(-\mathrm{Im}\omega_n t) = \theta_+(t)\, \eta(t);\ \mathrm{Im}\omega_n > 0; \qquad (9)$$

$$\chi_-(t) = [1 - \eta(t)]\, (\mathrm{Re}\omega_n)^{-1} \exp(\mathrm{Im}\omega_n t) = \theta_-(t)\, \eta(t);\ \mathrm{Im}\omega_n < 0; \qquad (10)$$

Substituting (9) and (10) in equation (8), we achieve the estimation of the error in L_1:

$$\Delta f(t\,|\,\mathrm{Im}\omega_n > 0) = -2[\eta(t) - \eta(t - T)]\ \{[\,|\,\omega_n\,|\,|\,\delta\omega_n\,| - \mathrm{Im}\omega\mathrm{Im}\delta\omega_n]F_+(t) - \mathrm{Im}\delta\omega_n\mathrm{Re}\omega_n\, F_+^*(t)\} \qquad (11)$$

where:

$$F_+(t) = \int_0^t \theta_+(t - t')\, f('t)\, dt' \qquad (12)$$

$F_+^*(t)$ — Gilbert transformation of the signal from $F_+(t)$

$$\Delta f(t\,|\,\mathrm{Im}\omega_n < 0) = -2[\eta(t) - \eta(t - T)]\ \{[\,|\,\omega_n\,|\,|\,\delta\omega_n\,| - \mathrm{Im}\omega\mathrm{Im}\delta\omega_n]F_+(t) - \mathrm{Im}\delta\omega_n\mathrm{Re}\omega_n\, F_-^*(t)\} \qquad (13)$$

where: $F_{-}(t) = \int_0^t \theta_{-}(t - t')\, f(t')\, dt'$ (14)

$F_{-}^{*}(t)$ — Gilbert transformation of the signal from $F_{-}(t)$.

Using relation $d/dt[f(t)e^{At}] = Af(t)\, e^{At} + f'(t)\, e^{At}$, we achieve asymptotical estimations of the (11), (13):

$$\delta f(t) \approx 2\, \mathrm{Im}\delta\omega_n \left| \omega_n \right|^{-1} f(t)[\eta(t) - \eta(t - T)];\ \left| \omega_n \right| >> \left| f'(t)/f(t) \right| \quad (15)$$

$$\delta f(t) \approx 2\, \mathrm{Im}\delta\omega_n\, [\eta(t) - \eta(t - T)] \int_0^t f(t')dt';\ \left| \omega_n \right| << \left| f'(t)/f(t) \right| \quad (16)$$

Let's show the estimations of the distortions caused by attribute coordinates changing $\delta\omega_n$ и $\delta\omega_n^{*}$ in L_2:

$$\Delta\varepsilon = \int_0^T [\delta f(t)]^2 dt \quad (17)$$

$$\Delta\varepsilon \approx 4 \left| \mathrm{Im}\delta\omega_n/\omega_n \right|^2 \varepsilon;\ \left| \omega_n \right| >> \left| f'(t)/f(t) \right| \quad (18)$$

$$\Delta\varepsilon \approx 4 \left| \mathrm{Im}\delta\omega_n \right|^2 \int_0^T dt \iint_{-\infty}^{t} f(t')\, f(t'')\, dt'dt'';\ \left| \omega_n \right| << \left| f'(t)/f(t) \right| \quad (19)$$

$$\varepsilon = \int_0^T f^2(t) dt \quad (20)$$

Let's take a look at the pure imaginary roots case

$$\omega_k^{\text{воз}} = \omega_k + \delta\omega_k = i\mathrm{Im}\omega_k + i\mathrm{Im}\delta\omega_k \quad (21)$$

The offset of the attribute $\mathrm{Im}\delta\omega_k$ leads to the formation of the additive signal in spectral area:

$$\Delta f(\omega) = i\, \mathrm{Im}\delta\omega_k\, (\omega - i\mathrm{Im}\omega_k)^{-1}\, f(\omega)$$

In time area additive signal $\delta f(t)$ is being evaluated in the following way:

$$\Delta f(t) = \left[\int_{-\infty}^{+\infty} f(t')\, \gamma_n(t - t')dt'\right] \mathrm{Im}\delta\omega_k \quad (22)$$

$$\gamma_n^{+}(t) = \eta(t) \exp(-i\mathrm{Im}\omega_k t);\ \mathrm{Im}\omega_k > 0 \quad (23)$$

$$\gamma_n^{-}(t) = [1 - \eta(t)] \exp(i\mathrm{Im}\omega_k t);\ \mathrm{Im}\omega_k < 0 \quad (24)$$

Equation (23) lets the asymptotical estimation:

$$\delta f(t) = [\eta(t) - \eta(t - T)]\mathrm{Im}\delta\omega_k \left| \omega_k \right|^{-1} f(t);\ \left| \mathrm{Im}\omega_k \right| >> \left| f'(t)/f(t) \right| \quad (25)$$

$$\delta f(t) = [\eta(t) - \eta(t - T)]\mathrm{Im}\delta\omega_k \int_{-\infty}^{t} f(t')dt';\ \left| \mathrm{Im}\omega_k \right| << \left| f'(t)/f(t) \right| \quad (26)$$

Distortion, caused by the changing of $Im\delta\omega_k$ in L_2, are estimated in the following way:

$$\Delta\varepsilon \approx (Im\delta\omega_k/Im\omega_k)^2\,\varepsilon;\ \left|\, Im\omega_k \,\right| >> \left|\, f'(t)/f(t) \,\right| \tag{28}$$

$$\Delta\varepsilon \approx (Im\delta\omega_k)^2 \int_0^T dt \iint_{-\infty}^{t} f(t')\, f(t'')\, dt'dt'';\ \left|\, Im\omega_k \,\right| << \left|\, f'(t)/f(t) \,\right| \tag{29}$$

Let's discuss the achieved results. According to the received estimations there are two asymptotes: high frequency equations (28) and (29) not distorting the signal in fact, but only changing its amplitude, and low frequency equations (26) and (27), leading to the additional additive member, that is an integral from the original signal f(t).

So there are 3 areas: Ω_1, Ω_2, Ω_3, where the offset of the attribute coordinates influence the norm of the original signal in different way. Let's take a look at the influence of these areas in L_1. In low frequency area Ω_1 where $\left|\, \omega \,\right| >> \left|\, f'(t)/f(t) \,\right|$, only the signal amplitude, not depending on the coordinate $\left|\, \omega_n \,\right|$ and proportional to its offset $\left|\, \delta\omega_n \,\right|$. In high frequency area Ω_3 where $\left|\, \omega \,\right| << \left|\, f'(t)/f(t) \,\right|$,the signal value is being increased by its integral value, proportional to $\left|\, \delta\omega_n/\omega_n \,\right|$. In area Ω_2 that is the most interesting for the analysis asymptotical distortions similar to areas Ω_1 and Ω_3 were not achieved.

It is important to keep the same number of the attributes in area Ω_1, as that even coordinates of the remote attributes are not significant while solving the reverse problems. In area Ω_3 the attributes having maximum dispersion from selected standard and are located closer to the beginning of the coordinate plane should be removed.

Picture 1 shows the result of acoustic pulse restoration, having passed through different paths (segments of pipes). Doing this we must keep in mind, that signals $f_1(t)$ and $f_2(t)$ are distorted pulse f(t), having travelled through different paths (pipes combinations).

Now let's switch our attention to the problem of not minimal phase signal processing using the attribute method. In this case it is possible to skip to another problem: the problem of optimal filtration, selecting the signal, having travelled apriory unknown path.

If the signal doesn't belong to the minimal phase class, the solvation of the inverse problem using, for example, kepstral method [5] can be more difficult because it is necessary to perform analytic elongations for ω- and z- signal transformations. There are some difficulties, while performing such evaluations on PC. The use of the attribute method eases the procedure of evaluation gomomorf transformation of the signal in ω- and z- planes. Let's look at the interconnection between the attributes method and the gomomorf view.

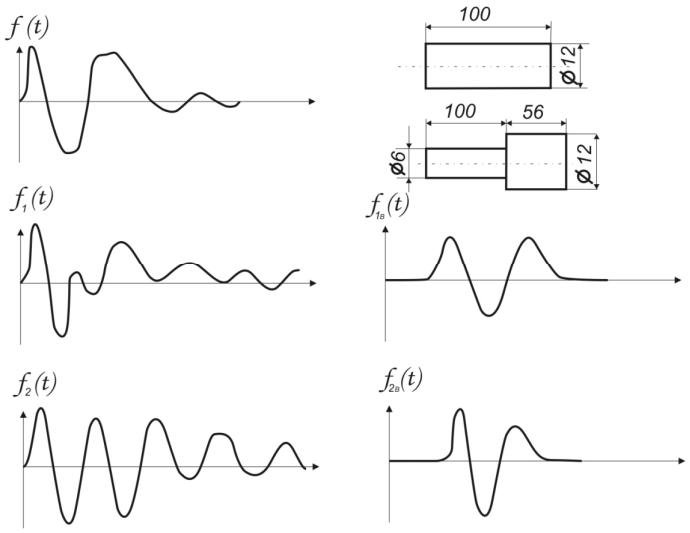

FIGURE 1. Restored signals $f_{1в}(t)$ and $f_{2в}(t)$ of the acoustic pulse f(t), having travelled through different paths (segments of pipes). The restoration was based upon the distorted signals $f_1(t)$ and $f_2(t)$.

We have straight and reverse ω- and z- transformations for the original function f(t):

$$f(\omega) = \int f(t)\, e^{i\omega t}\, dt;\ f(t) = (2\pi)^{-1} \int f(\omega)\, e^{i\omega t}\, d\omega \tag{30}$$

$$f(z) = \int f(t)\, z^{t/\Delta t}\, dz;\ f(t) = (2\pi i/\Delta t) \int f(z)\, z^{-t/\Delta t - 1}\, dz \tag{31}$$

and the concepts of generalized function are introduced:

$$\delta(t) = (2\pi)^{-1} \int e^{i\omega t}\, d\omega;\ \delta(t) = (2\pi i/\Delta t) \int z^{-t/\Delta t - 1}\, dz \tag{32}$$

and there is a decomposition f(t) on the generalized functions for its digitalized values f_n:

$$f_n = \sum_{n=0}^{n=N} f(t)\, \delta(t - n\Delta t) \tag{33}$$

where: Δt — time interval of the discretiztion

Equations (30, 31) will be the following for the signal (33):

$$f(\omega) = \sum_{n=0}^{n=N} f_n\, e^{-i\Delta t n \omega}\ f(z) = \sum_{n=0}^{n=N} f_n\, z^n \tag{34}$$

Using the attributes coordinates equations (34) can look the following way:

$$f(\omega) = B \prod_{n=1}^{n=N} (\omega - \omega_n)\ f(z) = A \prod_{n=1}^{n=N} (z - z_n) \tag{35}$$

where: B, A — some complex numbers.

Let's introduce gomomorf view $\Gamma\{f(t)\}$ for ω- and z- transformations [5]:

$$\Gamma_\omega\{f(t)\} = (2\pi)^{-1}\int_{-\infty}^{\infty} e^{i\omega t}\,\mathrm{Ln}[f(\omega)]\,d\omega \qquad (36)$$

$$\Gamma_z\{f(t)\} = 2\pi i\int_{-\infty}^{\infty} \mathrm{Ln}[f(z)]\,z^{-n-1}\,dz \qquad (37)$$

Putting (35) in (36,37), we'll achieve:

$$\Gamma_\omega\{f(t)\} = \delta(t)\mathrm{Ln}B + \delta(t-n\Delta t)\{\sum_{n=1}^{n=N}\{(n\Delta t)^{-1}\eta(n\Delta t)\,[\sum_{n=1}^{n=N}\exp(-i\mathrm{Im}\omega_l n\Delta t) + 2\sum_{k=1}^{k=K}\exp(-i\mathrm{Im}\omega_k n\Delta t)\cos(\mathrm{Re}\omega_k n\Delta t)] + (n\Delta t)^{-1}[1-\eta(n\Delta t)]\cdot [\sum_{n=1}^{n=N}\exp(i\mathrm{Im}\omega_n n\Delta t) + 2\sum_{m=1}^{m=K}\exp(i\mathrm{Im}\omega_m n\Delta t)\cos(\mathrm{Re}\omega_m n\Delta t)]\}\} \qquad (38)$$

where: ω_l — attributes with imaginary coordinate $\mathrm{Im}\omega_l > 0$;
ω_k — attributes with complex conjugate coordinate $\mathrm{Im}\omega_k > 0$;
ω_n — attributes with imaginary coordinate $\mathrm{Im}\omega_n < 0$;
ω_m — attributes with complex conjugate coordinate $\mathrm{Im}\omega_m < 0$;
N — number of the signal counts f(t).

$$\Gamma_z(n\Delta t) = \delta(n\Delta t)\,\mathrm{Ln}A + \sum_{n=1}^{n=N}\delta(t-n\Delta t)\,\{\sum_{l=1}^{l=L} z_l^{-n} + \sum_{k=1}^{k=N/2-L-1}[z_k^{\,n} + (z_k^{\,*})^n]\,\big|\,z_k\,\big|^{-2n}\} \qquad (39)$$

where: z_l — real roots of the polynomial (34); z_k — complex conjugate roots of the polynomial (34).

It is seen from the equations (35, 38, 39), that gomomorf view carries the information about the amplitude of the signal and its shift in time (factors A and B). This information can't be used if the first additive members in equations (38) and (39) are removed. Gomomorf view in ω-plane gives the attribute division with $\mathrm{Im}\omega > 0$, $t > 0$ and $\mathrm{Im}\omega < 0$, $t < 0$. In gomomorf view the selection of the signal from the source, having travelled through different paths is done equally to the selection of the signal from the additive noise background, similar to the Viner's filtration problem.

1. *Арсенин В.Я., Иванов В.В.* Об оптимальной регуляризации // ДАН СССР. 1969. № 1.

2. *Иванов В.В., Гарднер О.И.* О восстановлении источника по сигналу сложной формы // Вопросы радиоэлектроники. М., 1984. Серия ЭВТ Вып. 8.

3. *Иванов В.В., Степанов Б.М.* Восстановление формы сигнала, свободной от искажений, обусловленной трассой распространения, как этап оптимального распознавания // Импульсные электромагнитные поля и измерения их параметров. М., 1976.

4. *Иванов В.В., Черный Г.П.* Метод восстановления в источнике, основанный на методе признаков // Обратные задачи теории рассеяния и теории статически нерегулярных трактов. М., 1979.

5. *Оппенгейм Э.* Цифровая обработка речевых сигналов // Применение цифровой обработки сигналов. М., 1980.

6. *Чудновский Л.С., Конкин А.Н.* Применение метода признаков к анализу акустических и речевых сигналов // Тез. докл. и сообщений 13-ой Всес. школы-семинара «Автоматическое распознавание слуховых образов» (АОСО-13). Новосибирск, 1984.

The Fluctuation Amplitude Variation of Navigation Signals of GLONNAS Space Satellites

L. S. Chudnovskyi[1], M. G. Golubkov[2], V. L. Frolov[3], S. G. Kuzin[1], U. P. Vagin[1]

[1] OJSc "Research and production company "Precision system and instruments", Moscow
[2] Institute of chemical physics (Russian Academy of Science), Moscow
[3] Radio Physica Research Institute, Nizhny Novgorod
E-mail: lsc2004@mail.ru

The ionosphere exposure experiments were carried out in August-September 2012 by "Sura" bench. The result of exposure was estimated by GLONASS-M spacecraft (SC) radio signal amplitude variation at frequencies F1 and F2. Highly-energetic processes space monitoring system (EPSM) multi-channel units were used as a radio signal receivers. Unit registers pulse radiation situation on SC at different spectral ranges. Pulse source coordinates are determined by range-difference method, so EPSM receive units constantly record navigation signals from 16 SC to obtain their coordinates. Receiver units sensibility – 160 dB, with 1 dB resolution relative to noise sensibility. SC GLONASS radiation was simultaneously recorded in Moscow (Aviamotornaya subway station) and in Krasnoznamensk. Amplitude of SC signals was recorded with period of 12 sec., in some periods of time 4 sec. The coordinates of points are presented in Table 1.

TABLE 1. The coordinates of receive points.

	Receive points	
	Aviamotornaya	Krasnoznamensk
Latitude (deg)	55,7	55,6
Longitude (deg)	37,7	37,0
X (km)	2846	2883
Y (km)	2202	2176
Z (km)	5248	5238

Liters and frequencies correlation and also their belonging to SC distribution points are represented in Table 2.

TABLE 2. Frequency belonging to liter and its correspondence to point.

Liter	F1 (MHz)	F2 (MHz)	Points
6	1605,375	1248,625	4,8
5	1604,813	1248,188	3,7
4	1604,25	1247,75	17,21
3	1603,688	1247,313	19,23
2	1603,125	1246,875	20,24
1	1602,563	1246,438	1,5
0	1602	1246	11,15
– 1	1601,438	1245,563	12,16
– 2	1600,875	1245,125	9,13
– 3	1600,313	1244,688	18,22
– 4	1599,75	1244,25	2,6
– 5	1599,188	1243,813	
– 6	1598,625	1243,375	
– 7	1598,063	1242,938	10,14

As we have 14 liters and 24 points, then liters are less than space crafts, in other words, we have 2 space crafts for 1 liter. But space crafts are not misrecognized, while the same liters correspond to antipodes, in other words, space crafts placed in opposite points of surface. So space crafts with one liter are placed on one surface and their numbers are differed by 4. Signal-to-noise ratio for frequency F2 is marked by red color and for F1 by black color on figures of this paper.

EPSM system receive module antenna is represented on Figure 1. Unique feature of module is the opportunity of 16 “GLONASS-M” SC navigation signals simultaneous record with high-powered narrowband and pulse noise cancellation. Dependence of sensibility of receiving module on elevation is represented on Figure 2.

2 resulting experiments were carried on: 18 September 2012 (14^{40}—15^{15} and 22^{21}—23^{16}, Moscow time); 20 September 2012 (14^{40}—16^{25}, Moscow time). The rest experiments did not conform to conditions of receiving.

Go on to experiment results discussion.

FIGURE 1. EPSM system receive module antenna depending on elevation.

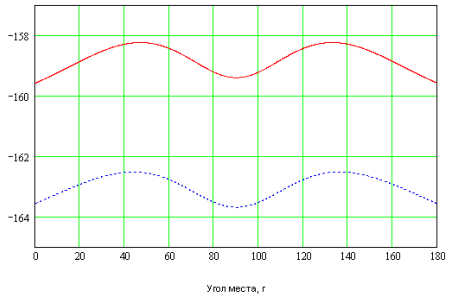

FIGURE 2. Power of received signal.

Experiment in 18 September 2012.
Time of experiment 14^{40}—15^{50}.

Recording of radio signal by SC "GLONNAS-M" was obtained in Moscow (Aviamotornaya metro station) and Krasnoznamensk. Time of experiment corresponds to the sub-satellite points 2, 3 and 4.

Signal-to-noise ratio variation for Moscow site with average level + 52.5 dB to frequency F2 is represented on Figure 3a. Evidently, that full time range of session is captured. Similar recordings for Krasnoznamensk are represented on Figure 3b. Average level for frequency F2 was comprised + 44 dB that corresponds to greater value of recording at zenith angle. At the moment of session, oscillations of signal ratio with period of 1.6 minutes and low-graded low-frequency modulation of primary oscillations with period of 10 minutes were observed.

Conclusion. At moment of experiment were registered perturbed zones of signal-to-noise ratio with recording angles approaching to 90^0. Two minimums were observed in Moscow, and signal-to-noise ratio oscillations were observed in Krasnoznamensk.

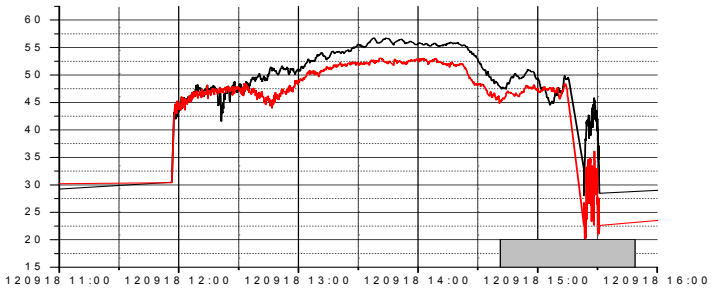

FIGURE 3a. Signal level (Moscow, Aviamotornaya subway station).

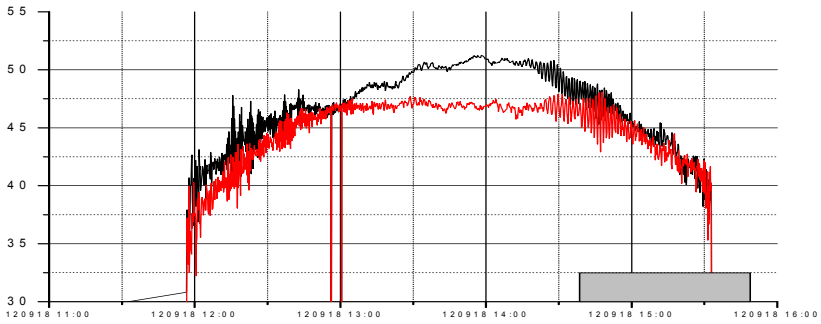

FIGURE 3b. Signal level (Krasnoznamensk).

Experiment in 18 September 2012.
Time of experiment 21^{21}—23^{16}.

Record of radio signal by SC "GLONNAS-M" was done in Moscow (Aviamotornaya subway station) and Krasnoznamensk. Time of experiment corresponds to the sub-sattelite points 7,8,9.

Variation of signal-to-noise ratio for Moscow point with average level +46 dB on frequency F2 is represented on Figure 4a. Evidently, that full time range of session is captured. It was apparently occurred because of radio signal receiving zenith angle changing, that cause to heating zone encounter in the end of session with delay of 15 minutes that corresponds to increasing zone with enhanced electronic concentration. Similar data for point Krasnoznamensk is represented on Figure 4b. Average level for frequency F2 is + 42 dB that corresponds to greater value of zenith angle recording. Registration of heating zone was not occurred. One hour before session oscillations with period of 1 minute were registered.

Conclusion. At time of experiment were partly registered perturbed zone with enhanced electronic concentration and with recording angles approaching to 90^0 and oscillations with period of 1.0 minute, which are not related to heating zone.

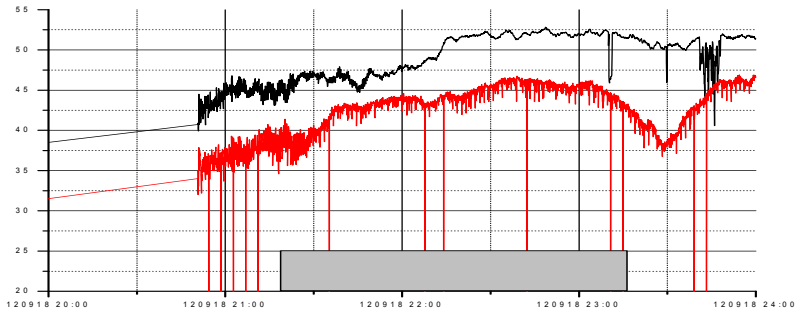

FIGURE 4a. Signal level (Moscow, Aviamotornaya subway station).

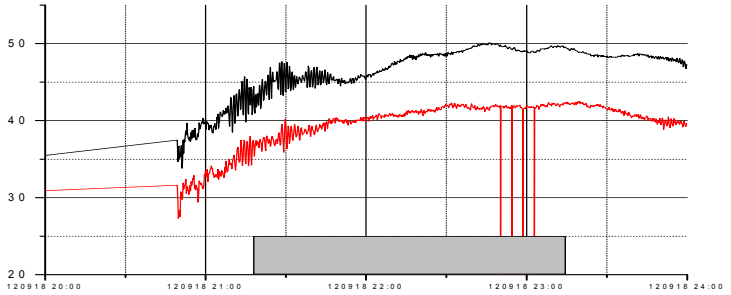

FIGURE 4b. Signal level (Krasnoznamensk).

Experiment in 18 September 2012.
Time of experiment 14^{40}—16^{25}.

Radio signal by SC "GLONNAS-M" was recorded in Moscow (Aviamotornaya subway station). Time of experiment corresponds to the sub-satellite points 3, 4, 5, 6 and 7.

Signal-to-noise ratio variation for Moscow site with average level + 52 dB on frequency F2 is represented on Figure 5a. Evidently, that the middle and the end range of session is captured. It was apparently occurred because of radio signal recording zenith angle changing, that cause the encounter into heating zone in the middle and the end of session.

Conclusion. At time of experiment were registered perturbed zone with ehanced electronic density. Registration of perturbed zone was occurred with east-azimuth angles that corresponds to perturbed zone encounter.

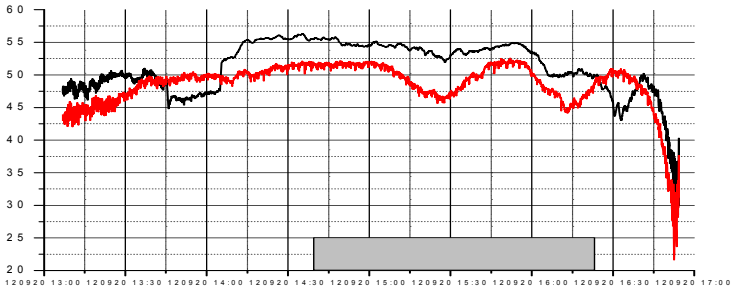

FIGURE 5a. Signal level (Moscow, Aviamotornaya subway station).

Conclusions.

1. 18 September data on Figure 5 demonstrates more obvious power signal decreasing while heating zone encounter.

2. Similar decrease is also registered, but it is not related to the heating zone of bench on Figure 3b.

3. EPSM system radio signal receive hardware on zenith angles approaching to 90^0 registers:

— Formations in ionosphere with enhanced concentration of electronic density;

— Fluctuations of electronic density with period of 1—3 minutes on time range 0.5—1.5 hour;

— Fluctuations of electronic density with period of 5—10 minutes on time range 0.5—1 hour.

4. Preliminary conclusions can be made after recorded data summarizing:

— Anthropogenic formations with enhanced density with whether technogenic or geophysical nature exist in ionosphere, that cause to registered radiation power absorption;

— $\sim \exp(-Df^{-2})$, D — value is proportional to integral electronic density and effective frequency of collisions;

— Fluctuations of electronic density with period of 5—10 minutes on time range 0.5—1 hour does not depend on frequency of receiving signal;

— Fluctuations of electronic density with period of 1—3 minutes on time range 0.5—1.5 hour does not depend on frequency of receiving signal.

5. Radio signal power attenuation while ionosphere anthropogenic formations transmission is — 5dB and more.

S-6

Designing a System of Recognition of Key Words

L. S. Chudnovskiy[1], V. M. Ageev[1], I.N Chudnovskaya[2]

[1] Open Joint-stock Company "Research-and-Production Corporation "Precision System and Instruments"
[2] Moscow State University
E-mail lsc2004@mail.ru

The trend of increasing terrorist threats makes it necessary to create a global system of recognition of "key" words in order to prevent risks arising ing. Search for "key" words in text files is not particularly difficult. Detection of "key" words in continuous speech is a challenging task. Creating a detection device "key" words of interest to the fifth generation of computers, as well as the management of industrial and military robots. The problem of detection of "key" words should be addressed to the following conditions for admission: speaker posts any, limits on the communication channel and the type of microphone was absent.

Speech recognition systems are based on the following principle. Original time sequence functionally converted into comfortable for further pattern recognition of view. This procedure is called the primary analysis. Result of the initial analysis is segmented into time segments, each segment is assigned a code. Next on the code sequence assembles words primary analysis.

Widely used as a spectral and cepstral transformation, linear prediction, the shape recovery of the vocal tract, the analysis pre otfilrovan-tion and ultimately bounded sequences and other methods. These methods does not ensure sustainable results when changing the speaker, the volume of verbal expression, such as a microphone, and other factors.

Figure 1 shows the dynamics of the emergence of false spectral resonance caused by the complex vibrations of the vocal cords.

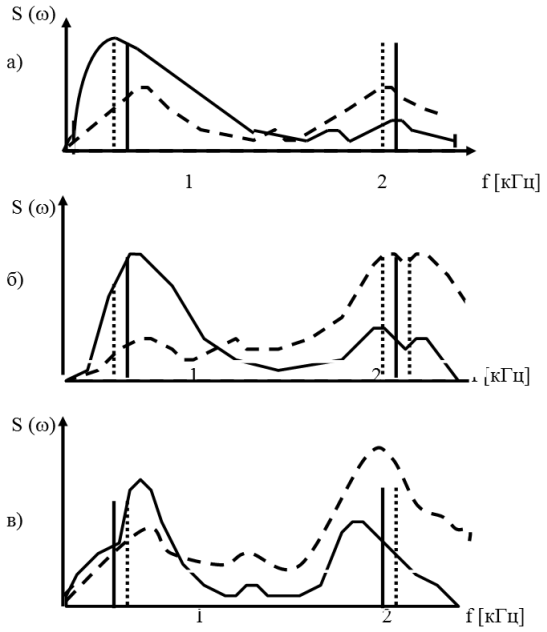

FIGURE 1. The spectral density of the resonance frequency value, measured at intervals of free oscillations, isolated vowel "e", spoken by a) low volume, b) the average volume c) high volume record with dynamic microphone record with a carbon microphone.

Figure 1 shows that if the speech signal is passed through a selective filters with different resonance frequencies, and then filter results ultimately limit the (otklippirovat) and pass through the detector counting, we can identify areas of free oscillations, when the effect of vibrations of the vocal cords and little portions of the forced oscillation, when the contribution of the tone source on the formation of oscillation — venen there exists [1]. In the interval of free oscillations of the detector readings stabilize countable — smiling and frequency of free oscillations are allocated Fashion speech signal. The first measurements of the frequency charac-

teristics of the speech signal in the areas of free oscillations showed their resistance values for the same phoneme when changing the type of microphone and speaker volume and verbal expression [1]. Measuring the frequency of free vibrations of the vocal tract were carried out in the analog-to- digital primary analyzer "Array 2" to highlight the "key" words in a stream of continuous speech [1]. Besides the rather stable frequencies of free oscillations of the vowels (for different speakers) have been allocated frequency half-wave dipole moments in the formation of commissures in the vocal tract. Frequency interval of half-wave vibrator mode can serve as an informative feature length tract speaker speech production.

Segmentation voice message on phonemic units is mainly done by an internal timerand otsegmentirovanny speech segment is identified as a non- vector in which a given codebook or already recorded patterns of speech. In the speech analyzer "Array-2" [1] in sync with the voice signal is dynamically determined and fixed segments. To allocate dynamic segments used extrema we modified phonetic A. A. Pirogova The AI function of the i-th parameter. At the moment of the signal The AI = 1, and at the time of shutdown The AI = 0. Stationary segments were sought in the interval the AI = 1 ± m (m < 0,15). Analyzer "Array 2" voice messages recorded in the frequency range of 0.3—3.4 kHz in 8 spectral bands. In each band were measured: ωi — free vibration frequency; Gi — band at the resonant frequency and the ratio of the energy of free oscillations of temporary sites to the total energy of the signal; the relative time duration of free oscillations. Since the "Array-2" was intended for the detection of "key" words in a stream of continuous speech training was alternation of static and dynamic segments of a given word for family announcers.

Upon detection of segments in automatic speech recognition is often used comparison metric L_2 segment with given generalized standard. In the "Array-2 " was used a completely different metric. The first step was the correct choice of histograms for the null hypothesis. For this analysis of a large sample of long-term the neutral continuous speech. The AI for the histogram parameters were built for static and dynamical segments. Depending on the number of measurements for the defined number of randomly spaced intervals lyalos analysis the AI for each. The number of these intervals is proportional to the cube root of the number of measurements and determined the accuracy of compromise histogram and mean square error within the set-val. Then, for the null hypothesis for each parameter The AI built finely rippled probability of hitting a predetermined interval are not equidistant.

When training on the word for a given segment of static or dynamic histogram different from uniform. Histogram itself and was likelihood ratio for optimal recognition. This approach allowed us to obtain a more accurate metric for detecting segment than L_2. Detection segment carried maximum likelihood ratio.

Consider the features of the "assembly" of the word. Segmentation of verbal communication by an internal timer assembly word forcibly chopped segments carries Xia using dynamic programming or Markov chain. As in "Array 2" automatic segmentation performed by a predetermined developing kidney Tse — alternation

of static and dynamic segments, the assembly is carried by the words of the likelihood ratio for each segment. Maximum likelihood ratio memorable peak detector. Responses were summed peak detectors. Because the number of static and dynamic segments of course, but also the sequence defined, the maximum reading on the total peak detectors and Sequence segment produces word recognition.

The very process of detecting a given "key" words was carried out continuously for a time window of duration T. At the end of Sequence of static and dynamic segments of speech measured response peak detector, which was compared with other responses of "foreign" words. By the maximum response implementation moose detection of "key" words. Tests proposed algorithms were implemented on three "key" words to the total number of realizations of the "key" words to the voice sample of 150 lasting 30 minutes. Was missed 5 "key" words and made 2 false. Education keyword carried cooperative 16 speakers, and the detection of "key" words was carried out on the speech material announcers non cooperative learning [1].

1. Chudnovsky L. S., Minayeff V. A., Chudnovskaya I. N. Speech technologies in kriminalistiche-ray phonoscopy, Tutorial, Part 1. Krasnoyarsk Russian MVD height-Shaya School, 1997.

2. L. S. Chudnovsky Measurement phenomenological characteristics nonstationary inhomogeneous waveguide its radiation (link will update the meeting)

3. Chudnovsky L. S., V. M. Ageev Calculation of the basilar membrane filters // Materials Conference "Theory and Practice of speech research (APCO-99)", Moscow, 1999, C. 145—151.

Ab Initio Calculations of the Low-Lying Electronic States of NO Molecule

S. O. Adamson

Laboratory of Molecular Structure and Quantum Mechanics, Department of Chemistry, Lomonosov Moscow State University, Leninskie Gory, 1, Moscow 119991, Russia

The excited states of NO molecule have been the object of theoretical studies during the several years [1—9]. During the *ab initio* calculations some problems have been registered due to the dramatic difference between the Rydberg and valence character of states accompanied by the number of avoided crossings [4—9]. Nevertheless the reliable *ab initio* potential energy curves together with the dipole moment functions (DMF) and transition dipole moment functions (TMF) are available for several electronic states [5—8].

In present study the potential energy curves and the dipole moment functions of $1—3^2\Pi$, $1—3^2\Sigma^+$, $1^2\Delta$, $1^2\Phi$ and $1^2\Sigma^-$ adiabatic electronic states were calculated using the icMRCI (internally contracted multireference configuration interaction method) and icMRCI + Q (with the Davidson corrected energies) methods [10]. The 6—311G ++ (3df,3dp) atomic basis sets augmented by diffuse functions of *s*- and *p*-types were used in all calculations.

The T_e values obtained by icMRCI method are in a reasonable agreement with the experimental ones and the icMRCI + Q reproduces the experimental results better than the icMRCI method (Tab. 1) [5—9]. The same situation is taking place for the r_e and w_e parameters.

TABLE 1. Theoretical and experimental T_e values. All data in cm^{-1}.

State	MRCI	MRCI[a]	MRCI+Q	MRCI + Q[a]	Exptl.[b]
$X^2\Pi$	0	0	0	0	0
$A^2\Sigma^+$	41198	42889	43945	43558	43966
$B^2\Pi$	45673	45236	45119	44803	45914
$C^2\Pi$	49366	51201	52149	51808	52126
$D^2\Sigma^+$	50230	52050	53003	52492	53085
$L'^2\Phi$	53427	53498	53619	52975	53676
$L^2\Pi$	62529	61497	61308	61126	61563
$B'^2\Delta$	62757	60482	60547	59911	60364
$G^2\Sigma^-$	65261	62708	61927	62334	62913

[a] Results are presented in Ref. [9].
[b] Experimental results are collected in Ref. [9].

The difference between the calculated dipole moment function of $X^2\Pi$ adiabatic electronic state and earlier published one is less than 3 % (Fig. 1). The analysis of the dipole moment functions of $1—3^2\Sigma^+$, $1^2\Delta$ states demonstrates that only the function of the $1^2\Delta$ is close to the calculated earlier [8]. For other functions ($1—3^2\Sigma^+$) the differences are significant (Fig. 1).

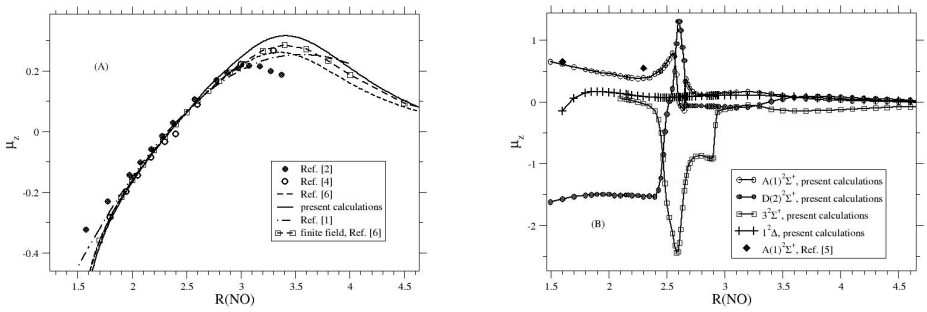

FIGURE 1. Dipole moment functions of the ground $X^2\Pi$ state (A) and $1—3^2\Sigma^+$, $1^2\Delta$ states (B). The positive sign corresponds to N^+O^- polarity. All values are given in atomic units.

The calculated transition dipole moment functions for $X^2\Pi$ — $A^2\Sigma^+$, $X^2\Pi$ — $D^2\Sigma^+$ and $A^2\Sigma^+$ — $D^2\Sigma^+$ transitions are differ slightly from the ones of [7]. The maximal difference value is about 3 %. Thus, taking into account that the both DMF and TMF functions are very sensitive to the wave function quality, it is possible to conclude that the presented results are in a good agreement with theoretical ones [5—8].

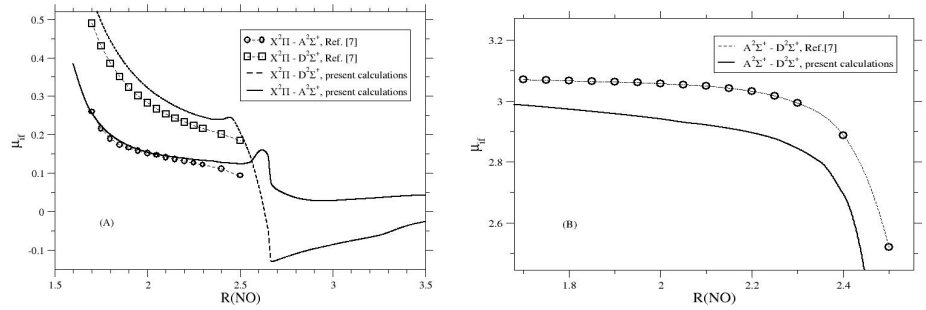

FIGURE 2. Transition dipole moment functions for the $X^2\Pi$ — $A^2\Sigma^+$, $X^2\Pi$ — $D^2\Sigma^+$ (A) and $A^2\Sigma^+$ — $D^2\Sigma^+$ transitions. All values are given in atomic units.

The authors acknowledge the support Russian Foundation for Basic Research under Project № 13-01-12091-ofi-m.

1. G. Chandraiah, C. W. Cho, *J. Mol. Spectr.*, **47**, 1973, pp. 134—147.
2. F. P. Billingsley II, *J. Chem. Phys.*, **62**, 1975, pp. 864—874.
3. F. Grein, A. Kapur, *J. Chem. Phys.*, 77, 1982, pp. 415—423.

4. R. de Vivie, S. D. Peyerimhoff, *J. Chem. Phys.*, **89**, 1988, pp. 3028—3043.
5. C. W. Bauschlicher Jr., S. R. Langhoff, H. Partridge, *J. Chem. Phys.*, **89**, 1988, pp. 4909—4917.
6. S. R. Langhoff, C. W. Bauschlicher Jr., H. Partridge, *Chem. Phys. Lett.*, **223**, 1994, pp. 416—422.
7. J. A. Sheehy, C. W. Bauschlicher Jr., S. R. Langhoff, H. Partridge, *Chem. Phys. Lett.*, **225**, 1994, pp. 221—228.
8. R. Polák, J. Fišer, *Chem. Phys. Lett.*, **377**, 2003, pp. 564—570.
9. H. Shi, A. L. East, *J. Chem. Phys.*, **125**, 2006, pp. 104311—1 -7.
10. H.-J. Werner, P. J. Knowles, G. Knizia, F. R. Manby, M. Schütz, and others, MOLPRO, version 2010.1, a package of *ab initio* programs, see http://www.molpro.net

POST-2

Ab Initio Potential Energy Surface Study of the C_2H_2O System

S. O. Adamson

Laboratory of Molecular Structure and Quantum Mechanics,
Department of Chemistry, Lomonosov Moscow State University,
Leninskie Gory, 1, Moscow 119991, Russia

The reactions involving the formation of C_2 molecule are very important in high-temperature chemistry and astrophysics [1]. The present investigation is devoted to the reaction between C_2 and H_2O giving the various products of the C_2H_2O composition. The *ab initio* study of the ground singlet potential energy surface (PES) of C_2H_2O system are carried out using the ab initio packages GAMESS [2, 3] и MOLPRO [4]. First step of investigation included the calculation of the stationary points by means of density functional approach (methafunctional M06—2x [5, 6]) with the aug-cc-pvtz sets [7,8]. Further, the energies of the discovered stable species and transition states were recalculated by the RHF/CCSD and RHF/CCSD(T) methods for the comparison with the earlier obtained results [1].

The obtained scheme of the C_2+H_2O reaction proves in general the proposed earlier scheme but several differences from the DFT/M06—2x functional results are found [1]. First, the DFT/M06—2x calculations don't give the earlier predicted transition states, corresponding to the CCHOH → HCCOH and CCOH + H → → C(O)C + H_2 processes (original notations T26-A, Tp1p2, ref. [1]), and discover the transition state, corresponding to the rearrangement process CCHOH → → $CCOH_2$ (Fig. 1).

The complex situation has been obtained for the dissociation process $CCOH_2 \rightarrow C_2(X^1\Sigma^+_g)+H_2O$. As it was proposed earlier this process has passed through the formation of the transition state ([T2]) with the further formation of the van-der-waals complex (PRT2):

$$CCOH_2 \rightarrow [T2] \rightarrow CC...OH_2\ (PRT2) \rightarrow C_2(X^1\Sigma^+_g)+H_2O. \qquad (1)$$

The relative energies (including the ZPE energy) of these species were estimated as 0.0 ($CCOH_2$), 5.4 (T2), 4.6 (PRT2) and 6.4 kcal/mol subsequently [1]. It is found that the DFT/M06—2x approach predicts the incorrect order of electronic states for the C_2 molecule. The same problem arises also in RHF/CCSD calculations and only the including of triple excitations leads to the correct order of the electronic states. Due to this fact the both DFT/M06—2x and RHF/CCSD methods give mistakes for $C_2 + H_2O$ dissociation energies and can't be applied to the calculation of this process.

POST-3

Spin Dependent Recombination of Multispin Nitrogen Atoms

Vitaly L. Berdinskiy, Alexander S. Letuta, Ekaterina S. Pichugina

Biophysics and Condensed Matter Physics Dept., Orenburg University, Orenburg, 460018 Russia Federation

Recombination of $N(^4S)$ atoms is the spin dependent process as far as two paramagnetic N atoms can recombine if the pair (N..N) is in the spin singlet state only. So the recombination probability obeys to spin selection rules and needs analysis of multispin processes. Multispin selection rules decrease the recombination probability and increase the decay of (N..N) contact complexes. The mechanism of nitrogen electron excitation will be discussed.

POST-4

Wideband Electrical Field Sensor Protected from Strays

A. Chudnovskiy

Open Joint-stock Company "Research-and-Production Corporation "Precision System and Instruments", Isc2004@mail.ru

Variety of practical problems like atmospheric discharges (thunderbolts), electrical precursors of the earthquakes, noise strays force creation of the wideband electrical field sensors with working on frequencies rom 10^{-3} Hz to 10 MHz. The construction of such sensor is rather complicated problem because of the powerful 50Hz stray produced by the electrical circuit. The stray, mentioned above, can be reduced by a special filter, ignoring the 50 Hz frequency. However the amplitude of the electrical circuit stray can be up to tens volts, so it is better to compensate it

at the antenna input. It is enough to set the compensation voltage equal to the stray voltage with opposite polarity at the antenna input to do this. This voltage can be taken from the secondary winding of the circuit transformer.

Electrical field intensity is being registered via pin antenna, that consists of a pin l with a length of several meters and grounding. Efficient voltage U_R from the antenna is taken from resistor R plugged to the pin and grounding (pic.1). The voltage source with equivalent voltage $U_a = 0{,}5lE$ and inner impedance C_a [pF] = $10l$ (l in meters, E — electrical field intensity V/m) — is the equivalent scheme of the pin antenna. If the length of the pin antenna is 2m and the lowest registration frequency is 10^{-3} Hz the active load impedance R will be 8 10^3 GOm. It is difficult to realize the value of the input impedance, mentioned above, in usual circumstances. The noise level in case of such realization will be 0.05 mcV, that can be increased because the noise factor of modern field devices with high impedance in low frequency area is 10÷20 Db. If we plug the capacity C = 1000pF parallel to the load resistor R, the equivalent load impedance will decrease to the values R = 160 GOm, and the equivalent noise level, taking the loss of the input voltage at the capacity divider into account will be 0,35 mcV, which fits the noise self-level of field transistors. Besides the maximum registered electrical field intensity increases up to 250 V/m.

Experimental measurement showed, that in conditions of big city industrial strays the noise level with 50 Hz frequency is more than 3V at the equivalent impedance CR.

Capacitor C was replaced by a circuit of capacitors C and $C_к$ (pic. 1)connected in series to decrease the background level. If $C << C_к$ the low frequency border of the electromagnetic sensor doesn't change and the level of self-noise stays the same. To suppress the background 50 Hz level at 60 ÷ 70Db we set the controlled circuit voltage from the secondary winding of the transformer to the point of connection between C and $C_к$ through the capacity $C_ф = C$ (pic. 1). The background 50 Hz level can be decreased to — 90 Db and the high frequency pulse strays radiated by the electrical circuit to —10 ÷ 20Db, if we correct the $C_ф$ and the value of the secondary circuit voltage. Upper registration frequency is 15 MHz in case of using the input repeater built on the КП302Б field transistor and the load capacity not less than 15 pF.

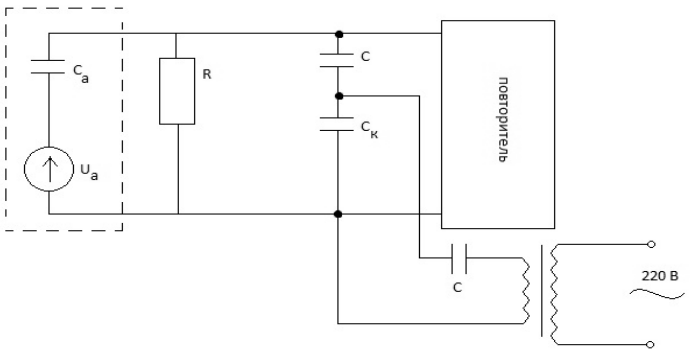

FIGURE 1. Equivalent scheme of the wideband sensor with background electrical stray compensation.

Extra experiments in high frequency electric strays interrupting high quality radio stations in middle and long wave region reception suppression were made. The level of these strays suppression reached – 10 ÷ 20Db, that let to the confident reception of the foreign radio stations at nighttime.

POST-5

Low-Energy Electronic Fluxes during Geomagnetic Storms

Tamara V. Gaivoronskaya

Pushkov Institute of Terrestrial Magnetism, Ionosphere and Radio Wave Propagation RAS (IZMIRAN), Troitsk, Moscow, 142190, Russia

The fluxes of auroral electrons registered by satellite AE-C were considered during several geomagnetic storms with index Kp = 7. After beginning of disturbances the electronic flux of range 100—500 eV was marked and then the greater density of electronic flux of range 25—30 eV was observed. On the whole the values of fluxes did not exceed 10^7 N /eV cm^2 s. Determined by AE-C satellite "in situ" the drift velocity of charged particles increased from a few units to more than 1000 m/s and the estimated values of electric field changed from 0.1 to 100 mV/m.

POST-6

Satellite Environmental Control of Atmospheric Pollution from Combustion Petroleum Gas from Orenburg Gas-Petroleum Field

A. L. Kharitonov, G. P. Kharitonova

Pushkov Institute of Terrestrial Magnetism, Ionosphere and Radio Wave Propagation of RAS, 142190, Moscow, Troitsk, IZMIRAN

In this report various questions of satellite environmental control of pollution of the atmosphere by products of combustion of hydrocarbonic aerosols of a natural origin over one of operated oil and gas fields of Russia are considered. On the basis of the solution of the return problems of a geopotential cross-sections of elec-

tromagnetic not uniformity of the atmosphere according to satellite geomagnetic monitoring were constructed. Some questions connected with the analysis of electromagnetic not uniformity, revealed on satellite geomagnetic cross-sections in various layers of the atmosphere and the low ionosphere on the basis of use of satellite measurements, for the solution of problems of definition of extent of pollution of the atmosphere by products of incomplete combustion of associated (hydrocarbonic) gas from wells in places of a big congestion of gas torches on operated oil fields and gas are considered. As a result of satellite environmental monitoring tracing in time of spatial changes of the electromagnetic not uniformity connected with pollution of the atmosphere by products of incomplete combustion of hydrocarbons around the Orenburg gas-condensate field also was made.

POST-7

A New Input for the Electric Potential Block of the UAM

Maria A. Knyazeva, Alexander A. Namgaladze and Konstantin E. Beloushko[1]

Department of Physics, Murmansk State Technical University, Murmansk, Russia

The electric potential block of the global numerical Upper Atmosphere Model (UAM) [1, 2] solves for the magnetospheric and thermospheric origin electric field potential (φ) equation:

$$\nabla\left(\hat{\sigma}\left(\nabla\varphi - \vec{V}\times\vec{B}\right) - \vec{j}_m\right) = 0\,, \qquad (1)$$

where $\hat{\sigma}$ is the ionospheric conductivity tensor, $\vec{V}$ is the velocity of the neutral gas weight-average motion, $\vec{B}$ is the geomagnetic induction vector, and $\vec{j}_m$ is the magnetospheric current density. The ionospheric conductivity tensor components are calculated by formulae presented in the monograph [3] with using thermospheric and ionospheric parameters calculated in the neutral atmosphere and lower ionosphere UAM blocks correspondingly.

The spherical geomagnetic coordinate system is used in the electric potential block of the UAM. At first the equation (1) is integrated over the height from the lower boundary (80 km in the UAM) of the current sheet to the top one (175 km in the UAM). We assume that the electric field components change very weakly with the height, the currents are absent below 80 km and the dipole geomagnetic field lines are equipotential above 175 km. After integration over the height the equation (1) reduces to a two-dimensional one and it is solved by the method of iterations.

The magnetospheric currents are the field-aligned currents in the regions 1 and 2 (FAC 1 and FAC 2, correspondingly). The geomagnetic latitudinal locations of FACs coincide with the locations of the auroral oval boundaries at the dawn and dusk sides (06 and 18 MLT, correspondingly) which are set in the UAM depending on Kp-index or from the satellite data (for example, the DMSP data) [4]. The FAC 1 amplitudes are chosen iteratively until the cross-polar cap potential drop ($\Delta\varphi$) is not equal to the value specified according to the Weimer's method [5].

This procedure of the FACs density latitudinal—longitudinal distribution setting does not take into account correctly the dependence of the ionospheric electric field global pattern on the interplanetary magnetic field (IMF). This is why a new input for the electric potential block of the UAM was proposed where the FACs distribution is set according to the Lukianova method based on statistical maps of FACs derived from the Orsted, CHAMP and Magsat satellites magnetic data [6].

For the new input verification two cases of the IMF orientation were chosen: $B_y = B_z = 0$ and $B_y = 0$, $B_z = -5$ nT. The model calculations were carried out for the quiet day representing December solstice.

The global distributions of the electric potential (φ) have been calculated by using the fully self-consistent version of the UAM. In this version the thermospheric temperature, composition and three-dimensional circulation are calculated by the numerical integration of the continuity, momentum and heat balance equations for the neutral atmosphere.

The geomagnetic polar plots of the field-aligned current density (j_m) distributions calculated according to UAM and obtained by Lukianova for $B_z = 0$ and $B_z = -5$nT are presented on the left-hand side in Fig.1 for the Northern Hemisphere (winter condition) and in Fig. 2 for the Southern one (summer condition). The corresponding geomagnetic polar plots of φ distribution calculated according to UAM are presented on the right-hand side in Figs. 1 and 2.

The principal difference between the geomagnetic latitudinal—longitudinal j_m distribution obtained by Lukianova and calculated according to UAM lies in the presence of the field-aligned currents in the region 3 according to the Lukianova's data.

The model results show that the seasonal variation of the geomagnetic latitudinal-longitudinal j_m distribution calculated according to UAM is absent. It explains the corresponding weak seasonal variation of the φ distribution at the high geomagnetic latitudes.

The distributions of j_m obtained by Lukianova for both values B_z have clear visible seasonal variation, but it is weaker for $B_z = -5$nT. In the Southern Hemisphere the amplitudes of the value j_m are higher than in the winter Northern one (0.2 $\mu A/m^2$ and 0.1 $\mu A/m^2$ for $B_z = 0$ correspondingly; 0.6 $\mu A/m^2$ and 0.5 $\mu A/m^2$ for $B_z = -5$nT correspondingly). But the cross-polar cap potential drop is higher in winter than in summer ($\Delta\varphi \sim 35$ kV in the Northern Hemisphere and $\Delta\varphi \sim 20$ kV in the Southern ones).

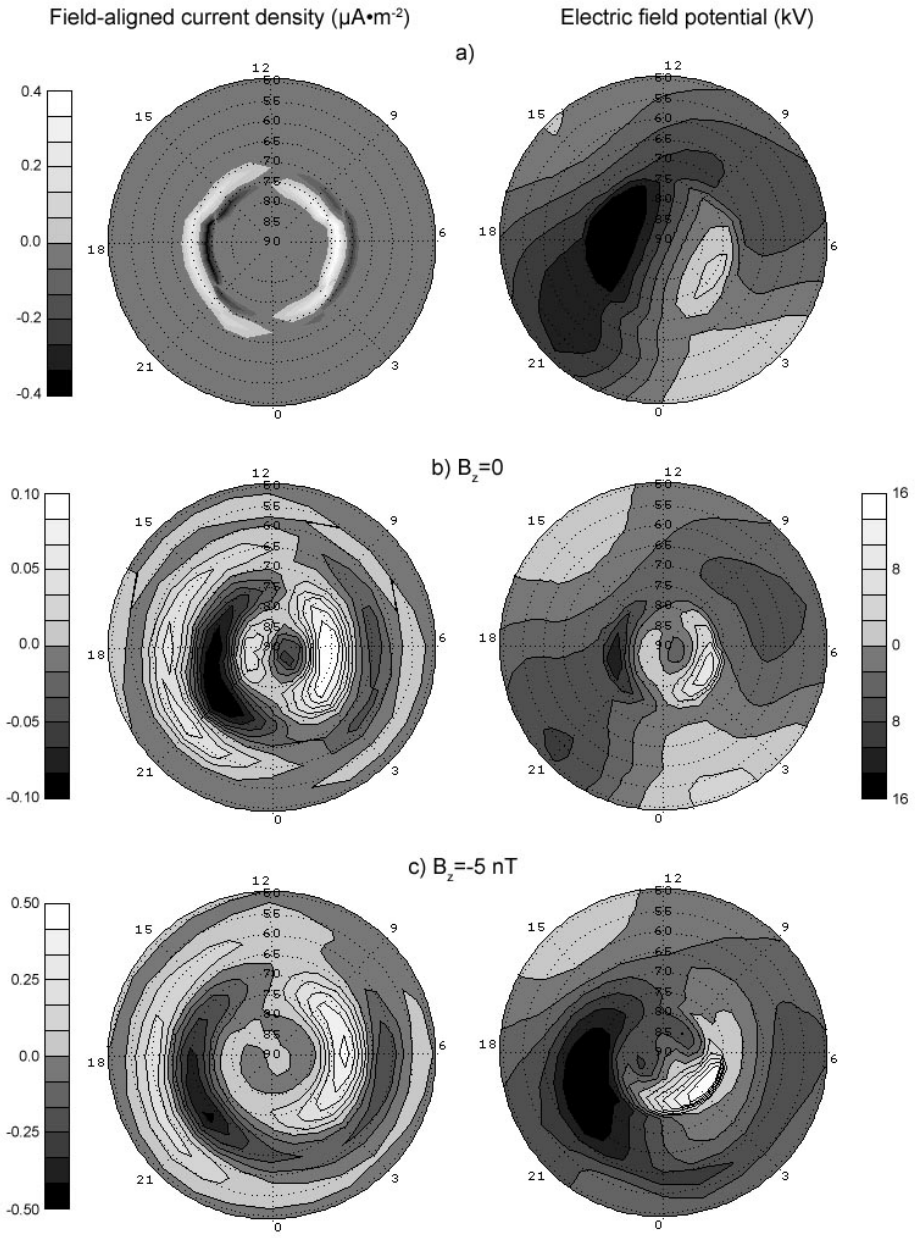

FIGURE 1. The geomagnetic polar plots (latitudes 50°—90°N) of j_m distributions calculated according to UAM (a) and obtained by Lukianova for B_z=0 (b) and B_z = – 5nT (c) and used as the UAM input are presented on the *left-hand side*. The corresponding geomagnetic polar plots (latitudes 50°—90°N) of φ distribution calculated according to UAM are presented on the *right-hand side*. The Sun position is at the top.

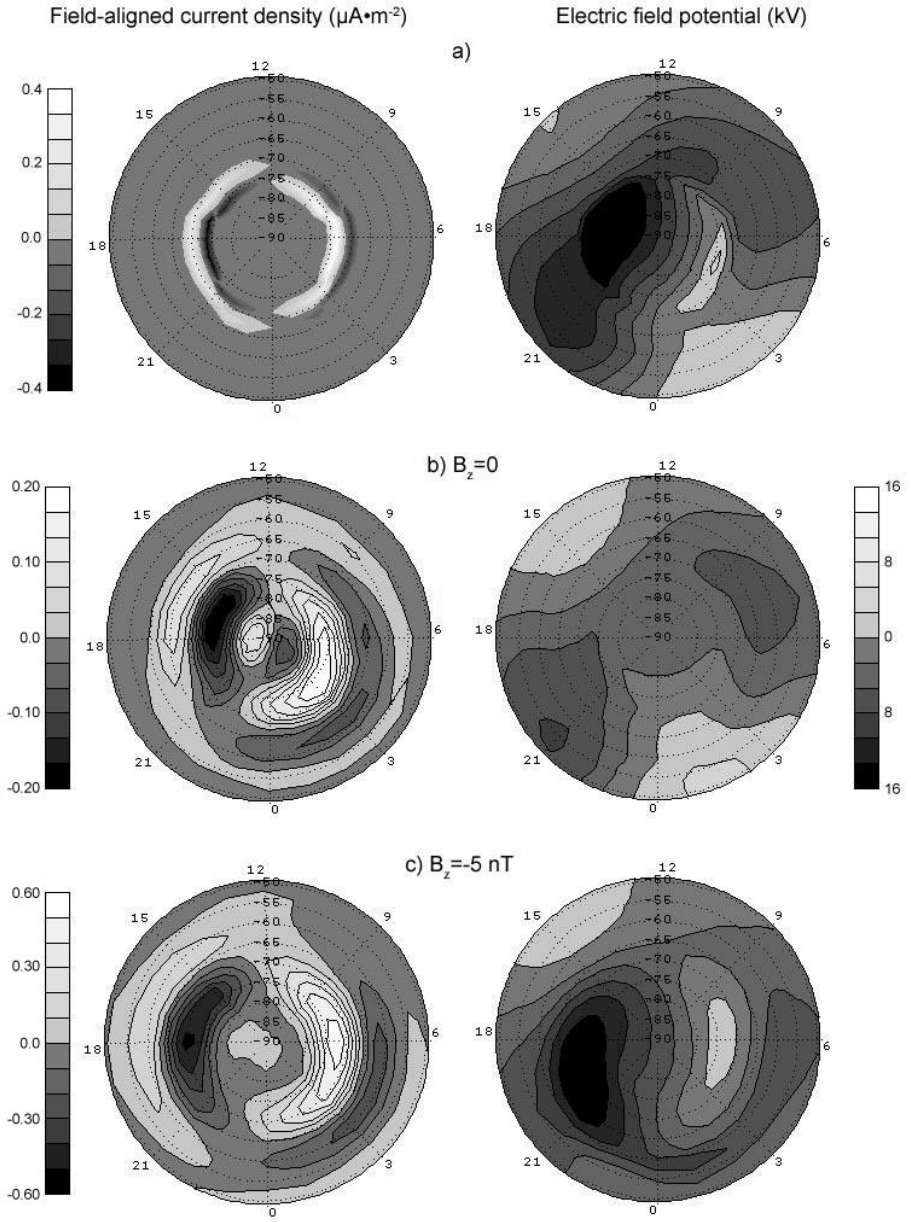

FIGURE 2. The same as in Fig. 1, but for the latitudes 50°—90°S.

In the summer Southern Hemisphere ionospheric convection patterns are invisible practically for $B_z = 0$ according to UAM. This seasonal effect of the ionospheric electric field is formed by the corresponding variations of the thermospheric wind velocity in the dynamo-region.

The FAC 1 and 2 locations project at the lower geomagnetic latitudes for $B_z = -5$nT, than for $B_z = 0$ in both hemispheres. The $\Delta\varphi$ values are higher and the ionospheric convection evening pattern center is projected at the lower latitudes for $B_z = -5$nT.

Thus, the verification of new input for the electric potential block of the UAM is successful. The FACs distribution in the UAM can be set taking into account their IMF dependence.

1. A.A. Namgaladze, Yu. N. Korenkov, V.V. Klimenko, I.V. Karpov, F.S. Bessarab, V.A. Surotkin, T. A. Glushchenko and N. M. Naumova, Global model of the thermosphere-ionosphere-protonosphere system, *Pure and Applied Geophysics*, 127(2/3), 1988, pp. 219—254.

2. A.A. Namgaladze, O.V. Martynenko and A.N. Namgaladze, Global model of the upper atmosphere with variable latitudinal integration step, *Geomagnetism and Aeronomy International*, 1(1), 1998, pp. 53—58.

3. B.E. Bryunelli and A.A. Namgaladze, Physics of the ionosphere, Moscow: Nauka, 1988 (in Russian).

4. A.A. Namgaladze,Yu. V. Zubova, A.N. Namgaladze, O.V. Martynenko, E.N. Doronina, L.P. Goncharenko, A. Van Eyken, V. Howells, J.P. Thayer, V.I. Taran, B. Shpynev and Q. Zhou, Modelling of the ionosphere/thermosphere behaviour during the April 2002 magnetic storms: A comparison of the UAM results with the ISR and NRLMSISE-00 data, *Advances in Space Research*, 37(2), 2006, pp. 380—391.

5. D. R. Weimer, N. C. Maynard and Burke W. J. and C. Liebrecht, Polar cap potentials and the auroral electrojet indicies, *Planetary Space Science*, 38 (9), 1990, pp. 1207—1222.

6. R. Lukianova and F. Christiansen, Modeling of the global distribution of ionospheric electric field based on realistic maps of field-aligned currents, *Journal of Geophysical Research*, 111, 2006, A03213, doi:10.1029/2005JA011465.

POST-8

Longitudinal Variations of the Ionosphere-Plasmasphere System for Winter Solstice in Solar Activity Minimum

Vladimir V. Klimenko[1], Maksim V. Klimenko[1], and Igor A. Nosikov[1, 2]

[1] *West Department of Pushkov IZMIRAN, RAS, Kaliningrad, Russia,*
e-mail: vvk_48@mail.ru, maksim.klimenko@mail.ru
[2] *I. Kant Baltic Federal University, Kaliningrad, Russia,*
e-mail: igor.nosikov@gmail.com

Abstract. Longitudinal variations in the parameters of ionosphere-plasmasphere system such as O^+/H^+ transition height, critical frequency of the *F*2 layer, total, ionospheric, and plasmaspheric electron content for 2009 winter are considered.

O^+/H^+ transition height is the boundary between the ionosphere and plasmasphere (protonosphere) above which H^+ ions are dominant. The value of the ionospheric and plasmaspheric contribution into the total electron content (*TEC*) depends on O^+/H^+ transition height. Integral electron content in the column from the

lower boundary of the ionosphere up to O^+/H^+ transition height represents the ionospheric electron content (*IEC*) and from O^+/H^+ transition height up to GPS satellite altitude (~ 20000 km) it represents the plasmaspheric electron content (*PEC*). There are many studies of this parameter. It is shown that during 2008/2009 the O^+/H^+ transition height dropped to it lowest ~ 450 km at night and ~ 750 km during daytime [1—3], that was not observed in the previous solar activity minima. The observed behavior of the transition height is in significant contrast to those predicted by the International Reference Ionosphere (IRI) [4]. In [1] it is compared the surface of the transition height observed by CINDI and predicted by the IRI model. Both by day and at night the transition height observed by CINDI is over 200 km lower than predicted by the IRI model. The model results of the transition height latitudinal profiles for different seasons in the day and night time obtained using two-dimensional SUPIM model are given in [2]. Our study was carried out using the Global Self-consistent Model of the Thermosphere, Ionosphere, and Protonosphere (GSM TIP) that developed in the West Department of IZMIRAN. The model is described in detail in [5] and complemented by a new simulation code of the electric field of ionospheric and magnetospheric origin [6].

Using the GSM TIP model results we can plot the global maps of the transition height for any geomagnetic conditions and epochs. Figure 1 presents the map of the O^+/H^+ transition height obtained in GSM TIP model for 12:00 UT on January 15, 2009. It is evident that the transition height: is less in the winter hemisphere than in the summer one; drops below 500 km in the middle latitudes of the Northern Hemisphere in the American longitudinal sector in the morning that is consistent with the observations and model calculations of other authors [1—3]; reaches the maximum values of ~ 700 km near the equator and about 1000 km at middle latitudes in the afternoon. The average value of the transition height for the selected date amounts to ~ 700 km. Thus, we can approximately assume that for the given conditions the *IEC* and *PEC* contribution into the *TEC* is determined in the altitude range below 700 km and from 700 km up to 20000 km, respectively.

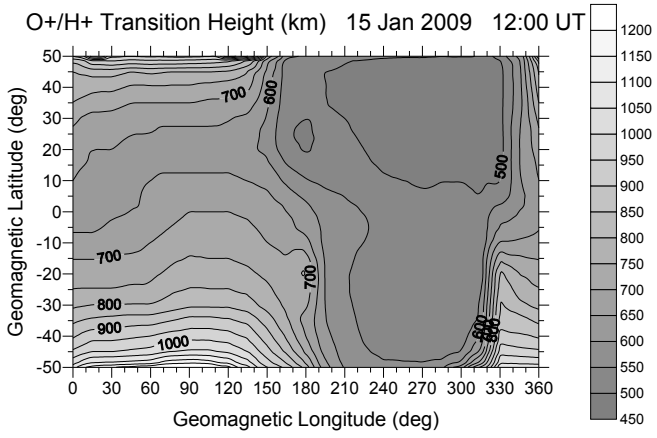

FIGURE 1. The global map of the O^+/H^+ transition height obtained on the basis of GSM TIP model for 12:00 UT on January 15, 2009.

Most of the existing models do not calculate the transition height due to height restrictions and neglect of H^+ ions in the calculations. Some models include the calculation of transition height, but do not have the opportunity to consider the longitudinal variations of ionospheric parameters due to their two-dimensionality. We for the first time present the simulation results of the longitudinal variations of O^+/H^+ transition height, obtained using the GSM TIP model. Note that the main cause of longitudinal variations is the mismatch of the geomagnetic dipole axis and the Earth's rotation axis that leads to the appearance of longitudinal variations in the thermospheric wind and electromagnetic drift.

Figure 2 shows the maps of longitudinal variations in O^+/H^+ transition height at 12:00 LT and 24:00 LT on December 22, 2009. It can be seen that at latitudes from $-50°$ up to 50° the O^+/H^+ transition height varies from 600 km up to 3000 km. On the transition height maps for night conditions it is evident the difference of longitudinal variations in the winter (northern) and summer (southern) hemisphere. So the longitudinal variations in the winter hemisphere are characterized by significant changes in the transition height at fixed latitudes, and in the summer hemisphere, on the contrary, these changes are insignificant. For daytime conditions, the longitudinal variations in the northern and southern hemispheres do not differ. Global maps of *TEC*, *IEC*, and *PEC* allow us to trace the dynamics of the variations in electron density at different heights of the ionosphere and protonosphere. So in [7] the global maps of *TEC*, *IEC*, and *PEC* for December 2009, plotted using COSMIC and *GPS TEC* observational data show the abnormally high values of the electron density near the Weddell Sea at 00:00 UT and 06:00 UT, when the main source of ionization (ultraviolet radiation from the Sun) is absent.

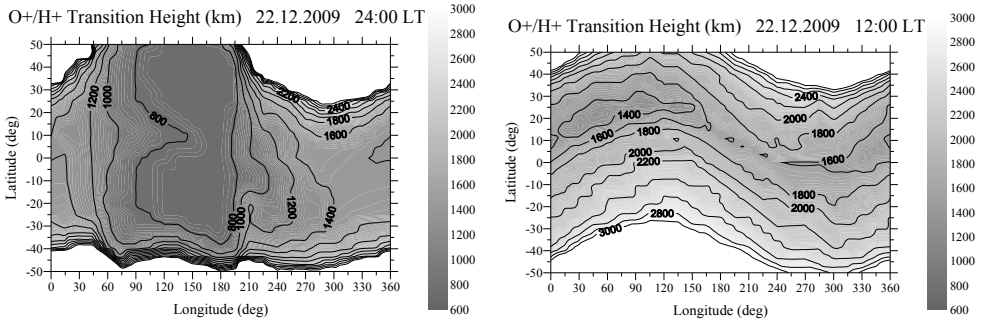

FIGURE 2. Longitudinal variations of the O+/H+ transition height for night time and day time conditions, plotted on the basis of GSM TIP model results obtained for 24:00 LT and 12:00 LT on December 22, 2009.

It should be noted that authors of this article did not pay attention to this fact. The behavior of the ionosphere over the Weddell Sea has attracted the attention of scientists for many years ago. According to the observations at mid-latitude ionospheric stations Halley Bay and Argentine Island located in the Southern Hemisphere the anomalous *foF*2 diurnal variation was found in the December-February, when the nighttime (~ 00:00—02:00 LT) *foF*2 values exceed the daytime *foF*2 [8]. Such anomalous ionospheric feature was named as the Weddell Sea Anomaly (WSA). It has been shown that the anomalous diurnal variations in electron density

are observed only in a certain longitudinal region [9, 10]. We have carried out the construction of global maps *TEC*, *IEC*, *PEC*, obtained in the calculation results using the model GSM TIP for the same UT epochs as in [7]. We have plotted the global *PEC*, *TEC* and *IEC* maps using GSM TIP model results (Fig. 3) that show the presence of the Weddell Sea anomaly (this region is located at longitudes of 270—330°). This suggests the agreement of GSM TIP model results with observational data. Thus, we firstly present a manifestation of the Weddell Sea anomaly in the total, ionospheric and plasmaspheric electron content.

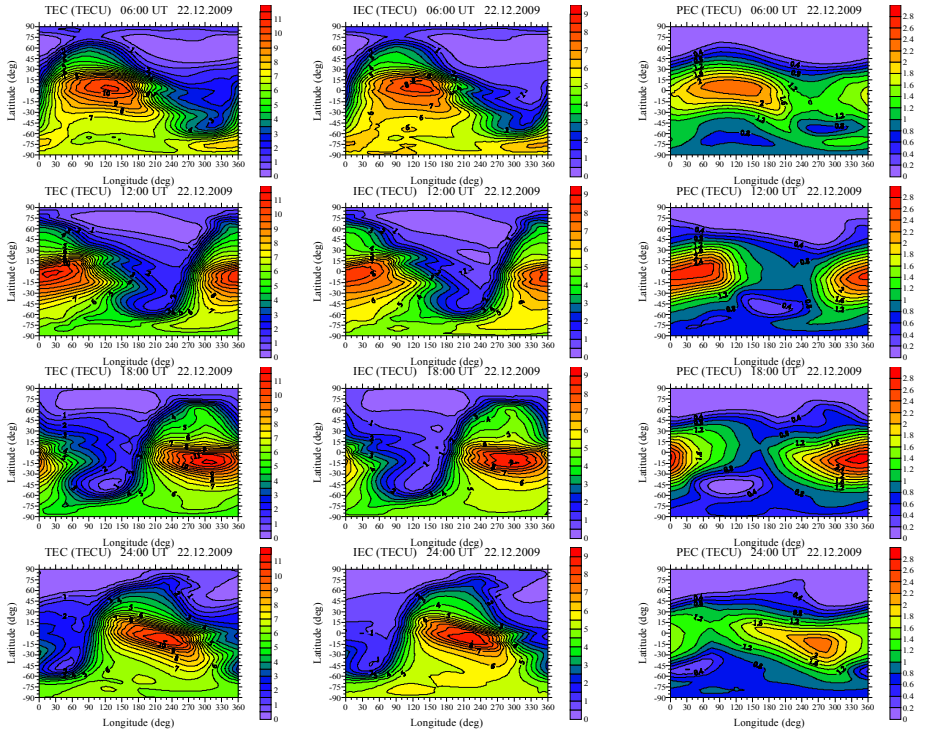

FIGURE 3. Global maps of *TEC*, *IEC*, and *PEC*, plotted on the basis of GSM TIP model results at 06:00, 12:00, 18:00 and 24:00 UT on December 22, 2009 in solar activity minimum.

To determine the spatial extent of WSA, we have plotted the global maps of various parameters for the day (12:00 LT) and night (24:00 LT) time. Figure 4 shows the maps of longitudinal variations of the *F*2 layer critical frequency, *foF*2, plotted for December 22, 2009 at 12:00 LT and 24:00 LT (solar activity minimum). The map for 24:00 LT shows the increase in the electron density in the region of Weddell Sea anomaly between longitudes 180º and 270º. Electron density in the WSA region at 24:00 LT is higher than the electron density at 12:00 LT. A similar comparison was made in [11], but for a solar activity maximum. It seems that the Weddell Sea anomaly during maximum of solar activity manifests itself more strongly than in solar activity minimum. In addition it is evident the presence of longitudinal variations in equatorial ionization anomaly and main ionospheric trough.

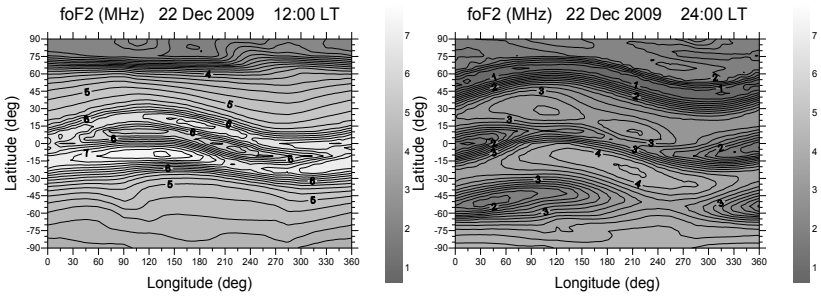

FIGURE 4. Maps of *foF*2 longitudinal variations plotted on the basis of GSM TIP model results obtained at 12:00 LT and 24:00 LT on December 22, 2009.

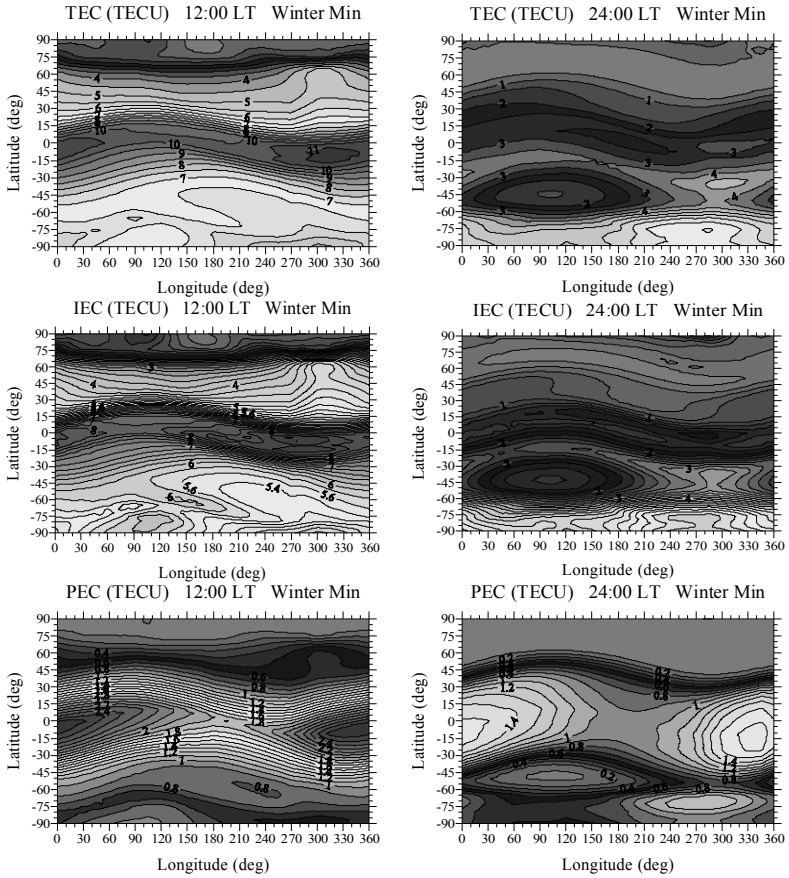

FIGURE 5. Maps of *IEC*, *TEC* and *PEC* longitudinal variations plotted on the basis of GSM TIP model results obtained at 12:00 LT and 24:00 LT on December 22, 2009.

Manifestation of the WSA, and longitudinal variations of the equatorial ionization anomaly and main ionospheric trough in *IEC*, *TEC*, and *PEC* obtained using GSM TIP model at 12:00 LT and 24:00 LT on December 22, 2009 are shown in Fig. 5. Here for the first time it is shown that the WSA exists not only in the *foF*2 and *IEC*, but also in the *TEC* and *PEC*. Maps constructed for the selected LT epochs, allowed us to estimate the spatial extent of the WSA that located between longitudes of 210—340° at latitudes of 60—90º.

Thus, we have constructed the global maps of the O^+/H^+ transition height and showed the appearance of the Weddell Sea anomaly on the foF2, IEC, TEC and PEC maps obtained using the GSM TIP model results. In addition, we compared the values of ionospheric parameters obtained in the GSM TIP model with the observational data and demonstrated that they are close enough to each other.

Acknowledgments. *These investigations were partially supported by the Russian Federation President Grant MK-4866.2014.5 and Russian Foundation for Basic Research (RFBR) — Grant № 14-05-00788.*

References

1. R. A. Heelis, W. R. Coley, A. G. Burrell, et al., *Behavior of the O^+/H^+ transition height during the extreme solar minimum of 2008*, Geophys. Res. Lett., 2009, 36, L00C03.

2. B. Nanan, C. Y. Chen, P. K. Rajesh, et al., *Modeling and observations of the low latitude ionosphere-plasmasphere system at long deep solar minimum*, J. Geophys. Res., 2012, 117, A08316.

3. N. Aponte, C. G. M. Brum, M. P. Sulzer, et al., *Measurements of the O^+ to H^+ transition height and ion temperatures in the lower topside ionosphere over Arecibo for equinox conditions during the 2008—2009 extreme solar minimum,* J. Geophys. Res., 2013, 118, pp. 4465—4470.

4. D. Bilitza, *International reference ionosphere 2000*, Radio Sci., 2001, 36, pp. 261—275.

5. A. A. Namgaladze, Yu. N. Korenkov, V. V. Klimenko, et al., *Global model of the thermosphere-ionosphere-protonosphere system,* Pure and Applied Geophysics (PAGEOPH), 1988, 127 (2/3), pp. 219—254.

6. M. V. Klimenko, V. V. Klimenko, V. V. Bryukhanov, *Numerical Simulation of the Electric Field and Zonal Current in the Earth's Ionosphere: The Dynamo Field and Equatorial Electrojet*, Geomagn. and Aeronomy, 2006, 46 (4), pp. 457—466.

7. Iu. V. Cherniak, I. E. Zakharenkova, A. Krankowski, et al., *Plasmaspheric electron content derived from GPS TEC and FORMOSAT-3/COSMIC measurements: Solar minimum condition*, Adv. Space Res., 2012, 50 (4), pp. 427—440.

8. W. H. Bellchambers, W. R. Piggott, *Ionospheric measurements made at Halley Bay*. Nature, 1958, 182, pp. 1596—1597.

9. C. H. Lin, J. Y. Liu, C. Z. Cheng, et al., *Three-dimensional ionospheric electron density structure of the Weddell Sea Anomaly,* J. Geophys. Res., 2009, 114, A02312.

10. A. T. Karpachev, N. A. Gasilov and O. A. Karpachev, *Morphology and Causes of the Weddell Sea Anomaly,* Geomagn. and Aeronomy, 2011, 51 (6), pp. 812—824.

11. V. V. Klimenko, A. T. Karpachev, M. V. Klimenko, *Mid-Latitude Anomalies in the Diurnal Variation of Electron Density in the Ionosphere*, Russian Journal of Physical Chemistry B, 2013, 7 (5), pp. 611—619.

Investigation of the EQs Precursors in the TEC 2005 Variations

Yulia V. Romanovskaya[1], Alexander A. Namgaladze[1]

[1] Department of Physics, Murmansk State Technical University,
Sportivnaya St.13, Murmansk, 183010, RUSSIA,
e-mail: y-romanovskaya@yandex.ru, namgaladze@yandex.ru

We have analysed the regular Global Positioning System observations to reveal the seismo-ionospheric precursors of earthquakes in the Total Electron Content (TEC) variations of the ionosphere. Global and regional relative TEC disturbances maps (%) have been plotted for seismic events of 2005 which have the following characteristics: the magnitude $M \geq 6$ and the hypocenter depth $D < 80$km. As background values for the investigated LT moment we apply the moving 7-days average TEC distributions. We have analysed the TEC disturbances maps calculated for eight days before each earthquake in order to find possible seismo-ionospheric precursors. The total number of the analysed seismic events was 27.

We consider as precursors negative or positive TEC disturbances lasting several hours near the epicenter or/and in the magnetically conjugated area.

Maps for 20 investigated events of 2005 showed effects in TEC which can be considered as precursors. About half of such events belong to the Oceania region. Most of maps demonstrated positive disturbances in TEC.

Examples of the regional relative TEC disturbances maps (%) for earthquakes happened in the Oceania region are shown in the Fig. 1 and the Fig. 2. Coordinates are magnetic latitude and magnetic longitude. In figures the EQ epicenter position is marked by the star, the magnetically conjugated point is marked by the diamond, the orange circle corresponds to the subsolar point, the black curve — to the terminator line. LT labels (above the panels) correspond to the EQ epicenter's position.

The figures show positive disturbances appearing in the evenings (at about 16—18 LT) and lasting 6 hours at least. The most evident precursors have the magnitude up to 60 %. The figures demonstrate that the TEC disturbed regions are aligned with geomagnetic parallels of the epicenter and the magnetically conjugated point. Usually regions extend for about 20º in latitude and for about 30—50º in longitude. In the cases of the low-latitudinal epicenter location (for example, in Indonesia) we can see one disturbed area over the geomagnetic equator or two areas which are merging into one after a time.

It is worth to notice in the Fig. 2 that the Loyalty Islands maps demonstrate strong positive TEC disturbances during daytime hours (09—15 LT). It can be related to the geomagnetic disturbances indicated by the Kp index equal to 7 at 11LT.

The work is to be continued by analyzing seismic events of years 2006—2010 with the magnitude $M \geq 6$ and the hypocenter depth $D < 80$km in order to reveal general features of the earthquakes ionospheric precursors.

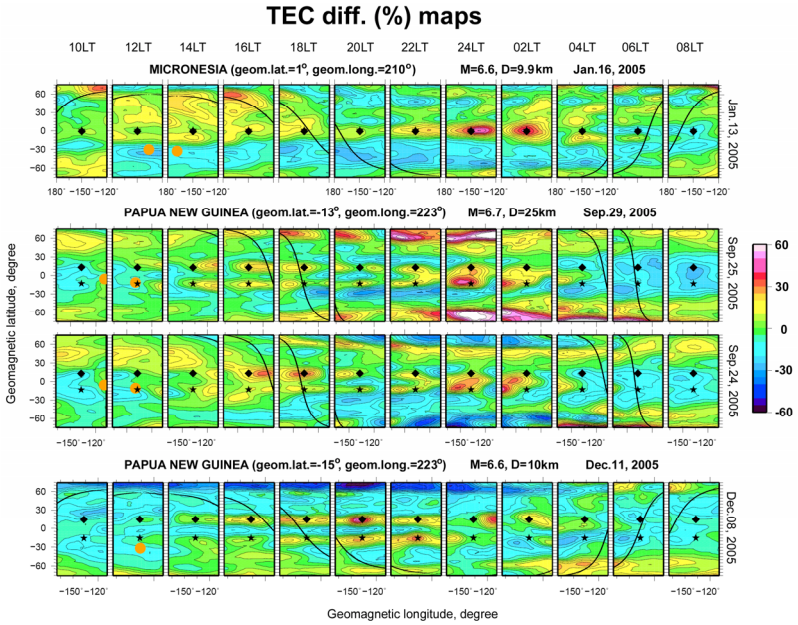

FIGURE 1. TEC relative deviations (%) from the quiet background variations before (from top to bottom) Micronesia M6.6 Jan. 16, Papua New Guinea M6.7 Sep. 29 and Papua New Guinea M6.6 Dec.11 EQs of 2005 respectively.

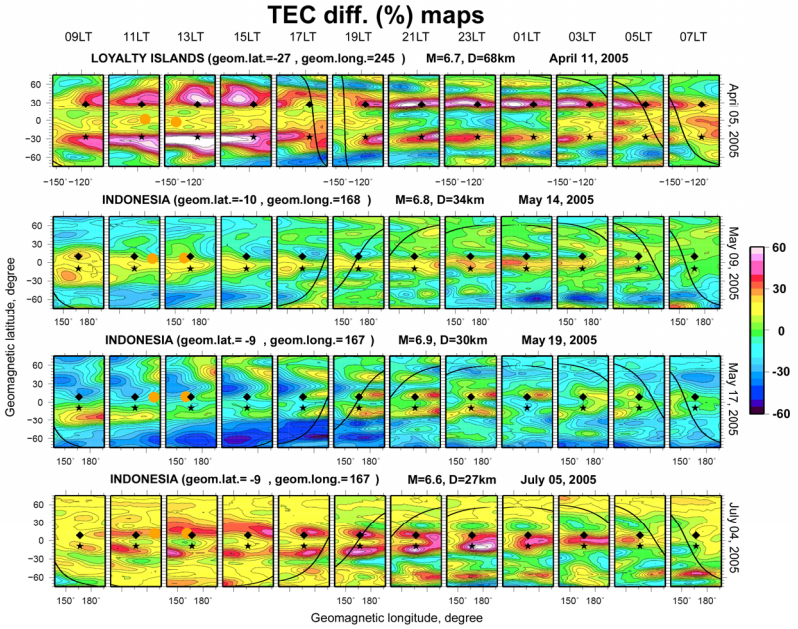

FIGURE 2. TEC relative deviations (%) from the quiet background variations before (from top to bottom) Loyalty Islands M6.7 Apr.11, Indonesia M6.8 May 14, Indonesia M6.9 May 19 and Indonesia M6.6 July 05 EQs of 2005 respectively.

Acknowledgments. Authors are grateful to Boris E. Prokhorov (Helmholtz Centre Potsdam, GFZ German Research Centre for Geosciences; University Potsdam, Applied Mathematics) for the help in GIM TEC maps processing.

POST-10

The Methodology of Regional TEC Maps Generation and Service for Data Processing and TEC Product Access

Irk Shagimuratov, Iurii Cherniak, Irina Zakharenkova, Galina Yakimova

WD IZMIRAN, Kaliningrad, prospect Pobedy, 41, Russia

Absrtact In this paper we describe methodology and service for continuous calculation of the ionospheric Total Electron Content (TEC) variation from GLONASS/GPS observations and generation of high resolution regional TEC maps for ionosphere over Europe region. The service will established to automatically download observational and navigational files, unzip and process data and generate TEC variations and maps. The TEC products will be available for users via service web page.

Introduction

Nowadays there is a high demand to increase the performance and reliability of GNSS positioning. The spatial and temporary dynamics of ionosphere depends on geophysical conditions, and detailed study of these effects is very important, especially during space weather events.

Currently, the main sources of information on the TEC in the global scale are GNSS measurements, which in their entirety exceed all other known methods. TEC measurements are provided by an extensive international net work of GPS stations, which currently numbers more than 4000 stations. The spatial — temporal behavior of the ionosphere is most effectively analyzed using TEC maps [1, 2]. The maps of total electron contents of the ionosphere (TEC) is required in a different fields of science and technology — at study of the processes in the upper atmosphere, space weather condition estimation, for users of space communications, navigation, and geodesy. At present the global IGS global ionospheric maps (GIMs) of the TEC in IONEX format are most widely used *(ftp//:cddis.gsfc.nasa.gpv /gps/products/ionex)*. But IGS GIMs has a low spatial and temporal resolution. TEC maps are constructed with a resolution of 2.5° in latitude and 5° in longitude and a time resolution of 2 h.

Regional TEC maps are constructed by different research groups for different regions: USA, Europe, Japan, Canada, and Turkey [3—5]. It is necessary to note that such TEC maps are represented only in the form of graphic files and, therefore, cannot be used for effective solving of above mentioned specific tasks.

In the WEST Department of IZMIRAN is developed the methodology and techniques for obtaining of TEC variations using data of permanent GNSS networks and generation the regional ionospheric TEC maps by processing of multi-station TEC measurements [6].

Data and methodolodgy

As already mentioned, the advantage of the using GNSS navigation system signals for ionosphere probing based on widespread networks of observing stations, the number of which is increasing. The most developed IGS (International GNSS Service) global system of satellite tracking stations, data and analysis centers puts high-quality GNSS data and data products online with free access. The IGS collects, archives, and distributes GNSS raw observation in standard RINEX format via ftp protocol. Also raw GNSS data available from UNAVCO and EUREF ftp servers.

Fig. 1 shows the overall scheme of the TEC variations and TEC maps product generation at West Department of IZMIRAN.

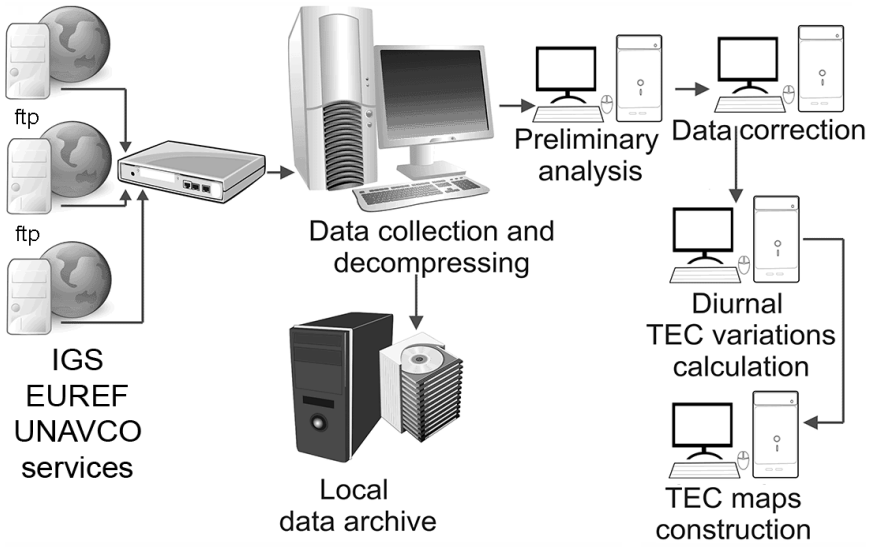

FIGURE 1. The GNSS data processing and ionospheric TEC product generation operation diagram.

The service is established to automatically download RINEX observational and navigational files, unzip and process data and generate ionospheric products. The GNSS RAW data in the RINEX format regularly collected from IGS, EUREF and UNAVCO ftp servers and stored in the local replenishable database.

The preliminary data analysis consists of two main phases:

— Quality analysis: collected data files are the subject of the initial quality control in the form of screening bad measurements (e. g., incomplete data file, data gaps within block of continuous measurements during session navigation satellite — receiver, absence of any signal at the data stream etc).

— Prognosis calculation: file with navigation information is used for calculations of trajectories of all satellites, which can be visible over the considered ground-based GNSS station during 24 h. As the next step there is calculation of trajectories of ionospheric pierce points and sub-ionospheric points, used for spatial representing of measured parameters. All results of calculations are gathered in prognosis file. For every permanent GNSS station prognosis file must be generated separately.

At the following stages the data processed with the original algorithms developed in the WD IZMIRAN and realized in Fortran-based program packages. This algorithms realized methodology of single and multistation GNSS signals processing briefly described below.

Over the each observation point at least 6—8 satellites are visible simultaneously. Navigation satellites broadcast highly stable and coherent navigation signals. In GPS system used two carriers at frequencies of f1 = 1575.42 MHz (L1) and f2 = 1227.60 MHz (L2). Dual-frequency radio signals, propagated through the ionosphere, are subject to a differential phase change due to the dispersive nature of the plasma.

The GNSS technique realizes simultaneous measurements of pseudo-range (code) P1 and P2, and carrier phase delays of signals L1(λ1) and L2(λ2), which can be written as follows:

$$P_1 = \rho' - I_1 + c \cdot (\delta t_{s\_1} + \delta t_{r\_1})$$

$$P_2 = \rho' - I_2 + c \cdot (\delta t_{s\_2} + \delta t_{r\_2})$$

$$L_1 = \rho' - I_1 + \lambda_1 N_1, \; L_2 = \rho' - I_2 + \lambda_2 N_2$$

where: ρ' includes geometric distance between receiver and satellite, tropospheric delay and other frequency-independent delays, N1 and N2 — carrier phase ambiguity parameters of both frequencies, c — light speed, δts_1,2 and δtr_1,2 — satellite and receiver hardware delays.

Differential delay of both signals is proportional to the ionospheric TEC:

$$\Delta L = \Delta I + B, \; \Delta P = \Delta I + \delta$$

$$\Delta I = 40.3 \frac{f_1^2 - f_2^2}{f_1^2 f_2^2} TEC = M \cdot TEC$$

where ΔI — differential delay due to the ionosphere, B — unknown phase ambiguity, δ — satellite and receiver hardware delays, M = 10.5·1018 m^3/el.

Processing procedures result in resolving of phase ambiguities and determination of hardware delays for phase and code measurements respectively. Using procedure of ambiguities' removal, an absolute value of TEC along path satellite-receiver is calculated for all visible satellites. This slant TEC is converted into vertical one by geometrical factor.

The TEC obtained from GNSS measurements is relative. To obtain absolute value of the ionospheric TEC instrumental biases must be removed. These instrumental biases are the main source of error at the estimation of TEC using GNSS signals measurements.

When TEC derived from GNSS signals observation, the ionosphere was approximated by a spherical shell on a fixed height of 400 km above the Earth's surface. A simple geometric factor was used to convert the slant TEC into a vertical one. To reduce the influence of the horizontal gradients only signals of the satellites with lowest elevation angle 20^o involved into analysis. The phase ambiguities were removed by fitting phase measurements to the code data collected along an individual satellite pass. After pre-processing, the phase measurements contained an instrumental bias only. The biases were determined for each station using GPS measurements of all satellite passes over a given site in a 24-hour period. The diurnal variations of TEC over a site and the biases for all satellites were estimated simultaneously. At all stations, before the technique was run, the instrumental biases were removed in all satellite passes. Using this procedure, an absolute line of sight TEC for all satellite-receiver paths was calculated.

A further development of the methodology will be its transition from a local model of the distribution of ionospheric TEC over the station to a global (or regional) spatial distribution of the ionospheric TEC. In the global model of the ionospheric TEC distribution, it is convenient to use the expansion of the TEC in the form of spherical functions for the spatial distribution:

$$\mathrm{N_h}(\varphi\ ,\lambda\ ) = \sum_{\mathrm{n=0}}^{\mathrm{n_{max}}} \sum_{\mathrm{m=0}}^{\mathrm{n}} \bar{\mathrm{P}}_{\mathrm{nm}}(\sin\varphi)(\mathrm{a_{nm}}\cos\mathrm{m}\lambda + \mathrm{b_{nm}}\sin\mathrm{m}\lambda\ )$$

where n_{max} is the maximum degree of expansion of the spherical harmonics, are the normalized associated Legendre functions of the first kind of degree n and order m; ($\Lambda(n, m)$ is the normalizing function, and P_{nm} is the Legendre function); a_{nm} and b_{nm} are unknown coefficients of the spherical harmonics in the expansion of the ionospheric TEC, i. e., the parameters of the global ionospheric model that must be evaluated; □ is the colatitude; $\lambda = (UT \times 15 + L) \times \frac{\pi}{180} - \pi$ is the solar fixed longitude of the ionospheric pierce point; and L is the geographic latitude in degrees.

The normalizing function looks as:

$$\Lambda(n,m) = \sqrt{\frac{(n-m)!\ (2n+1)(2-\delta_{0m})}{(m+n)!}},\ \delta_{0m} = \begin{cases} 1, & m = 0, \\ 0, & m \neq 0 \end{cases}$$

As can be seen from equation the model does not explicitly include the time. However, the time enters into the expression for the parameter λ. Thus the equation for the differential delay for the satellite within the framework of the global model of the ionospheric TEC distribution takes the following form:

$$\Delta P^j(\varphi\ ,\lambda\ ) = M \sum_{n=0}^{n_{\max}} \sum_{m=0}^{n} \overline{P}_{nm}(\sin\varphi)(a_{nm}\cos m\lambda + b_{nm}\sin m\lambda\ ) / \cos\chi + A^j_{R,S}$$

So, if we processed all data for considered regional or global network and using the results of TEC measurements over the corresponded stations spaced in both latitude and longitude, we can examine the behavior of the ionospheric TEC in the selected area, global or regional. The spatial and temporal resolution of resulting TEC maps depends of data quality and quantity of stations involving into processing.

The final TEC maps generated in WD IZMIRAN within described methodology and service provide a spatial resolution of 1° on geographic latitudes and longitudes and covers regions from -10° to 60° E on latitudes and from 35° to 70° N on longitudes. The ionosphere TEC maps generated standard temporal resolution of 1 h, but temporal resolution can be increased up to 5 min for solving of the specific tasks.. During the test ionospheric TEC products will be available for users via WD IZMIRAN observatory web page *http://wdizmiranobs.no-ip.biz/tec.html*

The methodology developed and used at the WD IZMIRAN for obtaining the absolute TEC values and ionospheric TEC mapping the proved to be effective in studies of the structure and dynamics of the ionosphere during disturbances of various kinds. As the example on Fig. 2 shown the TEC maps of the European region that represents simultaneously the temporal behavior and spatial structure of the ionosphere during geomagnetic storm. Such informativeity is inaccessible to most other means for the ionosphere diagnostics.

Summary

In this paper we presented the methodology and new service for generating of the high resolution ionospheric TEC maps for European region. The service is based on the GPS/GLONASS measurements provided by international permanent GNSS networks such as IGS, UNAVCO, EPN. The methodology of TEC map creation based on the original approach developed in West Department of IZMIRAN. The described above algorithm has been refined and is currently used for processing data from more than 200 stations. In developed method of the TEC maps generation are used at the simultaneous measuriements of the group delay and phase of radio signals. At each time point, the algorithm processes more than 1500 satellite—receiver communication lines. Upgrading the algorithm enabled to construct TEC maps with a high spatial and temporal resolution.

The constructing service will provide for users the 1h TEC maps with $1^o \times 1^o$ resolution as well as the diurnal TEC variations for each station involved into processing. For TEC map generations there are used measurements of more than 200 stations, that belong to international permanent GNSS networks. One of the advantages of

such approach is the high spatial resolution of the resulted maps. Another advantage of the service will be a freely access to these products for the scientific community and availability to download and analyze data on a continuous daily basis for several previous years.

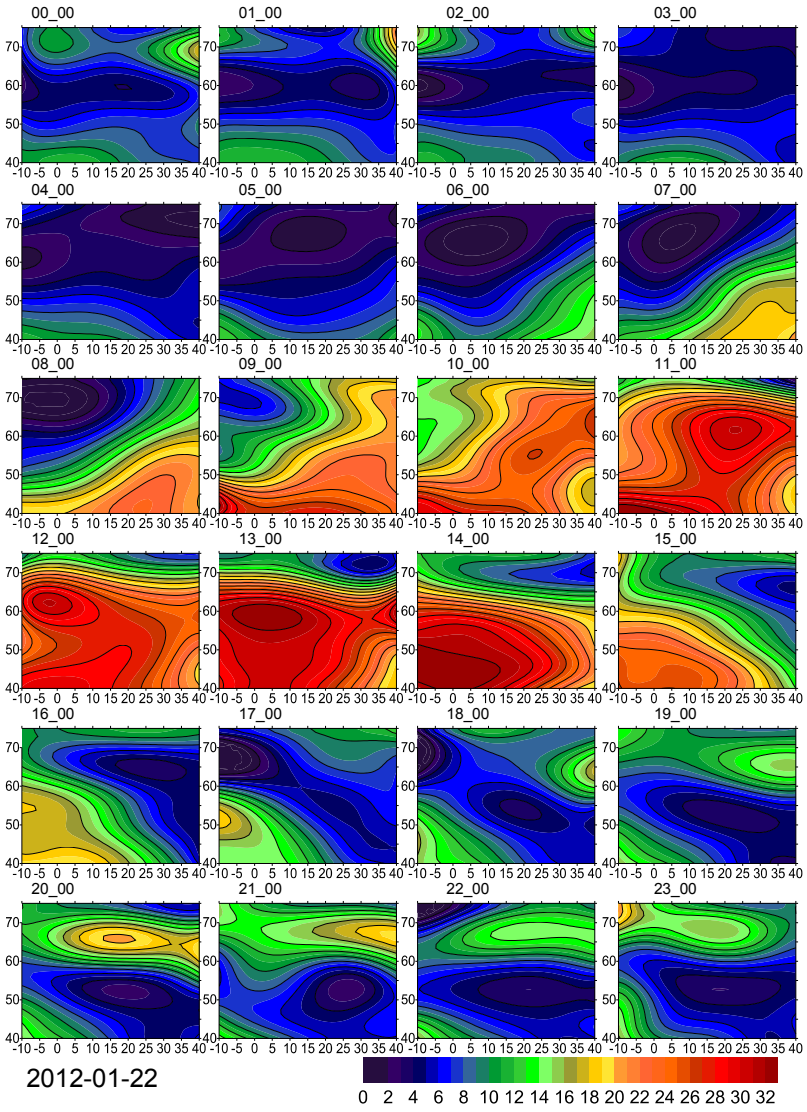

FIGURE 2. The TEC maps for January 22, 2012, ionospheric storm conditions.

Aknowledgements. The work was supported by RFFI, grant 14-07-00512. The authors thank IGS, UNAVCO and EUREF for making available GPS measurements data.

References

1. Mannucci A. J., Wilson B. D.,Yuan D. N.,Ho C. H.,Lindqwister U. J. et al. // A global mapping technique for GPS-derived ionospheric total electron content measurements // Radio Sci. 1998.V. 33. N 3. P. 565.

2. Zhao B., Wan W., Liu L. and Mao T. // Features of annual and semiannual variations derived from the global ionospheric maps of total electron content //Ann. Geophys. 2007. V. 25. P. 1555.

3. Jakowski N., Mayer C., Hoque M. and Wilken V. //Total electron content models and their use in ionosphere monitoring //Radio Sci. 2011. 46, RS0D18, doi:10.1029/2010RS004620.

4. Yilmaz A., Akdogan K. E. and Gurun M. // Regional TEC mapping using neural networks // Radio Sci. 2009. 44, RS3007, doi:10.1029/2008RS004049.

5. Ghoddousi-Fard R, Héroux P, Danskin D, Boteler D.// Developing *a* GPS TEC mapping service over Canada // Space Weather 2011. 9(S06D11).

6. Shagimuratov I. I., Yu. V. Chernyak, I. E. Zakharenkova, G. A. Yakimova. Use of Total Electron Content Maps for Analysis of Spatial-Temporal Structures of the Ionosphere / Russian Journal of Physical Chemistry B, Vol. 7, No. 5, 2013, p. 656.

POST-11

Study of GPS Positioning Deviations During Aurora

Sergey Chernouss[1], Mikhail Shvec[1], Mikhail Filatov[1],
Irk Shagimuratov[2], Nikolay Kalitenkov[3]

[1] Polar Geophysical Institute of the Kola Science Centre RAS
Murmansk-Apatity, 184200, Russia
[2] West Department of IZMIRAN, Kaliningrad, Russia
[3] Murmansk State Technical University, Murmansk,183010, Russia

Abstract

The work is an experimental study of GPS and GLONASS positioning errors depending on the spatial and temporal distribution of auroras, which are markers of the current state of the polar ionosphere. The experimental evidence of positioning errors connected with spatial and temporal variations in the intensity of auroral arcs are demonstrated. Errors in the GPS are expressed as the increase in positioning deviations and in violation of the integrity of the system. It is shown that the rayed arc aurora are an indicator of GPS break, which are explained in the framework of the concept of a signal phase fluctuations caused by inhomogeneities of the total electron content (TEC) elongated along the magnetic field.

Introduction

The basis for the preparation of this work was frequently observed association of the total electron content (TEC) and its variations with spatial-temporal variations of auroral intensity [1—4]. Figure 1 shows us the likeness of azimuthally distributions of inhomogeneities of TEC and auroral oval from observations in the Antarctic [4].

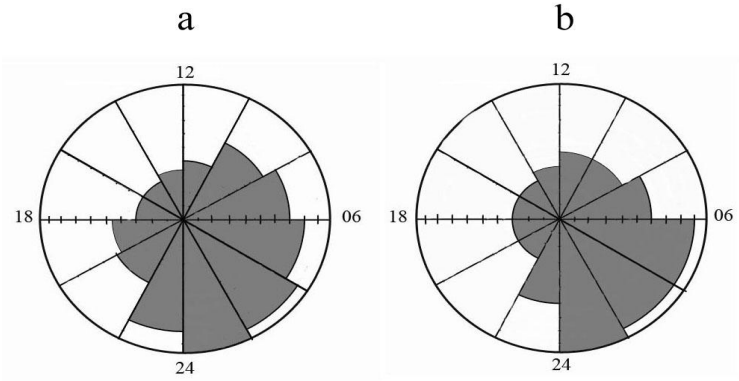

FIGURE 1. a) Normalized vector azimuth diagram of the number of ionospheric irregularities (TEC patches) occurred inside 30° sectors (the sector radius is proportional to the area square). b) The diagram of the areas covered by the auroral oval in the 30° sector (the sector radius is proportional to the area square).

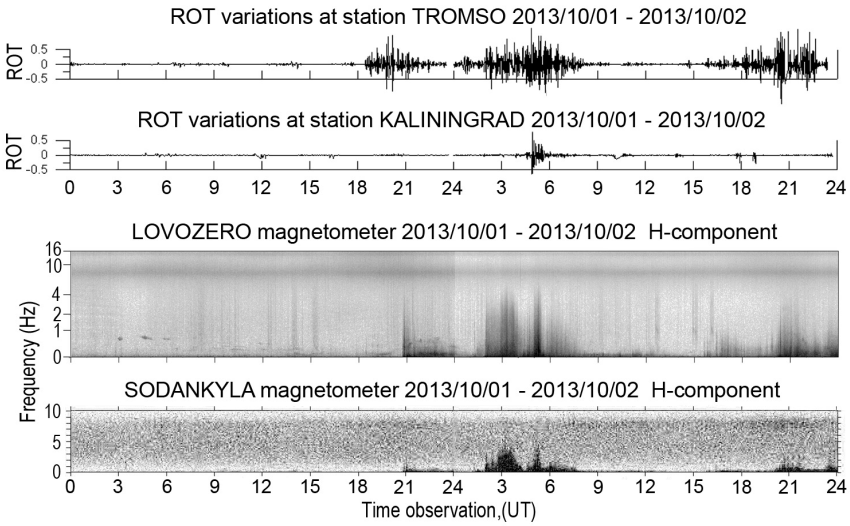

FIGURE 2. Time series of ROT variations at stations Tromso ($69^0$39`N $18^0$57`W) and Kaliningrad ($54^0$43`N $20^0$30`W) and geomanetic pulsations at Lovozero ($68^0$02`N $35^0$00`W) and Sodankyla ($67^0$22`N $26^0$38`W) observatories.

The following figure shows the variations Rate of TEC (ROT) at stations Tromsø ($69^0$39`N $18^0$57`W) and Kaliningrad ($54^0$43`N $20^0$30`W), and occurring in the same time slot geomagnetic pulsation observatories Lovozero ($68^0$02`N $35^0$00`W) and Sodankylä ($67^0$22`N $26^0$38`W). Similarity temporary variations in the observed deviations in the case of a magnetic storm period 1—2 October 2013 and apparently quantitative study of the spatial variation of the amplitudes can lead to interesting results on the source positioning errors associated with auroral phenomena. However, studies of TEC variations in the conditions of the development of geophysical disturbances and their account is not yet provide full deterministic positioning errors, and therefore of interest to investigate the direct measurement of these errors during auroral activity.

Materials and methods

The data of GPS and GLONASS signals were received in the Arctic stations. We used the method of obstruction receiver to increase its sensitivity to external influences [1], when used of single-frequency receivers (Garmin-128). In order to reveal physical effects that are induced by the aurora and which influence the GPS signal propagation, it was suggested to block a part of the receiver field of view, south of receiver position (Fig 3). In doing so, the number of GPS satellites, of which the system chose the constellation of the working satellites, was smaller, with all of these located in the northern part of the sky. The radio signals from these satellites propagated through the auroral ionosphere (which is practically continuously disturbed) and only the degree of its disturbance varied. Thus the limitation of the number of the working satellites caused a decrease in the accuracy of the coordinate determination, which in turn made the receiving system more sensitive to the external effects when the signal passed through the auroral zone. This method allowed us to reveal experimentally the errors in positioning not only under rare planetary magnetic storms but also under local auroral disturbances. Auroral activity was assessed by observing auroral all-sky cameras at Kola Peninsula and Svalbard (Lovozero and Barentsburg) and in Scandinavia, as well as the network of magnetometers in there. Data processing was performed using the “Visual GPSXP” and “GPS Analyzer” programs, allowing to construct a time series of errors of positioning.

Reception and registration of signals from navigation GPS / GLONASS satellites were carried out on the Barentsburg station ($78^0$05`N $14^0$12`W) by receiver complex, which included a dual-frequency receiver Maxor-GGDT of Javad Company. Javad receiver obtains the signals of the two satellite navigation systems GPS and GLONASS and the data are collected at a frequency of 1 Hz. The frequency of 1 Hz allows to determine the small-scale irregularities and dynamic processes in the ionosphere. The greatest interest in this experiment is the study of passing satellites GPS / GLONASS signals through the area of the disturbed ionosphere at 18:00 -21:00 (UT). The raw data obtained with a dual frequency receiver Javad were prepared and converted into data format RINEX (Receiver-INdependent EXchange).

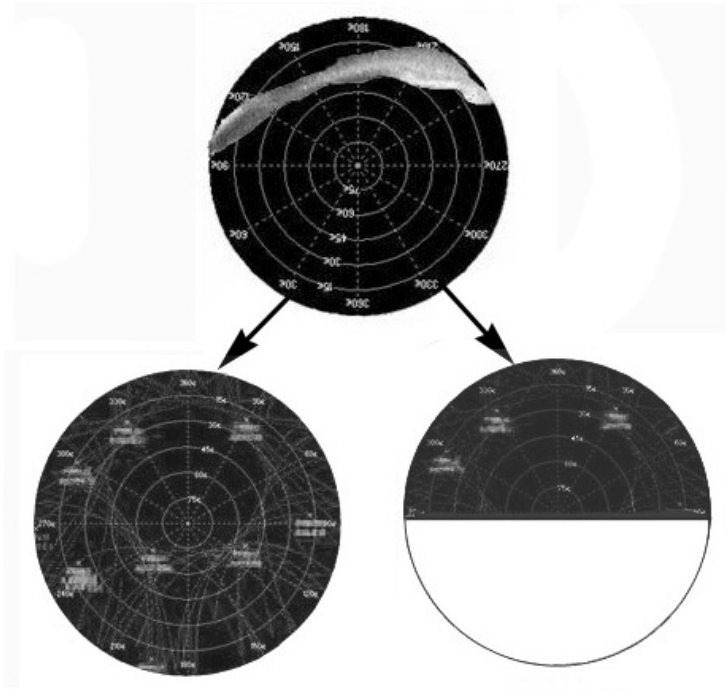

FIGURE 3. Scheme of an all-sky camera image with the auroral arc in the northern part of sky (top) and the GPS-receiver's whole and south part blocked field of view (bottom).

Results and discussion

Sodankyla keogram shows the auroral forms moving from north to south, with some fluctuations of the auroral south boundary. It is clear that at 21.30 UT, a more intensive and southern aurora is observed in the oval, that is, when the GPS system integrity was disrupted. It is obvious that the GPS deviations depend on the GPS satellite signal quality and on the possibility of selecting the satellite signal that does not go through the disturbed ionosphere. When the signals from the southern part of the sky are blocked, the system can use only a limited number of the satellite signals only from the northern part of the sky, which could be occupied by the ionosphere disturbances conjugated with the aurora. The above example was obtained from measurements of a single-frequency receiver with the restriction of its field of view, and on this basis it was assumed that the navigation receiver can give us a great deviations in positioning. Against this statement, there are usually objections that violations to individual satellites signal will not be affected to the positioning accuracy.

But it is important that in a situation, when the aurora (ionospheric disturbances) completely cover a field of view of the receiver, receiving signals from all satellites in the field may be destroyed. This conclusion was the basis to an applica-

tion for an invention of the correction method of navigation systems GPS and GLONASS by optical auroral observations, on which patent [5] was obtained. Another objection to our results may be the assertion that the use of high-precision dual-frequency receivers navigation signals will allow them to adjust to the impact of the TEC variations. It should be noted that evidence of navigation signal reception during its passage through the auroral arc when using a dual frequency reception was presented in [6]. Below we will analyze the events in the polar ionosphere, which lead to a deterioration in the accuracy of the systems GPS / Glonass in a situation full coverage of the field of view of the receiver during polar ionosphere disturbances conjugated with aurora. In a situation, when the aurora completely cover the field of view of GPS-GLONASS receiver, positioning quality should be deteriorated. This hypothesis was checked by the precision observational data from dual-frequency receiver "Javad" installed and work in the Polar Geophysical Institute station Barentsburg in Spitsbergen. This station is rather convenient to study affects of auroral disturbances on GPS-GLONASS because navigation satellite signal must pass through the auroral oval, which represented disturbed polar ionosphere as marker.

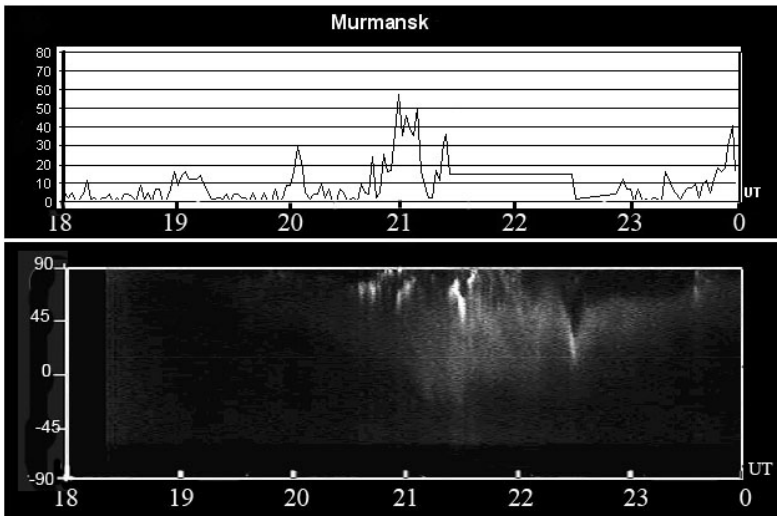

FIGURE 4. (*a*) The GPS absolute positioning deviations in meters and (*b*) keograms from the Sodankyla all-sky camera obtained on 25 March 2007.

Thus, the signals of all satellites in working constellation, both equatorial and polar ones, should pass through the disturbed ionosphere. Therefore, if we will to analyze together data from the GPS receiver, magnetometers and all-sky cameras, we must obtain direct results of the effect. Day of 24.11.2009 characterized by a magnetic storm, and the aurora, which covered the entire sky. We provided an analysis of pictures of all-sky camera installed at the station Barentsburg and geomagnetic disturbances at the IMAGE network (Fig. 5, 6).

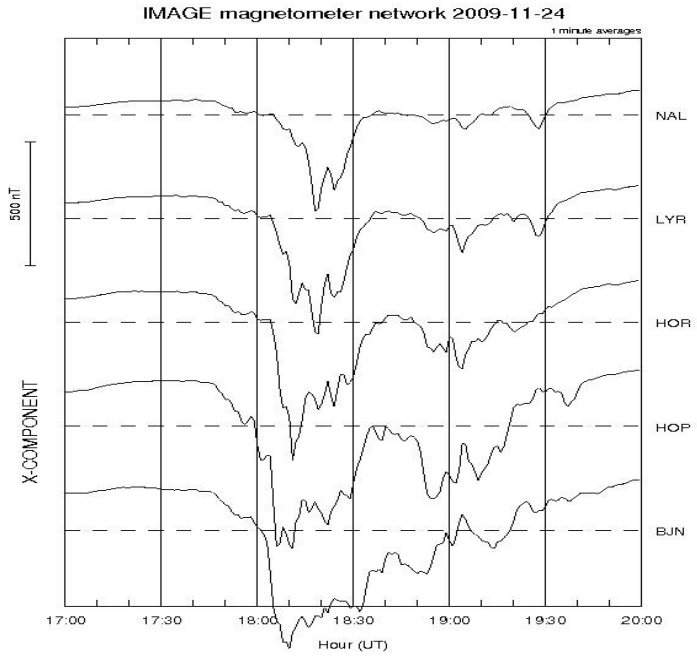

FIGURE 5. X-component of geomagnetic disturbances November 24, 2009 at the IMAGE network.

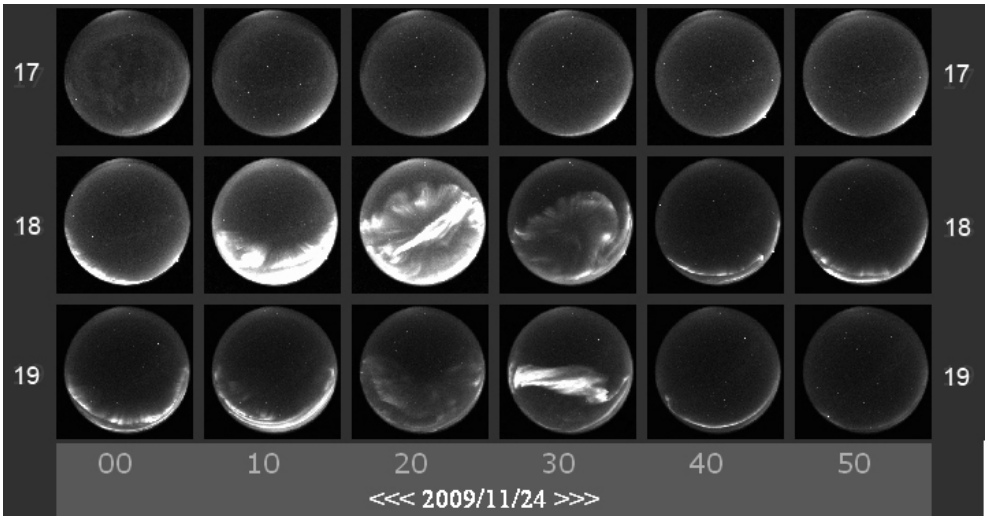

FIGURE 6. All-Sky camera data from the Barentsburg station with 10 min resolution in November 24, 2009.

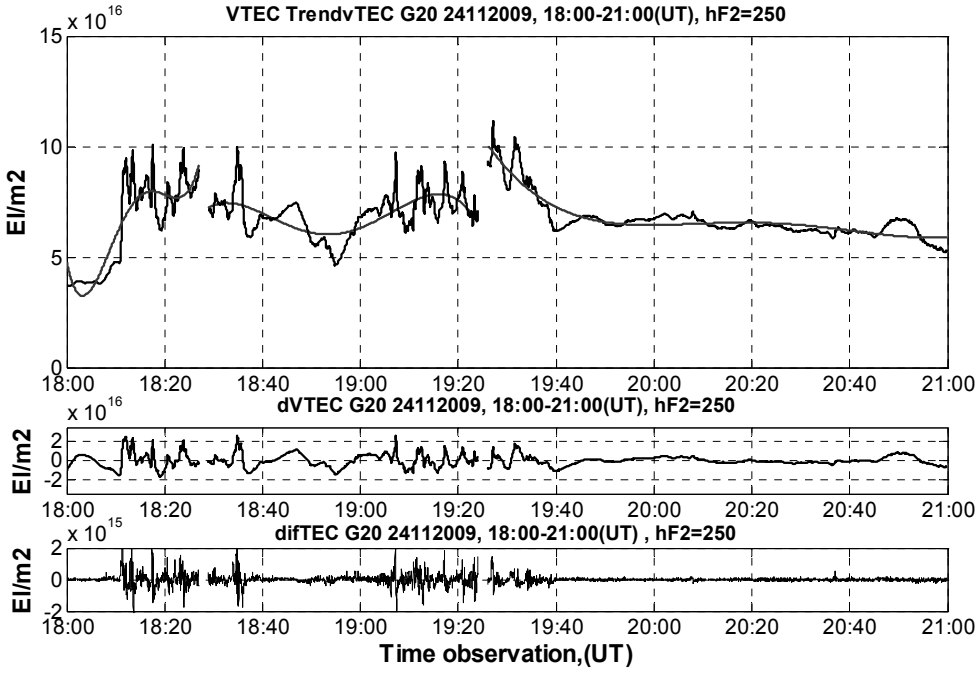

FIGURE 7. The time dependence of the vertical total electron content (vTEC), variations of vertical total electron content (dVTEC) and the rate of change vTEC (difvTEC) from satellite G20 data receiver at Barentsburg station in November 24, 2009.

We can see aurora take up most of the sky, and completely cover the field of view of the receiver in the image at Figure 6 at 18:20 UT. We also see that at this time the satellite signal G20 disappears completely. Figure 7 shows the data obtained from the single satellite of working constellation. Signal of the other satellites indicate the same effect as on the illustration or an increase of TEC variability. Satellite signal G20 also disappears at 19.25 UT, but other satellite signals less exposed to violation than in the case of 18.20 UT. This occurs presumably because the aurora is not completely cover a field of view of other receivers.

Maps of the navigation satellites positions and the aurora were constructed over the point of both devices in different times. It was concluded that, in the time series of positioning errors, these errors increase with the navigation signal propagation through the disturbed polar ionosphere, which characterized by occurrence of the aurora. Figure 9 shows short period positioning deviations at 18.20 UT, which looks like signal scintillations. We believe that it is an evidence of impact of ionospheric disturbances conjugated with aurora.

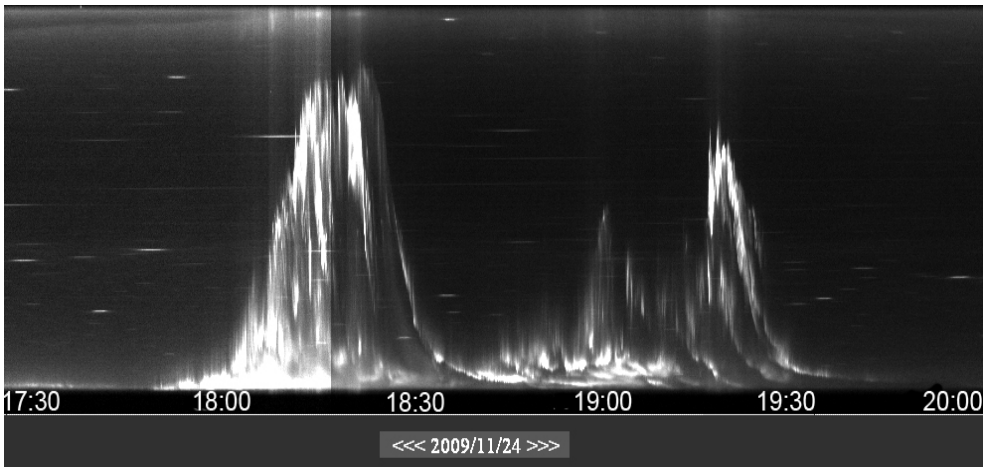

FIGURE 8. All-Sky keogram from the Barentsburg station in November 24, 2009.

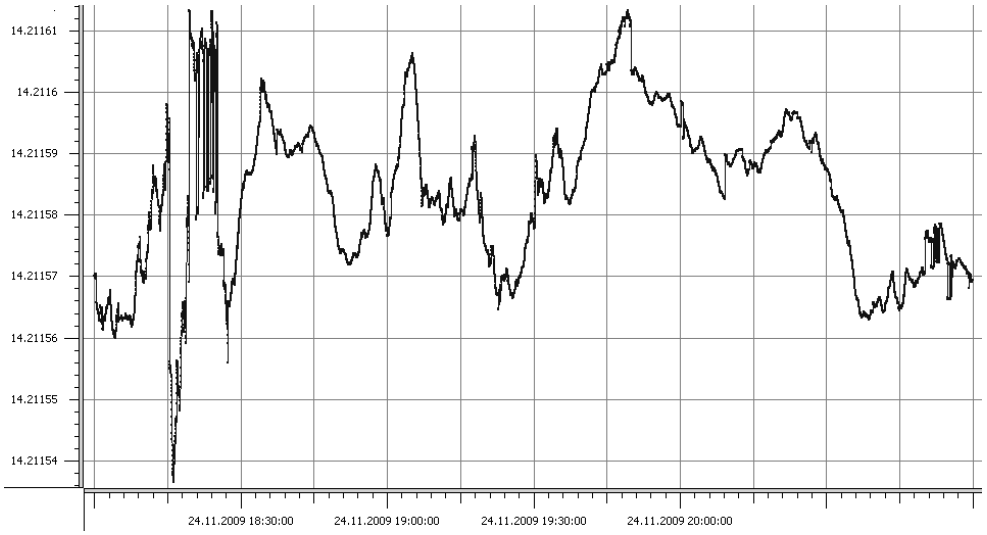

FIGURE 9. Positioning deviations in W-E direction from the Barentsburg station data in November 24, 2009.

Conclusions

Evidences of auroral activity impact on GPS/GLONASS dual frequency receiver presented. It can be realized as variations of TEC fluctuations during aurora and falling of integrity of system.

Acknowlegements

We thank the Institutes who maintain the IMAGE Magnetometer Array, Grant of RFBR 14-05-98820 r-sever-a and grant of RFBR 14-07-00512.

Work was supported by RAS Presiduim Program N 22.

Reference

1. Aarons J., B. Lin, M. Mendillo, K. Liou and M. Codrescu. *GPS phase fluctuations and ultraviolet images from the Polar satellite*. Journal Geophysical Research, 105, 2000, pp. 5201—5213.

2. Afraimovich E. I. and N. P. Perevalova. *GPS-monitoring of the Earth's upper atmosphere*. Irkutsk: SC RRS SB RAMS, 2006, p. 480.

3. Chernouss S. A, N. V. Kalitenkov. *The dependence of GPS positioning deviation on auroral activity*. International Journal of Remote Sensing,.32(1), 2011, pp. 3005—3017.

4. Shagimuratov I., S. Chernouss, I. Efishov, N. Tepenitsyna and L. Koltunenko *Conjugate And Inter-Hemispheric Occurrence of GPS TEC Fluctuations in High Latitude Ionosphere.* "Physics of Auroral Phenomena", Proc. XXXIII Annual Seminar, Apatity, 2011, pp. 151—154.

5. Kalitenkov N. V., A. N. Kalitenkov, V. I. Milkin, E. D. Tereschenko, S. A. Chernouss. *Method of location object*. Abstract of invention. RU 2484494 C1., 07.11.2011.

6. Smith A. M., C. N., Mitchell, R. J. Watson, R. W. Meggs, P. M., Kintner, K. Kauristie and F. Honary. *GPS scintillation in the high arctic associated with an auroral arc*. Space Weather, 6, 2008, p. S03D01.

POST-12

TEC Fluctuations Occurrence in High Latitudes Ionosphere during September 9, 2011 Geomagnetic Storm

Irk Shagimuratov[1], Sergej Chernouss[2], Ivan Efishov[3, 1], Yurij Cherniak[1], Luisa Koltunenko[1]

[1] *WD IZMIRAN, Kaliningrad, Russia*
[2] *PGI, Murmansk, Russia*
[3] *Immanuel Kant Baltic Federal University, Kaliningrad, Russia*

In the paper there are presented occurrence of TEC fluctuations in high latitudes ionosphere during September 9, 2011 storm. The simultaneously GPS observations from more than 30 Greenland network stations provided to obtain similarly auroral oval, irregularity oval. It is shown that irregularity oval very sensitive to changes of solar-geomagnetic activity and can use as indicator space weather conditions.

Introduction

The scintillations of trans-ionospheric radio signals are very well known indicator space weather condition. The electron density irregularities presented in high latitude ionosphere may experience phase and amplitude fluctuations of GPS sig-

nals. The small irregularities with scale less than 1 km cause fast fluctuations it is usually called scintillations. The medium and large scale ionospheric irregularities are responsible for slow fluctuations. The low frequency GPS phase fluctuations may be directly due to electron density changes along the radio ray path or the total electron content (TEC) changes. The GPS observations of Greenland network were used for diurnal TEC variations in the high latitude ionosphere to represent. This network provides unique opportunity to monitor TEC variability in polar ionosphere on a regular base. GPS stations are arranged along the latitude over the range 60—83° N (65—87° Corrected Geomagnetic Latitude) near of 25—50° W longitudes. It covers subauroral, auroral and polar ionosphere. In the report occurrence of phase fluctuations (TEC changes) in the high latitude ionosphere during September 9, 2011 storm is presented. Dual-frequency GPS measurements for individual satellite passes served as raw data. As a measure of fluctuation activity the rate of TEC (ROT, in the unit of TECU/min, 1 TECU=10^{16} electron/m^2) at 1 min. interval was used [1], as the measure of TEC fluctuations intensity do index ROTI [2].

In Fig. 1 Dst, Kp, AE indices and Bz component of IMF during 8—15 September 2011 are presented. Over Europe storms started in daytime about 14 UT. Maximal value of Dst reached ~70nT, Kp~6.

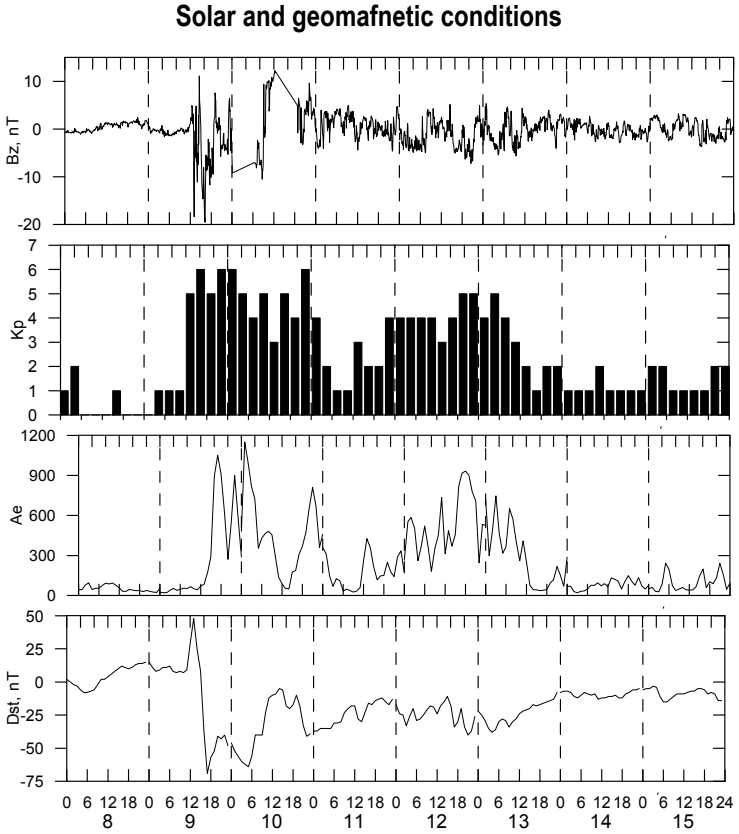

FIGURE 1. The solar and geomagnetic conditions during September 2011.

Temporal occurrence of tec fluctuations

The temporal occurrence of TEC fluctuations is clearly observed in time variations in the dual frequency carrier phase along satellite passes. Figure 2 presents the development of TEC fluctuations for all passes of the satellites observed at NNVN, KELY and RINK stations over a 24-hour interval on quiet and disturbed days. For quiet day at subauroral NNVN station fluctuations were very low. At auroral KELY station moderate fluctuations in evening time. At RINK station located at polar edge of auroral oval the low and moderate intensity of TEC fluctuations were registered whole day. During driven phase of storm (9 September) strong fluctuations were observed in 15—19 MLT at all latitudes In this time sharply increase also AE index. The increasing intensity of fluctuations began simultaneously on all stations (UT effect). The development TEC fluctuations next days have been occurred according with evolution substorm activity on recovery phase storm.

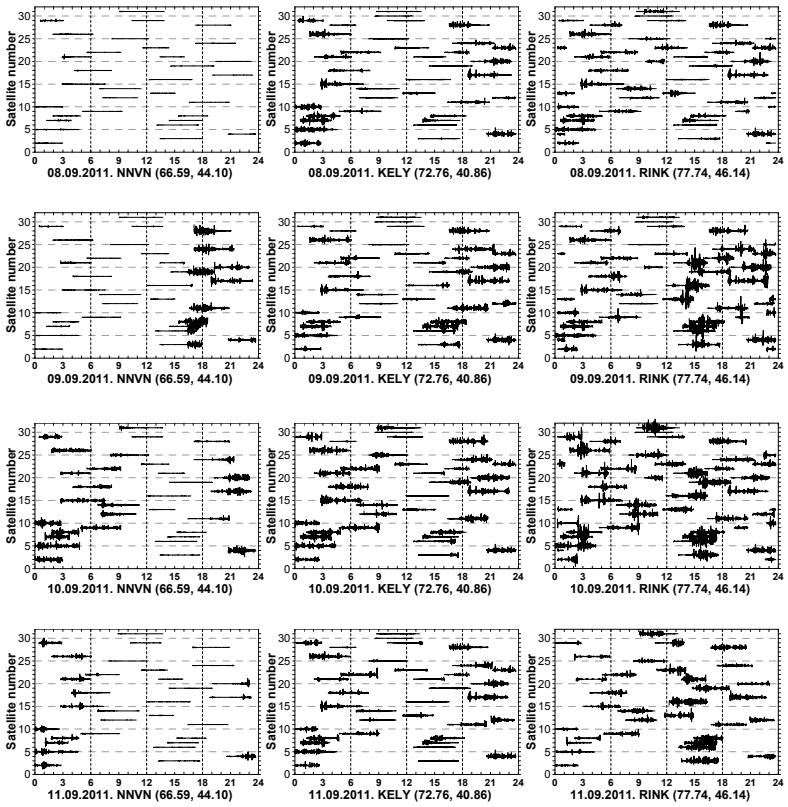

FIGURE 2. TEC fluctuations over stations YMER, SCOR and NNVN during September 2011.

Spatial occurrence of tec fluctuations

The occurrence of TEC fluctuations essentially depends on geomagnetic latitude. Latitudinal behavior of TEC was analyzed using ROTI measurements over stations located at different latitudes. For spatial and temporal distribution of TEC fluctuations to obtain it was formed images ROTI in Corrected Geomagnetic Latitude (CGL) and Magnetic Local Time (MLT) coordinates. The stations were chosen in according their location relative to auroral oval. In quiet day at subauroral station NNVN (Fig. 3) weak TEC fluctuations were observed. During storms the intensity of fluctuations increase, maximal effect took place 15—18 MLT. On next day of 10 September, strong fluctuations were registered after 18 MLT. At recovery phase storm of 11 September TEC fluctuations were registered near midnight. At auroral station KELY in quiet day fluctuations registered near midnight. During storm day of 9 September the strong fluctuations were observed as well as at NNVN station in day time. During 10 September substorm activity have been developed. In accordance it at KALY station strong TEC fluctuations were observed night as well as day time. At recovery phase (11 September) of storm the TEC fluctuation activity have been decrease.

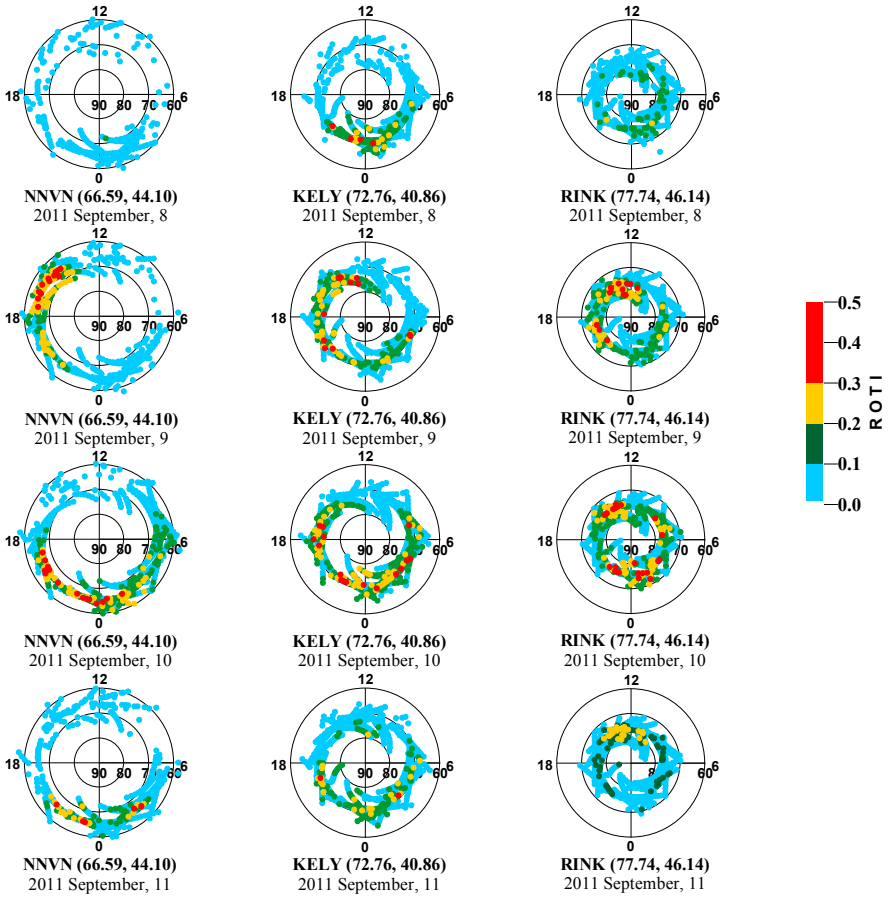

FIGURE 3. The development of TEC fluctuations over stations NNVN, KELY and RINK.

At RINK station during quiet day weak fluctuations were observed all day. The station during storm appear located in casp region. Here during storm strong TEC fluctuations were registered all day. On the whole the storm time development fluctuations activity followed by evolution solar-magnetic activity. At the same time behavior of TEC fluctuations rather is differ against auroral ionosphere. As seen on the Fig. 3 at the station the strong fluctuations were prevailed near day time.

Oval irregularities

Based on the daily GPS measurements from 30—40 selected stations, the images of spatial distribution TEC fluctuations (index ROTI) in CGC and MLT coordinates was formed. Similarly to the auroral oval, these images demonstrate the irregularity oval [3]. The occurrence of the irregularity oval relates with auroral oval, cusp and polar cap. With increase of the magnetic activity the irregularity oval expands equatorward. In Fig. 5, as example, presented dynamics irregularity oval in depended geomagnetic activity. As it seen from Fig. 5 activity and intensity TEC fluctuations weak relate with behavior of Kp and more depend on changes of IMF. Dynamics of irregularity oval well correspond also with dynamics of AE index.

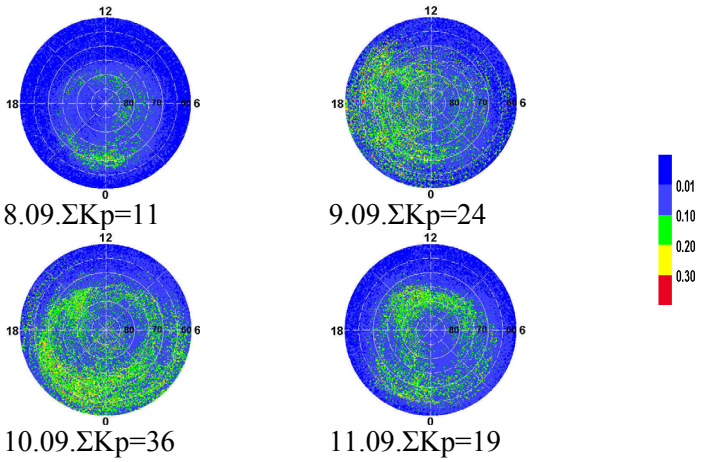

FIGURE 4. The day by day dynamics of irregularity oval for September 2011 disturbances.

Conclusions

Analyses showed that fluctuation activity of GPS signals in the high latitude ionosphere is depended on geomagnetic conditions. Intensity of fluctuations essentially increases during geomagnetic storm. Similarly to the auroral oval the spatial distribution of the fluctuations demonstrate the irregularity oval images. The occurrence of GPS-TEC fluctuations is very sensitive to solar-geomagnetic changes and can use to evaluate space weather conditions. The study showed that the operating high-latitudes GPS stations can provide to monitor in near real-time of the space weather.

Aknowledgements

The work was supported by RFFI, grant 14-05-98820 and by RAS Presiduim Program N 22.

References

1. J. Aarons. *GPS system phase fluctuations at auroral latitudes*. Journal of Geophysical Research, 102(A8), 1997, pp. 17219—17231.

2. X. Pi, A. J. Manucci, U. J. Lindqwister, C. M. Ho. *Monitoring of global ionospheric irregularities using the worldwide GPS network*. Geophysical Research Letters, 24, 1997, pp. 2283—2286.

3. I. I. Shagimuratov, A. Krankowski, I. Efishov, Yu. Cherniak, P. Wielgosz, I. Zakharenkova. *High latitude TEC fluctuations and irregularity oval during geomagnetic storms*. Earth Planets Space, 64(6), 2012, pp. 521—529.

POST-13

Why Seismo-Ionosphere Speculations Do Matter

Oleg V. Zolotov

Physics Department, Murmansk State Technical University, Sportivnayay St., 13, Murmansk, 183010 Russia; e-mail: ZolotovO@gmail.com, Namgaladze@yandex.ru

First we should do some remarks on the article's title. The word "Speculations" we use in *Latin "speculation"* meaning, i. e. some kind of discussion *without* often implied negative value. This paper we give brief review and answers on the comments — we were asked for — from journal reviewers and conferences debates. Therefore, here we limit the discussion specifically to the pre-earthquakes' ionosphere TEC (total electron content) and /or electron number density disturbances in the frame of electromagnetic physical mechanism of the Lithosphere-Ionosphere coupling. Main debatable questions we were asked for may be generalized as:

- The so called seismogenic 'features' are unreliable and due to the natural variability but not the earthquake preparation processes.
- Nobody observed ionosphere electric fields of seismic origin. The fields observed are unrelated to seismity.
- Sesmogenic electric fields do not penetrate from the ground into ionosphere, and neither the seismogenic vertical electric currents do.
- What about "something believed to be not related" to the electricity?

- "Bullets" above then summarized in *"There should be at least any experimental evidence of such current existence. Except papers of Sorokin et al. who also introduce artificial current to obtain necessary results there no any paper reporting such currents reality. So it looks like reproduction of pseudo-science. One paper based on the wrong assumptions gives birth to other paper and creates impression of some trend, but in reality this trend is based on nothing." (anon. reviewer)*

Seismo-ionosphere manifestations: Pro vs Contra

This is a very large research topic and we will rapidly overfull the pages' limit if try to cover all the "pro" and "contra" battles exist. We only provide a small example: Fraser-Smith & coauthors [1] reported magnetic noise emissions as possible precursor to M_s7.1 Loma Prieta earthquake; Campbell [2] criticized the disturbances as being due to the natural geomagnetic activity — not the earthquake-related ones. Fraser-Smith & coauthors [3] argued that the revealed anomalies are hardly to be explained by magnetic storms and other geomagnetic activity changes.

Nevertheless, the fact exists the large part of the scientific community agrees that the processes of strong earthquakes' preparation manifest themselves in parameters of the ionosphere plasma, although the physical mechanism of the Lithosphere-Atmosphere-Ionosphere coupling is a subject of scientific discussions.

Have anybody ever seen seismogenic electric fields in the ionosphere?

In our first papers we numerically checked the vertical electromagnetic drift of the ionosphere plasma under action of zonal electric field of seismic origin as the principal reason for TEC pre-earthquakes' anomalies formation. Upper Atmosphere Model (UAM) simulations showed the zonal electric fields of a few *mV/m* are required to generate TEC disturbances similar to the observed before strong seismic events [4—6]. Their values are *2—4 mV/m* for low latitudes and *4—10 mV/m* for mid-latitudes. Other researches obtained similar results [7—9] using another ionosphere models. So we can say that *F2*-region ionosphere plasma drift mechanism was independently verified. The usual reviewers' argument is — "that is synthetic fields not related to anything". Well, global measurements of ionosphere electric fields are absent, but a few papers on ionosphere quasi-static electric fields registered over the earthquakes' epicenters (and magnetically conjugated to it areas) exist (see Table 1).

Here we highlight the data presented in Tab. 1 are related to the quasi-stationary electric field, not pulsations. These disturbances were observed at both (moderately) disturbed and quiet geomagnetic conditions and the latter cases are hard to explain without considering the impact from below.

It also worth to be mentioned that significantly greater number of publications report earthquake-related ionosphere electric field spectra density disturbances. We do not cite them here, but note they support the existence of the quasi-stationary electric fields of seismic origin, although it is harder to estimate quasi-stationary disturbances from that data.

TABLE 1. Quasi-stationary ionosphere electric field disturbances observed round EQs' time in the near-epicenter and /or magnetically conjugated to it areas.

N	Instr., cite ref.	Observed effects
1.	INTERCOSMOS BULGARIA — 1300; Cmyrev & coauth. [10]	Reported quasi-stationary vertical electric field disturbances of *3—7 mV/m* (at 17:38UT over the epicenter and at 17:35.15UT over the magnetically conjugated point). Used data from 1 satellite pass, other orbits were too far from the EQ epicenter.
2.	INTERCOSMOS BULGARIA — 1300; Gousheva & coauth. [11]	Reported quasi-stationary horizontal electric field disturbances up to *7 mV/m* a few days before and after earthquakes at low and middle latitudes.
3.	INTERCOSMOS BULGARIA — 1300; Gousheva & coauth. [12]	Reported mid-latitudinal quasi-stationary electric field disturbances of *2—25 mV/m* for 30 min-4 h before and after earthquakes. E_x, E_y and E_z disturbances were *10*, *14* and *25 mV/m*, respectively. Disturbed area was shifted northward from the EQ epicenter and occupied 5—20° along the meridian.
4.	INTERCOSMOS BULGARIA — 1300; Gousheva & coauth. [13]	Reported quasi-stationary vertical electric field disturbances: (1) at polar latitudes: (a) up to *26 mV/m* for 33 min before EQ; (b) *~15 mV/m* for 31 min before EQ; (c) *10 mV/m* for 58—59 h after EQ; (2) at mid-latitudes: (a) *~15 mV/m* for 89 h before EQ; (b) *~15 mV/m* for 43 h after EQ; (3) low-latitudinal and equatorial region: (a) *5—10 mV/m* for 12 h before EQ; (b) *~10 mV/m* for 32—33 h before EQs.
5.	INTERCOSMOS BULGARIA — 1300; Gousheva & coauth. [14]	Considered 73 EQs, registered quasi-stationary electric field disturbances for 52 cases, including 27 cases before EQ and 25 cases after. Disturbances manifested themselves as E_z increases up to *~18 mV/m*, took place at the near-epicenter as well as magnetically conjugated regions. Night-time domination and dependency of the E_z increased values on the EQ magnitude and hypocenter's depth were reported.
6.	DEMETER; Zhang & coauth. [15]	Investigated three components of the quasi-stationary electric field disturbances. Reported electric field disturbances of about *1.5—16 mV/m*, in most cases less than *10 mV/m*. For 10 EQs of 27 disturbances were registered 1 day before the EQ. For 3/17 cases in Indonesia region and 1/12 cases in Chile region for EQs with M≥7 no disturbances were observed.
7.	Ionosondes Lhasa, Chongqing, Kunming, Guangzhou and Haikou Xu & coauth. [16]	Basing on five lower latitude ground-based ionosondes data analysis reported anomalous enhancement of electric field in F2-region close to the epicenter with maximal amplitude *~2 mV/m* (about 10 times of the background) at 15:00 LT on May 9 before Wenchuan earthquake.

Have anybody ever seen seismogenic electric currents in the ionosphere?

This topic is hardly linked to the previous one. The problem is the *in situ* measurements of the vertical electric current at the lower boundary of ionosphere (i. e. at 80 km above the Earth's surface) are absent. All we here may speak about is the electric currents near the ground-air interface. The problem of their penetration in the ionosphere will be discussed later this paper.

There are two main sources of near-ground air ionization referred to in articles: (1) radon and other radioactive gases; (2) breakdown ionization by the electric fields. For the first mechanism we refer to the Pulinets & coauthors researches. The second one relay on electric current generation in the ground, charge arrival at the air-ground interface and breakdown ionization of the neutral air. So called "positive holes" are often called as candidates for such charge carriers (see Freund and coauth.).

UAM calculations showed vertical electric current $\sim 10\ nA/m^2$ is required to generate TEC disturbances similar to the observed before strong earthquakes. This value is huge over the so called "fair-weather" currents which are $1—10\ pA/m^2$. This fact will be discussed later this article.

Appearance of the sesmogenic electric currents at ionosphere heights

All the above called a question on lower boundary condition we used to model impacts of seismic origin. Therefore, the reviewers faced us with the problem of mediator (i. e., underlying neutral atmosphere) between the ground and ionosphere modeling.

Pierce [17] used 1D simplified model to estimate the magnitude of the vertical electric current due to radon ionization. Here we present one of the assumptions used in his model: "*A vertical air-surface current I is due to only the conduction* and given by $I = V_H/R_H$ where V_H is potential difference between the ground and the level $h = H$." (*). Pierce [17] obtained vertical radon-related electric current of a few units of pA/m^2. This will be discussed later this section.

A few model studies tried to explain penetration of the seismogenic electric field into the ionosphere [18—19]. Denisenko & coauth. [20] performed an excellent validation of the proposed models. They all used the same approach, but differed in the upper boundary conditions. Paper [20] demonstrated that all these models had drawbacks and unable physically consistent explain seismogenic electric fields' appearance at the ionosphere heights.

This seems to forbid our results, but not. Pierce [17] as well as Denisenko results show the models, based on the (*) assumption are unable to describe the appearance of vertical electric current of required magnitude at the ionosphere heights. The problem is the assumption (*) contradict the proposed physical mechanism of the electric current formation: this current is formed presumably by the convective upward transport of charged aerosols and their gravitational sedimentation in the lower atmosphere. That means the action of gravity and pressure gradient forces is implied, but the assumption (*) neglects it.

Denisenko [21] also verified Sorokin et al. [22—23] approach and showed the assumptions made lead to unreliable results like hurricanes etc.

Let us firstly discuss the results and ways to generate such current consistently and present the first attempt to describe the problem. Our model simulations require vertical electric current density $\sim 10^{-8} A/m^2$ while the so called "fair-weather" current is a few units of pA/m^2. From this we estimate $n_d \sim 10^4 n_Q$, where n_d is seismo-disturbed numerical density values and n_Q correspond to the quiet ones (for the "fair-weather" current $\sim 2—3\ pA/m^2$). Electric current is $\boldsymbol{j} = \sum q_i n_i \boldsymbol{v_i}$ by definition. That gives two ways for the electric current number density to increase, namely via $q_i n_i$ or $\boldsymbol{v_i}$ multiplier term increase. If we consider vertical electric current (as desired), we can increase the vertical velocity; but the natural variability of the vertical wind velocity is of about one order; remind 4 orders electric currents' magnitude increase over the quiet conditions is required. If one look inside Denisenko [21], one can see that all the electric current increase he checked is due to the variability of the velocity term, and the increase lead to "hurricanes" etc. Due to this, main deposit in the vertical electric current of seismic origin over earthquake preparation zones should be from the $q_i n_i$ term; as q_i is not subject to changes we have to consider n_i term changes. n_i is proportional to the Q/L rate, where Q is the rate of electric charges generation rate (due to the ionization) and L is the loss rate. The Q term may be increased by appearance of additional ionization sources, and this is discussed more often in the papers available. The L term (which actually determine the lifetime of the charged spice) is defined by the media changes (neutral atmosphere properties). To increase vertical current one need to reduce the rate of charged spices' losses in ion-electron and ion-ion recombination reactions. As the physical mechanism is based on aerosol formation and attachment of the charges carriers, we have the following: aerosol (ion clusters) and water vapor can attach a lot of charges (possibly to millions ones), the life time of the attached to aerosols charges is much larger over the free ones. From this we have: "heavy" negative "multi-charged" particles are "tiered" to the Earth's surface by gravitation, "light" positive ions are flowing up under Archimedes' force.

The second phenomena related to the charges separation and vertical current formation is the so called *electrode effect*: existence of the regular vertical component of the electric field (maintained between the Earth and ionosphere) lead to the charges separation, blowing up positive charges carriers and "linking" towards a ground negative ones. As one can see, both mechanisms cooperate.

Therefore the reviewers faced us up with the mesosphere modeling, specially aerosol chemistry and vertical turbulent transport.

1. A.C. Fraser-Smith, A. Bernardi, P.R. McGill, et al., *Low-frequency magnetic field measurements near the epicenter of the Ms 7.1 Loma Prieta Earthquake*, GRL, 1990, V. 17, N. 9, pp. 1465—1468, doi:10.1029/GL017i009p01465

2. W.H. Campbell, *Natural magnetic disturbance fields, not precursors, preceding the Loma Prieta earthquake*, JGR, 2009, V. 114, doi:10.1029/2008JA013932

3. A.C. Fraser-Smith, P.R. McGill, A. Bernardi, *Comment on 'Natural magnetic disturbance fields, not precursors, preceding the Loma Prieta earthquake' by Wallace H. Campbell'*, JGR, 2011, V. 116, doi:10.1029/2010JA016379

4. A.A. Namgaladze, O.V. Zolotov, I.E. Zakharenkova, I.I., et al., *Ionospheric total electron content variations observed before earthquakes: Possible physical mechanism and modeling*, Proc. of the MSTU, 2009, V. 12, N. 2, pp. 308—315, URL: http://vestnik.mstu.edu.ru/v12_2_n35/articles/22_namgal.pdf

5. O.V. Zolotov, A.A. Namgaladze, I.E. Zakharenkova, et al., *Physical interpretation and mathematical simulation of ionospheric precursors of earthquakes at midlatitudes*, Geomagnetism and Aeronomy, 2012, V. 52, N. 3, pp. 390—397, doi: 10.1134/S0016793212030152.

6. A.A. Namgaladze, M. Förster, B.E. Prokhorov, O.V. Zolotov, *Electromagnetic Drivers in the Upper Atmosphere: Observations and Modeling*, In: "The Atmosphere and Ionosphere: Elementary Processes, Discharges and Plasmoids", Springer, 2013, pp. 165—220, doi: 10.1007/978-94-007-2914-8_4.

7. Liu J.Y., H. Le, Y.I. Chen, et al., *Observations and simulations of seismoionospheric GPS total electron content anomalies before the 12 January 2010 M7 Haiti earthquake*, JGR, 2011, V. 116, pp. A04302, doi:10.1029/2010JA015704.

8. M.V. Klimenko, V.V. Klimenko, I.E. Zakharenkova, et al., *Formation mechanism of great positive TEC disturbances prior to Wenchuan earthquake on May 12, 2008,* ASR, 2011, V. 48, pp. 488—499, doi:10.1016/j. asr.2011.03.040.

9. M.V. Klimenko, V.V. Klimenko, I.E. Zakharenkova, S.A. Pulinets, *Variations of equatorial electrojet as possible seismo-ionospheric precursor at the occurrence of TEC anomalies before strong earthquake,* ASR, 2012, V. 49, pp. 509—517, doi:10.1016/j. asr.2011.10.017.

10. V.M. Chmyrev, N.V. Isaev, S.V. Bilichenko, G.A. Stanev, *Observation by spaceborne detectors of electric fields and hydromagnetic waves in the ionosphere over on earthquake center,* Phys. Earth Planet. Int., 1989, V. 57. pp. 110—114, doi: 10.1016/0031-9201(89)90220-3.

11. M. Gousheva, R. Glavcheva, D. Danov, et al., *Satellite monitoring of anomalous effects in the ionosphere probably related to strong earthquakes*, ASR, 2006, V. 37. N. 4. pp. 660 665. doi:10.1016/j. asr.2004.12.050

12. M.N. Gousheva, R.P. Glavcheva, D.L. Danov, et al., *Electric field and ion density anomalies in the mid latitude ionosphere: Possible connection with earthquakes?*, ASR, 2008, V. 42, N. 1, pp. 206—212, doi:10.1016/j. asr.2008.01.015.

13. M. Gousheva, D. Danov, P. Hristov, M. Matova, *Quasi-static electric fields phenomena in the ionosphere associated with pre- and post earthquake effects*, NHESS, 2008, V. 8, N. 1, pp. 101—107, doi:10.5194/nhess-8-101-2008.

14. M. Gousheva, D. Danov, P. Hristov, M. Matova, *Ionospheric quasi-static electric field anomalies during seismic activity in August—September 1981*, NHESS, 2009, V. 9, N. 1, pp. 3—15, doi:10.5194/nhess-9-3-2009.

15. X. Zhang, X. Shen, S. Zhao, et al., *The characteristics of quasistatic electric field perturbations observed by DEMETER satellite before large earthquakes,* JAES, 2014, V. 79, pp. 42—52, doi: 10.1016/j. jseaes.2013.08.026

16. T. Xu, Ya. Hu, J. Wu, et al., *Anomalous enhancement of electric field derived from ionosonde data before the great Wenchuan earth-quake,* ASR, 2011, V. 47, pp. 1001—1005, doi:10.1016/j. asr.2010.11.006

17. E.T. Pierce, *Atmospheric electricity and earthquake prediction,* GRL, 1976, V. 3, N. 3, pp. 185—188, doi:10.1029/GL003i003p00185

18. S.A. Pulinets, A.D. Legen'ka, T.V. Gaivoronskaya, V. Kh. Depuev, *Main phenomenological features of ionospheric precursors of strong Earthquakes,* JASTP, 2003, V. 65, pp. 1337—1347.

19. V. V. Grimalsky, M. Hayakawa, V. N. Ivchenko, Yu. G. Rapoport, V. I. Zadorozhnii, *Penetration of an electrostatic field from the lithosphere into the ionosphere and its effect on the D-region before earthquakes,* JASTP, 2003, V. 65, pp. 391—407.

20. V. V. Denisenko, W. Hausleitner, G. Stangl, H. K. Biernat, *Mathematical simulation of quasi-stationary electric fields penetration through the earth's atmosphere*, Proc. 9th Int. conf. "Problems of Geocosmos", 2012, pp 81—86. URL: http://geo.phys.spbu.ru/materials_of_a_conference_2012/Geocosmos2012proceedings. pdf

21. V. V. Denisenko, *Discussion of the model of atmospheric conductor with extrinsic currents which is often used for explanation of the electric field penetration into the ionosphere from ground,* Proc. 9th Int. conf. "Problems of Geocosmos", 2012, pp. 77—80.

22. V. M. Sorokin, V. M. Chmyrev, A. K. Yaschenko, *Electrodynamic model of the lower atmosphere and the ionosphere coupling,* JASTP, 2001, V. 63, pp. 1681—1691.

23. V. M. Sorokin, A. K. Yaschenko, M. Hayakawa, *A perturbation of DC electric field caused by light ion adhesion to aerosols during the growth in seismic-related atmospheric radioactivity,* NHESS, 2007, V. 7, pp. 155—163.

POST-14

Characteristics of Global Mesospheric, Thermospheric and Ionospheric Response to 2009 Major SSW Event as Derived from Satellite and Ground-Based Observation and Obtained using Different Models of Lower and Upper Atmosphere

Maxim V. Klimenko[1], Vladimir V. Klimenko[1], Fedor S. Bessarab[1], Yurij N. Korenkov[1], Konstantin G. Ratovsky[2], Eugen V. Rozanov[3], Tommas Rodmann[4], Hanli Liu[5], Irina E. Zakharenkova[1], and Larisa P. Goncharenko[6]

[1] West Department of Institute of Terrestrial Magnetism, Ionosphere and Radio Wave Propagation RAS, Kaliningrad, 236017, Russia
[2] Institute of Solar-Terrestrial Physics SB RAS, Irkutsk, 664033, Russia
[3] Physikalisch-Meteorologisches Observatorium, World Radiation Center, Davos, Switzerland
[4] Karlsruher Institut für Technologie IMK-ASF Postfach 3640, Karlsruhe, 76021, Germany
[5] High altitude observatory NCAR 3090 Center Green Drive, Boulder, CO 80301, USA
[6] Haystack Observatory, Massachusetts Institute of Technology Off Route 40, Westford, MA 01886—1299, USA

Introduction. The interrelation between the stratosphere, mesosphere, thermosphere, and ionosphere is a very important scientific objective for the upper atmosphere forecast and knowledge of the upper atmospheric physics. The extremly prolonged minimum of the solar and geomagnetic activity of the years 2007—2009 allows to examine more carefully the relationship between processes in the middle and upper atmosphere, as this period had minimized solar and magnetospheric

sources in the upper atmosphere variability. One of the interesting examples of this relationship is Sudden Stratospheric Warming (SSW) that represents the most dramatic meteorological event in the high latitude stratosphere. The January 2009 presents a unique major SSW event that was very strong and long-lasting. Due to unique conditions during 2009 SSW event there were many observational and theoretical studies that attempted to consider different aspects of the upper atmosphere response to this SSW event [1—13]. Large part of these investigations discussed, attempted to reproduce and tried to explain the morning-noon SSW positive effects in the electron density at low latitudes [2—5, 7, 8, 10]. Only limited number of studies tried to consider separately the global mesospheric or thermospheric/ionospheric response to 2009 SSW event [1, 3, 5, 6, 9, 11]. There are numbers of the hypotheses of the main global coupling processes that lead to the ionospheric disturbances during this SSW event and should be verified [4, 7, 9, 12, 13]. There is a need to perform theoretical investigations with use of global self-consistent models of the mesosphere-thermosphere-ionosphere system. An attempt of such investigations has been made recently [1, 3, 5, 8, 13]. However, the model calculation results presented in these papers were not able to exactly reproduce the ionospheric response to this major SSW event. In this study we examined the observational results, model reproduction and ex-planation of the global response of the mesosphere-thermosphere-ionosphere system as a whole to 2009 SSW event.

Observation data and scenarios of model simulation. The main objective of our report is to study the middle and upper atmosphere response to the 2009 SSW event that was simulated separately and jointly by 4 different models: SOCOL [14] with free model run, Karlsruhe Simulation Model of the Middle Atmosphere (KASIMA) [15], Thermosphere-Ionosphere-Mesosphere-Electrodynamics General Circulation Model (TIME-GCM) [16], and Global Self-consistent Model of Thermosphere, Ionosphere, and Protonosphere (GSM TIP) [17]. All these models were previously used for study of the upper atmosphere response to SSW events [1, 18—21]. In spite of the recent progress in model developments the disagreement exists between model simulation and observations of the upper atmosphere response to the SSW 2009 event due to some spatial and temporal model limitations and the neglect of fully non-linear interaction between stationary planetary waves, atmospheric tides, and gravity waves. One of the problems that need to be clarified is the link between 2009 SSW event and mesospheric disturbances. Our attempt to use GCM SOCOL output is based on the suggestion that the model results may represent some typical or average SSW event and help to produce model runs of the response of the upper atmosphere to the perturbations, that appeared below 80 km. As expected, the variability in neutral temperature in the SOCOL model results is much less pronounced than the observed during the unique SSW 2009 event. We also produced model runs with new TIME-GCM and KASIMA simulations that better reproduce the global atmospheric temperature disturbances obtained with use of AURA and MIPAS [6] satellite data analysis during the 2009 SSW event. On the other hand, due to the lack of understanding of the correct source of disturbances at mesosphere altitudes during the 2009 SSW event and/or some model

simplifications, the global and regional thermospheric/ionospheric dynamics is not completely reproduced in the model studies. As examples, (1) the morning-noon 2009 SSW positive effects in the electron density at low latitudes, that have been recently discussed [2], are absent in GSM TIP model results; (2) the TIME-GCM simulated low-latitude ionospheric response is smaller than in the observational data; (3) there are GSM TIP model/COSMIC data disagreements in the location of maxima in global negative *foF*2 deviations during 2009 SSW event.

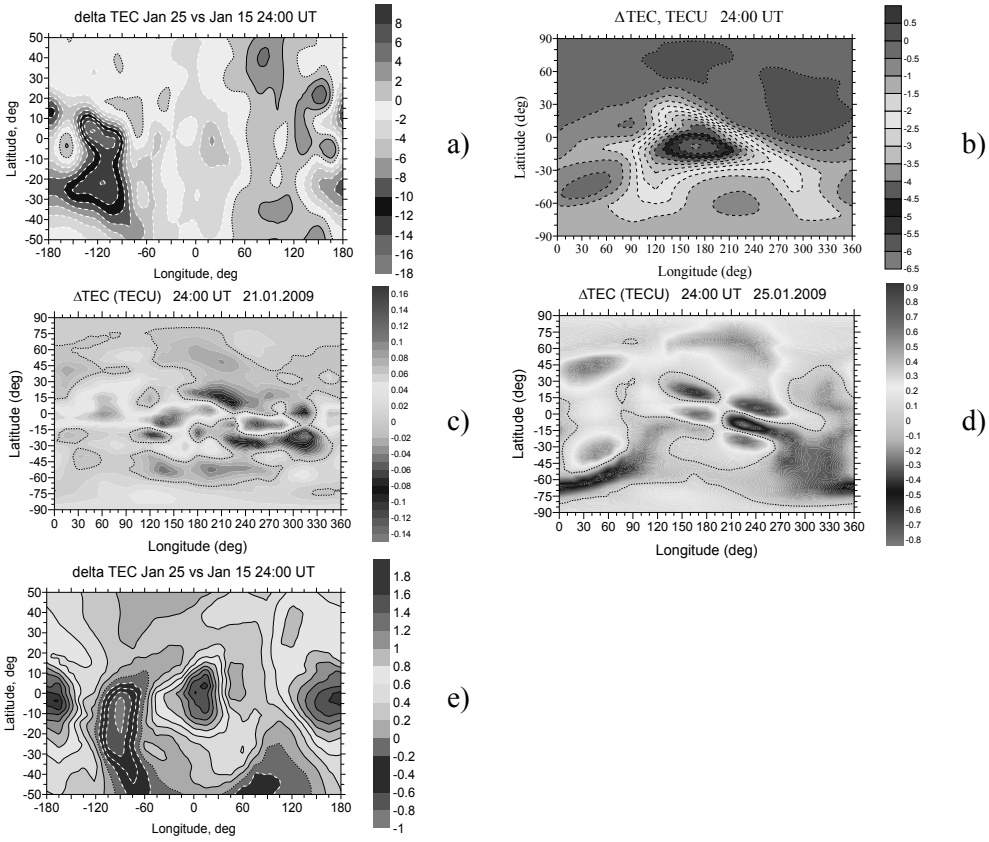

FIGURE 1. Global maps of *TEC* disturbances at 24:00 UT cased by SSW 2009 event. a) GPS TEC data observations and model results obtained using the GSM TIP model with different lower boundary conditions at an height of 80 km b) idealized mesospheric boundary; c) the calculation results of the GCM SOCOL; d) the calculation results of the KASIMA model; e) the results of calculation results of the TIME GCM model.

For the current study we perform new GSM TIP model runs using the middle and lower atmosphere models to specify more realistic perturbations in neutral parameters at the heights of mesopause in order to reproduce the global ionospheric disturbances during SSW 2009 event. Figures 1 and 2 show the compassion of

GSM TIP model results obtained using differ-ent model approach with observation data. As the ionospheric observation data source before and during the SSW 2009 event, we used ionosonde-derived *foF*2 data at different latitudes and longitudes, as well as *TEC* values calculated with use of IGS combined global ionospheric maps, that allow us to compare the global ionospheric response to this major SSW event. So this study presents the results of recent advances obtained using GCM SOCOL, KASIMA, TIME-GCM, and GSM TIP models for reproduction of the main global phenomenological features of mesospheric, thermospheric and ionospheric response to the 2009 SSW event, that was observed by different instrumentations and techniques. It is shown that the selected low boundary conditions (both idealized PW1 and output of different middle atmosphere models) do not allow fully reproduce the observed variation in the ionospheric parameters during SSW 2009 event.

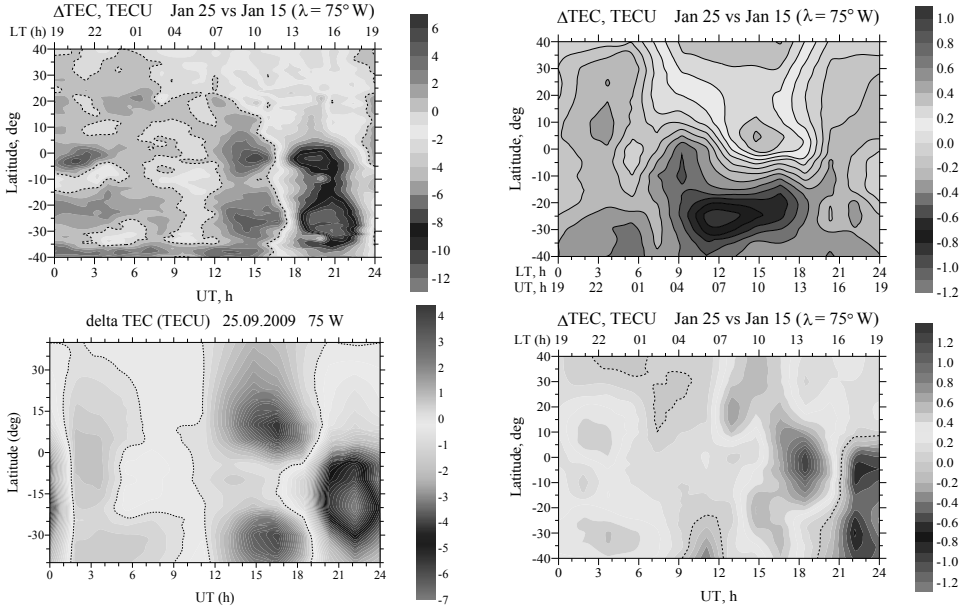

FIGURE 2. Observed by GPS receivers (top left) and simulated by GSM TIP model diurnal variations of TEC disturbances at different latitudes in American longitudinal sector (75ºW). All model results were obtained at three different model statement: (1) using KASIMA model output (top right); (2) using TIME GCM model out-put (bottom right); (3) using TIME GCM model output with additional electric potential which peak is at the equator.

Further, using the observational data of the vertical plasma drift velocity obtained by the incoherent scatter radar at Jicamarca, we set in the GSM TIP model the additional electric potential, that allow to reproduce the zonal electric field (E × B vertical plasma drift) and the observed SSW effects in the low-latitude ionosphere (see Fig. 2). In addition, we tried to reproduce the SSW ionospheric effects,

setting the internal gravity waves in the high-latitude mesosphere. We discuss the model calculation results and possible reasons for model/data disagreements and give the suggestions for further investigations.

Summary. This report presents a study of the upper atmosphere response to the 2009 major Sudden Stratospheric Warming (SSW). Here we used the global experimental data of the atmospheric temperatures, obtained by Aura satellite, ionospheric total electron content (TEC) derived from GPS TEC measurements, as well as ground-based ionosondes data at different locations. We attempted to reproduce the main characteristics of the global mesospheric, thermospheric and ionospheric SSW response using different models of the lower and upper atmosphere: (1) Karlsruhe Simulation Model of the Middle Atmosphere (KASIMA), (2) Global Circulation Model (GCM) SOCOL, (3) Thermosphere-Ionosphere-Mesosphere-Electrodynamics General Circulation Model (TIME-GCM), (4) Global Self-consistent Model of Thermosphere, Ionosphere and Protonosphere (GSM TIP).

These investigations were supported by RFBR Grants №14-05-00578 and 12-05-00392. The authors thank the International Space Science Institute (ISSI) for sponsoring the team meetings on this research topic.

References

1. F.S. Bessarab, Yu.N. Korenkov, M.V. Klimenko, V.V. Klimenko, I.V. Karpov, K.G. Ra-tovsky, M. Chernigovskaya, *Modeling the effect of Sudden Stratospheric Warming with-in the thermosphere-ionosphere system*, Journal of Atmospheric and Solar-Terrestrial Physics, Elsevier, 2012, 90—91(December 2012), pp. 77—85, doi:10.1016/j.jastp.2012.09.005.

2. J.L. Chau, L.P. Goncharenko, B.G. Fejer, H.L. Liu, *Equatorial and low latitude ionospher-ic effects during sudden stratospheric warming events*, Space Science Reviews, Springer, 2011, 168(1—4), pp. 385—417, doi: 10.1007/s11214-011-9797-5.

3. T.-W. Fang, T. Fuller-Rowell, R. Akmaev, F. Wu, H. Wang, D. Anderson, *Longitudinal variation of ionospheric vertical drifts during the 2009 sudden stratospheric warming*, J. Geophys. Res., United States, 2012, 117, A03324, doi: 10.1029/2011JA017348.

4. B.G. Fejer, B.D. Tracy, M.E. Olson, J.L. Chau, *Enhanced lunar semidiurnal equatorial vertical plasma drifts during sudden stratospheric warmings*, Geophysical Research Let-ters, United States, 2011, 38, L21104, doi: 10.1029/2011GL049788.

5. T. Fuller-Rowell, H. Wang, R. Akmaev, F. Wu, T.-W. Fang, M. Iredell, A.D. Richmond, *Forecasting the dynamic and electrodynamic response to the January 2009 sudden strato-spheric warming*, Geophysical Research Letters, United States, 2011, 38, L13102.

6. B. Funke, M. López-Puertas, D. Bermejo-Pantaleón, M. García-Comas, G.P. Stiller, T. von Clarmann, M. Kiefer, A. Linden, *Evidence for dynamical coupling from the lower atmosphere to the thermosphere during a major stratospheric warming*, Geophysical Research Letters, United States, 2010, 37, L13803, doi: 10.1029/2010GL043619.

7. L.P. Goncharenko, A.J. Coster, J.L. Chau, C.E. Vallandares, *Impact of sudden stratospheric warming on equatorial ionization anomaly*, J. Geophys. Res., United States, 2010, 115, A00G07, doi: 10.1029/2010JA015400.

8. L.P. Goncharenko, J.L. Chau, H.-L. Liu, A.J. Coster, *Unexpected connection between the stratosphere and ionosphere*, Geophysical Research Letters, United States, 2010, 37, L10101.

9. D. Pancheva, P. Mukhtarov, *Stratospheric warmings: The atmosphere—ionosphere coupling paradigm*, Journal of Atmospheric and Solar-Terrestrial Physics, Elsevier, 2011, 73(13), pp. 1697—1702, doi: 10.1016/j. jastp.2011.03.006.

10. N.M. Pedatella, J.M. Forbes, *Evidence for stratosphere sudden warming-ionosphere cou-pling due to vertically propagating tides*, Geophysical Research Letters, United States, 2010, 37(13), L11104, doi: 10.1029/2010GL043560.

11. X. Yue, W.S. Schreiner, J. Lei, C. Rocken, D.C. Hunt, Y.-H. Kuo, W. Wan, *Global iono-spheric response observed by COSMIC satellites during the January 2009 stratospheric sudden warming event*, J. Geophys. Res., United States, 2010, 115, A00G09.

12. L.P. Goncharenko, A.J. Coster, R.A. Plumb, D.I.V. Domeisen, *The potential role of stratospheric ozone in the stratosphere-ionosphere coupling during stratospheric warmings*, Geophysical Research Letters, United States, 2012, 39, L08101, doi: 10.1029/2012GL051261.

13. H. Jin, Y. Miyoshi, D. Pancheva, P. Mukhtarov, H. Fujiwara, H. Shinagawa, *Response of migrating tide to the stratospheric sudden warming in 2009 and their effects on the iono-sphere studied by a whole atmosphere-ionosphere model GAIA with COSMIC and TIMED/SABER observations*, J. Geophys. Res., United States, 2012, 117, A10323.

14. T. Egorova, E. Rozanov, V. Zubov, E. Manzini, W. Schmutz, T. Peter (2005), *Chemis-try-Climate Model SOCOL: a validation of the present-day climatology*, Atmospheric Chemistry and Physics, Germany, 2005, 5, pp. 1557—1576.

15. W. Kouker, I. Langbein, Th. Reddmann, R. Ruhnke, *The Karlsruhe Simulation Model of the Middle Atmosphere (KASIMA), Version 2, FZK Report, 6278*, Karlsruhe, 1999.

16. R.G. Roble, E.C. Ridley, *A thermosphere-ionosphere-mesosphere-electrodynamics general circulation model (time-GCM): equinox solar cycle minimum simulations (30—500 km)*, Geophysical Research Letters, United States, 1994, 21, pp. 417—420.

17. A.A. Namgaladze, Yu.N. Koren'kov, V.V. Klimenko, I.V. Karpov, F.S. Bessarab, V.A. Surotkin, T.A. Glushenko, N.M. Naumova, *Global model of the thermosphere-ionosphere-protonosphere system*, Pure and Applied Geophysics (PAGEOPH), Springer, 1988, 127(2/3), pp. 219—254.

18. H.-L. Liu, R.G. Roble, *A study of a self-generated stratospheric sudden warming and its mesospheric-lower thermospheric impacts using the coupled TIME-GCM/CCM3*, J. Geophys. Res., United States, 2002, 107(D23), ACL15, doi:10.1029/2001JD001533.

19. H.-L. Liu, R.G. Roble, *Dynamical coupling of the stratosphere and mesosphere in the 2002 Southern Hemisphere major stratospheric sudden warming*, Geophysical Research Letters, United States, 2005, 32, L13804, doi:10.1029/2005GL022939.

20. M. Stowasser, H. Oelhaf, R. Ruhnke, G. Wetzel, F. Friedl-Vallon, W. Kouker, A. Kleinert, A. Lengel, G. Maucher, H. Nordmeyer, Th. Reddmann, O. Trieschmann, T.v. Clarmann, H. Fischer, M.P. Chipperfield, *A characterization of the warm 1999 Artic winter by observations and modelling: NOy partitioning and dynamics*, J. Geophys. Res., United States, 2002, 107(D19), ACH4, doi:10.1029/2001JD001217.

21. Yu.N. Korenkov, V.V. Klimenko, M.V. Klimenko, F.S. Bessarab, N.A. Korenkova, K.G. Ratovsky, M. Chernigovskaya, A. Shcherbakov, Y. Sahai, P.R. Fagundes, R. de Jesus, A.J. de Abreu, P.J. Condor Patilongo, *The global thermospheric and ionospheric response to the 2008 minor sudden stratospheric warming event*, J. Geophys. Res., United States, 2012, 117, A10309, doi:10.1029/2012JA018018.

Сверхкритические флюидные технологии – платформа «зеленой» химии для фармации и биотехнологий

СКФ хроматография

- Разделение в 3–5 раз быстрее, чем в ВЭЖХ
- Стоимость расходуемых растворителей в 10–100 раз ниже, чем для аналогичных разделений в ВЭЖХ
- Эффективное разделение энантиомеров

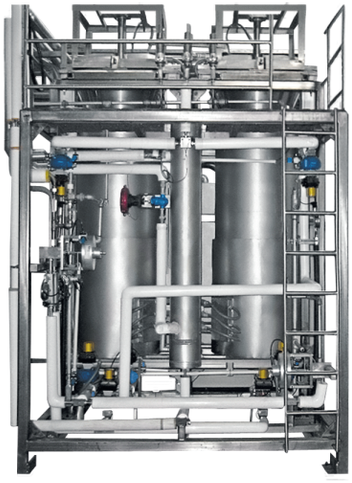

СКФ экстракция

- Физиологическая безопасность растворителя (диоксид углерода)
- Возможность работы с термолабильными соединениями
- Отсутствие стадии осушки (удаления) растворителя
- Эффективная очистка белков и полисахаридов без деградации

СКФ микронизация

- Широкий диапазон возможностей по получению требуемого размера частиц (нано-микро)
- Микронизация термически неустойчивых соединений
- Получение частиц с требуемым распределением по размеру (моно- или полидисперсность порошка)
- Отсутствие стадии сушки
- Возможность получения порошков полимеров, инкапсулированных активным ингредиентам

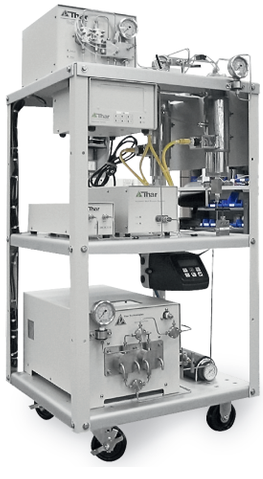

ЗАО «ШАГ»

119002, Москва,
Карманицкий пер., 9
Арбат Бизнес Центр, офис 501А
Тел.: (495) 956-1309
Факс: (495) 956-1310
www.schag.ru

- Полный спектр оборудования для осуществления СКФ технологий от лабораторных (www.schag.ru) до пилотных и промышленных систем (www.thar.ru)
- Собственная научно-исследовательская база
- Издание научно-практического журнала «Сверхкритические флюиды: теория и практика» (www.scf-tp.ru)

Scientific issued

ATMOSPHERE, IONOSPHERE, SAFETY

Proceedings
of IV International conference

Компьютерная верстка *Г. И. Винокуровой*

Подписано в печать 09.06.2014 г.
Формат 70×100 $^{1}/_{16}$. Усл. печ. л. 21,8
Тираж 500 экз. (1-й завод 100 экз.). Заказ 105

Издательство Балтийского федерального университета им. И. Канта
236041, г. Калининград, ул. А. Невского, 14